

DEVELOPMENT AND ANALYSIS OF A CLASS OF TELEGRAPH-DIFFUSION MODELS: APPLICATION TO IMAGE RESTORATION

A Thesis

Submitted to the Indian Institute of Technology Mandi

In partial fulfilment of the requirements for award of the degree

of

Doctor of Philosophy

by

Sudeb Majee

(D15028)

Under the esteemed guidance of

Dr. Rajendra K. Ray



SCHOOL OF BASIC SCIENCES

INDIAN INSTITUTE OF TECHNOLOGY MANDI

December 2020

©2020 Sudeb Majee. All rights reserved.

*Dedicated
To My Beloved Parents
&
My Family
for their endless love, support, and compromise*

CERTIFICATE BY SUPERVISOR

This is to certify that the thesis titled "**DEVELOPMENT AND ANALYSIS OF A CLASS OF TELEGRAPH-DIFFUSION MODELS: APPLICATION TO IMAGE RESTORATION**", submitted by **SUDEB MAJEE (D15028)**, to the Indian Institute of Technology Mandi, for the award of the degree of **Doctor of Philosophy**, is a bonafide record of the research work done by him under my supervision. The contents of this thesis, in full or in parts, have not been submitted to any other institute or university for the award of any degree or diploma.

Date :

Dr. Rajendra K. Ray
School of Basic Sciences
Indian Institute of Technology Mandi
Kamand-175005, INDIA.

DECLARATION BY RESEARCH SCHOLAR

I hereby declare that the entire work embodied in this thesis is the result of investigations carried out by me in the School of Basic Sciences, Indian Institute of Technology Mandi, under the supervision of Dr. Rajendra K. Ray, and that it has not been submitted elsewhere for any degree or diploma. In keeping with the general practice, due acknowledgments have been made wherever the work described is based on finding of other investigators.

Kamand 175005

Date:

Signature:

SUDEB MAJEE

LIST OF PUBLICATIONS

The thesis is based on the following research papers published/submitted in international journals.

1. **S. Majee**, R. K. Ray, and A. K. Majee, A Gray Level Indicator-Based Regularized Telegraph Diffusion Model: Application to Image Despeckling, *SIAM Journal on Imaging Sciences (SIIMS)*, 13(2): 844-870 (2020).
2. **S. Majee**, S. K. Jain, R. K. Ray, and A. K. Majee, On the Development of a Coupled Nonlinear Telegraph-Diffusion Model for Image Restoration, *Computers & Mathematics with Applications (CAMWA)*, 80(7): 1745-1766 (2020).
3. S. K. Jain, **S. Majee**, R. K. Ray, and A. K. Majee, On the Existence and Uniqueness of Weak Solutions of a Coupled Diffusion System Related to Image Restoration (Under Review).
4. **S. Majee**, R. K. Ray, and A. K. Majee, An Efficient Nonlinear Hyperbolic-Parabolic Coupled PDE Model for Image Despeckling (Under Review).
5. **S. Majee**, S. K. Jain, R. K. Ray, and A. K. Majee, A Fuzzy Edge Detector Driven Telegraph Total Variation Model for Image Despeckling (Under Review).

Acknowledgments

In this brief acknowledgment, I wish to sincerely thank all who have encouraged and provided me inspiration, guidance, and support in every situation and contributed to the successful completion of this work. First and foremost, I wish to express my sincere and humble gratitude to the Almighty, who has provided me the strength from the start to the completion of this study. Next, I am very grateful for the opportunity I have been given to do a Ph.D. at the School of Basic Sciences at IIT Mandi. I want to express my sincere gratitude to my supervisor Dr. Rajendra K. Ray, for accepting me in his research group. He introduced me to the exciting research field of partial differential based image processing. I have been highly favored to have a supervisor who provided me with supervision to lead research and the liberty to explore independently. His passion, responsibility, and compassion he has for his disciples are exceptional. He continuously supported me during my frustrations. He is friendly, concerned, and inspiring during my Ph.D. It has been a tremendously pleasant experience working under his guidance. I acknowledge full support and help during the work with this dissertation and how he has supervised me to grow as an independent researcher. Moreover, I am thankful to the additional members of my doctoral committee: Dr. Suman K. Pal, Dr. Muslim Malik, Dr. Manoj Thakur, and Dr. Rajesh Ghosh, for their valuable remarks and suggestions. I want to express my deepest gratitude to my senior Dr. Subit K. Jain, Department of Mathematics, NIT Hamirpur. I have been fortunate to have such a senior in our research group. From the beginning of this thesis work to the successful completion, I have gained a lot of ideas from him. Moreover, his friendship and supportive behavior gave me fresh air to living in the research work when I have disappointed with my failures. Also, I want to express my sincere thanks to my other senior, Dr. Atendra Kumar, a person who always makes me realized that time has value and must be spent wisely and in an organized manner. I have to give a big “thanks” to Dr. Manotosh Kumbhakar. I have learned a lot of things related to research work from him. Also, we have immensely enjoyed working together. It was a fantastic time with him at the Kamand campus.

I want to give a special thanks to Dr. Ananta K. Majee, Department of Mathematics, Indian Institute of Technology Delhi, for his help and support in accomplishing my doctoral work. At any moment, when I needed his guidance, he was evermore available despite his busy schedule. He cared so much about my work and answered my questions and doubts immediately. I consider myself very blessed that I have found a very attentive and supportive collaborator like him.

I also wish to thank Dr. Adrian L. Jannetta for providing me the MATLAB code for his Maximum Entropy Method algorithm.

I want to extend my thanks to Dr. Liu Qiang for providing me a collection of relevant documents related to the theoretical PDE and a beneficial discussion about one of his research work.

Also, I acknowledge the support and help given by staff members of IIT Mandi.

Moreover, I acknowledge monetary assistance from the Ministry of Human Resource Development (MHRD).

I want to give a big thanks to the other group members of our research group, Amarjit, Pankaj, Ashwani, Mandira, and Amit, for their support, affection, love, and care in this journey.

Especial thanks to my friends Dr. Dushyant, Dr. Gourab, Dr. Pravat, Dr. Rajesh, Dr. Sekhar, Dr. Somnath, Dr. Subhashis, Dr. Supriyo, Dr. Syamantak, Dr. Swati, Aranya, Chinmoy, Koushik, Partha, Raktim, Sumanta, Nishith, Vikas, Vipin, Subhash, Sourabh, Kartik, Manoj, Pawan, Salman, and many more for their friendship and great memories.

Last but not least, I passionately offer my sincerest gratitude to all my family members, relatives, and Sudeshna for their generous love and care. I thank my parents, elder brother Bhudeb Majee, and late grandmother for their support, inspiration, eternal love, and the compromise they made to give me the best possible education. This journey would not have been possible without their constant support and guidance over the years.

Sudeb Majee

Abstract

In digital image processing applications, the detailed analysis of images always relies on the quality of the acquired image. In the real scenario, images are often degraded by different types of noises, e.g., additive, multiplicative, or mixed nature. These types of noises affect the acquired images during image formation, transmission, and recording processes and diminish the purity of the edge/texture information in the images. Hence the development of an advanced noise removal algorithm is always an essential aspect of the image processing community. It has been known for a long time that partial differential equation (PDE) based models can be efficient strategies for the noise removal process in digital images.

This thesis work mainly focuses on the development and analysis of a class of PDE based models and their applications to image restoration. Also, an extensive computational study is presented in this thesis to validate and confirm the ability of the developed models. In the existing literature, most of the researchers have concentrated their interest only on parabolic PDE based approaches for the noise removal process; a few researchers have used the hyperbolic-parabolic PDE based techniques only for the additive noise removal process. To the best of our knowledge, the present work marks the first step towards the use of hyperbolic-parabolic PDE based techniques for the multiplicative speckle noise elimination process. Details analysis of existence and uniqueness of weak solution is carried out for each developed model using fixed point theorem. Extensive numerical experiments are performed on natural as well as synthetic and real images to illustrate and compare the performance of each developed model with the performance of various existing approaches. The experimental results show that the proposed models are efficient for image denoising and can upgrade the visual appearance of the located edges better than other existing models.

Chapter 1 describes a concise introduction about the aims and objectives of the research problem considered here, along with details literature survey.

In **Chapter 2**, the existence and uniqueness of the weak solution of a coupled diffusion system is presented. Moreover, the computational experiments show that the considered model could be applied for image denoising.

A coupled telegraph equation based image denoising model for additive Gaussian noise removal is proposed in **Chapter 3**. First, we verify that the present system has a unique global weak solution using Banach's fixed point theorem. Then apply this approach over a set of grayscale images to illustrate the superiority of the proposed model over the recently developed telegraph diffusion-based techniques as well as the model discussed in Chapter 2.

In **Chapter 4**, a gray level indicator based nonlinear telegraph diffusion model is presented for image despeckling. The proposed model uses the benefit of the combined effect of the diffusion equation as well as the wave equation. In this method, the diffusion coefficient depends not only on the image gradient but also on the gray level of the image, which controls the diffusion process better than only gradient-based diffusion techniques. Moreover, we establish the well-posedness of the system using Schauder fixed point theorem. We show the superiority of the proposed model over three recently developed techniques on a set of gray level test images. Also, check the noise removal ability of the present model over some real

SAR images corrupted by speckle noise with different noise levels. To the best of our knowledge, this is the first work that utilizes a telegraph diffusion based model for image despeckling.

In **Chapter 5**, a hyperbolic-parabolic coupled system is presented for image despeckling. A separate equation is used to calculate the edge variable, which improves the quality of edge information in the despeckled images. A well-posedness result of the proposed system is established via Schauder fixed point theorem. A generalized weighted average finite-difference scheme, along with the Gauss-Seidel iterative technique, is used to solve the coupled system. Computational analyses are reported to show the effectiveness of the proposed model, with recently developed models, over a set of test images contaminated by speckle noise. Additionally, we check the noise removal capability of the present model over real SAR and Ultrasound images corrupted by speckle noise. Overall, our study confirms that the proposed approach is more effective than the other existing image despeckling models.

In **Chapter 6**, we discuss a telegraph total variation based model, with fuzzy edge detector, for image despeckling. A new attempt has been made to utilize the benefits of the total variation framework and fuzzy set theory. The proposed approach combines the telegraph equation and the fuzzy edge detector function, which is robust to noise as well as preserves the image structural details efficiently. Moreover, we establish the existence and uniqueness of a weak solution of a regularized version of the proposed system using Schauder fixed point theorem. With the proposed model, despeckling is carried out on natural and real SAR images. The experimental results of the proposed model are reported, which found better in terms of noise suppression and detail preservation as compared to various existing approaches. To the best of our knowledge, this is the first work that utilizes a telegraph total variation based model for image despeckling.

Chapter 7 describes a computational study on different color images when they are degraded by additive Gaussian noise, multiplicative speckle noise, and blurring effect.

Chapter 8 provides a general conclusion of the whole thesis work and future scope of the research work.

Keywords: Image restoration; Nonlinear diffusion; Telegraph equation; Total-Variation methods; Gray level indicator; Fuzzy edge detector; Texture preservation; Finite difference method; Numerical scheme; Well-posedness; Weak solution; Fixed point theorem.

Contents

1	Introduction	1
1.1	Basics of Digital Image Processing	2
1.1.1	Digital Image	2
1.1.2	Image Noise	3
1.1.3	Inverse Problem & Image Restoration	4
1.2	PDE Based Image Denoising: An Overview	6
1.3	Numerical Method & Stopping Criterion	15
1.4	Image Quality Measures	17
1.5	Motivation & Objectives	18
1.6	Thesis Overview	20
2	On the Existence and Uniqueness of Weak Solutions of a Coupled Diffusion System Related to Image Restoration	23
2.1	General Introduction	23
2.2	Existence and Uniqueness of Weak Solution	24
2.2.1	Technical framework & statement of the main result	24
2.2.2	Linearized model & its well-posedness	25
2.2.3	Proof of Theorem 2.1	29
2.2.4	Uniqueness of weak solution	30
2.3	Numerical Implementation	32
2.4	Computational Results & Discussion	33
2.5	Conclusion	39
3	On the Development of a Coupled Nonlinear Telegraph-Diffusion Model for Image Restoration	41
3.1	General Introduction	41
3.2	Well-posedness of Weak Solutions	44
3.2.1	Technical framework & statement of the main result	44
3.2.2	Linearized model & its well-posedness	45

3.2.3	Well-posedness of a local solution	50
3.2.4	Proof of Theorem 3.1	54
3.3	Numerical Implementation	54
3.4	Computational Results & Discussion	55
3.4.1	Selection of parameters	55
3.4.2	Results and Discussion	59
3.5	Conclusion	71
3.6	Appendix	71
4	A Gray Level Indicator-Based Telegraph Diffusion Model: Application to Image Despeckling	73
4.1	General Introduction	73
4.2	TDM Model for Image Despeckling	77
4.3	Well-posedness of Weak Solutions	78
4.3.1	Technical framework & statement of the main result	78
4.3.2	Linearized model & existence of weak solution	79
4.3.3	Proof of Theorem 4.1	82
4.3.4	Uniqueness of weak solution	83
4.4	Numerical Implementation	87
4.5	Computational Experiments	87
4.5.1	Image Quality Measurement	88
4.5.2	Computational Results & Discussion	88
4.6	Conclusion	98
5	An Efficient Nonlinear Hyperbolic-Parabolic Coupled PDE model for Image Despeckling	101
5.1	General Introduction	101
5.2	The Proposed Method	102
5.3	Existence and Uniqueness of Weak Solution	103
5.3.1	Technical framework & statement of the main result	103
5.3.2	Linearized model & its wellposedness	104
5.3.3	Proof of Theorem 5.1	105
5.3.4	Uniqueness of weak solution	107
5.4	Computational Results & Discussion	109
5.4.1	Numerical Implementation	110
5.4.2	Results for the Artificially Noised Images	111
5.4.3	Results for the Real Images	112
5.5	Conclusion	121

6 A Fuzzy Edge Detector Driven Telegraph Total Variation Model For Image Despeckling	125
6.1 General Introduction	125
6.2 Intuitionistic Fuzzy Sets	127
6.3 Proposed Telegraph Total Variation Model	129
6.3.1 The Proposed Model	129
6.3.2 The advantages & novelty of the proposed model	130
6.4 Existence and Uniqueness of Weak Solution	131
6.4.1 Technical framework & statement of the main result	131
6.4.2 Linearized model & existence of weak solution	132
6.4.3 Uniqueness of weak solution	137
6.5 Numerical Implementation	139
6.6 Computational Results & Discussion	140
6.6.1 Setup and Parameters	140
6.6.2 Image Quality Measurement	141
6.6.3 Results on Synthetic Images	141
6.6.4 Results on Real Images	148
6.7 Conclusion	149
7 A Computational Study On Color Images	153
7.1 Color Image Denoising	153
7.1.1 Results for Additive Gaussian Noise	154
7.1.2 Results for Multiplicative Speckle Noise	154
7.2 Color Image Deblurring	156
7.3 Conclusion & Future Scope	161
8 Conclusion and Future Scope	165
8.1 General Conclusions	165
8.2 Major Contributions	165
8.3 Future Scopes	167
Bibliography	182

LIST OF SYMBOLS

Symbol	Description
Ω	Open and bounded subset of \mathbb{R}^n ($n \in \mathbb{N}$).
$\partial\Omega$	Boundary surface of Ω .
dx	Lebesgue measure in \mathbb{R}^n .
T	A specified time.
Ω_T	$\Omega \times (0, T)$.
$\partial\Omega_T$	$\partial\Omega \times (0, T)$.
∂_n	Normal derivative on $\partial\Omega$.
∂_t	1st-order time derivative.
∂_{tt}	2nd-order time derivative.
∂_{ttt}	3rd-order time derivative.
*	Convolution operator.
G_ξ	Gaussian kernel on space only of width ξ .
∇	Gradient operator.
div	Divergence operator.
Δ	Laplace operator.
$D^n u$	n th-order weak derivative of u .
$C(\Omega)$	Space of real-valued continuous functions.
$C_0^1(\Omega)$	Space of real-valued functions, continuously differentiable with compact support.
$L^p(\Omega)$	Space of Lebesgue measurable functions u such that $\int_{\Omega} u ^p dx < \infty$, ($1 \leq p < \infty$).
$L^\infty(\Omega)$	Space of Lebesgue measurable functions u such that there exists a constant c with $ u(x) \leq c$, a.e. $x \in \Omega$.
$H^r(\Omega)$	Sobolev space of functions $u \in L^2(\Omega)$ such that all derivatives up to order $r \in \mathbb{N}$ belong to $L^2(\Omega)$.
$(H^r(\Omega))'$	Dual space of $H^r(\Omega)$.

Symbol	Description
$\ \cdot\ _{\mathbb{X}}$	Norm on a Banach space \mathbb{X} .
$L^p(0, T; \mathbb{X})$	Space of all measurable functions $u : [0, T] \rightarrow \mathbb{X}$ such that $\ u\ _{L^p(0, T; \mathbb{X})} := \left(\int_0^T \ u(t)\ _{\mathbb{X}}^p dt \right)^{1/p} < \infty \text{ for } 1 \leq p < \infty.$
$L^\infty(0, T; \mathbb{X})$	Space of all measurable functions u such that $\ u\ _{L^\infty(0, T; \mathbb{X})} := \text{ess sup}_{0 \leq t \leq T} \ u(t)\ _{\mathbb{X}} < \infty.$
$BV(\Omega)$	Space of functions with bounded variation defined as a space of L^1 valued functions u on Lipschitz domain Ω such that $\int_{\Omega} Du := \sup \left\{ \int_{\Omega} u \operatorname{div}(\varphi) dx \mid \varphi \in C_0^1(\Omega; \mathbb{R}^n), \varphi \leq 1 \right\} < \infty.$

LIST OF ABBREVIATIONS

PDE	Partial Differential Equation
PDEs	Partial Differential Equations
CPDE	Coupled Partial Differential Equation
SSIM	Structural Similarity Index Measure
MSSIM	Mean Structural Similarity Index Measure
SNR	Signal to Noise Ratio
PSNR	Peak Signal to Noise Ratio
SI	Speckle Index
NSD	Noise Standard Deviation
BRISQUE	Blind/Referenceless Image Spatial Quality Evaluator
SAR	Synthetic Aperture Radar
MEM	Maximum Entropy Method
PSF	Point spread function

List of Tables

2.1	MSSIM and PSNR values of restored images. Selected parameter values for the numerical experiments.	37
3.1	Parameter values for the numerical experiments.	58
3.2	MSSIM and PSNR values of restored images.	69
3.3	MSSIM and PSNR values of restored images.	70
4.1	MSSIM and PSNR values of despeckled images.	96
4.2	Parameter values for the numerical experiments.	97
4.3	SI values for the real SAR images using the proposed model.	98
5.1	MSSIM and PSNR values of despeckled images.	117
5.2	Parameter values for the numerical experiments.	118
6.1	MSSIM, PSNR, and SI values of despeckled images.	142
6.2	Comparison of SI and BRISQUE (BQ) values of despeckled images.	151

List of Figures

1.1	Peppers image: (a) Clear image. (b) Degraded by Gaussian noise with standard deviation (σ)= 40. (c) Degraded by speckle noise with $L = 5$.	4
2.1	Clean images.	35
2.2	Barbara image corrupted by additive Gaussian noise with $\mu = 0$ and $\sigma = 30$ and restored by different models.	35
2.3	A brick image corrupted by additive Gaussian noise with $\mu = 0$ and $\sigma = 30$ and restored by different models.	35
2.4	Ratio images of the image Figure 2.1b and images; Figures 2.3b–2.3d.	35
2.5	Part of the 50th slice of the brick image corrupted by additive Gaussian noise with $\mu = 0$ and $\sigma = 30$ and restored by different models.	36
2.6	A starfish image corrupted by additive Gaussian noise with $\mu = 0$ and $\sigma = 30$ and restored by different models.	37
2.7	Ratio images of the clear image Figure 2.1c and the images; Figures 2.6a–2.6d.	37
2.8	Contour maps of the clear starfish image Figure 2.1c and the images; Figures 2.6a–2.6d.	38
3.1	Set of test images: (a)–(b) natural images (c) synthetic image (d)–(e) texture images (f) aerial image (g) satellite image.	56
3.2	Influence of the parameter α . (a)–(b) Results for circle image. (c)–(d) Results for peppers image.	57
3.3	A 512×512 peppers image corrupted by Gaussian noise with $\sigma = 20$ and restored by different models. (a) Indicate the one-dimensional slices. (b) Results for the Slice-1. (c) Results for the Slice-2. (d) Results for the Slice-3.	61
3.4	A 256×255 tree image corrupted by Gaussian noise with $\sigma = 20$ and restored by different models.	62
3.5	(a) 2D contour map of the clean circle image 3.1c. (b) 3D surface plot of the clean circle image 3.1c.	62

3.6	A 299×299 circle image corrupted by Gaussian noise with $\sigma = 20$ and restored by different models. (g) Ratio image for the clean circle image Figure 3.1c, (h)–(l) Ratio image for the restored images; Figure 3.6b–3.6f.	63
3.7	(a)–(f) 2D contour plot of the the imgaes; Figure 3.6a–3.6f. (g)–(l) 3D surface plot of the images; Figure 3.6a–3.6f.	64
3.8	A 512×512 mosaic image corrupted by Gaussian noise with $\sigma = 100$ and restored by different models. (g)–(l) 2d contour plot of the the imgaes; Figure 3.8a–3.8f.	65
3.9	A 512×512 brick image corrupted by Gaussian noise with $\sigma = 40$ and restored by different models. (g)–(k) Ratio image for the restored images; Figure 3.9b–3.9f.	66
3.10	A 512×512 brick image corrupted by Gaussian noise with $\sigma = 20$ and restored by different models. (a) Indicate the one-dimensional slices. (b) Results for the Slice-1. (c) Results for the Slice-2. (d) Results for the Slice-3.	67
3.11	A 256×255 moon image corrupted by Gaussian noise with $\sigma = 60$ and restored by different models.	68
3.12	Improved PSNR value vs. the corresponding iteration number for different models. Both the graphs are plotted for the result of the circle image: (a) The circle image is degraded by Gaussian noise with $\sigma = 20$ and restored by different models. (b) The circle image is degraded by Gaussian noise with $\sigma = 80$ and restored by different models.	68
4.1	Clear test images.	90
4.2	Restored image for different values of τ : $K = 0.5$, $\nu = 1$, and $\gamma = 0.5$. (a) Noisy image with $L = 1$. (b) MSSIM=0.96441, PSNR=34.6963, CPU time=69.8468s. (c) MSSIM=0.96441, PSNR=34.6963, CPU time=46.832s. (d) MSSIM=0.96441, PSNR=34.6960, CPU time =32.4649s. (e) MSSIM=0.96439, PSNR=34.6959, CPU time=27.48s. (f) MSSIM=0.94058, PSNR=33.8212, CPU time=15.3603s.	90
4.3	Image corrupted by speckle noise with $L = 1$ and restored by different models.	91
4.4	Image corrupted by speckle noise with $L = 3$ and restored by different models.	91
4.5	Image corrupted by speckle noise with $L = 5$ and restored by different models.	92
4.6	Image corrupted by speckle noise with $L = 1$ and restored by different models.	92

4.7	Image corrupted by speckle noise with $L = 3$ and restored by different models.	93
4.8	Image corrupted by speckle noise with $L = 5$ and restored by different models.	93
4.9	Image corrupted by speckle noise with $L = 1$ and restored by different models.	94
4.10	Image corrupted by speckle noise with $L = 3$ and restored by different models.	94
4.11	Image corrupted by speckle noise with $L = 5$ and restored by different models.	95
4.12	First row: (a) Image corrupted by speckle noise with $L = 10$. (b)–(e) Restored images by different models. Second row: (f) Ratio image for the clear image Figure 4.1c, (g)–(j) Ratio images for the restored images Figures 4.12b–4.12e.	95
4.13	Contour maps of the clear circle image Figure 4.1c and the images Figure 4.12a–4.12e.	96
4.14	3D surface plots of the clear circle image Figure 4.1c and the images Figure 4.12a–4.12e.	97
4.15	Real SAR images and restored images using the proposed model.	99
5.1	Image corrupted with speckle look $L = 1$ and restored by different models.	112
5.2	Image corrupted with speckle look $L = 3$ and restored by different models.	113
5.3	Image corrupted with speckle look $L = 5$ and restored by different models.	113
5.4	Image corrupted with speckle look $L = 1$ and restored by different models.	114
5.5	Image corrupted with speckle look $L = 3$ and restored by different models.	114
5.6	Image corrupted with speckle look $L = 5$ and restored by different models.	115
5.7	Image corrupted with speckle look $L = 1$ and restored by different models.	115
5.8	Image corrupted with speckle look $L = 3$ and restored by different models.	116
5.9	Image corrupted with speckle look $L = 5$ and restored by different models.	116

5.10	Contour plots of the images in Figure 5.9.	117
5.11	3D surface plots of the images in Figure 5.9.	118
5.12	Part of the 88 th slice of the peppers image corrupted with speckle look $L = 10$ and restored by different models.	119
5.13	Part of the 60 th slice of the texture image corrupted with speckle look $L = 10$ and restored by different models.	120
5.14	Space Radar Image and restored by different models.	121
5.15	(a) Improved Speckle Index value vs. the corresponding iteration number for various models, (b) Improved BRISQUE values vs. the corresponding iteration number for various models. Parameter val- ues for the numerical experiments: (i) MCPDE: $\alpha = 1.5, k = 10$, (ii) Shan: $\alpha = 1.5, \beta = 0.5$, (iii) TDM: $\gamma = 5, \nu = 2, K = 4$, (iv) Proposed: $\gamma = 5, \alpha = 2, \beta = 1, \iota = 0.1, \nu = 1$.	122
5.16	Ultrasound Image and restored by different models.	122
5.17	(a) Comparison of Speckle Index values after 100 iterations for var- ious models, (b) Comparison of NSD values after 100 iterations for various models. Parameter values for the numerical experiments: (i) MCPDE: $\alpha = 1.5, k = 10$, (ii) Shan: $\alpha = 1.5, \beta = 0.8$, (iii) TDM: $\gamma = 2, \nu = 2, K = 4$, (iv) Proposed: $\gamma = 1, \alpha = 1, \beta = 2, \iota =$ $0.1, \nu = 0.1$.	123
6.1	Clear images.	142
6.2	Boat image (512×512). (a) Speckled image: $L = 3$. (b)–(f) De- speckled by various approaches. (g) Speckled image: $L = 10$. (h)–(l) Despeckled by various approaches.	143
6.3	Brick image (256×256). (a) Speckled image: $L = 3$. (b)–(f) De- speckled by various approaches. (g) Speckled image: $L = 10$. (h)–(l) Despeckled by various approaches.	144
6.4	(a) Ratio image for the original image 6.1b, (b)–(f) Ratio images for the despeckled images 6.3h–6.3l. (g) Indicate the one-dimensional slices. (h) Results for the Slice-1. (i) Results for the Slice-2. (j) Results for the Slice-3.	145
6.5	Circle image (299×299). (a) Speckled image: $L = 3$. (b)–(f) Despeckled by various approaches. (g) Speckled image: $L = 10$. (h)–(l) Despeckled by various approaches.	146
6.6	(a)–(f) 2D Contour map of the images 6.5g–6.5l. (g)–(l) 3D surface plot of the images 6.5g–6.5l.	147

6.7	Improved PSNR value vs. the corresponding iteration number for various models. (a) Results for the brick image; 6.3g–6.3l. (b) Results for the circle image; 6.5g–6.5l.	148
6.8	(a) SAR Image-1: One look radar image (Agency, n.d.). (b)–(d) Restored by different models.	149
6.9	(a) SAR Image-2: Image of KOMPSAT/Arirang-5 of a part of the Himalayan Arc (eoPortal: Sharing Earth Observation Resources, 2005). (b)–(d) Restored by different models.	150
6.10	A Ultrasound image of fetal foot and restored by different models.	150
6.11	A Ultrasound image of liver cyst and restored by different models.	151
6.12	Relative error vs. the iteration number for various models.	151
7.1	Clear images.	154
7.2	(a) PSNR=15.00, (b) 20.90, (c) PSNR=21.05.	155
7.3	(a) PSNR=15.03, (b) 25.80, (c) PSNR=25.99.	155
7.4	(a) PSNR=14.73, (b) 22.65, (c) PSNR=22.70.	155
7.5	(a) PSNR=14.89, (b) 28.38, (c) PSNR=28.51.	156
7.6	(a) PSNR=17.84, (b) 22.55, (c) PSNR=22.73.	156
7.7	(a) PSNR=17.13, (b) 27.11, (c) PSNR=27.99.	157
7.8	(a) PSNR=16.83, (b) 23.65, (c) PSNR=24.08.	157
7.9	(a) PSNR=17.91, (b) 28.47, (c) PSNR=28.61.	158
7.10	A degraded baboon image and restored by MEM.	161
7.11	A degraded peppers image and restored by MEM.	161
7.12	A degraded cemetery image and restored by MEM.	162
7.13	A degraded parrots image and restored by MEM.	162
7.14	A degraded rapids image and restored by MEM.	162
7.15	A degraded text image and restored by MEM.	163

Chapter 1

Introduction

Images are entirely interfering with the real-world, and as it is commonly known, “ a picture is worth a thousand words ” . However, due to the natural barriers of acquiring equipment or the presence of intermittent fluctuations in the medium, the images acquired by a scanner or digital camera are generally contaminated by different types of noises (Castleman, 1993; Nakamura, 2016). Hence the image restoration is a crucial stage for high-level image analysis, e.g., image segmentation, object recognition, scene understanding, etc. The fundamental aim of image restoration is to distinguish between essential image features that should be kept or even improved and those parts of the image that are considered as noise and should be removed. Precisely, this is an elementary research area in the field of imaging science, where an image is deemed to be an input. A set of operations acting on the input image and produces an output, which may be an image, a collection of characteristics or data (profiles, objects, etc.) or parameters associated with the input image. Initially, digital image processing originated as a research area for computer scientists and electrical engineers and showed not to take the attention of mathematicians. Slowly, it changes to an interdisciplinary research area, and it has attracted much attention from the mathematical society. Nowadays, several mathematical strategies, in various frameworks, are available to operate and to investigate images: Statistical and stochastic modeling (Geman and Geman, 1984; Armstrong *et al.*, 1997), Fourier transform methods (Kim *et al.*, 2001; Yaroslavsky, 2014), wavelets methods (DeVore *et al.*, 1992; Chambolle *et al.*, 1998; Stephane, 1999), Bayesian methods in spatial domain (Lee, 1980; Frost *et al.*, 1982; Kuan *et al.*, 1985), Bayesian methods in transformed domain (Meer *et al.*, 1994; Aiazzi *et al.*, 1998; Hao *et al.*, 1999), Maximum entropy based methods (Frieden, 1972; Gull and Skilling, 1984; Jannetta *et al.*, 2004), order-statistics and morphological filters (Crimmins, 1985; Alparone *et al.*, 1995; Alparone and Garzelli, 1998; Prager *et al.*, 2001), nonlocal filtering (Buades *et al.*, 2005a; Coupé *et al.*, 2008; Deledalle *et al.*, 2009; Teuber and Lang, 2012), simulated annealing despeckling

(White, 1994), wavelet-based approaches (Achim *et al.*, 2001; Sudha *et al.*, 2009), nonlinear diffusion in Laplacian pyramid domain (Zhang *et al.*, 2007), and PDE based methods (Perona and Malik, 1990; Rudin *et al.*, 1992; Catté *et al.*, 1992; Weickert, 1998; Masnou, 2002; Yu and Acton, 2002; Rudin *et al.*, 2003; Aubert and Kornprobst, 2006; Ratner and Zeevi, 2007; Aubert and Aujol, 2008; Cao *et al.*, 2010; Prasath and Vorotnikov, 2014; Theljani, 2015; Jain *et al.*, 2015b; Zhou *et al.*, 2015, 2018; Shan *et al.*, 2019; Majee, Ray and Majee, 2020; Majee, Jain, Ray and Majee, 2020), etc.

1.1 Basics of Digital Image Processing

Due to the extensive applications of images in our daily life, digital image processing plays an essential task in various ongoing research areas such as computer graphics, remote sensing, medical imaging, molecular imaging, video surveillance, and auto-piloting, etc. Usually, the techniques of digital image processing can be categorized into three distinct levels: Low-level, Mid-level, and High-level. Low-level processing includes fundamental processes such as noise removal, image sharpening, contrast enhancement. In low-level processing, both input and output are images. Mid-level processing includes object recognition, image segmentation, etc. In mid-level processing, inputs are usually images, but the outputs are characteristics. The high-level process includes “making sense” from a collection of identified objects. This processing is usually linked with computer vision (Gonzalez and Woods, 2002).

1.1.1 Digital Image

A digital image is a numeric description of a physical scene from the real scenario. It is created through an image acquisition apparatus such as a digital camera, and it stored and managed by a digital computer. A digital image can also be defined as a matrix representation of a collection of discrete points, called Pixels (or Picture Elements). Pixels are the smallest element in the image. An image is named binary when each pixel value is either 0 (black) or 1 (white), whereas it is called a grayscale image if the pixel values are varying within 0 (black) and 255 (white). A digital color image can be represented as a combination of three color channels; a red channel, a green channel, and a blue channel; commonly known as RGB image. The pixel values of each color channel are varied as grayscale images, from 0 to 255. Any color can be generated by coupling the three primitive colors, “Red, Green, and Blue”. Usually, television and computer monitors use the RGB

system to perform the colorful pictures we see on screen ([Theljani, 2015](#)).

A digital image can be defined in a continuous setting as a function $I : \Omega \rightarrow R_I$, where Ω (in general rectangular) is a bounded open subset of \mathbb{R}^2 , and R_I is the range of the function I . For a binary image the range $R_I \subseteq [0, 1]$. For a gray value image the range $R_I \subseteq [0, 255]$, whereas the color images are described as a vector-valued function with range $R_I \subseteq [0, 255] \times [0, 255] \times [0, 255]$. The mathematical analysis of the image restoration model in terms of partial differential equations (PDEs) is commonly established in the continuous setting ([Theljani, 2015](#)).

1.1.2 Image Noise

Image noise is a random fluctuation of brightness or color information in images, or image noise is an undesirable signal that degraded the quality of the images. This degradation occurs due to the different varieties of noises such as Gaussian noise, Speckle noise, Salt and Pepper noise, Poisson noise, and many more fundamental noise classes in the case of digital images ([Gonzalez and Woods, 2002; Boncelet, 2009; Boyat and Joshi, 2015](#)). Usually, noise models are two types additive and multiplicative. If the noise term in the model summed with the original image, it is called an additive noise model. On the other hand, if the noise term multiplied with the original image, then the model is called multiplicative.

A Mathematical representation for an additive noise model can be described as

$$J = \mathcal{O}I + \eta, \quad (1.1)$$

whereas for the case of multiplicative noise we can express the model as

$$J = \mathcal{O}I\eta, \quad (1.2)$$

where J is the degraded image and I is the noise-free image. Here, \mathcal{O} is a linear map describing the blurring effect (usually a convolution also called point spread function) and η signifies the noise component.

For the first case, we consider additive Gaussian noise ([Gonzalez and Woods, 2002](#)) $\eta \sim \text{Normal}(0, \sigma)$, follows the standard normal distribution as

$$p_N(\eta) = \frac{1}{\sigma\sqrt{2\pi}} \exp^{-\frac{\eta^2}{2\sigma^2}}, \quad (1.3)$$

where σ signifies the standard deviation.

For the latter case, we consider $\eta \sim \text{Gamma}(L, L)$, follows the probability

density function as

$$g_G(\eta) = \begin{cases} \frac{L^L}{\Gamma(L)} \eta^{L-1} \exp(-L\eta), & \text{for } \eta > 0, \\ 0, & \text{for } \eta = 0, \end{cases} \quad (1.4)$$

where $L \in \mathbb{N}$ signifies the number of “looks” which is related to the number of spatial observations (Argenti *et al.*, 2013; Hao *et al.*, 2015; Liu and Fan, 2016) and $\Gamma(\cdot)$ denotes the gamma function.

An example of a clear grey-scale image, affected by additive Gaussian noise, and affected by multiplicative speckle noise is displayed in Figure 1.1 (excluding the blurring effect). The degraded images do interpretation wrong; therefore, before

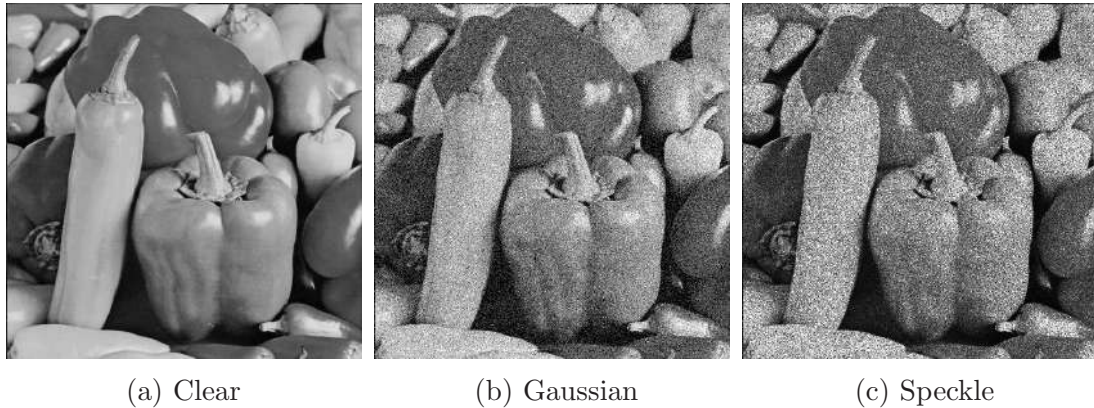


Figure 1.1: Peppers image: (a) Clear image. (b) Degraded by Gaussian noise with standard deviation (σ)= 40. (c) Degraded by speckle noise with $L = 5$.

going to detail interpretation or high-level processing, noise removal is essential to avoid the misinterpretation.

1.1.3 Inverse Problem & Image Restoration

The inverse problem (Bertero and Boccacci, 1998; Kirsch, 2011) is a broad subject area, and its applicability can be found in several disciplines (e.g., geophysics, oceanography, astronomy, imaging, etc.). An inverse problem can be defined as a transformation between two normed spaces, P and Q as follows:

$$J = \mathcal{O}I, \quad I \in P \quad \text{and} \quad J \in Q. \quad (1.5)$$

The direct problem consists in evaluating the output J given the input I and the transform operator \mathcal{O} . In contrast, the inverse problem is to obtain the input I , considering that both \mathcal{O} and the output of the system J are given.

Hadamard (2003) set a significant notion of well-posedness for the latter problem defined as follows:

Definition 1.1. Let P and Q be normed spaces, $\mathcal{O} : P \rightarrow Q$ a (linear or non-linear) mapping. The equation $\mathcal{O}I = J$ is called well-posed if the following three conditions hold:

- i. *Existence:* For every $J \in Q$ there is at least one $I \in P$ such that $\mathcal{O}I = J$.
- ii. *Uniqueness:* For every $J \in Q$ there is at most one $I \in P$ with $\mathcal{O}I = J$.
- iii. *Stability:* The solution I depends continuously on J ; that is, for every sequence $\{I_n\} \subset P$ with $\mathcal{O}I_n \rightarrow \mathcal{O}I$ ($n \rightarrow \infty$), it follows that $I_n \rightarrow I$ ($n \rightarrow \infty$).

Due to the notion of Hadamard, if (at least) one of the previous properties does not hold, we say that (1.5) is an ill-posed problem.

The technique that reduces the noise along with protecting the characteristics of images is called image restoration. Image restoration can also be considered as an important inverse problem, where the original image I is recovered from an observed data J , which is initially diminished and corrupted by blurring effect and noise. A similar mathematical representation consists in approximating I solution of (1.1) by the minimizer of the following energy:

$$\|\mathcal{O}I - J\|_Q^2 . \quad (1.6)$$

Numerous digital processors can be applied to the image J to produce another image I . However, one of the crucial issues of (1.6) is its ill-posedness, and minimizing (1.6) is very sensitive to data exchanges and yields in many situations enormously oscillating minimizers. Hence there is an increasing demand for correctly implemented theoretical and computational techniques for its execution.

Regularization: It is not an easy task to overcome the ill-posedness issues, except additional knowledge about the solution is possible to expand the solution space. An ideal way to remove ill-posedness is to add a regularization term to the energy (1.6), Tikhonov and Arsenin (1977) first introduced this idea. After introducing the regularization term, the problem is converted into a well-posed one, which can be presented as below:

$$I^* := \min_I \left\{ \alpha_0 R(I) + \lambda_0 \|\mathcal{O}I - J\|_Q^2 \right\} , \quad (1.7)$$

where $\alpha_0 > 0$ and λ_0 are regularization parameters. The first term $R(I)$ is the regularization term, which signifies the smoothing influence (diffusion) of the model and has to be chosen according to the desired characteristics of the solution. The minimization problem (1.7) is converted using the Euler-Lagrange equation into solving a PDE having the following form:

$$\left. \begin{array}{ll} \partial_t I = \mathcal{F}(x, I, DI, \dots, D^n I) + \lambda(J - I) & \text{in } \Omega_T := \Omega \times (0, T), \\ \partial_n I = 0 & \text{in } \partial\Omega_T := \partial\Omega \times (0, T), \\ I(x, 0) = J(x) & \text{in } \Omega, \end{array} \right\} \quad (1.8)$$

where \mathcal{F} is a n th-order differential operator depend on the regularization term $R(I)$, λ is a weight parameter that can be calculated as discussed in (Rudin *et al.*, 1992; Aubert and Kornprobst, 2006), and ∂_n denotes the derivative at the boundary surface $\partial\Omega$ in the outward normal direction n . A similar technique can be used for the multiplicative noise model (Rudin *et al.*, 2003).

An alternative way to handle the image restoration problem is to work directly on PDEs without considering any energy. The image is viewed as a smoothed solution of a PDE formally written as follows:

$$\left. \begin{array}{ll} \partial_t I = \mathcal{F}(x, I, DI, \dots, D^n I) & \text{in } \Omega_T, \\ \partial_n I = 0 & \text{in } \partial\Omega_T, \\ I(x, 0) = J(x) & \text{in } \Omega. \end{array} \right\} \quad (1.9)$$

A brief survey of both energy minimization and direct PDE based image restoration techniques are discussed in the next section.

1.2 PDE Based Image Denoising: An Overview

The present work mainly concentrates on the PDE based models for the noise removal process in the digital images. Among the various mathematical approaches, PDE based approaches are extensively utilized, and they are proven to be effective and quite successful in the last three decades. Most popular PDE based approaches are nonlinear diffusion models (Perona and Malik, 1990; Catté *et al.*, 1992; Weickert, 1997, 1998, 2001; Yu and Acton, 2002; Aubert and Kornprobst, 2006; Jain and Ray, 2015; Zhou *et al.*, 2015; Jain *et al.*, 2018; Zhou *et al.*, 2018; Jain and Ray, 2019; Shan *et al.*, 2019), total variation models (Rudin *et al.*, 1992; Chambolle and Lions, 1997; Rudin *et al.*, 2003; Tsai and Osher, 2005; Aubert and Aujol, 2008; Shi and Osher, 2008; Elliott and Smitheman, 2009; Prasath and Singh, 2010a; Huang *et al.*,

2010; Jin and Yang, 2010, 2011; Jidesh and Bini, 2013; Dong *et al.*, 2013; Liu *et al.*, 2013; Zanetti *et al.*, 2016; Zanella *et al.*, 2018; Thanh *et al.*, 2019; Xu *et al.*, 2019), fourth-order diffusion methods (You and Kaveh, 1998, 2000; Lysaker *et al.*, 2003; Liu *et al.*, 2011, 2015; Zhang and Ye, 2017; Siddig *et al.*, 2018; Deng *et al.*, 2019), complex diffusion models (Araújo *et al.*, 2012, 2015), telegraph-diffusion methods (Ratner and Zeevi, 2007; Cao *et al.*, 2010; Zhang *et al.*, 2014; Jain and Ray, 2016; Baravdish *et al.*, 2019; Majee, Ray and Majee, 2020; Majee, Jain, Ray and Majee, 2020), and coupled diffusion models (Nitzberg and Shiota, 1992; Luo *et al.*, 2006; Guo *et al.*, 2011; Prasath and Vorotnikov, 2014; Guidotti, 2015). Due to the availability of well established numerical schemes and theoretical background (Alvarez *et al.*, 1993; Weickert, 1998, 2001; Mikula, 2002; Buades *et al.*, 2005b; Aubert and Kornprobst, 2006; Elliott and Smitheman, 2009; Nolen, 2009), PDE based image processing is an exciting research area for real-life applications as well as for the theoretical studies. The fundamental objective of PDE-based image restoration is to obtain the steady-state solution.

All the above-mentioned methods are utilize either the diffusion-based approach or the total variational framework. The simplest PDE based approach for image smoothing is the linear diffusion model (Witkin, 1983; Koenderink, 1984; Hummel, 1987; Weickert, 1998), also known as isotropic diffusion, which takes the form:

$$\left. \begin{array}{ll} \partial_t I = \Delta I & \text{in } \Omega_T, \\ I(x, 0) = J(x) & \text{in } \Omega. \end{array} \right\} \quad (1.10)$$

In the above model $I(x, t)$ is the image variable and $J(x)$ is the initial or degraded image to be restored. If $J \in C(\Omega)$ and bounded, then the solution of (1.10) can be given as a family of restored images (Weickert, 1998),

$$I(x, t) = (G_{\sqrt{2t}} * J)(x) \quad t > 0, \quad (1.11)$$

where $G_{\sqrt{2t}}$ is the two dimensional Gaussian kernel on space only of width $\sqrt{2t}$. Therefore, this method is equivalent to the Gaussian smoothing of a given image J . In this case, the speed of diffusion is equal in all directions of each point in the image hence fails to preserve the sharp edges during the noise removal process.

To overcome the drawbacks in the linear diffusion model, several nonlinear diffusion based algorithms are suggested for image denoising. To the best of our knowledge, Perona and Malik (1990) first proposed the novel and efficient nonlinear diffusion based model (the PM model) for image denoising, which removes noise as well as preserves the sharp edges during the noise removal process. The model

takes the form

$$\left. \begin{array}{ll} \partial_t I = \operatorname{div}(g(|\nabla I|)\nabla I) & \text{in } \Omega_T, \\ \partial_n I = 0 & \text{in } \partial\Omega_T, \\ I(x, 0) = J(x) & \text{in } \Omega, \end{array} \right\} \quad (1.12)$$

Here, the diffusion function $g(s)$ is chosen in such a way that the speed of diffusion is very fast in the homogeneous region, and slow in the non-homogeneous regions of an image, where the intensity of the image changing abruptly. The diffusion functions suggested by [Perona and Malik \(1990\)](#) satisfy $g(0) = 1$ and $g(s) \rightarrow 0$ as $s \rightarrow \infty$, and are represented as follows,

$$g(s) = \exp\left(-\frac{s}{k}\right), \quad (1.13)$$

$$g(s) = \frac{1}{1 + \left(\frac{s}{k}\right)^2}. \quad (1.14)$$

Here k is a threshold parameter utilized to classify low and high diversity regions for the forward diffusion (smoothing) and backward diffusion (edge preservation). It is well established that the PM model (1.12) is a potential method for image restoration. At the same time, from the theoretical point of view, the model is ill-posed, which means the solution of (1.12) may not be a unique optimal solution. The detail theoretical analysis, as well as improvements of the PM model, can be found in ([Catté et al., 1992](#); [Kichenassamy, 1997](#); [Weickert and Benhamouda, 1997](#)). To obtain a well-posed model, several improvements of the PM model are suggested by different researchers ([Nordström, 1990](#); [Catté et al., 1992](#); [Alvarez et al., 1992](#); [Weickert, 1997, 2001](#)). Theoretically, the model suggested by [Catté et al. \(1992\)](#) provides a non-degenerate and unique global solution, but introduces a blurring effect into the restored images, and thus stings the sharpening capabilities of the PM model. This shortcoming provides a requirement for further improvements of the PM model ([Cottet and Germain, 1993](#); [Guidotti, 2012](#)).

Alternatively, nonlinear PDE-based models for image denoising can be derived from the total variation (TV) framework or energy minimization method ([Aubert and Kornprobst, 2006](#)). [Rudin et al. \(1992\)](#) first introduced the concept of the total variation model (the ROF model) for the additive noise removal process. The total variational based approach restored the observed noisy image by minimizing the total variation norm of the image subject to the constraints, which are determined by the noise statistics ([Rudin et al., 1992](#)). For a function of two variables I the

total variation norm is denoted by $\text{TV}(I)$ and calculated as follows (Rudin, 1987):

$$\text{TV}(I) = \int_{\Omega} |DI| .$$

The total variation framework proposed by Rudin *et al.* (1992) is

$$\text{minimize } \text{TV}(I),$$

subject to the constraints

$$\int_{\Omega} (I - J) dx = 0, \quad \text{and} \quad \int_{\Omega} (I - J)^2 dx = \sigma^2,$$

or can be written as an unconstrained problem as

$$I^* := \underset{I \in BV(\Omega)}{\operatorname{argmin}} \left\{ \text{TV}(I) + \frac{\lambda}{2} \|I - J\|_{L^2(\Omega)}^2 \right\}, \quad (1.15)$$

where $BV(\Omega)$ denotes the space of functions with bounded variation (Evans and Gariepy, 2015). The first term (total variation of I) in (1.15) manages the measure of smoothing in the image, the second term is called fidelity term, which restrains the denoised image close to the degraded image J , and λ is the Lagrange multiplier to adjust the parity between smoothing and fidelity terms. Euler-Lagrange equation corresponding to the functional (1.15) is

$$\operatorname{div} \left(\frac{\nabla I}{|\nabla I|} \right) - \lambda(I - J) = 0 \quad \text{in } \Omega.$$

By introducing the time variable and boundary and initial conditions, the above equation becomes

$$\left. \begin{aligned} \partial_t I &= \operatorname{div} \left(\frac{\nabla I}{|\nabla I|} \right) - \lambda(I - J) && \text{in } \Omega_T, \\ \partial_n I &= 0 && \text{in } \partial\Omega_T, \\ I(x, 0) &= J(x) && \text{in } \Omega. \end{aligned} \right\} \quad (1.16)$$

Extensive studies have concluded that the total variation technique performs better in terms of edge preservation and noise removal compared to nonlinear diffusion. The drawback of this model is that it creates the blocking effect during the noise removal process in the flat regions of the image. Hence provides a loss of the local characteristics of the original image, such as textures. This phenomenon is

known as “staircase artifact” and is discussed in (Chambolle and Lions, 1997; Ring, 2000). To overcome this shortcoming, several articles with a more detailed survey of state-of-the-art knowledge in variational-based image reconstruction are available in the literature, discussing the deficiency and development in image restoration (Chambolle and Lions, 1997; Ring, 2000; Tsai and Osher, 2005; Tai *et al.*, 2006).

Apart from parabolic PDE based models hyperbolic PDE could upgrade the quality of the detected edges and improve the image better than parabolic PDE (Averbuch *et al.*, 2006; Ratner and Zeevi, 2007, 2011; Majee *et al.*, 2019; Majee, Ray and Majee, 2020). In the existing literature, the first hyperbolic model for image denoising is the telegraph-diffusion equation (TDE) model (Ratner and Zeevi, 2007), where the image is viewed as an elastic sheet placed in a damping environment, which interpolates between the diffusion equation and the wave equation. This system is named as telegraph-diffusion model because it is similar to the telegraph equation (Zauderer, 2011; Metzger, 2012). Original telegraphers’ equation is a linear coupled PDE that describes the voltage and current on an electrical transmission line with distance and time. The TDE model takes the form,

$$\left. \begin{array}{l} \partial_{tt}I + \gamma\partial_tI = \operatorname{div}(g(|\nabla I|)\nabla I) \quad \text{in } \Omega_T, \\ \partial_nI = 0 \quad \text{in } \partial\Omega_T, \\ I(x, 0) = J(x), \quad \partial_tI(x, 0) = 0 \quad \text{in } \Omega, \end{array} \right\} \quad (1.17)$$

where $g(|\nabla I|) = 1/(1 + (|\nabla I|^2/k^2))$ is an edge-controlled diffusion function which preserves the important features and smoothen the unwanted signals, $k > 0$ is a constant, and γ is the damping parameter. It is quite interesting to note that in a long time scenario, the TDE model converges to the diffusion equation (Gallay and Raugel, 1998; Zauderer, 2011). However, this regime is of no interest in the context of image processing. Although the TDE model (1.17) performs better, it is challenging to confirm the well-posedness of this model. To overcome the ill-posedness issue in the model (1.17), Cao *et al.* suggest a regularized TDE model (Cao *et al.*, 2010). They replace the gradient $|\nabla I|$ by $|\nabla I_\xi|$ in the edge-controlled function $g(\cdot)$ in (1.17) and proposed the following model

$$\left. \begin{array}{l} \partial_{tt}I + \gamma\partial_tI = \operatorname{div}(g(|\nabla I_\xi|)\nabla I) \quad \text{in } \Omega_T, \\ \partial_nI = 0 \quad \text{in } \partial\Omega_T, \\ I(x, 0) = J(x), \quad \partial_tI(x, 0) = 0 \quad \text{in } \Omega, \end{array} \right\} \quad (1.18)$$

The authors have established the well-posedness of the model (1.18). Although the model (1.17) can effectively preserve the sharp edges, it fails to produce satisfactory

smoothing in the presence of a large level of noise. To overcome this issue, several nonlinear telegraph diffusion models are proposed (Cao *et al.*, 2010; Yang and Zhang, 2014; Zhang *et al.*, 2014, 2015; Jain and Ray, 2016; Ghislain *et al.*, 2017; Baravdish *et al.*, 2019).

Most of the above-discussed models have utilized the absolute value of the image gradient to indicate the direction of diffusion in the image restoration process. Under noisy conditions, the direct application of the gradient-based edge indicator method can include spurious oscillations in the noise removal process (Catté *et al.*, 1992). Many researchers have applied several strategies to produce successful image restoration results obtained with the classical PDEs and to avoid gradient-based artifacts. Based on available literature, such improvements can be categorized into two general classes: (i) Adaptive techniques (Catté *et al.*, 1992; Chen and Wunderli, 2002; Shi and Chang, 2006; Barbu *et al.*, 2009; Prasath and Singh, 2010b, 2012)—a single PDE-based model along with some kind of adaptive edge map estimator and (ii) Coupled partial differential equation (CPDE) based models (Nitzberg and Shiota, 1992; Teboul *et al.*, 1998; Cottet and Ayyadi, 1998; Caselles *et al.*, 2000; Chen *et al.*, 2001; Chen and Bose, 2001; Wei and Jia, 2002; Chen and Levine, 2002; Belahmidi and Chambolle, 2005; Luo *et al.*, 2006; Amann, 2007; Prasath and Vorotnikov, 2014; Guidotti, 2015; Sun *et al.*, 2016)—where a separate PDE is used to calculate the edge map or the data fidelity. In the CPDE based approaches image edges or the data fidelity are calculated using separate evolution equations, hence it worked better than the single PDE-based approaches. To the best of our knowledge, Nitzberg and Shiota (1992) first introduced the time-delay CPDE model for image filtering. Their model takes the form

$$\left. \begin{aligned} \partial_t I &= \operatorname{div} \left(\frac{1}{1+u^2} \nabla I \right) && \text{in } \Omega_T, \\ \partial_t u &= \varphi(G_\xi * |\nabla I|^2 - u) && \text{in } \Omega_T, \end{aligned} \right\}$$

where $\varphi, \xi > 0$ are scale parameters. In the above model, a separate equation is used to calculate the edge variable u . So, the term u updates the edge information from the renewed image's gradient and prior knowledge of itself. A similar idea of CPDE model utilizing time-delay regularization was introduced by Luo *et al.* (2006). They suggested estimating a better edge map by replacing the isotropic diffusion using a nonlinear diffusion to provide a regularized variant of the diffusion coefficient for image smoothing. Subsequently, Guo *et al.* (2011) introduced and analyzed the well-posedness of a reaction-diffusion model (the RD model) for image

restoration. The model takes the form

$$\left. \begin{aligned} \partial_t I &= \operatorname{div} \left(\frac{\nabla I}{|\nabla I|} \right) - 2\lambda v && \text{in } \Omega_T, \\ \partial_t v &= \Delta v - (J - I) && \text{in } \Omega_T. \end{aligned} \right\} \quad (1.19)$$

In the above model, a separate PDE is used to calculate the fidelity variable v efficiently. In 2014, [Prasath and Vorotnikov \(2014\)](#) proposed an adaptive CPDE model (the VBS model) for image restoration. The model takes the form

$$\left. \begin{aligned} \partial_t I - \operatorname{div}(g(u)\nabla I) &= 0 && \text{in } \Omega_T, \\ \partial_t u - \lambda \operatorname{div}(\nabla u) - (1-\lambda)(|\nabla I| - u) &= 0 && \text{in } \Omega_T, \end{aligned} \right\} \quad (1.20)$$

where, $\lambda > 0$ is a balancing parameter. The authors have considered the following two diffusion functions:

$$g(s) = \frac{1}{1 + \left(\frac{s}{K}\right)^2} \quad \text{or} \quad g(s) = |s|^{-1} \quad \text{with } K > 0.$$

The authors have established the existence and uniqueness of dissipative solutions of the system (1.20). Subsequently, Jain et al. ([Jain, 2018](#)) proposed a CPDE model for additive Gaussian noise removal process. The model takes the form

$$\partial_t I = \operatorname{div}(g(u)\nabla I) - 2\lambda v \quad \text{in } \Omega_T, \quad (1.21)$$

$$\partial_t u = \alpha \left(|\nabla I_\xi|^2 - u + \frac{\beta^2}{2} \Delta u \right) \quad \text{in } \Omega_T, \quad (1.22)$$

$$\partial_t v = \Delta v - (J - I) \quad \text{in } \Omega_T, \quad (1.23)$$

where $g(u) = 1/(1 + \frac{u}{k^2})$, $I_\xi = G_\xi * I$, and $\alpha, \beta > 0$ are constants. Here, the smoothing equation (1.21) has edge variable u and fidelity variable v , obtained from two different PDEs. The data fidelity within I and J can be controlled by the variable v , obtained from equation (1.23), whereas the function u in the diffusion coefficient can be calculated from equation (1.22). This approach achieved an adequate edge map and fidelity within the noisy image and restored image, leading to quality denoising results. A good survey on the existing CPDE based approaches can be found in ([Guidotti, 2015](#)).

Besides additive noise, in many real situations such as SAR images, laser images, microscope images, and medical Ultrasound images are degraded by multiplicative speckle noise ([Burckhardt, 1978](#); [Prager et al., 2001](#); [Loizou et al., 2005](#); [Petrou and Petrou, 2010](#)). In this case, the original signal multiplied with some undesired

noise signals. Over the last two decades, nonlinear PDEs are extensively used to develop speckle-noise reduction models. Most popular PDE based approaches are nonlinear diffusion based methods (Weickert, 1998; Jin *et al.*, 2000; Yu and Acton, 2002; Zhou *et al.*, 2015; Jain *et al.*, 2018; Zhou *et al.*, 2018; Jain and Ray, 2019; Shan *et al.*, 2019), and variational based methods (Rudin *et al.*, 2003; Aubert and Aujol, 2008; Shi and Osher, 2008; Huang *et al.*, 2010; Jin and Yang, 2010, 2011; Jidesh and Bini, 2013; Dong *et al.*, 2013; Liu *et al.*, 2013).

Probably the first diffusion-based model for multiplicative speckle noise removal was proposed by Yu and Acton (2002). This model is an integration of a spatially adaptive filter with the PM model. The model takes the form

$$\left. \begin{array}{ll} \partial_t I = \operatorname{div}(g(q_0, q) \nabla I) & \text{in } \Omega_T, \\ \partial_n I = 0 & \text{in } \partial\Omega_T, \\ I(x, 0) = J(x) & \text{in } \Omega. \end{array} \right\} \quad (1.24)$$

Here $g(\cdot)$ is the diffusion coefficient, can be defined as

$$g(q, q_0) = \left(1 + \frac{q^2 - q_0^2}{q_0^2(1 + q_0^2)} \right)^{-1}, \quad (1.25)$$

where q is the instantaneous coefficient of variation (ICOV), serves as the edge detector function and determined by the formula

$$q = \sqrt{\frac{(1/2)(\nabla I/I)^2 - (1/16)(\nabla^2 I/I)^2}{[1 + (1/4)(\nabla^2 I/I)]^2}}, \quad (1.26)$$

and q_0 is the speckle scale function, serves as the diffusion threshold value determined by the ratio of the local standard deviation to mean

$$q_0 = \frac{\operatorname{std}(I)}{\operatorname{mean}(I)}.$$

This filter provides significant enhancement in edge preservation and speckle suppression when compared with conventional filters. Further, nonlinear diffusion based models for multiplicative speckle noise reduction are also proposed in the literature (Tauber *et al.*, 2004; Aja-Fernández and Alberola-López, 2006; Krissian *et al.*, 2007; Krissian and Aja-Fernández, 2009; Fabbrini *et al.*, 2013; Zhou *et al.*, 2015; Shan *et al.*, 2019). In 2018, Jain *et al.* (2018) developed a coupled diffusion based model (the MCPDE model) for the speckle noise elimination. The model

takes the form

$$\partial_t I = \operatorname{div}(\beta(I)g(u)\nabla I) - 2\lambda v \quad \text{in } \Omega_T, \quad (1.27)$$

$$\partial_t u = \varphi(\|\nabla I_\xi\|^2 - u + \frac{\psi^2}{2}\Delta u) \quad \text{in } \Omega_T, \quad (1.28)$$

$$\partial_t v = v - \frac{I - J}{I^2} \quad \text{in } \Omega_T, \quad (1.29)$$

$$\partial_n I = 0, \quad \partial_n u = 0, \quad \partial_n v = 0 \quad \text{on } \partial\Omega_T, \quad (1.30)$$

$$I(x, 0) = J(x), \quad v(x, 0) = 0, \quad u(x, 0) = G_\xi * |\nabla J|^2 \quad \text{in } \Omega. \quad (1.31)$$

In the above system, $g(u) = 1/(1 + \frac{u}{k^2})$, $\beta(I) = \frac{2|I|^\alpha}{M^\alpha + |I|^\alpha}$, $M = \sup_{x \in \Omega}(G_\xi * J)(x)$, and $I_\xi = G_\xi * I$, where α, ξ, k, φ , and ψ are positive constants. The authors in the above model use separate PDEs to calculate the edge variable u and the fidelity variable v .

Besides the diffusion-based filters, TV based approaches can also remove the multiplicative noise from the degraded images. To the best of our knowledge, [Rudin et al. \(2003\)](#) first introduced the TV model (the RLO model) for multiplicative noise removal. This framework takes the form

$$\text{minimize } \operatorname{TV}(I),$$

with the following hypotheses,

$$\int_{\Omega} \frac{J}{I} dx = 1,$$

and

$$\int_{\Omega} \left(\frac{J}{I} - 1 \right)^2 dx = \sigma^2,$$

or can be written as an unconstrained problem as

$$I^* := \operatorname{argmin}_{I \in BV(\Omega)} \left\{ \operatorname{TV}(I) + \lambda \int_{\Omega} \frac{J}{I} dx + \mu \int_{\Omega} \left(\frac{J}{I} - 1 \right)^2 dx \right\}. \quad (1.32)$$

Here, λ and μ are two Lagrange multipliers, dynamically updated as explained in [\(Rudin et al., 2003\)](#). The associated evolution equation of (1.32) is

$$\partial_t I = \operatorname{div} \left(\frac{\nabla I}{|\nabla I|} \right) - \lambda \frac{J^2}{I^3} - \mu \frac{J}{I^2}. \quad (1.33)$$

This filter gives improved results by protecting some essential details from over-

smoothing. But the authors in (Rudin *et al.*, 2003) do not make any assumption on the gamma noise, hence not guaranteed to work suitably for the speckle noise removal process. After that, Aubert and Aujol (2008) proposed a TV model for speckle noise reduction, which is derived from the maximum a-posteriori (MAP) estimation. The functional can be written as

$$I^* := \operatorname{argmin}_{I \in S(\Omega)} \left\{ \int_{\Omega} |DI| + \lambda \int_{\Omega} \left(\log I + \frac{J}{I} \right) dx \right\}, \quad (1.34)$$

where $S(\Omega) = \{I \in BV(\Omega), I > 0\}$ and λ is a regularization parameter. The authors established the existence of a minimizer of the functional (1.34). Also, the authors proved the existence and uniqueness results of the solution to the associated evolution problem of (1.34) named as AA model,

$$\partial_t I = \operatorname{div} \left(\frac{\nabla I}{|\nabla I|} \right) + \lambda \frac{J - I}{I^2}. \quad (1.35)$$

Furthermore, some other TV techniques are proposed in (Shi and Osher, 2008; Huang *et al.*, 2009; Jin and Yang, 2010; Huang *et al.*, 2010; Jin and Yang, 2011; Dong *et al.*, 2013; Jidesh and Bini, 2013; Liu *et al.*, 2013).

1.3 Numerical Method & Stopping Criterion

To solve the proposed models numerically, we use explicit/implicit finite difference scheme (LeVeque, 2007; Jovanović and Süli, 2013). Let $\mathcal{V} = \mathcal{V}(x, y, t)$, where $(x, y) \in \mathbb{R}^2$ and $t \in (0, T)$, be a function of space and time. Construct the finite difference scheme as follows:

Discretize the space domain using a step size h and time domain using a step size τ . In the following, $\mathcal{V}_{i,j}^n$ denotes the approximate value of $\mathcal{V}(x_i, y_j, t_n)$, where $x_i = ih$, $i = 0, 1, 2, \dots, M-1$; $y_j = jh$, $j = 0, 1, 2, \dots, N-1$; $t_n = n\tau$, $n = 0, 1, 2, \dots$, where n is the number of iterations, and $M \times N$ is the grid size.

We use the following finite difference approximations to replace the derivative terms in the proposed systems discussed in **Chapter 2–6**:

$$\begin{aligned} \partial_t \mathcal{V}_{i,j}^n &\approx \frac{\mathcal{V}_{i,j}^{n+1} - \mathcal{V}_{i,j}^n}{\tau}, & \partial_{tt} \mathcal{V}_{i,j}^n &\approx \frac{\mathcal{V}_{i,j}^{n+1} - 2\mathcal{V}_{i,j}^n + \mathcal{V}_{i,j}^{n-1}}{\tau^2}, \\ \nabla_x \mathcal{V}_{i,j}^n &\approx \frac{\mathcal{V}_{i+h,j}^n - \mathcal{V}_{i-h,j}^n}{2h}, & \nabla_y \mathcal{V}_{i,j}^n &\approx \frac{\mathcal{V}_{i,j+h}^n - \mathcal{V}_{i,j-h}^n}{2h}, \end{aligned}$$

$$\Delta_x \mathcal{V}_{i,j}^n \approx \frac{\mathcal{V}_{i+h,j}^n - 2\mathcal{V}_{i,j}^n + \mathcal{V}_{i-h,j}^n}{h^2}, \quad \Delta_y \mathcal{V}_{i,j}^n \approx \frac{\mathcal{V}_{i,j+h}^n - 2\mathcal{V}_{i,j}^n + \mathcal{V}_{i,j-h}^n}{h^2},$$

$$|\nabla \mathcal{V}_{i,j}^n| \approx \sqrt{(\nabla_x \mathcal{V}_{i,j}^n)^2 + (\nabla_y \mathcal{V}_{i,j}^n)^2}, \quad \Delta \mathcal{V}_{i,j}^n = \Delta_x \mathcal{V}_{i,j}^n + \Delta_y \mathcal{V}_{i,j}^n.$$

Neumann boundary conditions used in the [Chapter 2–6](#) approximated as

$$\left. \begin{aligned} \mathcal{V}_{0,j}^n &= \mathcal{V}_{1,j}^n, & \mathcal{V}_{M-1,j}^n &= \mathcal{V}_{M-2,j}^n, & j &= 0, 1, 2, \dots N-1, \\ \mathcal{V}_{i,0}^n &= \mathcal{V}_{i,1}^n, & \mathcal{V}_{i,N-1}^n &= \mathcal{V}_{i,N-2}^n, & i &= 0, 1, 2, \dots M-1. \end{aligned} \right\} \quad (1.36)$$

For the numerical simulation, we use the spatial step size $h = 1$ and choose a small time step τ to preserve the stability criterion ([Chan and Shen, 1987](#); [Li, 2009](#); [Zauderer, 2011](#); [Araújo et al., 2012](#); [Jain et al., 2015b](#)).

Apart from the discretization of the proposed models, we need to specify a stopping criterion for the convergence of the numerical simulation process. For this, we use two different stopping criteria; (i) when the ground truth image is available (for artificial noisy image), (ii) when the ground truth image is not available (for real image). For both cases, we start the simulation with the initial value (degraded image) $J(x, y, 0)$ and utilize the proposed techniques repeatedly, which results in a family of smoother images $I(x, y, t); t > 0$, which represents filtered versions of $J(x, y, 0)$:

(i) In the first case, when the ground truth image (clean image) is available, we use the best PSNR ([Gonzalez and Woods, 2002](#)) value as the stopping criterion for the iterative process. Here the PSNR value between the ground truth image and the filtered image is computed by the formula (1.40).

(ii) For the latter case (i.e., in the case of real images), when the ground truth image is not available, we use relative error ([LeVeque, 2007](#)) as the stopping criterion of the iterative process, computed as

$$\frac{\|I^{k+1} - I^k\|_2^2}{\|I^k\|_2^2} \leq \varepsilon, \quad (1.37)$$

where $\varepsilon > 0$ is a fixed threshold. In (1.37), I^k and $I^{(k+1)}$ denote the restored images at the k th and $(k+1)$ th iteration, respectively. For the numerical simulations we have used $\varepsilon \leq 10^{-4}$.

1.4 Image Quality Measures

To evaluate the denoising effect of noise removal methods, various qualitative and quantitative measures are available. Qualitative measures are basically checked by observing the visual quality of the restored images in compare to the noisy images, whereas quantitative measures are some numerical values calculated using noisy images and restored images. Few important quantitative measures with their formulae and mechanisms are briefly discussed below:

- SSIM: Structural similarity index (SSIM) ([Wang et al., 2004](#)), calculates the structural similarity between two images. Let I and J be two images then SSIM between them can be calculated as,

$$\text{SSIM}(I, J) = \frac{(2\mu_I\mu_J + c_1)(2\sigma_{IJ} + c_2)}{(\mu_I^2 + \mu_J^2 + c_1)(\sigma_I^2 + \sigma_J^2 + c_2)}, \quad (1.38)$$

where $\mu_I, \mu_J, \sigma_I^2, \sigma_J^2, \sigma_{IJ}$ are the mean, variance, and covariance of I and J , respectively. The variables c_1 and c_2 are used to stabilize the division with weak denominator. To measure the overall performance, mean structural similarity index (MSSIM) is used, which can be written as:

$$\text{MSSIM}(I, J) = \frac{1}{N} \sum_{i=1}^N \text{SSIM}(I_i, J_i), \quad (1.39)$$

where N is the number of local windows in the image, and I_i and J_i are the image contents at the i^{th} local window.

- PSNR: Peak signal to noise ratio (PSNR) ([Gonzalez and Woods, 2002](#)) can measure the match between the original and restored images and this can be written as:

$$\text{PSNR} = 10 \log_{10} \left(\frac{\max(I)^2}{\frac{1}{MN} \sum_{i=1}^M \sum_{j=1}^N (I(i, j) - I_t(i, j))^2} \right). \quad (1.40)$$

Here I denotes the clean image of size $M \times N$, $\max(I)$ is the maximum possible pixel value of I , and I_t denotes the denoised image at a certain time t .

- SI: Speckle index (SI) ([Dewaele et al., 1990](#)) treated as a measure of speckle removal which calculates the average contrast of an image and defined as:

$$SI = \frac{\text{Standard Deviation}(I)}{\text{Mean}(I)}. \quad (1.41)$$

- NSD: Noise standard deviation (NSD) ([Elyasi and Pourmina, 2016](#)) is defined as:

$$NSD = \sqrt{\frac{1}{MN} \sum_{i=1}^M \sum_{j=1}^N (NMV - I_t(i,j))^2}, \quad (1.42)$$

where I_t shows the denoised image and the noise mean value (NMV) is represented as:

$$NMV = \frac{\sum_{i=1}^M \sum_{j=1}^N I_t(i,j)}{MN}.$$

NSD determines the contents of the speckle in the real ultrasound image by calculating the standard deviation between the denoised image and its mean value.

- BRISQUE: Blind/referenceless image spatial quality evaluator (BRISQUE) ([Mit-tal et al., 2012](#)) refers to automatic no-reference image quality assessment of an image. This evaluator calculates possible losses of naturalness in the image, caused by the presence of degradation, by computing scene statistics of locally normalized luminance coefficients. The maximum value (i.e. 100) of BRISQUE represents worst quality whereas the minimum value (i.e. 0) indicates the best image quality.

Higher numerical values of MSSIM, PSNR and lower numerical values of SI, NSD, and BRISQUE confirms the efficient noise removal.

Other typical qualitative measures are also computed in terms of the ratio image ([Argenti et al., 2013](#)), which can be defined as the point-by-point ratio between the degraded and the denoised image.

1.5 Motivation & Objectives

A rigorous investigation of the existing research works exhibits a gap in the filtering methods. One can note that most of the researchers showing their interests only on parabolic PDE based models, but hyperbolic PDEs could improve the quality of the detect edges ([Averbuch et al., 2006](#)). In this regard, [Ratner and Zeevi \(2007\)](#) first introduced the idea of hyperbolic-parabolic PDE for the additive noise elimination process; after that, several hyperbolic-parabolic equation-based models have been proposed for additive noise removal process. However, to the best of

our knowledge, in spite of their imposing applications in the area of additive noise elimination, hyperbolic-parabolic PDE based approaches have not applied yet for the multiplicative speckle noise removal process. Furthermore, preservation of the main characteristic of the real-life images, which are influenced by multiplicative speckle noises, is another challenge during the noise removal process. Also, the theoretical study of the PDE models is an essential aspect before going to computational research. These are the main motivating factors behind this work.

The main objective of this research work is to develop efficient and novel image denoising models based on PDEs, also study their theoretical behavior (e.g., existence and uniqueness of weak solution, boundedness of weak solution, etc.), which is very important for numerical computation. We start with an additive Gaussian noise removal model, and then the research is extended to the study of multiplicative speckle noise removal models. Computational analyses are reported to show the effectiveness of the proposed models, with respect to the recently developed models, over a set of gray level test images contaminated by speckle noise with various noise levels. Additionally, we check the noise removal capability of the proposed models over real SAR and Ultrasound images. More precisely, the objectives of this thesis are as stated below

- To study the existence and uniqueness of weak solution of a new version of the coupled diffusion model discussed in ([Jain, 2018](#)) and apply the model for additive Gaussian noise removal.
- Extend the coupled diffusion model to a coupled telegraph diffusion-based model to show the additive Gaussian noise removal ability of the coupled hyperbolic-parabolic PDE based model. Also, establish the existence of a unique global weak solution of the model.
- Development of a telegraph diffusion-based model for image despeckling; also, to study the existence and uniqueness of weak solution of the developed model.
- Extend the telegraph diffusion-based model to a coupled telegraph diffusion-based model to show the image despeckling ability of the hyperbolic-parabolic coupled PDE based model. Also, to establish the existence and uniqueness of weak solution of the model.
- Development of a telegraph total variation model with fuzzy edge detector for multiplicative speckle noise removal. To establish the existence and uniqueness of weak solution of the developed model.

To the best of our knowledge, the present work marks the first step towards the use of telegraph equation ([Ratner and Zeevi, 2007](#); [Zauderer, 2011](#)) based models for multiplicative speckle noise removal process.

1.6 Thesis Overview

This thesis consists of six main chapters (Chapters [2-7](#)) along with an introductory chapter (Chapter [1](#)) and a conclusion chapter (Chapter [8](#)) describing the overall conclusion and future scope. Each main chapter begins with a general introduction that discusses a brief literature review and outlines the motivation of the work done. The mathematical model development is then described, followed by a rigorous study of the well-posedness of the developed model. Then extensive numerical tests are reported to demonstrate the effectiveness of the proposed model compared to recently developed models over a set of gray level test images which are contaminated by different level of noise. At the end of each chapter, concluding remarks of each of the studies are presented. A brief description associated with each chapter of the thesis is provided below.

[Chapter 1](#) provides a little impression about the motivation behind digital image processing, which is followed by a short description of the inverse problem and PDE based image restoration models. Moreover, we describe a literature review of PDE based noise removal models, a brief description of the numerical method, and explained some image quality measurement parameters related to the computational study. Finalize the chapter with the motivation and objective of this dissertation.

In [Chapter 2](#), we consider a new version of the coupled diffusion system previously proposed by Jain et al. ([Jain, 2018](#)) and established the existence and uniqueness of a weak solution of the proposed system using Schauder fixed point theorem. We use a generalized weighted average finite difference scheme to solve the coupled system efficiently, and experiment results show the effectiveness of the proposed coupled PDE model.

In [Chapter 3](#), a coupled telegraph diffusion-based image denoising model is presented for additive Gaussian noise removal. This new framework interpolates among two telegraph diffusion equations and a diffusion equation. The proposed strategy can be applied to significantly preserve the oscillatory and texture pattern in an image, even in a low signal-to-noise ratio. First, we prove that the present model has a unique global weak solution using Banach's fixed point theorem. Then apply the present method over a set of gray level images to illustrate the superior-

ity of the technique over the recently developed hyperbolic-parabolic PDE based models as well as the coupled diffusion system discussed in [Chapter 2](#).

In [Chapter 4](#), we describe the formulation of a gray level indicator based hyperbolic-parabolic PDE based model for image despeckling. The diffusion coefficient in the equation depends not only on the image gradient but also on the gray level of the image, which controls the diffusion process better than only gradient-based diffusion approaches. Furthermore, we establish the well-posedness of the system using Schauder fixed point theorem. A computational study performed to highlight the effectiveness of the suggested technique on different types of test images. Computational results of the present model indicate that the images are suitably recovered without introducing undesired artifacts, especially for the high noise level, as compare to recently developed PDE based methods.

The development of a nonlinear hyperbolic-parabolic coupled PDE based approach for image despeckling is described in [Chapter 5](#). In this approach, we use an extra equation to calculate the edge variable, which injects the past information into the diffusion process and improves the quality of edge information in the despeckled images. We determine the existence and uniqueness of a weak solution to the present system in a suitable function space. Also, we investigate the noise removal capability of the model over a set of gray level test images which are damaged by speckle noise, and then the proposed method is applied to restore a real SAR image and an Ultrasound image. Also, here we compare the computational results of the present approach with the performance of recently developed strategies. The overall performance of our study confirms that the present method is more efficient than the other existing models for image despeckling.

Detail derivation of a telegraph total variation model with fuzzy edge detector for image despeckling is presented in [Chapter 6](#). A new attempt has been made using the total variation framework and fuzzy edge indicator function. The intuitionistic fuzzy divergence (IFD) function ([Chaira and Ray, 2008](#)) has been used to differentiate between edges and noise. After deriving the associated Euler-Lagrange equation of the proposed energy functional, we introduce a second-order time derivative term of the image variable along with the first time derivative into the evaluation equation. Furthermore, we establish the existence and uniqueness of a weak solution of a regularized version of the evaluation equation. Finally, we apply our model over a set of gray level test images and real (SAR and medical ultrasound) images to illustrate the despeckling ability of the present approach with respect to the various existing PDE based methods.

Chapter 7 represents the restored results of RGB images using the methods discussed in **Chapter 2–5** and the Maximum entropy method ([Jannetta, 2005](#)).

Chapter 8 discusses the conclusions of the work done in this thesis. Also, summarize the main contribution of the research work, along with the scopes for future research.

Chapter 2

On the Existence and Uniqueness of Weak Solutions of a Coupled Diffusion System Related to Image Restoration

In this chapter, a CPDE based image denoising model is proposed for additive Gaussian noise. We establish the existence and uniqueness of a weak solution of the proposed model. Moreover, a generalized weighted average finite difference scheme is used to solve the coupled system. Computed results are compared with the results of existing models. The comparison shows the effectiveness of the present model.

2.1 General Introduction

Over the last three decades, PDE based techniques are widely used for the additive Gaussian noise removal process. Recently, Jain et al. proposed the CPDE model (1.21)–(1.23) for additive Gaussian noise removal process. In the present study, we consider a new version of the model (1.21)–(1.23). We have replaced u by u_ξ in the diffusion function $g(\cdot)$ in (1.21), where $u_\xi = G_\xi * u$, and choose the diffusion function as

$$g(u_\xi) = \frac{1}{1 + \frac{|u_\xi|}{k^2}}. \quad (2.1)$$

Also, in (1.22) replaced the term $|\nabla I_\xi|^2$ by a smooth truncate function h of $|\nabla I_\xi|$ ([Belahmidi and Chambolle, 2005](#)), and considered the following model (ACPDE)

$$\partial_t I = \operatorname{div}(g(u_\xi) \nabla I) - 2\lambda v \quad \text{in } \Omega_T, \quad (2.2)$$

$$\partial_t u = \alpha h(|\nabla I_\xi|) - u + \beta \Delta u \quad \text{in } \Omega_T, \quad (2.3)$$

$$\partial_t v = \Delta v - (J - I) \quad \text{in } \Omega_T, \quad (2.4)$$

$$\begin{cases} I(x, 0) = J, & u(x, 0) = G_\xi * |\nabla J|^2, & v(x, 0) = 0 \text{ in } \Omega, \\ \partial_n I = 0 = \partial_n u = \partial_n v & \text{in } \partial\Omega_T. \end{cases} \quad (2.5)$$

where $\alpha, \beta > 0$ are constants to be specified, and λ is a weight parameter. Also, $g : \mathbb{R}^+ \rightarrow \mathbb{R}^+$ is a bounded, decreasing, and smooth function with $g(0) = 1$ and $\lim_{s \rightarrow \infty} g(s) = 0$, and $k > 0$ is a threshold parameter. We prove the existence and uniqueness of weak solutions of the model (2.2)–(2.5). To solve the system, we employ an implicit finite difference scheme with an advanced iterative solver (Hybrid Bi-Conjugate Gradient Stabilized method) (Jain *et al.*, 2015b). The quality of the denoised image using the system (2.2)–(2.5), is also compared with the results obtained by the existing models.

The rest of this chapter is organized as follows. In section 2.2, we establish the existence and uniqueness of a weak solution to the present system. A numerical realization of the proposed model is shown in section 2.3. Numerical validation of the proposed approach using a computational study is carried out in section 2.4. We conclude the work in section 2.5.

2.2 Existence and Uniqueness of Weak Solution

In this section, we study the existence and uniqueness of weak solution of the proposed model (2.2)–(2.5). Since the model is coupled and nonlinear, we first consider the linearized problem, and then use Schauder fixed point theorem (Evans, 1998) to show the existence of a weak solution.

2.2.1 Technical framework & statement of the main result

Without loss of generality we choose all the constants involved in the system of equations (2.2)–(2.5) equals to 1. Throughout this section, C denotes a generic positive constant. For $r \in \mathbb{N}$, we write $(H^r, \|\cdot\|_{H^r})$ for usual Hilbert spaces on Ω , and $(H^1)'$ for the dual space of H^1 . Also, we write $L^p, H^1, (H^1)'$ instead of $L^p(\Omega)$, $H^1(\Omega)$, $(H^1(\Omega))'$, respectively. We introduce the solution space $W(0, T)$ for the

system (2.2)–(2.5) as $W(0, T) = V(0, T) \times V(0, T) \times V(0, T)$, where

$$V(0, T) = \left\{ w : w \in L^2(0, T; H^1); \partial_t w \in L^2(0, T; (H^1)') \right\}.$$

Note that $V(0, T)$ is a Hilbert space for the graph norm, see (Lions, 1968).

Definition 2.1 (Weak solution). A triplet (I, u, v) is called a weak solution of (2.2)–(2.5) if

- a) $(I, u, v) \in W(0, T)$ and (2.5) holds.
- b) For all $\phi \in H^1$ and a.e. $t \in (0, T)$, there hold

$$\begin{aligned} \langle \partial_t I, \phi \rangle + \int_{\Omega} g(u_{\xi}) \nabla I \cdot \nabla \phi \, dx + 2 \int_{\Omega} v \phi \, dx &= 0, \\ \langle \partial_t u, \phi \rangle + \int_{\Omega} u \phi \, dx + \int_{\Omega} \nabla u \cdot \nabla \phi \, dx &= \int_{\Omega} h(|\nabla I_{\xi}|) \phi \, dx, \\ \langle \partial_t v, \phi \rangle + \int_{\Omega} \nabla v \cdot \nabla \phi \, dx + \int_{\Omega} J \phi \, dx - \int_{\Omega} I \phi \, dx &= 0. \end{aligned}$$

As our aim is to establish wellposedness of weak solutions of the proposed model (2.2)–(2.5), we shall do so under the following assumptions:

A.1 The initial data $J \in H^1$.

A.2 The function $h : \mathbb{R} \rightarrow \mathbb{R}$ is a positive, bounded, and Lipschitz function. More precisely, there exist $\delta, C_h > 0$ such that

$$\begin{cases} \delta \leq h(\cdot) \leq 1, \\ |h(x) - h(y)| \leq C_h |x - y|, \quad \forall x, y \in \mathbb{R}. \end{cases}$$

Theorem 2.1. Let the assumptions **A.1**–**A.2** be true. Then the proposed model (2.2)–(2.5) has a unique weak solution in the sense of Definition 2.1.

2.2.2 Linearized model & its well-posedness

For any positive constants M_1, M_2 , and M_3 define

$$\begin{aligned} W_{M_1, M_2, M_3} = \left\{ (\bar{I}, \bar{u}, \bar{v}) \in W(0, T) : \right. & \left. \|\bar{I}\|_{L^{\infty}(0, T; L^2)} \leq M_1 \|J\|_{L^2}; \right. \\ & \left. \|\bar{u}\|_{L^{\infty}(0, T; L^2)} \leq M_2 \|J\|_{L^2}; \|\bar{v}\|_{L^{\infty}(0, T; L^2)} \leq M_3 \right\}. \end{aligned}$$

For any $(\bar{I}, \bar{u}, \bar{v}) \in W_{M_1, M_2, M_3}$, consider the linearized model

$$\partial_t I = \operatorname{div}(\bar{g} \nabla I) - 2\bar{v} \quad \text{in } \Omega_T, \quad (2.6)$$

$$\partial_t u = \bar{h} - u + \Delta u \quad \text{in } \Omega_T, \quad (2.7)$$

$$\partial_t v = \Delta v - (J - \bar{I}) \quad \text{in } \Omega_T, \quad (2.8)$$

with the conditions (2.5), where the functions \bar{g} and \bar{h} are given by

$$\bar{g} \equiv g(\bar{u}_\xi) := \frac{1}{1 + \frac{|\bar{u}_\xi|}{k^2}} \text{ and } \bar{h} := h(|\nabla \bar{I}_\xi|).$$

Claim 2.2.1. *There exist positive constants $\kappa > 0$, depending only on G_ξ , J , k , and M_2 , such that*

$$0 < \kappa \leq \bar{g} \leq 1. \quad (2.9)$$

Proof. Since $\bar{u} \in W_{M_1, M_2, M_3}$, by convolution property, we have

$$\begin{aligned} \|G_\xi * \bar{u}\|_{L^\infty(\Omega)} &\leq \|G_\xi\|_{L^2(\Omega)} \|\bar{u}\|_{L^2(\Omega)} \leq C_\xi M_2 \|J\|_{L^2} \\ \Rightarrow 1 &\leq 1 + \frac{|G_\xi * \bar{u}|}{k^2} \leq 1 + \frac{C_\xi M_2 \|J\|_{L^2}}{k^2} \\ \Rightarrow \kappa &:= \frac{1}{1 + \frac{C_\xi M_2 \|J\|_{L^2}}{k^2}} \leq \bar{g} \leq 1. \end{aligned}$$

This completes the proof of claim. \square

Thanks to the Claim 2.2.1, one can apply classical Galerkin method (Evans, 1998) to show that there exists a unique weak solution $(I, u, v) \in W(0, T)$ of the linearized model (2.6)–(2.8) with the initial and boundary conditions (2.5).

Lemma 2.2. *The unique solution $(I, u, v) \in W(0, T)$ of the linearized model (2.6)–(2.8) with the conditions (2.5) satisfies the following: there exists positive constants C_1 , C_2 , and C_3 depending only on G_ξ , J , h , k , M_1 , M_2 , M_3 such that*

$$(a) \|I\|_{L^\infty(0,T;L^2)} \leq C_1, \|I\|_{L^2(0,T;H^1)} + \|\partial_t I\|_{L^2(0,T;(H^1)')} \leq C_1,$$

$$(b) \|u\|_{L^\infty(0,T;H^1)} + \|\partial_t u\|_{L^2(0,T;(H^1)')} \leq C_2,$$

$$(c) \|v\|_{L^\infty(0,T;L^2)} \leq C_3, \|v\|_{L^2(0,T;H^1)} + \|\partial_t v\|_{L^2(0,T;(H^1)')} \leq C_3.$$

Proof. Proof of (b): Multiply (2.7) by $\partial_t u$, integrate by parts over Ω , use Cauchy-Schwarz and Young's inequalities, and then integrate w.r.t. time between 0 to t . We have, for a.e. $t \in (0, T)$

$$\|u(t)\|_{H^1}^2 \leq \|u(0)\|_{H^1}^2 + t|\Omega|.$$

The above inequality implies that

$$\|u\|_{L^\infty(0,T;H^1)} \leq C, \quad (2.10)$$

where C is a positive constant depends on G_ξ , Ω , J , and T . Multiplying the equation (2.7) by $\phi \in H^1$ such that $\|\phi\|_{H^1} \leq 1$, and integrating over Ω , we have

$$\langle \partial_t u, \phi \rangle = \int_{\Omega} \bar{h} \phi dx - \int_{\Omega} u \phi dx - \int_{\Omega} \nabla u \cdot \nabla \phi dx.$$

Using Cauchy-Schwarz inequality, we have

$$|\langle \partial_t u, \varphi \rangle| \leq (\|\bar{h}\|_{L^2} + \|u\|_{L^2} + \|\nabla u\|_{L^2}) \|\phi\|_{H^1}.$$

Hence, by the definition of norm in $H^1(\Omega)'$, we get

$$\|\partial_t u\|_{(H^1)'} \leq C \|J\|_{H^1}. \quad (2.11)$$

Moreover, squaring both sides of (2.11) and integrating over $(0, T)$, we have

$$\|\partial_t u\|_{L^2(0,T;(H^1)')} \leq C \|J\|_{H^1}. \quad (2.12)$$

Combining (2.10) and (2.12), one can arrive at the assertion (b).

Proof of (a): Multiplying the equation (2.6) by I and integrating over Ω , we obtain

$$\frac{1}{2} \frac{d}{dt} \left(\int_{\Omega} I^2 dx \right) + \int_{\Omega} \bar{g} |\nabla I|^2 dx = \int_{\Omega} \bar{v} I dx. \quad (2.13)$$

Utilizing Young's inequality yields

$$\frac{d}{dt} \left(\|I(t)\|_{L^2}^2 \right) \leq C + \|I(t)\|_{L^2}^2, \quad (2.14)$$

where, $C = \int_{\Omega} \bar{v}^2 dx$, is a positive constant dependent on Ω , J , and M_3 . Thanks to the Gronwall's inequality, we have

$$\|I(t)\|_{L^2}^2 \leq e^t (\|I(0)\|_{L^2}^2 + Ct).$$

The above inequality implies that

$$\|I\|_{L^\infty(0,T;L^2)} \leq C, \quad (2.15)$$

where C is a positive constant depends on Ω , J , and T . Again from the relation (2.13), we have

$$\frac{d}{dt} (\|I(t)\|_{L^2}^2) + 2 \int_{\Omega} \bar{g} |\nabla I|^2 dx \leq \|\bar{v}\|_{L^2}^2 + \|I(t)\|_{L^2}^2. \quad (2.16)$$

Using the argument as Claim 2.2.1, we have

$$\kappa \|\nabla I\|_{L^2}^2 \leq \int_{\Omega} \bar{g} |\nabla I|^2 dx. \quad (2.17)$$

Using (2.17), from (2.16), we obtain

$$\frac{d}{dt} (\|I(t)\|_{L^2}^2) + 2\kappa \|\nabla I\|_{L^2}^2 \leq \|\bar{v}\|_{L^2}^2 + \|I(t)\|_{L^2}^2. \quad (2.18)$$

Integrating the above relation w.r.t. time between 0 to t , we have

$$\begin{aligned} \|I(t)\|_{L^2}^2 + 2\kappa \int_0^t \|\nabla I\|_{L^2}^2 d\tau &\leq \|I(0)\|_{L^2}^2 + \int_0^t \|\bar{v}\|_{L^2}^2 d\tau + \int_0^t \|I(t)\|_{L^2}^2 d\tau \\ \int_0^t \|\nabla I\|_{L^2}^2 d\tau &\leq \frac{1}{2\kappa} (\|I(0)\|_{L^2}^2 + tM_3 + tC). \end{aligned}$$

The above inequality follow that

$$\|\nabla I\|_{L^2(0,T;L^2)} \leq C. \quad (2.19)$$

Multiplying the equation (2.6) by $\phi \in H^1$ such that $\|\phi\|_{H^1} \leq 1$, and integrating over Ω , we have

$$\langle \partial_t I, \phi \rangle = - \int_{\Omega} \bar{g} \nabla I \cdot \nabla \phi dx - \int_{\Omega} \bar{v} \phi dx.$$

Using Cauchy-Schwarz inequality, we have

$$|\langle \partial_t I, \phi \rangle| \leq (\|\bar{v}\|_{L^2} + \|\nabla I\|_{L^2}) \|\phi\|_{H^1}.$$

Hence, by the definition of norm in $H^1(\Omega)'$, we get

$$\|\partial_t I\|_{(H^1)'} \leq C \|J\|_{H^1}. \quad (2.20)$$

Moreover, squaring both sides of (2.11) and integrating over $(0, T)$, we have

$$\|\partial_t I\|_{L^2(0,T;(H^1)')} \leq C \|J\|_{H^1}. \quad (2.21)$$

Combining (2.15), (2.19), and (2.21), one can arrive at the assertion (a).

Proof of (c): Following the proof of assertion (a), one can establish the relations

$$\|v\|_{L^\infty(0,T;L^2)} \leq C; \quad \|\nabla v\|_{L^2(0,T;L^2)} \leq C, \quad (2.22)$$

and

$$\|\partial_t v\|_{L^2(0,T;(H^1)')} \leq C. \quad (2.23)$$

where C is a positive constant depends on Ω , J , T , and M_1 . Combining (2.22) and (2.23), one can arrive at the assertion (c). This completes the proof of the Lemma 2.2. \square

2.2.3 Proof of Theorem 2.1

In this section, we prove the existence of weak solution of the proposed model via Schauder fixed point theorem. To proceed further, we introduce the subspace W_0 of $W(0, T)$ defined by

$$\begin{aligned} W_0 = \left\{ (w, s, z) \in W(0, T) : & \|w\|_{L^2(0,T;H^1)} + \|\partial_t w\|_{L^2(0,T;(H^1)')} \leq C\|J\|_{H^1}, \\ & \|w\|_{L^\infty(0,T;L^2)} \leq C\|J\|_{H^1}, \|s\|_{L^\infty(0,T;H^1)} + \|\partial_t s\|_{L^2(0,T;(H^1)')} \leq C\|J\|_{H^1}, \\ & \|z\|_{L^2(0,T;H^1)} + \|\partial_t z\|_{L^2(0,T;(H^1)')} \leq C\|J\|_{H^1}, \|z\|_{L^\infty(0,T;L^2)} \leq C\|J\|_{H^1}, \\ & \text{and } (w, s, z) \text{ satisfies (2.5)} \right\}. \end{aligned}$$

Moreover, one can prove that W_0 is a non-empty, convex and weakly compact subset of W . Consider a mapping

$$\begin{aligned} \mathcal{P} : W_0 &\rightarrow W_0 \\ (w, s, z) &\mapsto (I_w, u_s, v_z). \end{aligned}$$

In order to use Schauder fixed point theorem on \mathcal{P} , only we need to prove that the mapping $\mathcal{P} : (w, s, z) \rightarrow (I_w, u_s, v_z)$ is weakly continuous from W_0 into W_0 . Let (w_k, s_k, z_k) be a sequence that converges weakly to some (w, s, z) in W_0 and let $(I_k, u_k, v_k) = (I_{w_k}, u_{s_k}, v_{z_k})$. We have to show that $\mathcal{P}(w_k, s_k, z_k) := (I_k, u_k, v_k)$ converges weakly to $\mathcal{P}(w, s, z) := (I_w, u_s, v_z)$.

Thanks to Lemma 2.2, one can use classical results of compact inclusion in Sobolev spaces (Adams, 1975) to extract subsequences $\{w_{k_n}\}$ of $\{w_k\}$, $\{s_{k_n}\}$ of $\{s_k\}$, $\{z_{k_n}\}$ of $\{z_k\}$, $\{I_{k_n}\}$ of $\{I_k\}$, $\{u_{k_n}\}$ of $\{u_k\}$ and $\{v_{k_n}\}$ of $\{v_k\}$, still denoted by $\{w_k\}$, $\{s_k\}$, $\{z_k\}$, $\{I_k\}$, $\{u_k\}$, and $\{v_k\}$, such that for some $(I, u, v) \in W_0$, the

followings hold as $k \rightarrow \infty$:

$$\left\{ \begin{array}{l} w_k \rightarrow w, \quad s_k \rightarrow s, \quad z_k \rightarrow z \text{ in } L^2(0, T; L^2) \text{ and a.e. on } \Omega_T, \\ \partial_{x_i} G_\xi * w_k \rightarrow \partial_{x_i} G_\xi * w \ (i = 1, 2) \text{ in } L^2(0, T; L^2) \text{ and a.e. on } \Omega_T, \\ h(|\nabla G_\xi * w_k|) \rightarrow h(|\nabla G_\xi * w|) \text{ in } L^2(0, T; L^2) \text{ and a.e. on } \Omega_T, \\ |G_\xi * s_k| \rightarrow |G_\xi * s| \text{ in } L^2(0, T; L^2) \text{ and a.e. on } \Omega_T, \\ g(|G_\xi * s_k|) \rightarrow g(|G_\xi * s|) \text{ in } L^2(0, T; L^2) \text{ and a.e. on } \Omega_T, \\ I_k \rightarrow I, \quad v_k \rightarrow v \text{ weakly in } L^2(0, T; H^1), \\ u_k \rightarrow u \text{ weakly-* in } L^\infty(0, T; H^1), \\ I_k \rightarrow I, \quad u_k \rightarrow u, \quad v_k \rightarrow v \text{ in } L^2(0, T; L^2), \\ \partial_{x_i} I_k \rightarrow \partial_{x_i} I, \quad \partial_{x_i} u_k \rightarrow \partial_{x_i} u, \quad \partial_{x_i} v_k \rightarrow \partial_{x_i} v \text{ weakly in } L^2(0, T; L^2), \\ \partial_t I_k \rightarrow \partial_t I, \quad \partial_t u_k \rightarrow \partial_t u, \quad \partial_t v_k \rightarrow \partial_t v \text{ weakly in } L^2(0, T; (H^1)'). \end{array} \right.$$

The above convergence allow us to pass to the limit in the problem (2.6)–(2.8) and obtain $(I, u, v) = \mathcal{P}(w, s, z)$. Moreover, since the solution of (2.6)–(2.8) is unique, the whole sequence $(I_k, u_k, v_k) = \mathcal{P}(w_k, s_k, z_k)$ converges weakly in W_0 to $(I, u, v) = \mathcal{P}(w, s, z)$. Hence \mathcal{P} is weakly continuous. Consequently, thanks to the Schauder fixed point theorem, there exists $(w, s, z) \in W_0$ such that $(w, s, z) = \mathcal{P}(w, s, z) = (I_w, u_s, v_z)$. Thus, the function (I_w, u_s, v_z) solves the model (2.2)–(2.5).

2.2.4 Uniqueness of weak solution

We use standard methodology (Evans, 1998) to prove the uniqueness of weak solution of (2.2)–(2.5). Let (I_1, u_1, v_1) and (I_2, u_2, v_2) be two set of solutions for the system (2.2)–(2.5) with $I_1 \neq I_2$, $u_1 \neq u_2$ and $v_1 \neq v_2$. Let

$$I := I_1 - I_2, \quad u := u_1 - u_2, \quad v := v_1 - v_2, \quad g_i = g(G_\xi * u_i) \text{ for } i = 1, 2.$$

Then, the following relations hold in the sense of distribution:

$$\partial_t I - \operatorname{div}(g_1 \nabla I) = \operatorname{div}((g_1 - g_2) \nabla I_2) - 2v \quad \text{in } \Omega_T, \quad (2.24)$$

$$\partial_t u - \Delta u = \left(h(|\nabla G_\xi * I_1|) - h(|\nabla G_\xi * I_2|) \right) - u \quad \text{in } \Omega_T, \quad (2.25)$$

$$\partial_t v - \Delta v = I \quad \text{in } \Omega_T, \quad (2.26)$$

$$\partial_n I = 0, \quad \partial_n u = 0, \quad \partial_n v = 0 \quad \text{on } \partial\Omega_T, \quad (2.27)$$

$$I(x, 0) = 0 = u(x, 0) = v(x, 0) \quad \text{in } \Omega. \quad (2.28)$$

Note that, there exists a constant $C > 0$ depends on Ω and ξ such that

$$\nu_1 := \frac{1}{1 + \frac{C\|u_1\|_{L^\infty(0,T;L^2)}}{k^2}} \leq g(u_1).$$

Multiply the equation (2.24) by I and then integrating over Ω and using Cauchy-Schwarz and Young's inequalities along with the above lower bound ν_1 of $g(u_1)$, we obtain

$$\begin{aligned} \frac{1}{2} \frac{d}{dt} \|I\|_{L^2}^2 + \nu_1 \|\nabla I\|_{L^2}^2 &\leq \|(g_1 - g_2)\|_{L^\infty} \|\nabla I_2\|_{L^2} \|\nabla I\|_{L^2} + \|I\|_{L^2}^2 + \|v\|_{L^2}^2 \\ &\leq \frac{\nu_1}{2} \|\nabla I\|_{L^2}^2 + C(\nu_1) \|(g_1 - g_2)\|_{L^\infty}^2 \|\nabla I_2\|_{L^2}^2 + \|I\|_{L^2}^2 + \|v\|_{L^2}^2 \\ &\leq \frac{\nu_1}{2} \|\nabla I\|_{L^2}^2 + \tilde{C}_I C(\nu_1) \|(g_1 - g_2)\|_{L^\infty}^2 + \|I\|_{L^2}^2 + \|v\|_{L^2}^2, \end{aligned}$$

where $\tilde{C}_I := \|\nabla I\|_{L^\infty(L^2)}^2$. Since g is Lipschitz continuous function with Lipschitz constant $\frac{C}{k^2}$, by using Hölder's inequality, we see that

$$\|(g_1 - g_2)\|_{L^\infty} \leq C\|(u_1 - u_2)\|_{L^2}.$$

Hence, for a.e. $t \in (0, T)$, we get

$$\frac{d}{dt} \|I\|_{L^2}^2 \leq \tilde{C} \|u\|_{L^2}^2 + \|I\|_{L^2}^2 + \|v\|_{L^2}^2. \quad (2.29)$$

Similarly, multiplying the equation (2.25) by u and then integrating over Ω , we get

$$\frac{d}{dt} \|u\|_{L^2}^2 + 2\|\nabla u\|_{L^2}^2 \leq C \|(h(|\nabla G_\xi * I_1|) - h(|\nabla G_\xi * I_2|))\|_{L^2}^2 + \|u\|_{L^2}^2.$$

Since h is Lipschitz continuous, by using Young's inequality for convolution, we see that

$$\|h(|\nabla G_\xi * I_1|) - h(|\nabla G_\xi * I_2|)\|_{L^2}^2 \leq C(c_h, \xi) \|I\|_{L^2}^2.$$

Therefore,

$$\frac{d}{dt} \|u\|_{L^2}^2 \leq C \|I\|_{L^2}^2 + \|u\|_{L^2}^2. \quad (2.30)$$

In a similar way, one can easily deduce that

$$\frac{d}{dt} \|v\|_{L^2}^2 \leq C \left(\|I\|_{L^2}^2 + \|v\|_{L^2}^2 \right). \quad (2.31)$$

We now add (2.29)–(2.31) and then apply Gronwall's inequality to infer that $I \equiv 0$, $u \equiv 0$, and $v \equiv 0$. In other words, weak solution of the proposed model (2.2)–(2.5) is unique.

2.3 Numerical Implementation

This section presents the numerical implementation of the model (2.2)–(2.5). To solve the system (2.2)–(2.5), we use an implicit finite difference method. Derivative terms in (2.2)–(2.5) are approximated by the finite difference formulas discussed in [section 1.3](#). The discretized form of (2.2)–(2.5) can be written as

$$I_{i,j}^{n+1} - \frac{\tau}{2} ((\operatorname{div}(g \nabla I))_{i,j}^{n+1} - 2\lambda v_{i,j}^{n+1}) = I_{i,j}^n + \frac{\tau}{2} ((\operatorname{div}(g \nabla I))_{i,j}^n - 2\lambda v_{i,j}^n), \quad (2.32)$$

$$u_{i,j}^{n+1} = u_{i,j}^n + \tau \left\{ \alpha h(|\nabla I_{\xi_{i,j}}^n|^2) - u_{i,j}^{n+1} + \beta \Delta u_{i,j}^{n+1} \right\}, \quad (2.33)$$

$$v_{i,j}^{n+1} = v_{i,j}^n + \tau \left\{ \Delta v_{i,j}^{n+1} - (I_{i,j}^n - I_{i,j}^0) \right\}, \quad (2.34)$$

with the initial conditions $I_{i,j}^0 = J(x_i, y_j)$, $u_{i,j}^0 = G_\xi * |\nabla I_{i,j}^0|^2$, and $v_{i,j}^0 = 0$ and the boundary conditions as discussed in [section 1.3](#). Moreover, the diffusion term in (2.32) is discretized by the central difference formula as

$$\begin{aligned} \operatorname{div}(g \nabla I)_{i,j} = & g_{i+\frac{1}{2},j} (I_{i+1,j} - I_{i,j}) - g_{i-\frac{1}{2},j} (I_{i,j} - I_{i-1,j}) + \\ & g_{i,j+\frac{1}{2}} (I_{i,j+1} - I_{i,j}) - g_{i,j-\frac{1}{2}} (I_{i,j} - I_{i,j-1}), \end{aligned} \quad (2.35)$$

where

$$g_{i,j} = \frac{1}{1 + \frac{|G_\xi * u_{i,j}|}{k^2}}.$$

Further, to solve the algebraic system of the form $AI^{n+1} = B$, generated from numerical discretization, hybrid Bi-Conjugate Gradient Stabilized ([Jain et al., 2015a,b](#)) solver is used.

2.4 Computational Results & Discussion

In this section, image denoising results of the proposed model are compared with the results of the RD model (1.19) and VBS model (1.20). In this process, the considered existing models are discretized using an explicit finite difference scheme. Also, to terminate the iterative process of each algorithm, the same stopping criterion is used discussed in [section 1.3](#). The effectiveness of results is evaluated through four standard gray level test images (see [Figure 2.1](#)). We have artificially generated Gaussian noise with mean $\mu = 0$ and standard deviation $\sigma = \{10, 30, 50\}$ using MATLAB built-in normally distributed random numbers generator function “randn” as $\eta = \sigma * \text{randn}(M, N)$ and then added with the ground truth images in [Figure 2.1](#), where $M \times N$ is the image dimensions. To compare the quantitative results, we compute the values of the parameters PSNR and MSSIM. Moreover, we compute the ratio image for the restored images. Apart from the ratio image, we also compute the two-dimensional (2D) contour plot for the better visualization of the restored images. For numerical experiments we use uniform time step sizes $\tau = 0.1$ and $\xi = 1$, additionally for the proposed model we choose $\alpha = 0.2$ and $\beta = 0.01$. Other parameter values for the numerical experiments are given in detail in the [Table 2.1](#).

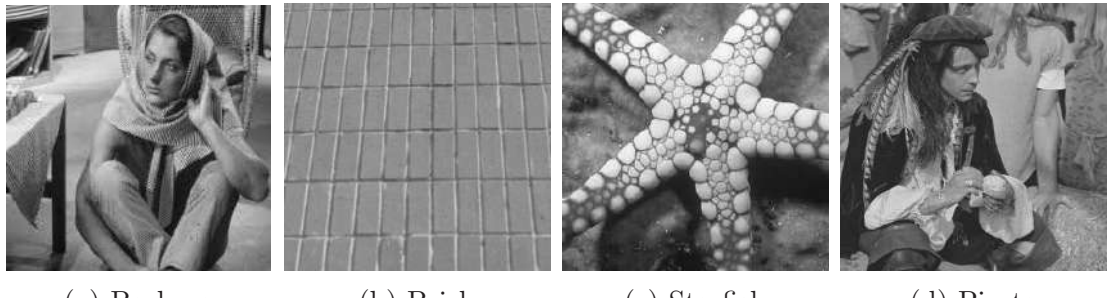
Restored results of barbara image, contaminated by additive Gaussian noise with $\sigma = 30$, are displayed in [Figure 2.2](#). From the quality of the restored images, one can observe that the result computed by the present model is more apparent than the results of the other discussed models.

To further test the effectiveness of the proposed model, Figures 2.3–2.5 present the restored results for a brick image that contains additive Gaussian noise with $\sigma = 30$. From [Figure 2.3](#), one can see that the restored image using the proposed model depicts better clarity of edges than the results of other existing approaches. [Figure 2.4a](#) represents the ratio image of the clear brick image, which indicates that it has no background information. Now from Figures [2.4b–2.4d](#), one can

observe that ratio image corresponding to the present model has less background information, which confirms that the present approach preserves the image edges better than the other models. Along with the results of a full image, we examine a particular slice of the restored image. [Figure 2.5](#) shows the signals of the original, noisy, and restored one obtained by the proposed CPDE model and other discussed CPDE models. From these figures, it is easy to conclude that the restored signal computed by the proposed model is more closure to the clean signal in comparison to other discussed models.

To check further the reconstruction ability of the present method, we illustrate the restored images, ratio images, and their 2D contour plots of a starfish image, which is initially degraded by additive Gaussian noise with $\sigma = 30$; ([Figures 2.6–2.8](#)). In [Figure 2.6](#), we display the denoised results using the present model and the other discussed models. One can recognize from the [Figure 2.6](#), that the present model preserves the image contrast better than the other considered models. [Figure 2.7](#), described the ratio image of the restored images which indicates the edge preservation ability of the present method. Also, from the contour plots in [Figure 2.8](#), we can see that the results using the existing methods introduce some false contours into the homogeneous regions, but the result obtained by the present model is more closure to the result of the original image. It indicates that the proposed model not only removes noise efficiently but also preserves the fine structure in comparison with the other discussed models.

In addition to qualitative comparisons, the quantitative result, in terms of PSNR and MSSIM values, are shown in [Table 2.1](#). The highest values of MSSIM and PSNR are mentioned (in bold fonts) in the table. Along with the qualitative results discussed above, the quantitative results also confirm the superiority of the proposed approach in comparison with other presented models. From the overall performance, it can be concluded that the suggested CPDE method preserves the texture pattern and edge information more efficiently than the other existing CPDE based approaches.



(a) Barbara (b) Brick (c) Starfish (d) Pirate

Figure 2.1: Clean images.



Figure 2.2: Barbara image corrupted by additive Gaussian noise with $\mu = 0$ and $\sigma = 30$ and restored by different models.

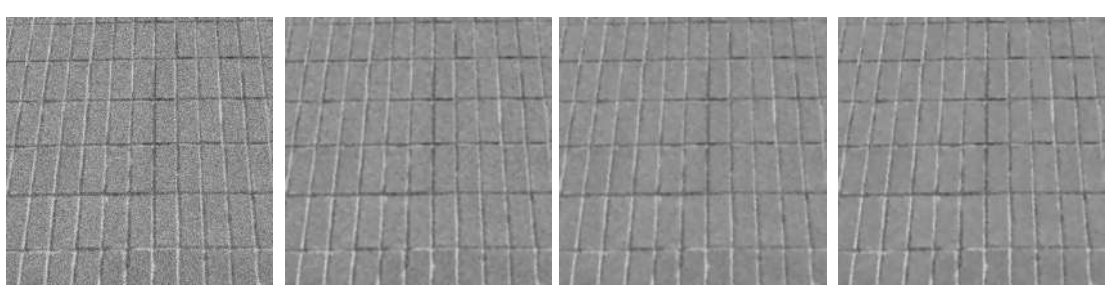


Figure 2.3: A brick image corrupted by additive Gaussian noise with $\mu = 0$ and $\sigma = 30$ and restored by different models.

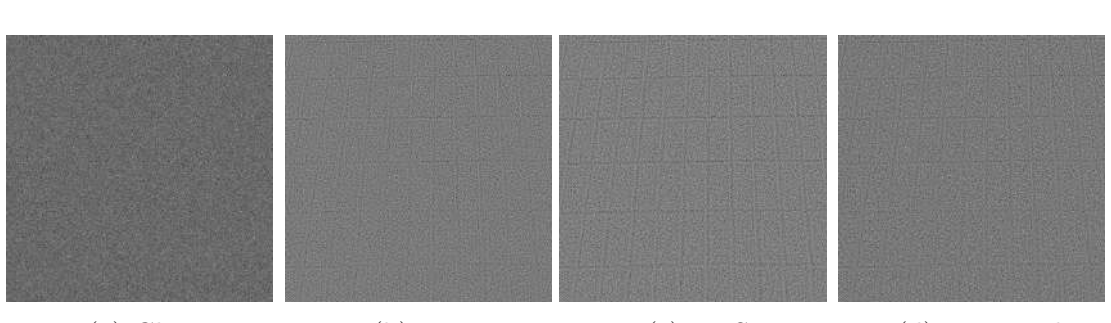


Figure 2.4: Ratio images of the image Figure 2.1b and images; Figures 2.3b–2.3d.

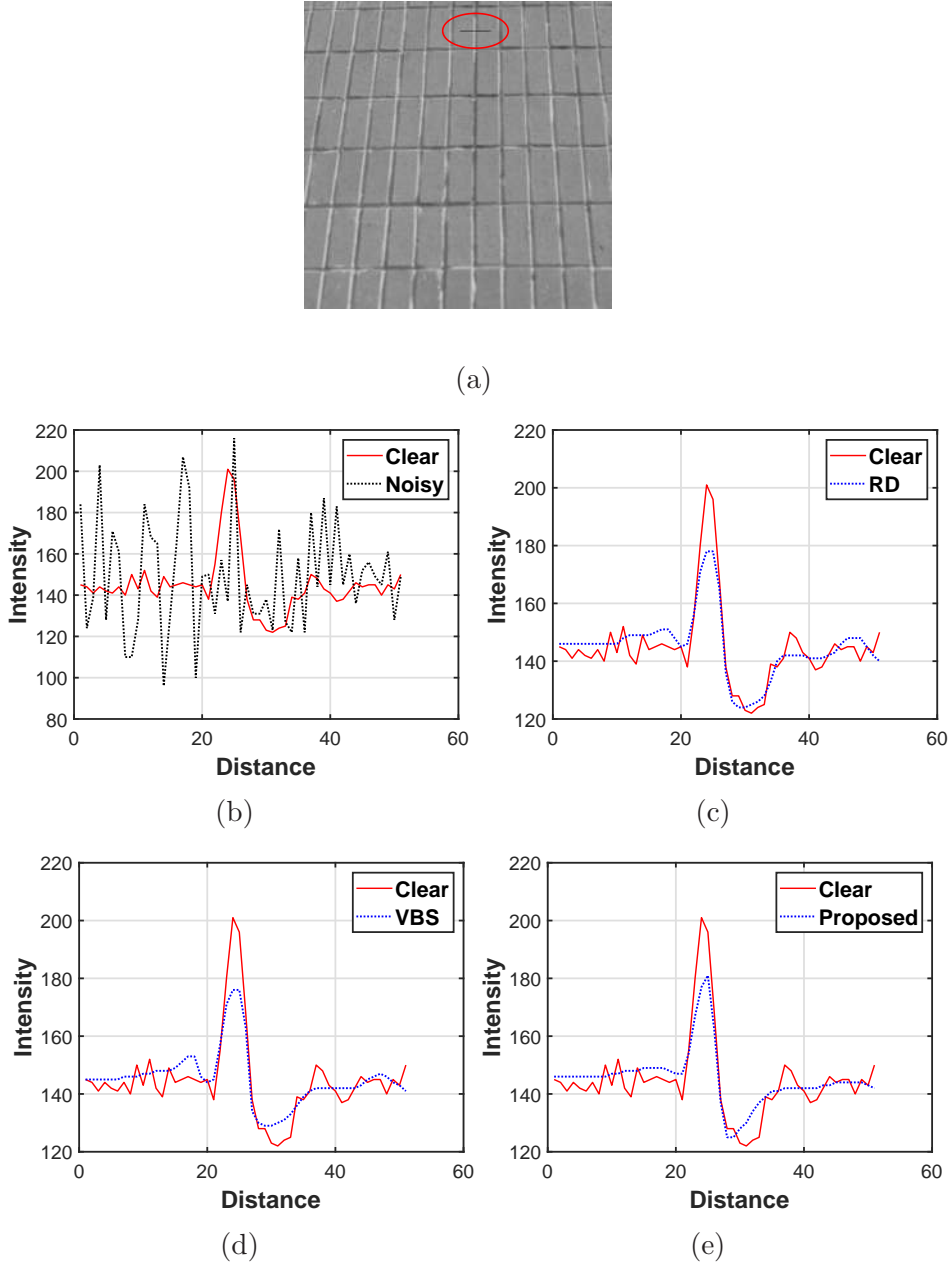


Figure 2.5: Part of the 50th slice of the brick image corrupted by additive Gaussian noise with $\mu = 0$ and $\sigma = 30$ and restored by different models.

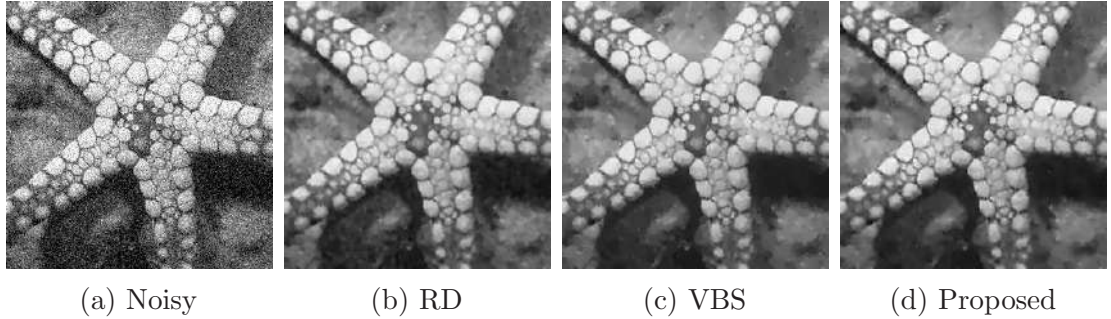


Figure 2.6: A starfish image corrupted by additive Gaussian noise with $\mu = 0$ and $\sigma = 30$ and restored by different models.

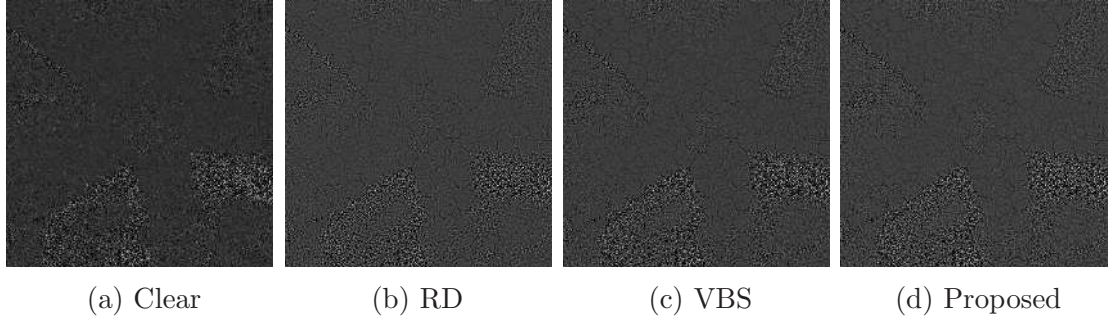


Figure 2.7: Ratio images of the clear image Figure 2.1c and the images; Figures 2.6a–2.6d.

Table 2.1: MSSIM and PSNR values of restored images. Selected parameter values for the numerical experiments.

Image	σ	RD model			VBS model			Proposed Model			
		MSSIM	PSNR	λ	MSSIM	PSNR	λ	K	MSSIM	PSNR	k
Barbara	10	0.8754	30.06	0.1	0.8696	29.99	0.1	2	0.8970	31.06	1
	30	0.7346	25.86	0.05	0.7483	26.05	0.1	2	0.7565	26.21	3
	50	0.6025	23.28	0.05	0.6655	24.02	0.1	5	0.6674	24.12	3.5
Brick	10	0.9448	34.17	0.05	0.9456	34.38	0.1	5	0.9458	34.52	1
	30	0.8436	30.30	0.02	0.8459	30.21	0.1	6	0.8654	30.63	1.5
	50	0.7438	28.00	0.01	0.7495	28.05	0.1	7	0.7746	28.29	1.5
Starfish	10	0.9237	31.96	0.1	0.9235	31.95	0.1	2	0.9286	32.62	3
	30	0.7910	26.50	0.05	0.8035	26.79	0.1	2	0.8135	26.92	3
	50	0.7091	24.01	0.02	0.7161	24.03	0.1	3	0.7257	24.19	3.5
Pirate	10	0.9550	32.68	0.1	0.9555	32.70	0.1	2	0.9580	33.17	1.5
	30	0.8512	28.08	0.02	0.8556	28.15	0.1	5	0.8572	28.23	2.5
	50	0.7469	25.77	0.02	0.7763	26.10	0.1	5	0.7790	26.15	3

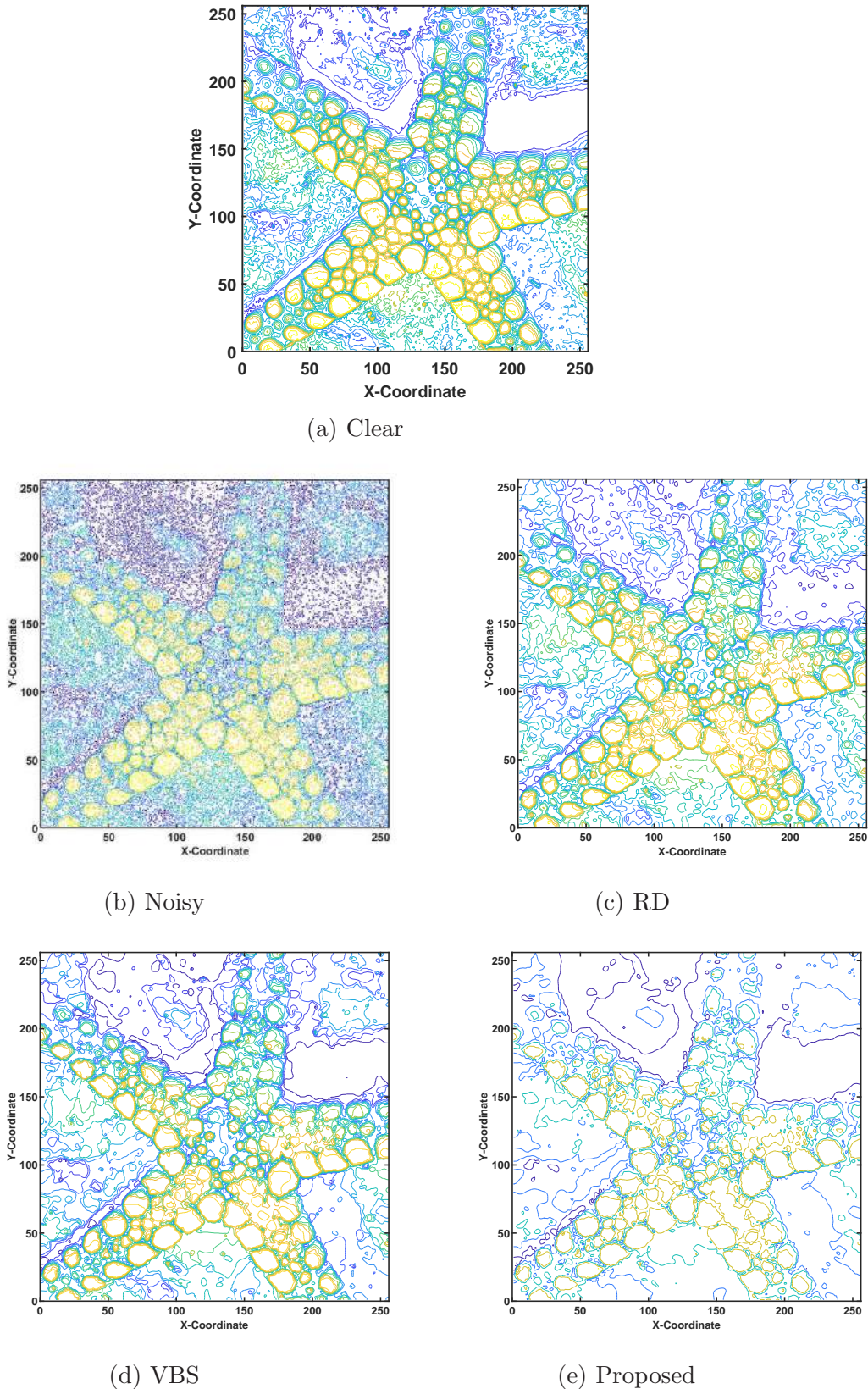


Figure 2.8: Contour maps of the clear starfish image Figure 2.1c and the images; Figures 2.6a–2.6d.

2.5 Conclusion

In this work, we present a nonlinear coupled diffusion model for image restoration, when an image is corrupted by additive Gaussian noise. The proposed model uses two separate PDEs to calculate the image edges and the data fidelity. First, we established the well-posedness of the proposed model. Then, the proposed model is solved numerically using implicit finite difference scheme along with an advance iterative solver. Experimental studies clearly confirm the noise removal ability of the proposed model for grayscale images.

Chapter 3

On the Development of a Coupled Nonlinear Telegraph-Diffusion Model for Image Restoration

In this chapter, a telegraph coupled PDE based image restoration model is described when the image is corrupted with additive Gaussian noise. The new framework interpolates between a couple of telegraph equation and a diffusion equation. The proposed strategy can be applied to preserve the oscillatory and texture pattern in an image significantly. We confirm that the present model has a unique global weak solution using Banach's fixed point theorem. Moreover, the proposed model applies over a set of gray level images to illustrate the superiority of the method over the recently developed hyperbolic-parabolic PDE based techniques.

3.1 General Introduction

In digital image processing applications, image smoothing is often considered as a significant pre-processing step to make accurate and reliable subsequent image analysis ([Aubert and Kornprobst, 2006](#); [Scherzer, 2010](#)). The principal objective of image denoising algorithms is to achieve the balance between the noise removal and preservation of edges and key features. In the field of PDE based image processing techniques, parabolic PDE has acquired the center stage for image denoising. In [Chapter 2](#), we have considered the coupled diffusion system [\(2.2\)–\(2.5\)](#) for additive Gaussian noise removal problem. Besides parabolic PDEs, hyperbolic PDEs which describe oscillations within objects, could also improve the quality of the detected edges more suitable than diffusion-based models and so enhance the image better than parabolic PDE ([Averbuch *et al.*, 2006](#); [Ratner and Zeevi, 2007](#); [Cao](#)

⁰The research work of this chapter is published in *Computers & Mathematics with Applications*, vol. 80(7), pp. 1745–1766, 2020, <https://doi.org/10.1016/j.camwa.2020.08.010>.

et al., 2010; Yang and Zhang, 2014; Jain and Ray, 2016; Sun *et al.*, 2016). In 2007, Ratner and Zeevi propose the TDE model (1.17), which interpolates between the diffusion equation and the wave equation. Although, the model (1.17) performs well, but it is challenging to confirm the well-posedness of this model. To overcome the ill-posedness issue in the model (1.17), Cao et al. suggest the regularized TDE model (1.18) and established the well-posedness of their proposed model. Also, it has been proved that the PDEs of the form of telegraph equation provide better edge preservation and image enhancement than the ordinary diffusion based methods. For different elasticity coefficients, the telegraph model can be treated as the improved versions of the corresponding nonlinear diffusion models. Although these methods are efficient in the restoration of discontinuous and noisy signals, their performance is not satisfactory in the case of higher noise level or low SNR images. To overcome this issue, several nonlinear telegraph diffusion-based methods are proposed (Cao *et al.*, 2010; Yang and Zhang, 2014; Zhang *et al.*, 2015; Jain and Ray, 2016; Sun *et al.*, 2016). In low SNR images, the appropriate separation of noise and important texture information can be viewed as a highly complex problem. The parabolic PDE based image restoration methods strongly depend on the diffusion function $g(\cdot)$, to preserve small variations in the image. In conventional approaches, spatial regularization has been used for the diffusion coefficient, which cannot include past knowledge into the diffusion process. To alleviate this shortcoming in the parabolic PDE based models as well as single hyperbolic PDE based models a hyperbolic-parabolic coupled system (the SYS model) is introduced by Sun *et al.* (2016) for image restoration, which takes the form,

$$\partial_t I - \operatorname{div}(g(u) \nabla I) = 0 \quad \text{in } \Omega_T, \quad (3.1)$$

$$\partial_{tt} u + \partial_t u - \lambda \operatorname{div}(\nabla u) - (1 - \lambda)(|\nabla I| - u) = 0 \quad \text{in } \Omega_T, \quad (3.2)$$

$$\partial_n I = 0, \quad \partial_n u = 0 \quad \text{on } \partial\Omega_T, \quad (3.3)$$

$$I(x, 0) = J(x), \quad u(x, 0) = u_0(x), \quad u_t(x, 0) = 0 \quad \text{in } \Omega. \quad (3.4)$$

$\lambda > 0$ is a balancing parameter. They consider the following two diffusion functions:

$$g(s) = \frac{1}{1 + \left(\frac{s}{K}\right)^2} \quad \text{or} \quad g(s) = |s|^{-1} \quad \text{with } K > 0.$$

In the above model, the authors have used the telegraph equation only for the edge variable u , but it would be better to use the telegraph equation for the image variable I as well as for the edge variable u . Also, they have not incorporated the

fidelity term (Jain *et al.*, 2019) into the model (3.1)–(3.4), which keeps the restored image close to the original image. To overcome these issues, the present work introduces a nonlinear coupled telegraph diffusion system to deal with the additive Gaussian noise problem. Our motivation is based on the improvement in the restoration ability of the proposed coupled system for low SNR images. Inspired by the merit of the CPDE system (2.2)–(2.5) discussed in **Chapter 2** and telegraph-diffusion equation based models (Ratner and Zeevi, 2007; Sun *et al.*, 2016), we propose the following telegraph coupled partial differential equation (TCPDE) model

$$\partial_{tt}I + \alpha\partial_t I = \operatorname{div}(g(u_\xi)\nabla I) - 2\lambda v, \quad \text{in } \Omega_T, \quad (3.5)$$

$$\partial_{tt}u + \beta\partial_t u = \kappa \left(h(|\nabla I_\xi|) - u + \frac{\nu^2}{2}\Delta u \right), \quad \text{in } \Omega_T, \quad (3.6)$$

$$\partial_t v = \Delta v - (J - I), \quad \text{in } \Omega_T, \quad (3.7)$$

$$\partial_n I = 0, \quad \partial_n u = 0, \quad \partial_n v = 0, \quad \text{on } \partial\Omega_T, \quad (3.8)$$

$$\begin{cases} I(x, 0) = J(x), \quad \partial_t I(x, 0) = 0, \quad v(x, 0) = 0, \\ u(x, 0) = G_\xi * |\nabla J|^2, \quad u_t(x, 0) = 0, \end{cases} \quad \text{in } \Omega. \quad (3.9)$$

where $\alpha, \beta, \kappa, \nu > 0$ are parameters to be specified. In the above system, the diffusion function $g(\cdot)$ is chosen same as (2.1). In this method, the closeness between I and J can be measured by the variable v [see equation (3.7)], whereas the edge variable u is obtained from equation (3.6).

The advantages of the proposed model are: (i) parabolic nature of the equation (3.5) removes the noise efficiently, and the hyperbolic nature enhances the image edges better than parabolic PDE based models, (ii) hyperbolic nature of the equation (3.6) detects the image edges better than parabolic PDE, this extra equation calculates the edge variable u which inject the past information into the diffusion process in equation (3.5), (iii) fidelity variable v keeps the restored image close to the original image. Overall the present technique enables us to provide more versatility in the diffusion process along the curves of discontinuities. Furthermore, we study the existence and uniqueness of the weak solution of the proposed model using Banach's fixed point theorem on an appropriate function space. Further, to solve the present model, we utilize a robust numerical scheme, which is fast and easy to implement (Jain *et al.*, 2015a,b). The proposed model is then applied to several gray scale images. Numerical results illustrate that the proposed algorithm outperforms the TDE model (1.17), Cao model (1.18), SYS model (3.1)–(3.4), and ACPDE model (2.2)–(2.5) in terms of noise removal and preservation of image structures.

The rest of this chapter is organized as follows. In section 3.2, we study the well-posedness of the proposed model. A numerical realization of the proposed model is shown in section 3.3. In section 3.4 numerical experiments are carried out and compared with other existing models. Finally, the work is concluded in section 3.5.

3.2 Well-posedness of Weak Solutions

In this section we study the well-posedness of the proposed model (3.5)–(3.9) using Banach’s fixed-point theorem (Evans, 1998).

3.2.1 Technical framework & statement of the main result

For simplicity we choose all the constants involved in the equations (3.5)–(3.9) equals to 1. Throughout this section, C denotes a generic positive constant and for simplicity, we write $L^p, H^1, (H^1)'$ instead of $L^p(\Omega), H^1(\Omega), (H^1(\Omega))'$, respectively. We introduce the solution space $W(0, T) = (W_1(0, T))^2 \times W_2(0, T)$ for the model (3.5)–(3.9), where

$$\begin{aligned} W_1(0, T) &= \left\{ w : w \in L^\infty(0, T; H^1), \partial_t w \in L^\infty(0, T; L^2); \partial_{tt} w \in L^2(0, T; (H^1)') \right\}, \\ W_2(0, T) &= \left\{ w : w \in L^\infty(0, T; H^1); \partial_t w \in L^2(0, T; L^2) \right\}. \end{aligned}$$

Note that, $W_i(0, T)$ ($i = 1, 2$) is a Hilbert space for the graph norm (Lions, 1968).

Definition 3.1 (Weak solution). *A triplet (I, u, v) is called a weak solution of (3.5)–(3.9) if*

a) $I, u \in W_1(0, T), v \in W_2(0, T)$ and (3.9) holds.

b) For all $\phi \in H^1$ and a.e. $t \in (0, T)$, there hold

$$\begin{aligned} \langle \partial_{tt} I, \phi \rangle + \int_{\Omega} \partial_t I \phi \, dx + \int_{\Omega} g(u_\xi) \nabla I \cdot \nabla \phi \, dx &= 2 \int_{\Omega} v \phi \, dx, \\ \langle \partial_{tt} u, \phi \rangle + \int_{\Omega} \partial_t u \phi \, dx + \frac{1}{2} \int_{\Omega} \nabla u \cdot \nabla \phi \, dx + \int_{\Omega} u \phi \, dx &= 2 \int_{\Omega} h(|\nabla I_\xi|) \phi \, dx, \\ \int_{\Omega} \partial_t v \phi \, dx + \int_{\Omega} \nabla v \cdot \nabla \phi \, dx &= - \int_{\Omega} (J - I) \phi \, dx. \end{aligned}$$

As we mentioned, our aim is to establish well-posedness of weak solution of the proposed model (3.5)–(3.9), we will do so under the following assumptions:

A.1 The function $h : \mathbb{R} \rightarrow \mathbb{R}$ is a positive, bounded, Lipschitz function. More precisely, there exist $\delta, c_h > 0$ such that

$$\begin{cases} \delta \leq h(\cdot) \leq 1, \\ |h(x) - h(y)| \leq c_h|x - y|, \quad \forall x, y \in \mathbb{R}. \end{cases}$$

Moreover, h' is Lipschitz continuous with Lipschitz constant $c_{h'}$.

A.2 $J \in H^2$.

We observe from (2.1) that, $g : \mathbb{R} \rightarrow \mathbb{R}^+$ is a bounded, decreasing and Lipschitz continuous function with Lipschitz constant $\frac{C_\xi}{k^2}$. Moreover, $g(0) = 1$ and $\lim_{u \rightarrow +\infty} g(u_\xi) = 0$. We are now ready to state the main results of the proof.

Theorem 3.1. *Under the assumptions **A.1-A.2**, the proposed model (3.5)–(3.9) has a unique weak solution (I, u, v) in the sense of Definition 3.1.*

Following (Zheng, 1995), we first prove a local well-posedness result, and then establish a uniform a-priori estimate for the solution. Using uniform moment estimates and continuation method, we prove a global existence result.

3.2.2 Linearized model & its well-posedness

For any positive constants M_1 , M_2 , and M_3 , we define the following convex set $\mathcal{B}^\mathcal{T}$ with fixed $\mathcal{T} > 0$:

$$\mathcal{B}^\mathcal{T} = \begin{cases} (u, \partial_t u, \partial_{tt} u) \in \mathcal{B}_1^\mathcal{T} \equiv L^\infty(0, \mathcal{T}; H^1) \times L^\infty(0, \mathcal{T}; L^2) \times L^\infty(0, \mathcal{T}; L^2), \\ (v, \partial_t v) \in \mathcal{B}_2^\mathcal{T} \equiv L^\infty(0, \mathcal{T}; H^1) \times L^2(0, \mathcal{T}; L^2), \\ (I, \partial_t I, \partial_{tt} I) \in \mathcal{B}_3^\mathcal{T} \equiv L^\infty(0, \mathcal{T}; H^1) \times L^\infty(0, \mathcal{T}; L^2) \times L^\infty(0, \mathcal{T}; L^2), \\ \|u\|_{L^\infty(0, \mathcal{T}; L^2)} + \|\partial_t u\|_{L^\infty(0, \mathcal{T}; L^2)} + \|\partial_{tt} u\|_{L^\infty(0, \mathcal{T}; L^2)} \leq M_1, \\ \|v\|_{L^\infty(0, \mathcal{T}; L^2)} + \int_0^\mathcal{T} \|\partial_t v\|^2 dt \leq M_2, \\ \|I\|_{L^\infty(0, \mathcal{T}; L^2)} + \|\partial_t I\|_{L^\infty(0, \mathcal{T}; L^2)} + \|\partial_{tt} I\|_{L^\infty(0, \mathcal{T}; L^2)} \leq M_3. \end{cases}$$

For any fixed $(\bar{I}, \bar{u}, \bar{v}) \in \mathcal{B}^\mathcal{T}$, consider the following linearized model:

$$\partial_{tt} I + \partial_t I - \operatorname{div}(g(\bar{u}_\xi) \nabla I) = -2\bar{v}, \quad \text{in } \Omega_T \quad (3.10)$$

$$\partial_{tt} u + \partial_t u - \frac{1}{2} \Delta u + u = h(|\nabla \bar{I}_\xi|), \quad \text{in } \Omega_T, \quad (3.11)$$

$$\partial_t v - \Delta v = \bar{I} - J, \quad \text{in } \Omega_T, \quad (3.12)$$

with the initial and boundary conditions (3.9). Since $J \in H^1$, by using the properties of convolution (L_2 -estimate), one can easily check that the followings hold:

$$(i) \quad \gamma := \frac{1}{1 + \frac{C_\xi M_1}{k^2}} \leq \bar{g} \leq 1, \quad (ii) \quad |\partial_t \bar{g}| \leq \frac{C_\xi}{k^2} M_1, \text{ where } \bar{g} = g(\bar{u}_\xi). \quad (3.13)$$

Proof of (i): Let $\bar{u} \in \mathcal{B}^\mathcal{T}$. Since G_ξ is positive, by convolution property, we have

$$\begin{aligned} \|G_\xi * \bar{u}\|_{L^\infty} &\leq \|G_\xi\|_{L^2} \|\bar{u}\|_{L^2} \leq C_\xi M_1 \\ \text{Or, } 1 &\leq 1 + \frac{|G_\xi * \bar{u}|}{k^2} \leq 1 + \frac{C_\xi M_1}{k^2} \\ \text{Or, } \frac{1}{1 + \frac{C_\xi M_1}{k^2}} &\leq \frac{1}{1 + \frac{|G_\xi * \bar{u}|}{k^2}} \leq 1 \\ \Rightarrow \gamma &= \frac{1}{1 + \frac{C_\xi M_1}{k^2}} \leq \bar{g} \leq 1. \end{aligned}$$

Proof of (ii) : Observe that

$$\begin{aligned} \partial_t \bar{g} &= \frac{1}{\left(1 + \frac{|G_\xi * \bar{u}|}{k^2}\right)^2} \frac{1}{k^2} |G_\xi * \partial_t \bar{u}| \\ \text{Or, } \|\partial_t \bar{g}\|_{L^\infty} &\leq \frac{1}{k^2} \|G_\xi\|_{L^2} \|\partial_t \bar{u}\|_{L^2} \\ \Rightarrow |\partial_t \bar{g}| &\leq \frac{C_\xi M_1}{k^2}. \end{aligned}$$

Hence by classical Galerkin approximation, there exists a unique solution $(I, u, v) \in \mathcal{B}_3^\mathcal{T} \times \mathcal{B}_1^\mathcal{T} \times \mathcal{B}_2^\mathcal{T}$ of the linearized model (3.10)–(3.12) with the conditions (3.9). Moreover, (I, u, v) satisfies the following estimates.

Lemma 3.2. *The unique solution $(I, u, v) \in \mathcal{B}^\mathcal{T}$ of the linearized model (3.10)–(3.12) with the conditions (3.9) satisfies the following: there exists a constant $C > 0$, depending only on $\mathcal{T}, \xi, M_1, M_2, M_3, |\Omega|$ and $\|J\|$, such that*

- (i) $\|I\|_{L^\infty(0, \mathcal{T}; H^2)}^2 + \|\partial_t I\|_{L^\infty(0, \mathcal{T}; L^2)}^2 + \|I_{tt}\|_{L^\infty(0, \mathcal{T}; L^2)}^2 \leq C,$
- (ii) $\|u\|_{L^\infty(0, \mathcal{T}; H^1)}^2 + \|u_t\|_{L^\infty(0, \mathcal{T}; L^2)}^2 + \|u_{tt}\|_{L^\infty(0, \mathcal{T}; L^2)}^2 \leq C,$
- (iii) $\|v\|_{L^\infty(0, \mathcal{T}; H^1)}^2 + \|v_t\|_{L^2(0, \mathcal{T}; L^2)}^2 \leq C.$

Proof. Proof of i) : Multiplying (3.10) by $\partial_t I$ and integrating by parts over Ω and

using Cauchy-Schwarz and Young's inequalities, we obtain

$$\frac{1}{2} \frac{d}{dt} \|\partial_t I\|_{L^2}^2 + \|\partial_t I\|_{L^2}^2 + \int_{\Omega} \bar{g} \nabla I \cdot \nabla (\partial_t I) dx \leq \|\bar{v}\|_{L^2}^2 + \|\partial_t I\|_{L^2}^2. \quad (3.14)$$

Note that, thanks to (3.13)

$$\int_{\Omega} \bar{g} \nabla I \cdot \nabla (\partial_t I) dx \geq \frac{1}{2} \frac{d}{dt} \int_{\Omega} \bar{g} |\nabla I|^2 dx - \frac{C_{\xi M_1}}{2k^2} \|\nabla I\|_{L^2}^2. \quad (3.15)$$

Combining (3.14) and (3.15), along with (3.13), we have

$$\frac{d}{dt} \|\partial_t I\|_{L^2}^2 + \frac{d}{dt} \int_{\Omega} \bar{g} |\nabla I|^2 dx \leq C \left(\|\partial_t I\|_{L^2}^2 + \int_{\Omega} \bar{g} |\nabla I|^2 dx \right) + 2 \|\bar{v}\|_{L^2}^2. \quad (3.16)$$

Using Gronwall's inequality, we obtain, for a.e. $t \in (0, \mathcal{T})$,

$$\begin{aligned} \|\partial_t I\|_{L^2}^2 + \int_{\Omega} \bar{g} |\nabla I|^2 dx &\leq e^{Ct} (C_1 + t C_2(M_2)), \\ \|\nabla I\|_{L^2}^2 &\leq \frac{1}{\gamma} \int_{\Omega} \bar{g} |\nabla I|^2 dx \leq \frac{1}{\gamma} e^{Ct} (C_1 + t C_2(M_2)). \end{aligned}$$

Thus, one has, for a.e. $t \in (0, \mathcal{T})$

$$\|\partial_t I\|_{L^2}^2 + \|\nabla I\|_{L^2}^2 \leq \widetilde{M}_1 e^{Ct} (C_1 + t C_2(M_2)), \quad (3.17)$$

where $\widetilde{M}_1 = \max\{\gamma^{-1}, 1\}$. By using the identity $I(x, t) = J(x) + \int_0^t \partial_t I(x, s) ds$, Young's inequality and (3.17), we get $\|I(t)\|_{L^2}^2 \leq (2 \|J\|_{L^2}^2 + t C'_1) e^{Ct}$ which then implies for a.e. $t \in (0, \mathcal{T})$

$$\|\partial_t I\|_{L^2}^2 + \|I(t)\|_{H^1}^2 \leq e^{Ct} (C'_2 + t C'_3), \quad (3.18)$$

where, $C'_2 = \widetilde{M}_1 C_1 + 2 \|J\|_{L^2}^2$ and $C'_3 = \widetilde{M}_1 (C_2(M_2) + C'_1)$ with $C'_1 = \frac{2\widetilde{M}_1}{C} (C_1 + \mathcal{T} C_2(M_2))$. We now show that $I \in L^\infty(0, \mathcal{T}; H^2)$, which will play an essential role in the later analysis. To do so, we follow the arguments as in [(Lions and Magenes, 1972), **Theorem 2.1, A Regularity Theorem (I), Page-95, Chapter 5**]. Let us (formally) differentiate the equation (3.10) w.r.t. time, we have

$$\partial_{ttt} I + \partial_{tt} I - \nabla (\partial_t \bar{g} \nabla I + \bar{g} \nabla (\partial_t I)) = -2 \partial_t \bar{v}. \quad (3.19)$$

Multiply the above equation by $\partial_{tt}I$ and integrate over Ω , we obtain

$$\begin{aligned} \int_{\Omega} \partial_{tt}I \partial_{ttt}I dx + \int_{\Omega} (\partial_{tt}I)^2 dx + \int_{\Omega} \partial_t \bar{g} \nabla I \cdot \nabla (\partial_{tt}I) dx + \int_{\Omega} \bar{g} \nabla (\partial_t I) \cdot \nabla (\partial_{tt}I) dx \\ = -2 \int_{\Omega} \partial_t \bar{v} \partial_{tt}I dx. \end{aligned} \quad (3.20)$$

Now using the inequality

$$\int_{\Omega} \bar{g} \nabla (\partial_t I) \cdot \nabla (\partial_{tt}I) dx \geq \frac{1}{2} \frac{d}{dt} \int_{\Omega} \bar{g} |\nabla (\partial_t I)|^2 dx - \frac{C_{\xi M_1}}{2k^2} \int_{\Omega} |\nabla (\partial_t I)|^2 dx$$

Hence from (3.20), we obtain

$$\begin{aligned} & \frac{d}{dt} \left(\int_{\Omega} (\partial_{tt}I)^2 dx + \int_{\Omega} \bar{g} |\nabla (\partial_t I)|^2 dx \right) \\ & \leq \frac{C_{\xi M_1}}{k^2} \int_{\Omega} |\nabla (\partial_t I)|^2 dx - 2 \int_{\Omega} \bar{g}_t \nabla I \nabla (\partial_{tt}I) dx - 4 \int_{\Omega} \partial_t \bar{v} \partial_{tt}I dx. \end{aligned}$$

Now integrate w.r.t. time variable from 0 to t , we have

$$\begin{aligned} \|\partial_{tt}I\|_{L^2}^2 + \int_{\Omega} \bar{g} |\nabla (\partial_t I)|^2 dx & \leq 3 \frac{C_{\xi M_1}}{k^2} \int_0^t \int_{\Omega} |\nabla (\partial_t I)|^2 dx dt - 2 \int_{\Omega} \partial_t \bar{g} \nabla I \cdot \nabla (\partial_t I) dx \\ & \quad + 2 \int_0^t \int_{\Omega} \partial_{tt} \bar{g} \nabla I \cdot \nabla (\partial_t I) dx dt - 2 \int_0^t \int_{\Omega} \partial_t \bar{v} \partial_{tt}I dx dt \\ & \leq 3 \frac{C_{\xi M_1}}{\gamma k^2} \int_0^t \left(\int_{\Omega} \bar{g} |\nabla (\partial_t I)|^2 dx \right) ds + \frac{1}{\epsilon} \|\partial_t \bar{g}\|_{L^\infty} \|\nabla I\|_{L^2}^2 + \epsilon \|\partial_t \bar{g}\|_{L^\infty} \|\nabla (\partial_t I)\|_{L^2}^2 \\ & \quad + \|\partial_{tt} \bar{g}\|_{L^\infty} \int_0^t (\|\nabla I\|_{L^2}^2 + \|\nabla (\partial_t I)\|_{L^2}^2) ds + \int_0^t \|\partial_t \bar{v}\|_{L^2}^2 ds + \int_0^t \|\partial_{tt}I\|_{L^2}^2 ds \\ & \leq \frac{1}{\epsilon} \|\partial_t \bar{g}\|_{L^\infty} \|\nabla I\|_{L^2}^2 + \|\partial_{tt} \bar{g}\|_{L^\infty} \int_0^t \|\nabla I\|_{L^2}^2 ds + \int_0^t \|\partial_t \bar{v}\|_{L^2}^2 ds \\ & \quad + \left(3 \frac{C_{\xi M_1}}{\gamma k^2} + \frac{\|\partial_{tt} \bar{g}\|_{L^\infty}}{\gamma} \right) \int_0^t \left(\int_{\Omega} \bar{g} |\nabla (\partial_t I)|^2 dx \right) ds + \int_0^t \|\partial_{tt}I\|_{L^2}^2 ds \\ & \quad + \frac{\epsilon \|\partial_t \bar{g}\|_{L^\infty}}{\gamma} \int_{\Omega} \bar{g} |\nabla (\partial_t I)|^2 dx. \end{aligned}$$

Observe that $\|\partial_t \bar{g}\|_{L^\infty}, \|\partial_{tt} \bar{g}\|_{L^\infty} \leq C(\xi, M_1, \|J\|)$. Now by the proper choice of ϵ , we can rewrite the above inequality as

$$X(t) \leq Y(t) + C \int_0^t X(s) ds,$$

where

$$\begin{cases} X(t) = \|\partial_{tt}I\|_{L^2}^2 + \int_{\Omega} \bar{g} |\nabla(\partial_t I)|^2 dx, \\ Y(t) = \frac{1}{\epsilon} \|\partial_t \bar{g}\|_{L^\infty} \|\nabla I\|_{L^2}^2 + \|\partial_{tt} \bar{g}\|_{L^\infty} \int_0^t \|\nabla I\|_{L^2}^2 ds + \int_0^t \|\partial_t \bar{v}\|_{L^2}^2 ds. \end{cases}$$

An application of Gronwall's lemma together with (3.18) yields

$$\|\partial_{tt}I\|_{L^\infty(0,\mathcal{T};L^2)} + \|\nabla(\partial_t I)\|_{L^\infty(0,\mathcal{T};L^2)} \leq C. \quad (3.21)$$

Since $\nabla \bar{g} \in L^\infty(0, \mathcal{T}; L^\infty)$, from (3.10), it is easily to show that $I \in L^\infty(0, \mathcal{T}; H^2)$, and hence (i) holds true. Moreover, using the Galerkin method one can prove that $I \in L^\infty(0, \mathcal{T}; H^2)$ [Hint: see the [section 3.6](#)].

Proof of (ii) : We multiply (3.11) by $\partial_t u$, integrate by parts over Ω and use Cauchy-Schwarz and Young's inequalities. The result is

$$\begin{aligned} \frac{1}{2} \frac{d}{dt} \|\partial_t u\|_{L^2}^2 + \|\partial_t u\|_{L^2}^2 + \frac{1}{4} \frac{d}{dt} \|\nabla u\|_{L^2}^2 + \frac{1}{2} \frac{d}{dt} \|u\|_{L^2}^2 &\leq \frac{1}{2} \|\bar{h}\|_{L^2}^2 + \frac{1}{2} \|\partial_t u\|_{L^2}^2 \\ &\leq 2|\Omega| + \frac{1}{2} \|\partial_t u\|_{L^2}^2. \end{aligned}$$

Integrating between the time interval form 0 to t , we obtain, for a.e. $t \in (0, \mathcal{T})$

$$\|u(t)\|_{H^1}^2 + \|\partial_t u\|_{L^2}^2 \leq C_3 + 2t|\Omega|.$$

Note that $\partial_t \bar{h} \in L^\infty(0, \mathcal{T}; L^2)$, and hence by regularity theory ([Evans, 1998](#)), one can easily prove that $\partial_{tt} u \in L^\infty(0, \mathcal{T}; L^2)$, with the estimate

$$\|\partial_{tt} u\|_{L^\infty(0,\mathcal{T};L^2)} \leq C(\|J\|, M_1, M_2, \xi).$$

This shows that (ii) holds as well.

Proof of (iii) : Multiplying (3.12) by $\partial_t v$, integrating by parts over Ω , using Cauchy-Schwarz and Young's inequalities, and then integrating between the time interval form 0 to t of the resulting inequality, we obtain, for a.e. $t \in (0, \mathcal{T})$

$$\|\nabla v\|_{L^2}^2 + \int_0^t \|\partial_t v\|_{L^2}^2 ds \leq C_4 + t M_3.$$

Again, multiplying (3.12) by v and integrating over Ω and using Cauchy-Schwarz and Young's inequalities along with Gronwall's lemma, we get $\|v(t)\|_{L^2}^2 \leq e^t (\widetilde{C}_4 +$

tM_3), and hence

$$\|v(t)\|_{H^1}^2 + \int_0^t \|\partial_t v\|_{L^2}^2 ds \leq e^t (C_5 + tM_3), \quad \text{a.e. } t \in (0, \mathcal{T}). \quad (3.22)$$

This finishes the proof. \square

3.2.3 Well-posedness of a local solution

We show that the model (3.5)–(3.9) admits a unique solution on a small time interval. Indeed, we have the following lemma.

Lemma 3.3. *There exists a positive time $\mathcal{T} \in (0, T]$, depending only on the data J, h and G_ξ , such that the model (3.5)–(3.9) admits a unique solution (I, u, v) in $\Omega_{\mathcal{T}}$. Moreover, we have*

$$\begin{cases} I \in L^\infty(0, \mathcal{T}; H^2), \partial_t I \in L^\infty(0, \mathcal{T}; L^2), \\ u \in L^\infty(0, \mathcal{T}; H^1), \partial_t u \in L^\infty(0, \mathcal{T}; L^2), \partial_{tt} u \in L^\infty(0, \mathcal{T}; L^2), \\ v \in L^\infty(0, \mathcal{T}; H^1), \partial_t v \in L^2(0, \mathcal{T}; L^2). \end{cases}$$

Proof. In view of Lemma 3.2, we see that for small t and hence for small \mathcal{T} , the solution $(I, u, v) \in \mathcal{B}^\mathcal{T}$, and hence the mapping $(\bar{I}, \bar{u}, \bar{v}) \mapsto (I, u, v)$ maps $\mathcal{B}^\mathcal{T}$ into itself. Well-posedness of the solution of (3.5)–(3.9) on the time interval $[0, \mathcal{T}]$ would then follows from the Banach fixed point theorem once we establish that the mapping $(\bar{I}, \bar{u}, \bar{v}) \mapsto (I, u, v)$ is a contraction.

For fixed $(\bar{I}, \bar{u}, \bar{v})$, $(\bar{\bar{I}}, \bar{\bar{u}}, \bar{\bar{v}}) \in \mathcal{B}^\mathcal{T}$, let (I, u, v) and $(\tilde{I}, \tilde{u}, \tilde{v})$ be the corresponding solutions of the linearized model (3.10)–(3.12). Let us denote $(\zeta, \theta, \eta) = (I - \bar{I}, u - \bar{u}, v - \bar{v})$ and $(\bar{\zeta}, \bar{\theta}, \bar{\eta}) = (\bar{I} - \bar{\bar{I}}, \bar{u} - \bar{\bar{u}}, \bar{v} - \bar{\bar{v}})$. Consider the equation for θ , i.e.

$$\partial_{tt}\theta + \partial_t\theta - \frac{1}{2}\Delta\theta + \theta = (\bar{h} - \bar{\bar{h}}), \quad (3.23)$$

where $\bar{h} = h(|\nabla \bar{I}_\xi|)$ and $\bar{\bar{h}} = h(|\nabla \bar{\bar{I}}_\xi|)$. Like an analogous way to the estimates established in Lemma 3.2, we multiply (3.23) by $\partial_t\theta$, integrate by parts over Ω , and then use Young's inequality to obtain

$$\|\partial_t\theta\|_{L^2}^2 + \frac{d}{dt} \left(\|\partial_t\theta\|_{L^2}^2 + \frac{1}{2} \|\nabla\theta\|_{L^2}^2 + \|\theta\|_{L^2}^2 \right) \leq \|\bar{h} - \bar{\bar{h}}\|_{L^2}^2.$$

Thanks to Lipschitz continuity of h and Young's inequality for convolution, we see

that $\|\bar{h} - \bar{\bar{h}}\|_{L^2}^2 \leq C(c_h, \xi) \|\bar{\zeta}\|_{L^2}^2$, and hence

$$\|\partial_t \theta\|_{L^2}^2 + \|\theta\|_{H^1}^2 \leq C t \sup_{0 \leq t \leq T} \|\bar{\zeta}\|_{L^2}^2.$$

We would like to estimate $\|\partial_{tt}\theta\|_{L^2}$. We use standard methodology (Evans, 1998), i.e., differentiate (3.23) w.r.t. time, multiply the resulting equation by $\partial_{tt}\theta$, integrate over Ω , and then use Young's inequality. The result is

$$\frac{d}{dt} (\|\partial_{tt}\theta\|_{L^2}^2 + \|\partial_t \theta\|_{H^1}^2) \leq \|\partial_t \bar{h} - \partial_t \bar{\bar{h}}\|_{L^2}^2.$$

In view of Lipschitz continuity of h' , one has $\|\partial_t \bar{h} - \partial_t \bar{\bar{h}}\|_{L^2}^2 \leq C(\|\bar{\zeta}\|_{L^2}^2 + \|\partial_t \bar{\zeta}\|_{L^2}^2)$, and hence

$$\|\partial_{tt}\theta\|_{L^2}^2 \leq C t \sup_{0 \leq t \leq T} (\|\bar{\zeta}\|_{L^2}^2 + \|\partial_t \bar{\zeta}\|_{L^2}^2).$$

Thus, we have

$$\|\partial_t \theta\|_{L^2}^2 + \|\theta\|_{H^1}^2 + \|\partial_{tt}\theta\|_{L^2}^2 \leq C t \sup_{0 \leq t \leq T} (\|\bar{\zeta}\|_{L^2}^2 + \|\partial_t \bar{\zeta}\|_{L^2}^2). \quad (3.24)$$

To derive estimate for the solution η , a weak solution of the PDE

$$\partial_t \eta - \Delta \eta = (\bar{I} - \bar{\bar{I}}),$$

we proceed similarly as in the derivation of (3.22), and obtain

$$\|\eta(t)\|_{H^1}^2 + \int_0^t \|\partial_t \eta\|_{L^2}^2 ds \leq t e^t \sup_{0 \leq t \leq T} \|\bar{\zeta}\|_{L^2}^2. \quad (3.25)$$

Now focus on the equation for ζ , i.e.

$$\partial_{tt}\zeta + \partial_t \zeta - \nabla(\bar{g} \nabla \zeta) = \nabla((\bar{g} - \bar{\bar{g}}) \nabla \tilde{I}) - 2\bar{\eta}, \quad (3.26)$$

where, $\bar{g} = g(\bar{u})$ and $\bar{\bar{g}} = g(\bar{\bar{u}})$. We multiply (3.26) by ζ_t and integrate over Ω to have

$$\begin{aligned} \frac{d}{dt} (\|\partial_t \zeta\|_{L^2}^2 + \int_\Omega \bar{g} |\nabla \zeta|^2 dx) &\leq 2\|\partial_t \zeta\|_{L^2}^2 + C \|\nabla \zeta\|_{L^2}^2 \\ &\quad + \tilde{C}_1 \|\bar{g} - \bar{\bar{g}}\|_{L^\infty}^2 + \tilde{C}_2 \|\nabla(\bar{g} - \bar{\bar{g}})\|_{L^\infty}^2 + \|\bar{\eta}\|_{L^2}^2, \end{aligned} \quad (3.27)$$

where $\tilde{C}_1 = \|\Delta \tilde{I}\|_{L^\infty(0,T;L^2)}^2$ and $\tilde{C}_2 = \|\nabla \tilde{I}\|_{L^\infty(0,T;L^2)}^2$. By Lipschitz continuity of g ,

L^p -estimate for convolution and (3.13) along with Hölder's inequality, we see that

$$\|\bar{g} - \tilde{g}\|_{L^\infty} \leq C\|\bar{u} - \tilde{u}\|_{L^2}; \quad \|\nabla(\bar{g} - \tilde{g})\|_{L^\infty}^2 \leq \tilde{C}_3\|\bar{\theta}\|_{L^2}^2,$$

where $\tilde{C}_3 = \left(\frac{2}{k^2} \|\nabla G_\xi\|_{L^2}^2 + \frac{2}{k^2} \|(\bar{g} + \tilde{g})\|_{L^\infty}^2 \|\nabla G_\xi * \bar{u}\|_{L^\infty}^2 \right)$. Hence from (3.27), we have

$$\|\partial_t \zeta\|_{L^2}^2 + \|\nabla \zeta\|_{L^2}^2 \leq C t e^{Ct} \sup_{0 \leq t \leq \mathcal{T}} (\|\bar{\theta}\|_{H^1}^2 + \|\bar{\eta}\|_{H^1}^2).$$

Moreover, one can easily show that

$$\|\partial_t \zeta\|_{L^2}^2 + \|\zeta\|_{H^1}^2 \leq C t e^{Ct} \sup_{0 \leq t \leq \mathcal{T}} (\|\bar{\theta}\|_{H^1}^2 + \|\bar{\eta}\|_{H^1}^2). \quad (3.28)$$

Combining (3.24), (3.25) and (3.28), we have

$$\begin{aligned} & \|\partial_t \zeta\|_{L^2}^2 + \|\zeta\|_{H^1}^2 + \|\partial_t \theta\|_{L^2}^2 + \|\theta\|_{H^1}^2 + \|\partial_{tt} \theta\|_{L^2}^2 + \|\eta\|_{H^1}^2 + \int_0^t \|\partial_t \eta\|_{L^2}^2 ds \\ & \leq C t e^{Ct} \sup_{0 \leq t \leq \mathcal{T}} \left\{ \|\partial_t \bar{\zeta}\|_{L^2}^2 + \|\bar{\zeta}\|_{H^1}^2 + \|\bar{\theta}\|_{H^1}^2 + \|\partial_t \bar{\theta}\|_{L^2}^2 \right. \\ & \quad \left. + \|\partial_{tt} \bar{\theta}\|_{L^2}^2 + \|\bar{\eta}\|_{H^1}^2 + \int_0^t \|\partial_t \bar{\eta}\|_{L^2}^2 ds \right\}. \end{aligned} \quad (3.29)$$

Hence the contraction property of the mapping $(\bar{I}, \bar{u}, \bar{v}) \mapsto (I, u, v)$, for t small enough, follows immediately from (3.29). This shows that, there exists a unique solution (I, u, v) of the proposed model (3.5)–(3.9) over a time interval $(0, \mathcal{T})$ for small $\mathcal{T} > 0$. This completes the proof. \square

Lemma 3.4 (Uniform a priori estimate). *There exists a positive constant $C_T = C(J, G_\xi, T, h)$ such that the solution (I, u, v) of the proposed model (3.5)–(3.9) verifies the following estimate:*

$$\begin{aligned} & \sup_{\tau \in (0, T]} \left\{ \|\partial_t I(\tau)\|_{L^2}^2 + \|I(\tau)\|_{H^1}^2 + \|\partial_t u(\tau)\|_{L^2}^2 + \|u(\tau)\|_{H^1}^2 \right. \\ & \quad \left. + \|\partial_{tt} u(\tau)\|_{L^2}^2 + \|v(\tau)\|_{H^1}^2 + \int_0^\tau \|\partial_t v(s)\|_{L^2}^2 ds \right\} \leq C_T. \end{aligned} \quad (3.30)$$

Proof. First consider the equation (3.5). Arguing similarly as in the derivation of (3.16), we get

$$\frac{d}{dt} \left(\|\partial_t I\|_{L^2}^2 + \int_\Omega g |\nabla I|^2 dx \right) \leq C \left(\|\partial_t I\|_{L^2}^2 + \int_\Omega g |\nabla I|^2 dx \right) + 2\|v\|_{L^2}^2.$$

Since $\frac{d}{dt}\|I\|_{L^2}^2 = \int_{\Omega} 2I\partial_t I dx \leq \|I\|_{L^2}^2 + \|\partial_t I\|_{L^2}^2$, we obtain

$$\begin{aligned} \frac{d}{dt} \left(\|\partial_t I\|_{L^2}^2 + \int_{\Omega} g|\nabla I|^2 dx + \|I\|_{L^2}^2 \right) &\leq C \left(\|\partial_t I\|_{L^2}^2 + \int_{\Omega} g|\nabla I|^2 dx \right) \\ &\quad + 2\|v\|_{L^2}^2 + \|I\|_{L^2}^2. \end{aligned} \quad (3.31)$$

Multiplying (3.6) by $\partial_t u$, and applying Cauchy-Schwarz and Young's inequalities, we have

$$\frac{d}{dt} (2\|\partial_t u\|_{L^2}^2 + \|\nabla u\|_{L^2}^2 + 2\|u\|_{L^2}^2) \leq 2|\Omega|. \quad (3.32)$$

Moreover, upon differentiating (3.6) w.r.t. time and then tested with u_{tt} , one has

$$\frac{d}{dt} (\|\partial_{tt} u\|_{L^2}^2 + \|\partial_t u\|_{H^1}^2) \leq \|\partial_t h\|_{L^2}^2 \leq C|\Omega|. \quad (3.33)$$

Next we multiply (3.7) by $\partial_t v$ and v respectively and then use integration by parts over Ω along with Cauchy-Schwarz and Young's inequalities to arrive at

$$\begin{aligned} \|\partial_t v\|_{L^2}^2 + \frac{d}{dt} \|\nabla v\|_{L^2}^2 &\leq 2 \left(\|J\|_{L^2}^2 + \|I\|_{L^2}^2 \right), \\ \frac{d}{dt} \|v\|_{L^2}^2 &\leq \|v\|_{L^2}^2 + \|J\|_{L^2}^2 + \|I\|_{L^2}^2. \end{aligned} \quad (3.34)$$

Combining (3.31), (3.32), (3.33), and (3.34), we have

$$\frac{d}{dt} p(t) \leq -\|\partial_t v\|_{L^2}^2 + (1+C)|\Omega| + 3\|J\|_{L^2}^2 + Cp(t), \quad (3.35)$$

where

$$p(t) = \|\partial_t I\|_{L^2}^2 + \int_{\Omega} g|\nabla I|^2 dx + \|I\|_{L^2}^2 + \|u\|_{H^1}^2 + 2\|\partial_t u\|_{L^2}^2 + \|\partial_{tt} u\|_{L^2}^2 + \|v\|_{H^1}^2.$$

From (3.35), we get

$$\frac{d}{dt} \{e^{-Ct} p(t)\} + e^{-Ct} \|\partial_t v\|_{L^2}^2 \leq C(|\Omega| + \|J\|_{L^2}^2).$$

Integration for $t \in (0, \tau)$, for any $\tau \in (0, T]$, yields the following inequality at time

τ :

$$\begin{aligned} \|\partial_t I\|_{L^2}^2 + \int_{\Omega} g |\nabla I|^2 dx + \|I\|_{L^2}^2 + \|u\|_{H^1}^2 + 2\|\partial_t u\|_{L^2}^2 + \|\partial_{tt} u\|_{L^2}^2 + \|v\|_{H^1}^2 \\ + \int_0^\tau \|\partial_t v\|_{L^2}^2 ds \leq e^{C\tau} \left\{ p(0) + C \int_0^\tau (|\Omega| + \|J\|_{L^2}^2) ds \right\}. \end{aligned}$$

Since g has a positive lower bound depending only on the u_0, T, ξ, Ω , from the above inequality we see that there exists a constant C_T , depending only on J, G_ξ, T , and h such that (3.30) holds true. This completes the proof. \square

3.2.4 Proof of Theorem 3.1

Thanks to Lemma 3.3 and Lemma 3.4, there exists a unique local solution (I, u, v) of the proposed model (3.5)–(3.9) over a time interval $(0, \mathcal{T})$ for small $\mathcal{T} > 0$, and satisfies the uniform moment estimate (3.30). More precisely, we extend the solution on a sequence of intervals $(0, t_n]$ such that $t_n \rightarrow \mathcal{T}$. Then considering the initial problem starting from \mathcal{T} , one can extend the solution up to a given final time T , thanks to (3.30). This completes the proof.

3.3 Numerical Implementation

To solve the system (3.5)–(3.9), we construct an explicit finite difference scheme. Using the finite difference formulas discussed in section 1.3, the discretized form of the equation (3.5) can be written as

$$(1 + \alpha\tau)I_{i,j}^{n+1} = (2 + \alpha\tau)I_{i,j}^n - I_{i,j}^{n-1} + \tau^2 \left\{ \nabla_x (g_{i,j}^n \nabla_x I_{i,j}^n) + \nabla_y (g_{i,j}^n \nabla_y I_{i,j}^n) \right\} - 2\tau^2 \lambda^n v_{i,j}^n, \quad n = 1, 2, 3, \dots \quad (3.36)$$

where

$$g_{i,j}^n = \frac{1}{1 + \frac{|G_\xi * u_{i,j}^n|}{k^2}},$$

with the initial condition $I_{i,j}^0 = J(x_i, y_j)$, $I_{i,j}^1 = I_{i,j}^0$, $0 \leq i \leq M-1$, $0 \leq j \leq N-1$,

λ^n is calculated using the formula as mentioned in [(2.9c) (Rudin *et al.*, 1992)].

Moreover, $u_{i,j}^n$ and $v_{i,j}^n$ are calculated from the discretized equations of (3.6) and

(3.7) respectively, and can be written as;

$$(1 + \beta\tau)u_{i,j}^{n+1} = (2 + \beta\tau)u_{i,j}^n - u_{i,j}^{n-1} + \kappa\tau^2 \left[h_{i,j}^n - u_{i,j}^n + \frac{\nu^2}{2}\Delta u_{i,j}^n \right], \quad n = 1, 2, 3, \dots \quad (3.37)$$

and

$$v_{i,j}^{n+1} = v_{i,j}^n + \tau\Delta v_{i,j}^n - \tau(I_{i,j}^0 - I_{i,j}^n), \quad n = 0, 1, 2, \dots \quad (3.38)$$

with the initial conditions $u_{i,j}^0 = G_\xi * |\nabla I_{i,j}^0|^2$, $u_{i,j}^1 = u_{i,j}^0$, $v_{i,j}^0 = 0$, and $h_{i,j}^n = h_\xi(|\nabla(G_\xi * I_{i,j}^n)|)$. We choose the function h as $h(\theta) = 0.1 + \min\{\theta^2, K\}$ for numerical experiments, where K is square of the maximum gray level value of the image I . We discretize the boundary conditions as discussed in [section 1.3](#).

3.4 Computational Results & Discussion

To assess the denoising performance, we present our computed results using the TCPDE model (3.5)–(3.9) and compare them with the results of the TDE model (1.17), Cao model (1.18), SYS model (3.1)–(3.4), and ACPDE model (2.2)–(2.5). We test all the filtering models on standard gray level test images (see [Figure 3.1](#)), which are contaminated by additive Gaussian noise with mean $\mu = 0$ and different levels of standard deviation $\sigma = \{20, 40, 60, 80, 100\}$ [Chapter 2, [section 2.4](#)]. For each experiment, we compute the values of the PSNR and MSSIM for the quantitative comparison with the other existing models. All the numerical tests are performed under Windows 7 and MATLAB version *R2019a* running on a desktop computer with an Intel Core i5 dual-core CPU at 2.53 GHz with 4 GB of RAM.

3.4.1 Selection of parameters

As discussed in [section 3.3](#), we use an explicit numerical scheme to solve the TDE model, the Cao model, the SYS model, and the proposed model. For the ACPDE model, we use an implicit numerical scheme as discussed in [Chapter 2](#). However, according to the CFL stability criterion, the numerical stability requirement for the explicit scheme is $\tau \leq \tilde{h}/2 \max g(x, t)$ (for parabolic PDE) and $\tau \leq \tilde{h}/\sqrt{\max g(x, t)}$ (for hyperbolic PDE) ([Chan and Shen, 1987](#); [Li, 2009](#); [Araújo et al., 2012](#); [Jovanović and Süli, 2013](#); [Zhang et al., 2014](#)), where \tilde{h} denotes the length of the spatial intervals. For all the methods, we choose time step size (τ) is 0.2 and spatial step size (\tilde{h}) is 1. Although, few existing studies have used the condition $\tau \geq 0.2$ for their

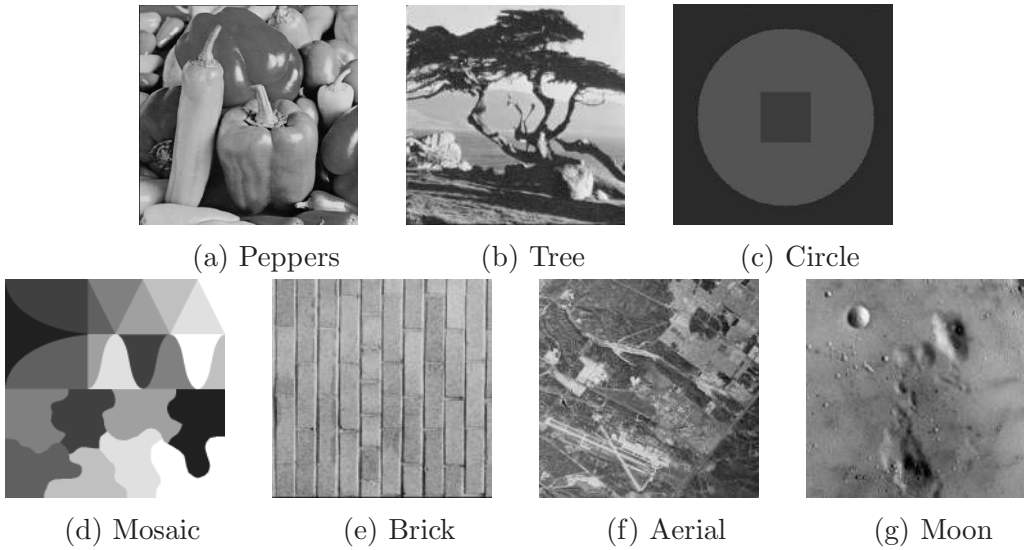


Figure 3.1: Set of test images: (a)–(b) natural images (c) synthetic image (d)–(e) texture images (f) aerial image (g) satellite image.

computations ([Cao et al., 2010](#); [Zeng et al., 2011](#); [Sun et al., 2016](#)). The parameter values for the existing models are chosen as the authors have discussed in their respective papers. Also, for fair and effective comparison, different parameters of the considered models are optimized manually to obtain their best performance level. For the ACPDE model we choose the fixed values $\kappa = 1$, $\nu = 0.01$, and $\xi = 1$. The parameters; α , β , and k ; influence the performance of the proposed model. The optimal values of these parameters are chosen from a large number of numerical experiments, where the other parameters, i.e., κ , ν , and ξ are fixed as 1.0, 0.01 and 1.0, respectively for all experiments. Moreover, we choose $1 \leq k \leq 12$ in the numerical experiments as the value of k depends on the noise levels. Higher the noise level is, larger the k is. [Figure 3.2](#) illustrates the effect of the parameter α on the quality of restored images, when other parameter values (i.e., β and k) are optimal. Here, one can observe that: (i) The smaller value of α gives better results (best PSNR value in fewer iterations) when the noise level is relatively low (shown in Figures [3.2a](#) and [3.2c](#)), and (ii) In case of relatively highly noised images, higher PSNR can be achieved with a relatively large value of parameter α (shown in Figures [3.2b](#) and [3.2d](#)), but it takes a large number of iterations to produce the optimum PSNR value. Hence for the numerical simulations, we select a suitable choice of α for different noise levels as well as for the different images. Moreover, to get the best possible outputs, in most cases, we choose $\beta = 1$ and for a few cases, we choose a relatively larger value of β . The detailed set of parameter values for the numerical experiments are given in [Table 3.1](#).

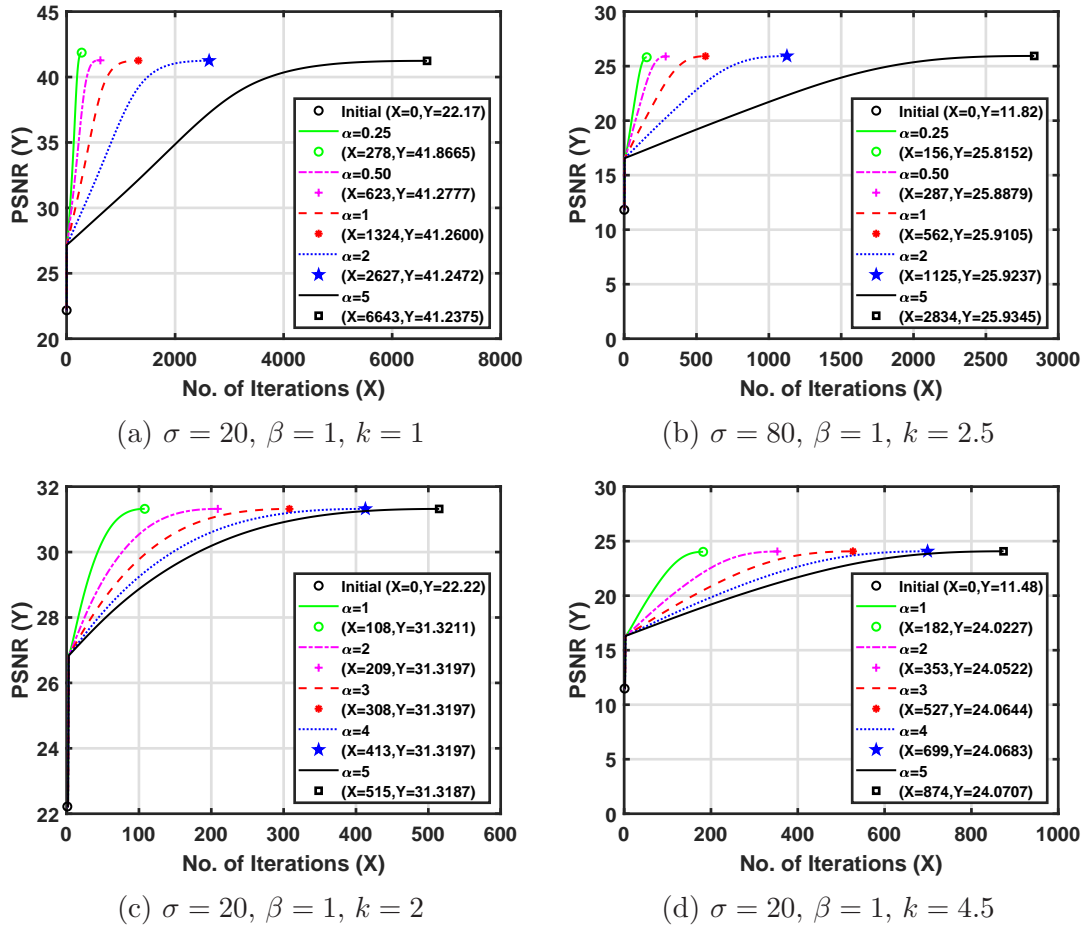


Figure 3.2: Influence of the parameter α . (a)–(b) Results for circle image. (c)–(d) Results for peppers image.

Table 3.1: Parameter values for the numerical experiments.

Image	σ	TDE		Cao		SYS		ACPDE		Proposed		
		λ	K	λ	K	λ	K	k	α	β	k	
Peppers	20	20	5	20	6	25	2	2	1	1	2	
	40	20	6	20	6	25	2	3	1.5	1	3	
	60	20	6	20	6	25	2	8	1.5	1	4	
	80	20	7	20	7	25	4	10	4	1	4.5	
	100	20	7	20	7	25	5	12	4	1	5	
Tree	20	20	8	20	2	25	2	3	0.5	1	1.5	
	40	20	8	20	2	25	2	4	1	1	1.8	
	60	20	8	20	2	25	2	4	1	1	2	
	80	20	9	20	3	25	2	4	1	1	2	
	100	20	9	20	3	25	2.5	4	1.5	1	2.5	
Circle	20	10	4	10	3	25	2	2	0.25	1	1	
	40	10	4	10	4	24	2	4	0.25	1	2	
	60	10	5	10	5	20	3	4	0.5	1	2.5	
	80	10	5	10	5	20	6	6	0.5	1	2.5	
	100	10	6	10	6	15	7	10	1	1	4	
Mosaic	20	20	6	20	6	25	2	4	0.5	1	1	
	40	20	7	20	6	25	2	5	0.5	1	1.5	
	60	20	8	20	6	24	3	5	0.5	1	1.5	
	80	20	9	20	7	24	3	5	0.5	1	2.5	
	100	20	9	20	8	24	4	6	1.0	1	4	
Brick	20	20	5	20	6	2	5	4	0.5	25	1	
	40	20	6	20	7	0.8	5	5	0.5	25	2	
	60	20	6	20	8	0.8	5	5	3	20	3	
	80	20	7	20	9	0.8	5	6	3	20	3	
	100	20	8	20	9	0.8	5	6	3	20	4	
Arial	20	5	10	20	5	25	2	2	1	1	2	
	40	5	15	20	6	25	3	4	5	2	7	
	60	5	15	20	7	24	4	5	5	2	8	
	80	5	17	20	7	24	5	6	5	2	10	
	100	5	17	20	8	22	6	7	8	2	12	
Moon	20	20	5	20	5	25	2	2	1	25	2.5	
	40	20	6	20	6	24	2	3	1	20	3	
	60	20	6	20	7	24	4	5	1	20	3	
	80	20	7	20	7	22	5	5	2	15	4	
	100	20	8	20	8	20	5	6	2	15	5	

3.4.2 Results and Discussion

We now demonstrate performance on several gray level images degraded by additive Gaussian noise. In [Figure 3.3](#), we have presented the restored results using three different slices of the peppers image. These figures show the one-dimensional signal of the original, noisy, and restored images. By observing Figures [3.3b](#), [3.3c](#), and [3.3d](#), one can conclude that the restored signals obtained by the proposed model are more closure to the respective original signals in comparison with the other discussed models.

In [Figure 3.4](#), the filtering performances of the discussed methods are tested on a tree image. Figure [3.4a](#) shows the noisy image, which is degraded by additive Gaussian noise of level $\sigma = 20$. Figures [3.4b](#)–[3.4f](#) illustrate the restored images. From the quality of the images, it can be observed that the proposed model works better in terms of noise suppression and edge preservation.

For better visual comparisons, in Figures [3.5](#)–[3.7](#), we illustrate the qualitative results of a circle image which is corrupted by additive Gaussian noise of level $\sigma = 20$. Figure [3.5](#) shows the 2D contour plot and 3D surface plot of the ground truth image [3.1c](#). Whereas, Figure [3.6](#) demonstrates the restored images and corresponding ratio images obtained using discussed approaches. It can be observed that the images restored by ACPDE model ([Figure 3.6e](#) and [Figure 3.6k](#)) and SYS model ([Figure 3.6d](#) and [Figure 3.6j](#)) have better visual quality than those of TDE model ([Figure 3.6b](#) and [Figure 3.6h](#)) and Cao model ([Figure 3.6c](#) and [Figure 3.6i](#)). Whereas, the proposed algorithm produces the best result with sufficient luminance enhancement in both dark and bright regions and demonstrates that it has less background information in ratio image, since it has flexibility and adaptiveness of the ACPDE model and SYS model. Another qualitative comparison on the circle image, among the discussed models, is shown using 2D contour plot and 3D surface plot in [Figure 3.7](#). Visual perception of these results indicates the effectiveness of the present algorithm. The results of the TDE model, the Cao model, the SYS model, and the ACPDE model left serious noise in the homogeneous regions and show a lot of false edges as can be seen in Figures [3.7b](#)–[3.7e](#) for 2D contours and Figures [3.7h](#)–[3.7k](#) for 3D surface plots. The results of the proposed approach are shown in Figures [3.7f](#) and [3.7l](#) which confirm that proposed model gives best edge map as well as surface plot among all the considered models.

To confirm further the effectiveness of our proposed model on the textured region, we consider the mosaic image that is contaminated by high-level additive Gaussian noise with $\sigma = 100$ as shown in [Figure 3.8](#). From the quality of the restored images and corresponding 2D contour plots, it can be concluded that the

filtered image obtained by the proposed filter is more closer to the noise-free image than the results of the other discussed models.

Further study on the brick image, contaminated by additive Gaussian noise of level $\sigma = 40$, is shown in [Figure 3.9](#). This image contains a lot of fine texture along with homogeneous regions. From the quality of restored images, it is easy to perceive that the restored output obtained from the TDE model, the Cao model, the SYS model, and the ACPDE model are not favorable as the edge information of the brick image is degraded and also stretch texture contents of the image. Whereas, the result obtained by the present method is more apparent than the results of the other discussed models in terms of denoising as well as edge-preserving. Also, to analyze the image quality, we have shown the ratio images of the corresponding restored images. From Figures [3.9g–3.9k](#), one can observe that the ratio image corresponding to the present model has very less background information which confirms that the present model works better in terms of edge preservation than the other models.

Moreover, in [Figure 3.10](#), we have presented the resultant images using three different slices of the brick image. These figures show the slice of the original, noisy, and restored images. By attentively observing Figures [3.10b](#), [3.10c](#), and [3.10d](#), one can find that the restored signals obtained by the proposed model are more closure to the respective original signals in comparison with the other discussed models.

To show the better structure preservation ability of the proposed model, in [Figure 3.11](#) we display the restored images of a satellite image which is initially degraded by additive Gaussian noise of level $\sigma = 60$. By observing the images in Figures [3.11b–3.11f](#), one can observe that the present model preserves the image structure better than the other discussed models.

Finally, in [Figure 3.12](#), we present the convergence of different models in terms of iteration numbers required for obtaining the best PSNR values. The results indicate that the present algorithm achieves the higher PSNR values in relatively fewer iterations.

Besides the qualitative results, the quantitative results in terms of PSNR and MSSIM values, number of iterations (NOI), and CPU time (in seconds) are also displayed in [Table 3.2](#) and [Table 3.3](#). The best PSNR and MSSIM values are obtained by using the proposed model. The highest values of PSNR and MSSIM for each noise level (mentioned in bold fonts) clearly show that the proposed model is better than the others. Although due to the highly coupled system, the proposed model takes relatively more time in some cases to achieve the best denoising results, the overall performance is better than the other considered techniques. Therefore,

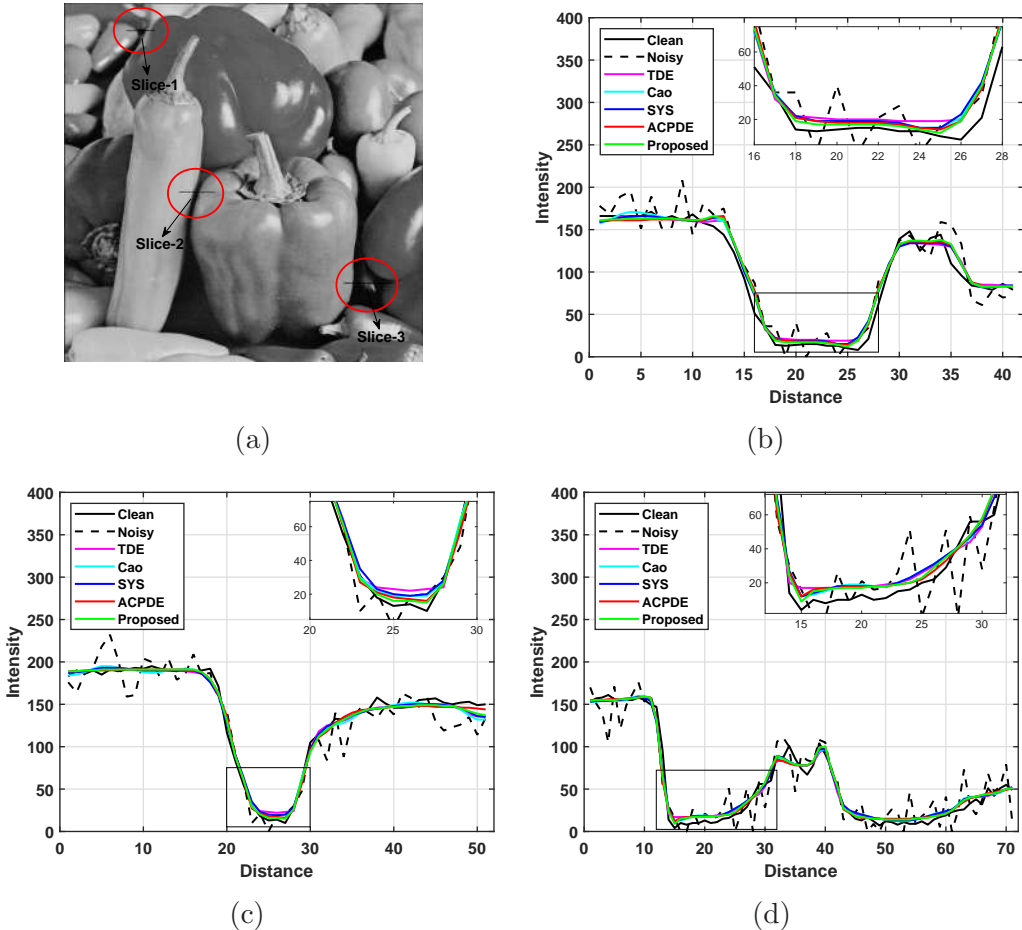


Figure 3.3: A 512×512 peppers image corrupted by Gaussian noise with $\sigma = 20$ and restored by different models. (a) Indicate the one-dimensional slices. (b) Results for the Slice-1. (c) Results for the Slice-2. (d) Results for the Slice-3.

referring to both visual and numerical comparisons, it is clear that under different noise variances proposed filter with optimized parameter values works better than the previously proposed and discussed algorithms.

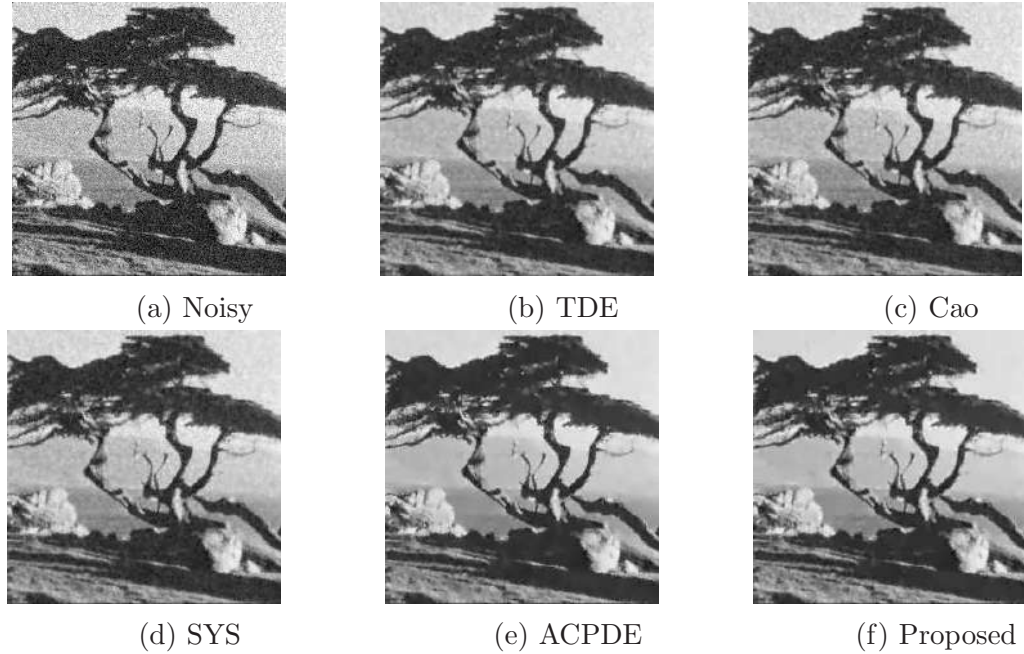


Figure 3.4: A 256×255 tree image corrupted by Gaussian noise with $\sigma = 20$ and restored by different models.

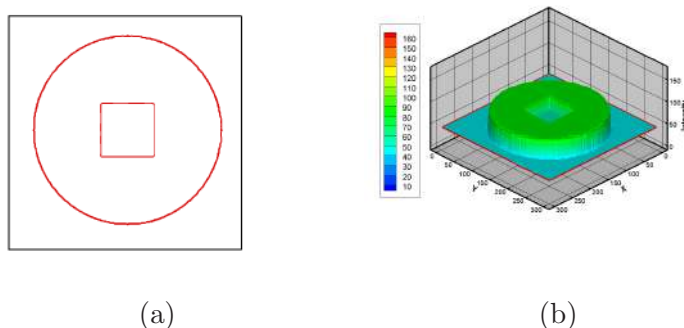


Figure 3.5: (a) 2D contour map of the clean circle image 3.1c. (b) 3D surface plot of the clean circle image 3.1c.

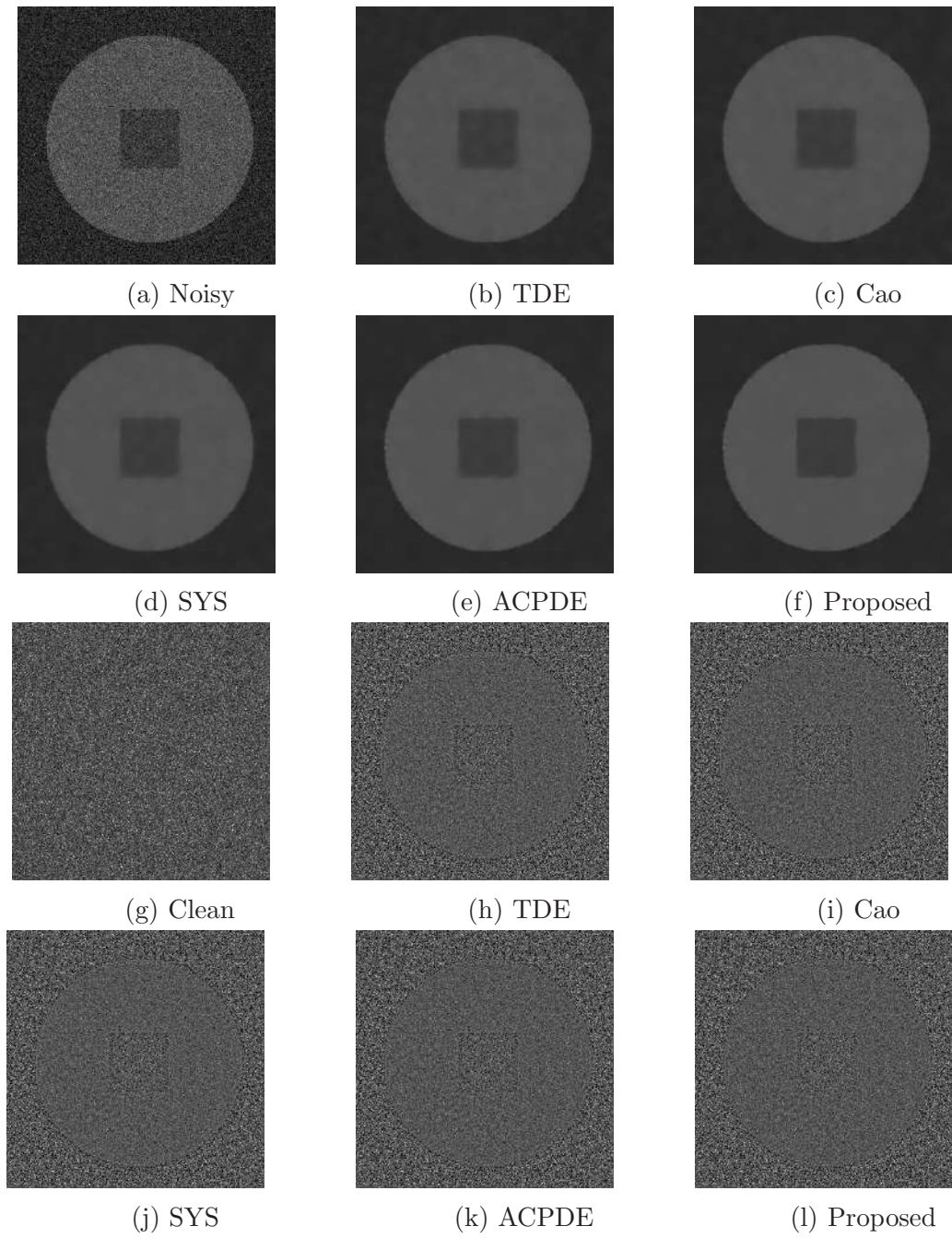
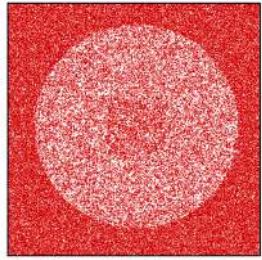
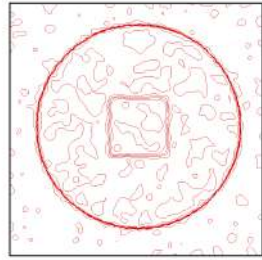


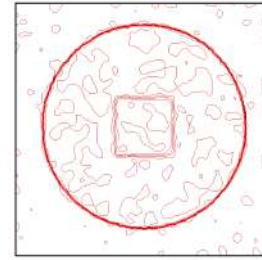
Figure 3.6: A 299×299 circle image corrupted by Gaussian noise with $\sigma = 20$ and restored by different models. (g) Ratio image for the clean circle image Figure 3.1c, (h)–(l) Ratio image for the restored images; Figure 3.6b–3.6f.



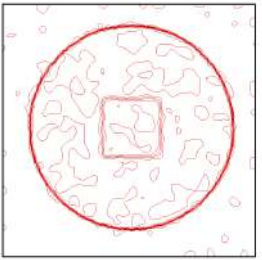
(a) Noisy



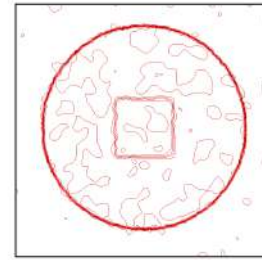
(b) TDE



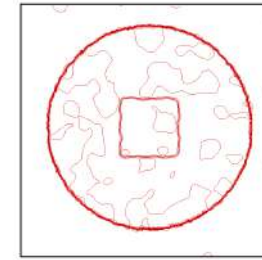
(c) Cao



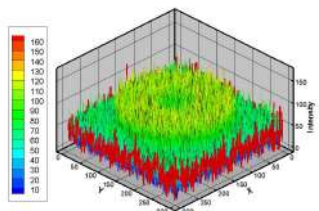
(d) SYS



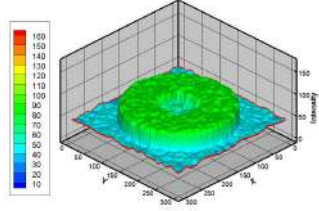
(e) ACPDE



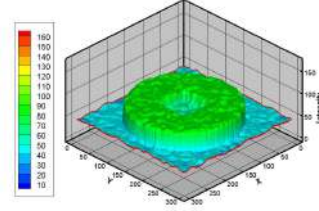
(f) Proposed



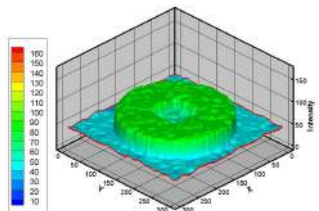
(g) Noisy



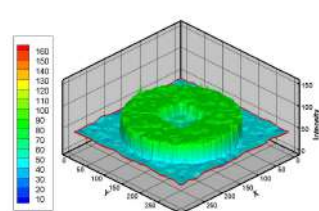
(h) TDE



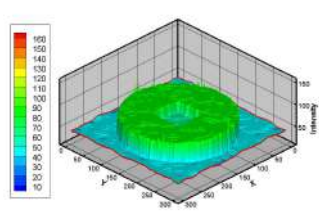
(i) Cao



(j) SYS



(k) ACPDE



(l) Proposed

Figure 3.7: (a)–(f) 2D contour plot of the the imgaes; Figure 3.6a–3.6f. (g)–(l) 3D surface plot of the images; Figure 3.6a–3.6f.

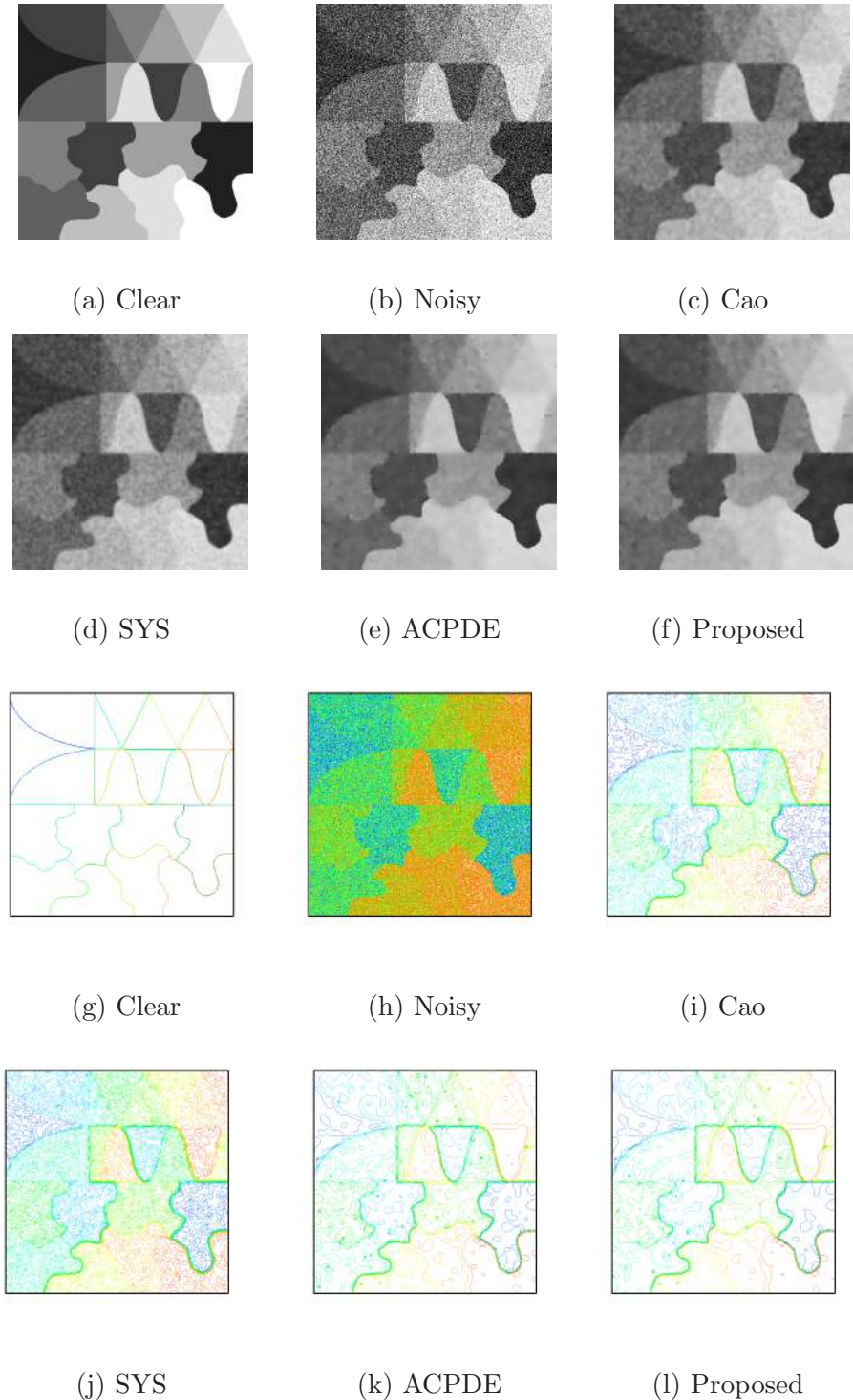


Figure 3.8: A 512×512 mosaic image corrupted by Gaussian noise with $\sigma = 100$ and restored by different models. (g)–(l) 2d contour plot of the the imgaes; Figure 3.8a–3.8f.

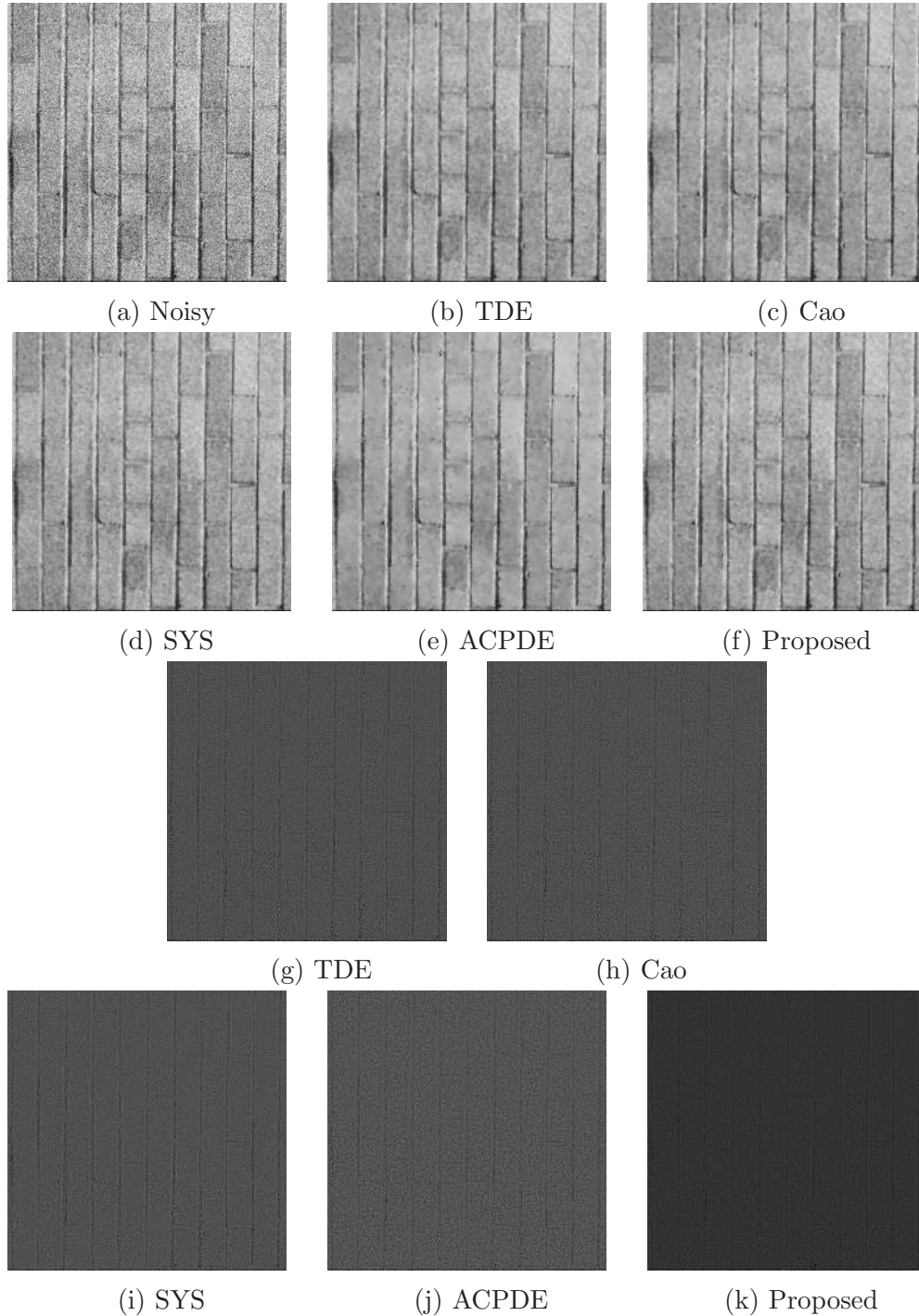


Figure 3.9: A 512×512 brick image corrupted by Gaussian noise with $\sigma = 40$ and restored by different models. (g)–(k) Ratio image for the restored images; Figure 3.9b–3.9f.

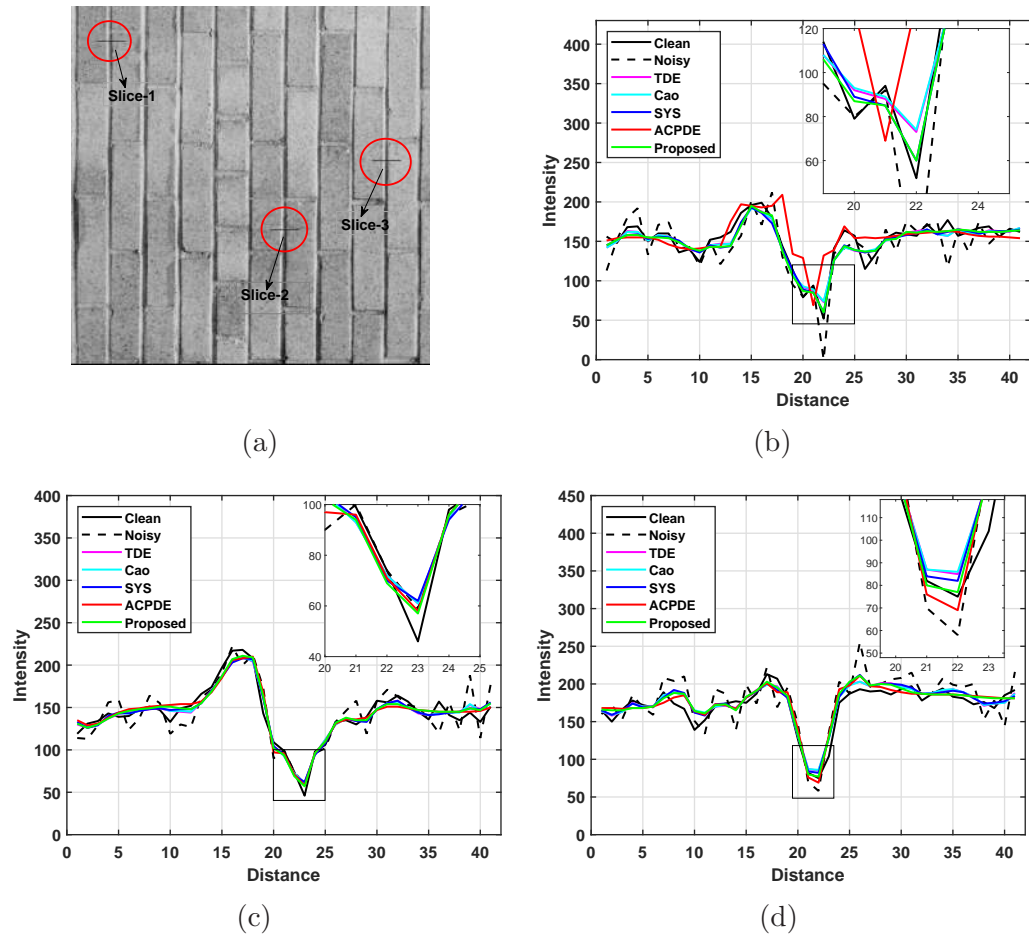


Figure 3.10: A 512×512 brick image corrupted by Gaussian noise with $\sigma = 20$ and restored by different models. (a) Indicate the one-dimensional slices. (b) Results for the Slice-1. (c) Results for the Slice-2. (d) Results for the Slice-3.

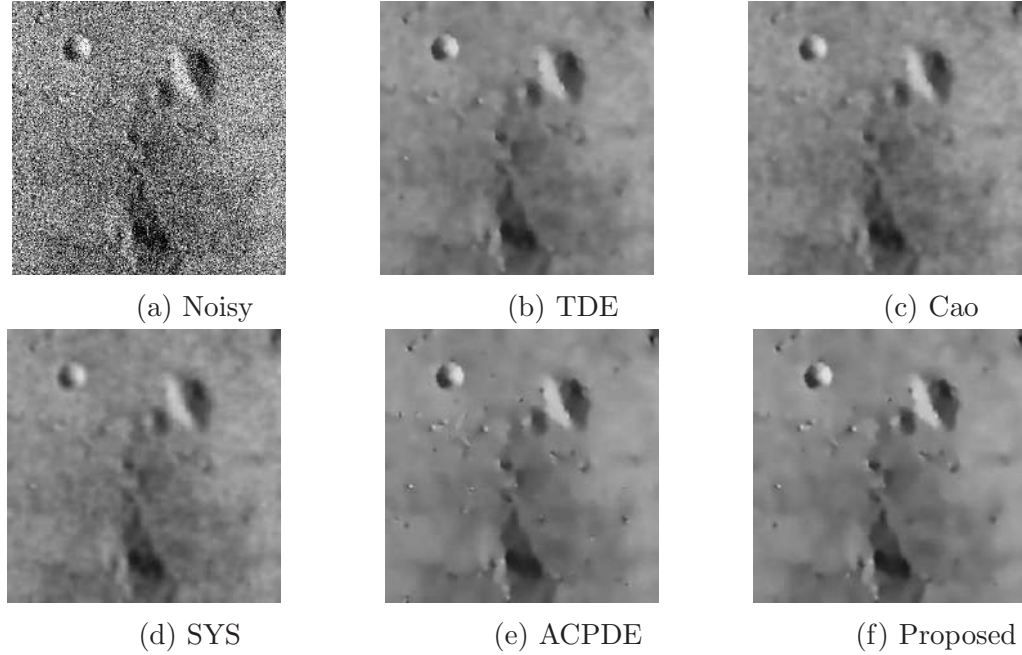


Figure 3.11: A 256×255 moon image corrupted by Gaussian noise with $\sigma = 60$ and restored by different models.

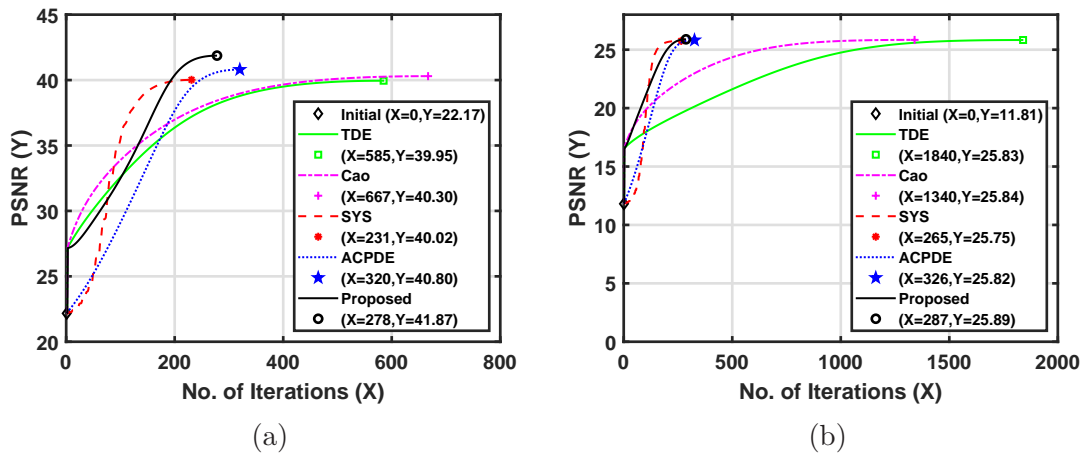


Figure 3.12: Improved PSNR value vs. the corresponding iteration number for different models. Both the graphs are plotted for the result of the circle image: (a) The circle image is degraded by Gaussian noise with $\sigma = 20$ and restored by different models. (b) The circle image is degraded by Gaussian noise with $\sigma = 80$ and restored by different models.

Table 3.2: MSSIM and PSNR values of restored images.

Image	σ	TDE	Cao	SYS	ACPDE	Proposed
		MSSIM/PSNR/NOI/CPU time	MSSIM/PSNR/NOI/CPU time	MSSIM/PSNR/NOI/CPU time	MSSIM/PSNR/NOI/CPU time	MSSIM/PSNR/NOI/CPU time
Peppers	20	0.9088/29.67/393/34.15	0.9124/29.92/175/16.14	0.9318/30.96/132/15.45	0.9320/31.14/463/403.53	0.9374/31.32/108/13.70
	40	0.8721/27.38/904/ 37.38	0.8705/27.49/646/62.02	0.8827/28.05/406/43.31	0.8809/28.03/732/634	0.8883/28.25/405/60.91
	60	0.8228/25.50/1522/159.13	0.8241/25.69/1051/98.65	0.8266/25.71/865/90.63	0.8248/25.81/ 226 /202.70	0.8410/26.08/428/63.21
	80	0.7718/23.67/1644/160.14	0.7714/23.81/1118/111.37	0.7797/23.84/295/ 29.75	0.7707/23.77/ 218 /182.56	0.7922/24.07/698/98.04
	100	0.7124/21.95/2016/184.64	0.7113/22.05/1342/122.83	0.7135/22.03/254/ 26.26	0.6996/21.99/ 197 /172.98	0.7398/22.24/1240/193.03
Tree	20	0.7847/26.94/ 63/1.38	0.7992/27.25/94/2.15	0.8203/27.46/113/2.49	0.8367/28.01/144/23.55	0.8417/28.16/169/5.55
	40	0.7501/24.28/389/8.28	0.7518/24.52/558/12.38	0.7634/24.74/363/ 8.02	0.7640/24.88/ 230 /37.79	0.7687/24.99/427/14.05
	60	0.6894/22.37/697/14.84	0.6949/22.57/1038/24.47	0.7075/22.64/779/17.52	0.7058/22.69/ 389 /65.28	0.7098/22.81/468/14.17
	80	0.6288/20.68/806/17.04	0.6258/20.80/753/ 16.70	0.6507/20.81/1177/26.59	0.6481/20.90/ 524 /88.15	0.6560/21.04/648/19.45
	100	0.5770/19.25/1018/22.14	0.5769/19.35/945/22.15	0.6002/19.38/932/ 21.06	0.5974/19.43/ 625 /104.53	0.6053/19.53/767/23.13
Circle	20	0.9768/39.95/585/14.02	0.9782/40.30/667/16.25	0.9769/40.02/ 231/5.87	0.9796/40.81/320/60.09	0.9822/41.87/278/10.90
	40	0.9641/35.50/1152/28.33	0.9613/35.35/870/12.79	0.9395/33.84/ 184/5.03	0.9580/35.17/253/63.96	0.9736/36.94/1036/41.30
	60	0.9371/29.91/2322/58.66	0.9370/29.92/1744/59.08	0.9286/29.64/ 232/6.48	0.9359/29.87/439/108.15	0.9496/30.36/745/31.07
	80	0.9180/25.75/1840/46.41	0.9191/25.80/1340/36.87	0.9133/25.54/ 264/6.87	0.9161/25.62/326/72.74	0.9213/25.89/287/10.33
	100	0.8962/22.85/275/ 6.43	0.8975/22.89/283/6.98	0.8945/22.86/309/7.90	0.8951/22.89/ 222 /51.05	0.8987/22.91/289/11.48
Mosaic	20	0.9716/33.65/675/59.23	0.9576/33.45/392/36.45	0.9798/34.23/193/ 19.88	0.9810/34.64/ 155 /148.81	0.9912/34.79/735/110.17
	40	0.9365/29.83/1328/117.94	0.9328/29.56/888/78.67	0.9649/29.98/475/ 48.82	0.9437/29.81/ 176 /160.37	0.9732/30.15/933/136.73
	60	0.9009/26.18/1310/115.63	0.9070/26.13/1350/121.87	0.9242/26.14/315/ 32.62	0.9156/26.17/ 298 /249.96	0.9513/26.44/1944/303.10
	80	0.8546/23.28/1428/127.99	0.8625/23.28/1432/128.71	0.8956/23.34/454/ 47.27	0.8839/23.34/ 411 /362.19	0.9125/23.48/997/143.33
	100	0.8202/21.11/1650/143.77	0.8175/21.10/1391/126.24	0.8479/21.12/ 332/34.70	0.8536/21.17/360/318.54	0.8783/21.26/926/134.58

Table 3.3: MSSIM and PSNR values of restored images.

Image	σ	TDE	Cao	SYS	ACPDE	Proposed
		MSSIM/PSNR/NOI/CPU time	MSSIM/PSNR/NOI/CPU time	MSSIM/PSNR/NOI/CPU time	MSSIM/PSNR/NOI/CPU time	MSSIM/PSNR/NOI/CPU time
Brick	20	0.8639/27.28/152/14.33	0.8635/27.37/63/6.24	0.8635/27.33/ 49/4.98	0.8613/27.32/72/50.03	0.8647/27.43/144/20.70
	40	0.7390/24.86/684/64.38	0.7407/24.91/343/32.72	0.7416/24.82/ 113/11.31	0.7356/24.98/167/122.32	0.7428/25.05/809/113.73
	60	0.6616/23.44/1272/120.87	0.6633/23.55/519/51.13	0.6508/23.24/ 110/11.04	0.6639/23.65/208/150.50	0.6681/23.76/941/120.47
	80	0.5958/22.18/1377/129.80	0.5986/22.28/585/55.87	0.5783/21.95/ 122/12.66	0.5993/22.32/278/217.31	0.6072/22.44/145/109/78
	100	0.5329/21.09/1368/129.56	0.5383/21.19/714/68.83	0.5166/20.93/ 130/13.85	0.5349/21.16/258/211.38	0.5431/21.26/853/111.35
Aerial	20	0.8981/26.39/ 14/1.30	0.8976/26.38/35/3.35	0.8978/26.33/88/9.33	0.8999/26.48/224/176.58	0.9005/26.50/46/6.55
	40	0.7804/23.86/ 42/4.14	0.7800/23.85/227/22.40	0.7766/23.85/136/15.31	0.7820/23.87/222/193.01	0.7831/23.91/185/28.50
	60	0.6816/22.57/ 82/9.06	0.6827/22.56/563/51.98	0.6792/22.56/147/15.70	0.6857/22.57/275/243.16	0.6910/22.62/487/75.34
	80	0.5893/21.56/ 103/9.80	0.5962/21.58/851/85.53	0.5928/21.57/159/16.34	0.5968/21.57/280/235.77	0.5970/21.60/187/27.86
	100	0.5363/20.79/ 128/12.51	0.5367/20.81/898/88.01	0.5346/20.76/153/17.89	0.5372/20.79/265/212.00	0.5380/20.85/267/43.29
Moon	20	0.6763/29.66/313/6.03	0.6676/29.54/184/3.72	0.6790/29.69/ 107/2.16	0.6815/29.75/133/20.86	0.6817/29.82/172/5.80
	40	0.5919/27.77/955/18.60	0.5894/27.76/704/14.10	0.5916/27.89/ 318/6.53	0.5960/27.90/432/59.31	0.5973/27.95/475/15.37
	60	0.5606/26.73/1733/35.30	0.5628/26.81/994/20.21	0.5645/26.84/ 207/4.21	0.5615/26.84/478/74.45	0.5663/26.97/801/26.11
	80	0.5356/25.72/1935/41.68	0.5381/25.80/1387/28.58	0.5341/25.65/ 196/4.02	0.5357/25.83/466/68.84	0.5416/25.97/1080/34.12
	100	0.5210/24.71/1892/39.82	0.5225/24.75/1376/27.96	0.5188/24.61/ 203/4.19	0.5209/24.77/392/62.04	0.5241/24.89/855/25.77

3.5 Conclusion

A coupled telegraph diffusion based model for image denoising is discussed in this chapter. We have taken telegraph equation for the image variable as well as for the edge variable, which improves the present model over the existing CPDE based models. Mathematical analysis of the model has been carried out using Banach's fixed point theorem. Numerical experiments are performed to highlight the efficiency of the proposed model for image denoising using different types of test images. Qualitative and quantitative results ensure that the present technique exhibits better performance than the single telegraph diffusion-based models and coupled parabolic PDE based models. This new model removes the noise, reduces the staircase artifacts, and improves the filtering performance, even in low SNR images.

3.6 Appendix

Using Galerkin finite dimensional approximation, we can write the equation (3.10) in the following form:

$$(I_m''(t), w_k) + (I_m'(t), w_k) + B[I_m(t), w_k; t] = (f, w_k), \quad (0 \leq t \leq T, k = 1, 2, \dots, m) \quad (3.39)$$

where m is a fixed positive integer and

$$I_m(t) = \sum_{k=1}^m d_m^k(t) w_k. \quad (3.40)$$

In the above, $w_k = w_k(x)$ are smooth functions, $\{w_k\}_{k=1}^m$ is a basis for the finite dimensional subspace V_m (say) of H^1 , and we intend to select the coefficients $d_m^k(t)$ ($0 \leq t \leq T, k = 1, 2, \dots, m$) so that

$$d_m^k(0) = (I(x, 0), w_k) \quad (k = 1, 2, \dots, m), \quad (3.41)$$

$$d_m^k'(0) = (I_t(x, 0), w_k) \quad (k = 1, 2, \dots, m). \quad (3.42)$$

(,) denotes the inner product in L^2 and

$$B[I, w; t] = \int_{\Omega} \bar{g} \nabla I \cdot \nabla w \, dx, \quad \text{and} \quad f = -2\bar{v}. \quad (3.43)$$

Now we can differentiate the equation (3.39) [**Theorem 5 (Improved regularity), Section 7.2, Chapter-7 (Evans, 2010)**] and we get

$$(I_m''', w_k) + (I_m'', w_k) + B[I'_m, w_k; t] + B'[I_m, w_k; t] = (f', w_k). \quad (3.44)$$

Multiply the above relation by $d_m^k(t)$ and taking summation over $k = 1, 2, \dots, m$, we have

$$(I_m''', I_m'') + (I_m'', I_m'') + B[I'_m, I_m''; t] + B'[I_m, I_m''; t] = (f', I_m''). \quad (3.45)$$

Following the subsequent steps as we have done in **Lemma 3.2** [from equation (3.20) to (3.21)] for I [note that, (3.20) and (3.45) represent a similar equation only difference by subscript], we establish the desired bound for the approximate solution I_m of the linear problem (3.10) with $I_m \in L^\infty(0, T; H^2)$. Now taking the limit as $m \rightarrow \infty$, we derive the same bound for the weak solution I of the linearized problem (3.10) with $I \in L^\infty(0, T; H^2)$.

Chapter 4

A Gray Level Indicator-Based Telegraph Diffusion Model: Application to Image Despeckling

From this chapter, we switch our focus from the additive noise removal process to the multiplicative noise removal process. In this chapter, the development of a gray level indicator-based telegraph diffusion model is explained for image despeckling. Moreover, we have established the well-posedness of the system using Schauder fixed point theorem. Furthermore, we show the superiority of the proposed method over three recently developed methods on a set of gray level test images. Also, check the noise removal ability of the present technique over real SAR images corrupted by speckle noise with different noise levels.

4.1 General Introduction

Purity of the edge/textured information in the SAR images, ultrasound images, and laser images are usually diminished by speckle noise (Burckhardt, 1978; Prager *et al.*, 2001; Loizou *et al.*, 2005). Due to the contamination by speckle noise, it is challenging to distinguish the hidden details in the images. Therefore, the development of an advanced speckle noise removal algorithm is an essential aspect for the image processing community. A mathematical representation is required to develop an efficient noise removal algorithm so that we can express each pixel of an image as a function of the speckle noise. The popularly used model for the noise image can be expressed as a product of the original signal and the speckle

⁰The research work of this chapter is published in *SIAM Journal on Imaging Sciences*, vol. 13(2), pp. 844–870, 2020, <https://doi.org/10.1137/19M1283033>.

noise (Goodman, 1976; Tur *et al.*, 1982)

$$J = I\eta,$$

where J indicates the noisy image, I is the noise-free image, and η signifies the speckle-noise process. In general, the speckle noise η is $Gamma(L, L)$ distributed **subsection 1.1.2**. From the initiation of the PM model (1.12), PDE are extensively used to develop noise removal algorithms: Among different types of PDE based models, the TV algorithms achieved remarkable results. The first variational based strategy to deal with multiplicative noise is the RLO model (1.32). Due to the non-convexity of the model (1.32), it may not give a globally unique solution. To succeed over this shortcoming, several authors suggested various convex functional with different data fidelity terms (Aubert and Aujol, 2008; Huang *et al.*, 2010; Jin and Yang, 2011; Liu *et al.*, 2013). In this regard, Dong *et al.* (2013) suggested a convex total variation model for multiplicative speckle-noise reduction with the following form:

$$I^* := \underset{I \in BV(\Omega)}{\operatorname{argmin}} \left\{ \int_{\Omega} \alpha(x) |DI| + \lambda \int_{\Omega} \left(I + J \log \frac{1}{I} \right) dx \right\}. \quad (4.1)$$

They choose the gray level indicator function α as

$$\left(1 - \frac{1}{1 + k|G_{\xi} * J|^2} \right) \frac{1 + kM^2}{kM^2} \quad \text{or} \quad \frac{G_{\xi} * J}{M},$$

with $M = \sup_{x \in \Omega} (G_{\xi} * J)(x)$, where $\xi > 0$, $k > 0$ are constants, and λ is a given parameter; see (Dong *et al.*, 2013). Later, based on a gray level indicator function, Zhou *et al.* (2015) proposed a diffusion model called “doubly degenerate diffusion” (DDD) for multiplicative noise removal problem. Their model takes the form

$$\partial_t I = \operatorname{div}(g(I, |\nabla I|) \nabla I) \quad \text{in } \Omega_T, \quad (4.2)$$

$$\partial_n I = 0 \quad \text{in } \partial\Omega_T, \quad (4.3)$$

$$I(x, 0) = J(x) \quad \text{in } \Omega. \quad (4.4)$$

They choose the diffusion coefficient as

$$g(I, |\nabla I|) = \frac{2|I|^{\nu}}{M^{\nu} + |I|^{\nu}} \cdot \frac{1}{(1 + |\nabla I|^2)^{(1-\beta)/2}},$$

where $\nu > 0$, $0 < \beta < 1$, and $M = \sup_{x \in \Omega} I$. In this case, the gray level indicator and edge detector function are

$$a(I) := \frac{2|I|^\nu}{M^\nu + |I|^\nu} \quad \text{and} \quad b(|\nabla I|) := \frac{1}{(1 + |\nabla I|^2)^{(1-\beta)/2}},$$

respectively. However, because of the degeneracy of the edge detector function, i.e., $b(|\nabla I|) \rightarrow 0$ as $|\nabla I| \rightarrow \infty$, it is challenging to establish the well-posedness of their model. Subsequently, Zhou *et al.* (2018) proposed another nonlinear diffusion-based model (the ZZDB model) for image despeckling. In this model, a region indicator was introduced as an exponential function in the PM model (1.12). The model takes the form

$$\partial_t I = \operatorname{div} \left(\frac{\nabla I}{1 + (|\nabla I_\xi|/K)^{\beta(I)}} \right) \quad \text{in } \Omega_T, \quad (4.5)$$

$$\partial_n I = 0 \quad \text{in } \partial\Omega_T, \quad (4.6)$$

$$I(x, 0) = J(x) \quad \text{in } \Omega. \quad (4.7)$$

Here $\beta(I)$ is a region indicator and the authors chosen it as follows:

$$\beta(I) = 2 - \frac{2|I|^\alpha}{M^\alpha + |I|^\alpha},$$

where $K, \alpha > 0$, $I_\xi = G_\xi * I$, and $M = \sup_{x \in \Omega} I$. Recently, Shan *et al.* (2019) proposed a regularized version of the DDD model (4.2)–(4.4). In (Shan *et al.*, 2019), the model takes on the form

$$\partial_t I = \operatorname{div}(g(I_\xi, |\nabla I_\xi|) \nabla I) \quad \text{in } \Omega_T, \quad (4.8)$$

$$\partial_n I = 0 \quad \text{in } \partial\Omega_T, \quad (4.9)$$

$$I(x, 0) = J(x) \quad \text{in } \Omega. \quad (4.10)$$

They choose the diffusion coefficient as

$$g(I_\xi, |\nabla I_\xi|) = \left(\frac{I_\xi}{M_\xi^I} \right)^\nu \cdot \frac{1}{1 + |\nabla I_\xi|^\beta},$$

where $I_\xi = G_\xi * I$, $M_\xi^I = \max_{x \in \Omega} |I_\xi(x, t)|$, and ν , β , and ξ are positive constants. Due to the introduction of the Gaussian kernel in the diffusion coefficient, which avoids the degeneracy in the model, the authors are able to study the well-posedness of the model (4.8)–(4.10).

To the best of our knowledge, most of the researchers concentrated their interest only on parabolic PDE based models, which are developed from either the variational based approach or diffusion based approach, for the speckle-noise removal process. The hyperbolic PDEs could upgrade the quality of the detected edges and improve the image better than parabolic PDEs ([Averbuch et al., 2006](#)). The first hyperbolic PDE model for image denoising is the telegraph-diffusion model ([1.17](#)). After that, several nonlinear telegraph diffusion-based methods have been proposed ([Cao et al., 2010](#); [Yang and Zhang, 2014](#); [Zhang et al., 2015](#); [Jain and Ray, 2016](#); [Baravdish et al., 2019](#)). However, in spite of their impressive applications in the additive noise removal process, hyperbolic PDE based approaches have not successfully been used for the speckle noise removal process.

To demonstrate the importance of the hyperbolic PDE based model for image despeckling, the present work suggests a gray level indicator-based telegraph diffusion model for multiplicative speckle noise elimination. The proposed technique uses the benefit of the combined effect of diffusion equation as well as the wave equation. Wave nature of the system preserves the high oscillatory and texture patterns in an image. In this model, the diffusion coefficient depends not only on the image gradient but also on the gray level of the image, which controls the diffusion process better than only gradient-based diffusion approaches. Furthermore, we study the well-posedness of the suggested model in an appropriate function space. We opt an explicit numerical method to solve the present model. Our numerical implementation allows computing of despeckled results on some standard test images. Quality of the despeckled images using the suggested model compares with the recently developed models ([Zhou et al., 2015, 2018](#); [Shan et al., 2019](#)). We compare the quantitative and qualitative results at different noise levels. The experiment results confirm that the proposed model performs better as compared to the existing models considered for the comparison. Along with the artificial noisy image, we apply our model on some real images, which indicates the potential ability of the present model for speckle noise removal.

The rest of the chapter is organized as follows. Section [4.2](#) describes the proposed telegraph diffusion model. In section [4.3](#), we study the well-posedness of weak solution of the proposed model. Section [4.4](#) describes the numerical discretization of the present model. The simulated despeckling results obtained by the proposed approach are compared with other discussed diffusion methods in section [4.5](#). We conclude the work in section [4.6](#).

4.2 TDM Model for Image Despeckling

Inspired by the ideas of (Zhou *et al.*, 2015) and (Majee *et al.*, 2019), initially we developed the model

$$\partial_{tt}I + \gamma\partial_tI - \operatorname{div}(g(I, |\nabla I|) \nabla I) = -\lambda h(J, I) \quad \text{in } \Omega_T, \quad (4.11)$$

$$\partial_n I = 0 \quad \text{in } \partial\Omega_T, \quad (4.12)$$

$$I(x, 0) = J(x), \quad \partial_t I(x, 0) = 0 \quad \text{in } \Omega. \quad (4.13)$$

The function g is defined as

$$g(I, |\nabla I|) = \frac{2|I|^\nu}{(M^I)^\nu + |I|^\nu} \cdot \frac{1}{1 + \left(\frac{|\nabla I|}{K}\right)^2}, \quad (4.14)$$

where, $\nu \geq 1$, $\gamma, K > 0$ are constants, $M^I = \max_{x \in \Omega} |I(x, t)|$, and $h(J, I)$ is the source term which comes due to the fidelity control term in the energy functional as discussed in (Majee *et al.*, 2019). Although the presence of fidelity term in the equation keeps the restored image close to the original image, the noise may not be removed sufficiently. Therefore we would like to choose $h(J, I) = 0$. Also, because of the degeneracy in the diffusion coefficient (4.14), the suggested model (4.11)–(4.13) may not be a well-posed problem (Shan *et al.*, 2019). To overcome these issues, we invoke the ideas of (Cao *et al.*, 2010) and (Shan *et al.*, 2019), and finally design the following model in the telegraph diffusion-based framework:

$$\partial_{tt}I + \gamma\partial_tI - \operatorname{div}(g(I_\xi, |\nabla I_\xi|) \nabla I) = 0 \quad \text{in } \Omega_T, \quad (4.15)$$

$$\partial_n I = 0 \quad \text{in } \partial\Omega_T, \quad (4.16)$$

$$I(x, 0) = J(x), \quad \partial_t I(x, 0) = 0 \quad \text{in } \Omega, \quad (4.17)$$

where the diffusion function $g(\cdot)$ is given by

$$g(I_\xi, |\nabla I_\xi|) = \frac{2|I_\xi|^\nu}{(M_\xi^I)^\nu + |I_\xi|^\nu} \cdot \frac{1}{1 + \left(\frac{|\nabla I_\xi|}{K}\right)^2}.$$

In the above, $I_\xi = G_\xi * I$, $M_\xi^I = \max_{x \in \Omega} |I_\xi(x, t)|$. Moreover the gray level indicator function

$$b(I) = \frac{2|I_\xi|^\nu}{(M_\xi^I)^\nu + |I_\xi|^\nu}$$

can be transformed into $b(s) = \frac{2s^\nu}{1+s^\nu}$, where $s = \frac{|I_\xi|}{M_\xi^I} \in [0, 1]$.

The use of Gaussian convolution in the proposed model has a lot of advantages, not only the robustness in denoising viewpoint but also the well-posedness in the theoretical perspective. There are two key advantages of this proposed approach:

- i) The quality of the edges detected through this noise removal approach is better than other non-telegraph based algorithms as the proposed model (4.15)–(4.17) consists of telegraph diffusion equation (Averbuch *et al.*, 2006; Ratner and Zeevi, 2007; Cao *et al.*, 2010)
- ii) It controls the diffusion process very well along with the gradient based edge detector coefficient specially for the speckle noise removal process (Dong *et al.*, 2013) as the gray level indicator function in the proposed model is incorporated into the telegraph diffusion framework.

4.3 Well-posedness of Weak Solutions

In this section, we prove the existence and uniqueness of weak solution of the proposed model (4.15)–(4.17). Since the system is nonlinear, we first consider the linearized model, and then use Schauder fixed point theorem (Evans, 1998) to show the existence of a weak solution.

4.3.1 Technical framework & statement of the main result

Without loss of generality, we assume $\gamma = 1$ in (4.15). Throughout this section, C denotes a generic positive constant and we write L^p , H^1 , $(H^1)'$ instead of $L^p(\Omega)$, $H^1(\Omega)$, $(H^1(\Omega))'$, respectively. We introduce the solution space $W(0, T)$ for the model (4.15)–(4.17), where

$$W(0, T) = \left\{ w \in L^\infty(0, T; H^1), \partial_t w \in L^\infty(0, T; L^2); \partial_{tt} w \in L^2(0, T; (H^1)') \right\}.$$

Note that the space $W(0, T)$ is a Hilbert space for the graph norm, see (Lions, 1968).

Definition 4.1 (Weak solution). *A function I is called a weak solution of (4.15)–(4.17) if*

- a) $I \in W(0, T)$ and (4.17) holds.

b) For all $\phi \in H^1$ and a.e. $t \in (0, T)$, there hold

$$\langle \partial_{tt} I, \phi \rangle + \int_{\Omega} \left(\partial_t I \phi + g(I_\xi, |\nabla I_\xi|) \nabla I \cdot \nabla \phi \right) dx = 0.$$

As we mentioned, our aim is to establish well-posedness of weak solutions of the proposed model (4.15)–(4.17), and we will do so under the following assumption:

A.1 The initial data J is an H^2 -valued function such that

$$0 < \alpha := \inf_{x \in \Omega} J(x).$$

Theorem 4.1. *Let the assumption **A.1** be true. Then the model (4.15)–(4.17) has a unique weak solution in the sense of definition 4.1.*

► See the proof in [subsection 4.3.3](#).

4.3.2 Linearized model & existence of weak solution

For any positive constant $M_1 > 0$, define

$$W_{M_1} = \left\{ \bar{I} \in W(0, T) : \|\bar{I}\|_{L^\infty(0, T; H^1)} + \|\partial_t \bar{I}\|_{L^\infty(0, T; L^2)} \leq M_1 \|J\|_{H^1}, \right. \\ \left. 0 < \alpha \leq \bar{I}(x, t) \text{ for a.e. } (x, t) \in \Omega_T \right\}.$$

For any $\bar{I} \in W_{M_1}$, consider the linearized model:

$$\partial_{tt} I + \partial_t I - \operatorname{div}(\bar{g}(x, t) \nabla I) = 0 \quad \text{in } \Omega_T, \quad (4.18)$$

with the conditions (4.16)–(4.17), where the function \bar{g} is given by

$$\bar{g}(x, t) \equiv g_{\bar{I}}(x, t) := \frac{|\bar{I}_\xi|^\nu}{(M_\xi^{\bar{I}})^\nu + |\bar{I}_\xi|^\nu} \cdot \frac{1}{1 + \left(\frac{|\nabla \bar{I}_\xi|}{K} \right)^2}.$$

Claim 4.3.1. *There exist positive constants $\kappa, C > 0$, depending only on G_ξ , J , M_1 , K , α , and ν such that*

- i) $0 < \kappa \leq \bar{g} \leq 1$,
- ii) $|\partial_t \bar{g}| \leq C$.

Proof. Proof of i): Let $\bar{I} \in W_{M_1}$. Since $0 < \alpha \leq \bar{I}$, and G_ξ is positive, by convolution property, we have

$$\alpha \|G_\xi\|_{L^1} = |G_\xi * \alpha| \leq |\bar{I}_\xi| \leq M_1 C_\xi \|J\|_{H^1}. \quad (4.20)$$

Thanks to the definition of $M_\xi^{\bar{I}}$, and (4.20), we have $|M_\xi^{\bar{I}}| \leq M_1 C_\xi \|J\|_{H^1}$, and hence for any $\nu > 0$

$$(\alpha \|G_\xi\|_{L^1})^\nu \leq |\bar{I}_\xi|^\nu \leq (M_\xi^{\bar{I}})^\nu \leq (M_1 C_\xi \|J\|_{H^1})^\nu.$$

Observe that, $(M_\xi^{\bar{I}})^\nu + |\bar{I}_\xi|^\nu \leq 2(M_1 C_\xi \|J\|_{H^1})^\nu$, and therefore

$$\frac{(\alpha \|G_\xi\|_{L^1})^\nu}{2(M_1 C_\xi \|J\|_{H^1})^\nu} \leq \frac{|\bar{I}_\xi|^\nu}{2(M_1 C_\xi \|J\|_{H^1})^\nu} \leq \frac{|\bar{I}_\xi|^\nu}{(M_\xi^{\bar{I}})^\nu + |\bar{I}_\xi|^\nu} \leq 1. \quad (4.21)$$

Furthermore, by using Young's convolution inequality, we see that $|\nabla \bar{I}_\xi| \leq M_1 C_\xi \|J\|_{H^1}$, and hence

$$\frac{1}{1 + \left(\frac{C_\xi M_1 \|J\|_{H^1}}{K}\right)^2} \leq \frac{1}{1 + \left(\frac{|\nabla \bar{I}_\xi|}{K}\right)^2} \leq 1. \quad (4.22)$$

Now i) follows from (4.21)–(4.22) for $\kappa = \frac{(\alpha \|G_\xi\|_{L^1})^\nu}{2(M_1 C_\xi \|J\|_{H^1})^\nu} \cdot \frac{1}{1 + \left(\frac{C_\xi M_1 \|J\|_{H^1}}{K}\right)^2}$.

Proof of ii) : Observe that

$$|\bar{g}_t| \leq \nu \frac{|\bar{I}_\xi|^{\nu-1} |G_\xi * \bar{I}_t|}{((M_\xi^{\bar{I}})^\nu + |\bar{I}_\xi|^\nu)^2} (M_\xi^{\bar{I}})^\nu + C(\xi, M_1, K) \|J\|_{H^1}^2 \equiv A + C(\xi, M_1, K) \|J\|_{H^1}^2.$$

Thanks to the property of convolution, and the condition $\bar{I} \in W_{M_1}$, it is easy to see that

$$A \leq \begin{cases} \frac{\nu (C_\xi M_1 \|J\|_{H^1})^\nu}{\alpha^\nu} & \text{if } \nu > 1, \\ \frac{\nu C_\xi M_1 \|J\|_{H^1}}{\left(\alpha \|G_\xi\|_{L^1}\right)^{1-\nu}} & \text{if } 0 < \nu \leq 1. \end{cases}$$

Hence

$$|\bar{g}_t| \leq C(\nu, \alpha, \xi, M_1, \|J\|_{H^1}) + C(\xi, M_1, K) \|J\|_{H^1}^2.$$

Thus ii) holds. This finishes the proof of claim. \square

Thanks to claim 4.3.1, one can apply classical Galerkin method (Evans, 1998) to show that there exists a unique weak solution $I \in W(0, T)$ of the linearized model (4.18) with the initial and boundary conditions (4.16)–(4.17).

Lemma 4.2. *The unique solution $I \in W(0, T)$ of the linearized equation (4.18) with the conditions (4.16)–(4.17) satisfies the following: there exists a constant $C > 0$, depending only on $G_\xi, J, M_1, \nu, \alpha, K$ such that*

$$a) \|I\|_{L^\infty(0,T;H^1)} + \|\partial_t I\|_{L^\infty(0,T;L^2)} \leq C\|J\|_{H^1},$$

$$b) \int_0^T \|\partial_{tt} I\|_{(H^1)'}^2 dt \leq CT\|J\|_{H^1}^2.$$

Proof. Proof of a): Note that $\partial_t I \in L^\infty(0, T; H^1)$. Multiplying equation (4.18) by $\partial_t I$ and integrating by parts we have

$$\frac{1}{2} \frac{d}{dt} \|\partial_t I\|_{L^2}^2 + \|\partial_t I\|_{L^2}^2 + \int_\Omega \bar{g} \nabla I \cdot \nabla (\partial_t I) dx = 0. \quad (4.23)$$

Note that, thanks to integration by parts formula and (4.19),

$$\begin{aligned} \int_\Omega \bar{g} \nabla I \cdot \nabla (\partial_t I) dx &= \frac{1}{2} \frac{d}{dt} \int_\Omega \bar{g} |\nabla I|^2 dx - \frac{1}{2} \int_\Omega \partial_t \bar{g} |\nabla I|^2 dx \\ &\geq \frac{1}{2} \frac{d}{dt} \int_\Omega \bar{g} |\nabla I|^2 dx - \frac{C}{2} \|\nabla I\|_{L^2}^2. \end{aligned} \quad (4.24)$$

Thanks to the lower bound of \bar{g} as in (4.19), we observe that

$$\|\nabla I\|_{L^2}^2 \leq \frac{1}{\kappa} \int_\Omega \bar{g} |\nabla I|^2 dx. \quad (4.25)$$

Now using (4.24) and (4.25) in (4.23), we have

$$\frac{d}{dt} \left[\|\partial_t I\|_{L^2}^2 + \int_\Omega \bar{g} |\nabla I|^2 dx \right] \leq C \left(\|\partial_t I\|_{L^2}^2 + \int_\Omega \bar{g} |\nabla I|^2 dx \right).$$

An application of Gronwall's lemma (Evans, 1998) gives: for a.e. $t \in (0, T]$

$$\|\partial_t I(t)\|_{L^2}^2 + \|\nabla I(t)\|_{L^2}^2 \leq \|J\|_{H^1}^2 e^{Ct}. \quad (4.26)$$

Since $I(x, t) = J(x) + \int_0^t \partial_t I(s) ds$, we have, thanks to Young's inequality and (4.26), also we have

$$\|I(t)\|_{L^2}^2 \leq 2 \|J\|_{H^1}^2 + 2T \int_0^t \|\partial_t I(s)\|_{L^2}^2 ds \leq 2 \|J\|_{H^1}^2 + 2T^2 \|J\|_{H^1}^2 e^{CT}. \quad (4.27)$$

We combine (4.26) and (4.27) to conclude

$$\|I\|_{L^\infty(0,T;H^1)} + \|\partial_t I\|_{L^\infty(0,T;L^2)} \leq C\|J\|_{H^1}. \quad (4.28)$$

Hence a) of Lemma 4.2 follows.

Proof of b): Multiplying the equation (4.18) by $\phi \in H^1$ with $\|\phi\|_{H^1} \leq 1$, and integrating over Ω , we have

$$\langle \partial_{tt}I, \phi \rangle + \int_{\Omega} (\partial_t I \phi + \bar{g} \nabla I \cdot \nabla \phi) dx = 0.$$

We use Cauchy-Schwarz inequality along with (4.28) and boundedness of \bar{g} to obtain

$$\left| \langle \partial_{tt}I, \phi \rangle \right| \leq (\|\partial_t I\|_{L^2} + |\bar{g}| \|\nabla I(t)\|_{L^2}) \|\phi\|_{H^1} \leq C \|J\|_{H^1} \|\phi\|_{H^1}.$$

Hence, by the definition of norm in $(H^1)'$, we get

$$\|\partial_{tt}I\|_{(H^1)'} \leq C \|J\|_{H^1}. \quad (4.29)$$

This implies that $\|\partial_{tt}I\|_{L^\infty(0,T;(H^1)')} \leq C \|J\|_{H^1}$. Moreover, squaring both sides of (4.29) and integrating over $(0, T)$, one arrives at the assertion b). This completes the proof. \square

4.3.3 Proof of Theorem 4.1

In this section, we prove well-posedness of weak solution of the proposed model via Schauder fixed point theorem. To proceed further, we introduce the subspace W_0 of $W(0, T)$ defined by

$$W_0 = \left\{ w \in W(0, T) : \begin{aligned} & \|w\|_{L^\infty(0,T;H^1)} + \|\partial_t w\|_{L^\infty(0,T;L^2)} \leq C \|J\|_{H^1}; \\ & \|\partial_{tt} w\|_{L^2(0,T;(H^1)')} \leq C; \\ & 0 < \alpha \leq w(x, t) \text{ for a.e. } (x, t) \in \Omega_T, \text{ and } w \text{ satisfies (4.17)} \end{aligned} \right\}.$$

Moreover, one can prove that W_0 is a non-empty, convex and weakly compact subset of W . Consider a mapping

$$\mathcal{P} : W_0 \rightarrow W_0$$

$$w \mapsto I_w.$$

In order to use Schauder fixed point theorem on \mathcal{P} , we need to prove only that the mapping $\mathcal{P} : w \mapsto I_w$ is weakly continuous from W_0 into W_0 . Let w_k be a sequence that converges weakly to some w in W_0 and let $I_k = I_{w_k}$. We have to show that $\mathcal{P}(w_k) := I_k$ converges weakly to $\mathcal{P}(w) := I_w$.

Thanks to Theorem 4.2, one can use classical results of compact inclusion in Sobolev spaces (Adams, 1975), to extract subsequences $\{w_{k_n}\}$ of $\{w_k\}$ and $\{I_{k_n}\}$ of $\{I_k\}$ such that for some $I \in W_0$, the following hold as $k \rightarrow \infty$:

$$\left\{ \begin{array}{l} w_k \longrightarrow w \text{ in } L^2(0, T; L^2) \text{ and a.e. on } \Omega_T, \\ G_\xi * w_k \longrightarrow G_\xi * w \text{ in } L^2(0, T; L^2) \text{ and a.e. on } \Omega_T, \\ |G_\xi * w_k|^\nu \longrightarrow |G_\xi * w|^\nu \text{ in } L^2(0, T; L^2) \text{ and a.e. on } \Omega_T, \\ \frac{|G_\xi * w_k|^\nu}{(M_\xi^{w_k})^\nu + |G_\xi * w_k|^\nu} \rightarrow \frac{|G_\xi * w|^\nu}{(M_\xi^w)^\nu + |G_\xi * w|^\nu} \text{ in } L^2(0, T; L^2) \text{ and a.e. on } \Omega_T, \\ \partial_{x_i} G_\xi * w_k \rightarrow \partial_{x_i} G_\xi * w \ (i = 1, 2) \text{ in } L^2(0, T; L^2) \text{ and a.e. on } \Omega_T, \\ \frac{1}{1 + \left(\frac{|\nabla G_\xi * w_k|}{K}\right)^2} \longrightarrow \frac{1}{1 + \left(\frac{|\nabla G_\xi * w|}{K}\right)^2} \text{ in } L^2(0, T; L^2) \text{ and a.e. on } \Omega_T, \\ I_k \rightarrow I \text{ weakly-* in } L^\infty(0, T; H^1), \\ I_k \rightarrow I \text{ in } L^2(0, T; L^2), \\ \partial_t I_k \rightarrow \partial_t I \text{ weakly-* in } L^\infty(0, T; L^2), \\ \partial_{tt} I_k \rightarrow \partial_{tt} I \text{ weakly-* in } L^2(0, T; (H^1)'). \end{array} \right.$$

The above convergence allow us to pass to the limit in the equation (4.18) and obtain $I = \mathcal{P}(w)$. Moreover, since the solution of (4.18) is unique, the whole sequence $I_k = \mathcal{P}(w_k)$ converges weakly in W_0 to $I = \mathcal{P}(w)$. Hence \mathcal{P} is weakly continuous. Consequently, thanks to the Schauder fixed point theorem, there exists $w \in W_0$ such that $w = \mathcal{P}(w) = I_w$. Thus, the function I_w solves the proposed model (4.15)–(4.17).

4.3.4 Uniqueness of weak solution

Following the idea as in (Evans, 1998), we prove the uniqueness of weak solutions of the system (4.15)–(4.17). Let I_1 and I_2 be two weak solutions of (4.15)–(4.17).

Then, we have

$$\partial_{tt}I + \partial_t I - \operatorname{div}(g_{I_1} \nabla I) = \operatorname{div}((g_{I_1} - g_{I_2}) \nabla I_2) \quad \text{in } \Omega_T, \quad (4.30)$$

$$\begin{cases} I(x, 0) = 0, \quad \partial_t I(x, 0) = 0 & \text{in } \Omega, \\ \partial_n I = 0 & \text{on } \partial\Omega_T, \end{cases} \quad (4.31)$$

where $I = I_1 - I_2$. It suffices to show that $I \equiv 0$. To verify this, fix $0 < s < T$, and set for $i = 1, 2$,

$$v_i(\cdot, t) = \begin{cases} \int_t^s I_i(\cdot, \tau) d\tau, & 0 < t \leq s, \\ 0, & s \leq t < T. \end{cases} \quad (4.32)$$

Note that, for $t \in (0, T)$,

$$\begin{cases} \partial_t v_i(x, t) = -I_i(x, t), & i = 1, 2, \\ v_i(\cdot, t) \in H^1, \quad \partial_n v_i = 0 & \text{on } \partial\Omega \text{ in the sense of distribution.} \end{cases} \quad (4.33)$$

Set $v = v_1 - v_2$. Then $v(\cdot, s) = 0$. Multiplying (4.30) by v , integrating over $\Omega \times (0, s)$ along with the integration by parts formula, (4.33), Cauchy-Schwarz inequality and the equality

$$g_{I_1} \partial_t \nabla v \cdot \nabla v = \frac{1}{2} \partial_t (g_{I_1} |\nabla v|^2) - \frac{1}{2} \partial_t g_{I_1} |\nabla v|^2, \quad \text{and } \nabla v(x, s) = 0,$$

we obtain

$$\begin{aligned} & \frac{1}{2} \|I(s)\|_{L^2}^2 + \int_0^s \|I(t)\|_{L^2}^2 dt + \frac{1}{2} \int_{\Omega} g_{I_1}(x, 0) |\nabla v(x, 0)|^2 dx \\ & \leq \frac{1}{2} \left| \int_0^s \int_{\Omega} |\nabla v|^2 \partial_t g_{I_1} dx dt \right| + \int_0^s \|g_1 - g_2(t)\|_{L^\infty} \|\nabla I_2(t)\|_{L^2} \|\nabla v(t)\|_{L^2} dt. \end{aligned} \quad (4.34)$$

As seen in the proof of claim 4.3.1, there exist positive constants $\kappa_1, C_1 > 0$ such that

$$\kappa_1 \leq g_{I_1} \leq 1, \quad |\partial_t g_{I_1}| \leq C_1.$$

Moreover, one can use property of convolution along the fact that solution I_i has positive lower bound to show that

$$\|(g_{I_1} - g_{I_2})(t)\|_{L^\infty} \leq C(\xi, \nu, \alpha, K, J) \|I(t)\|_{L^2}. \quad (4.35)$$

Indeed, we can rewrite the expression of $g_{I_1} - g_{I_2}$ as

$$\begin{aligned} g_{I_1} - g_{I_2} &= \frac{|G_\xi * I_1|^\nu}{(M_\xi^{I_1})^\nu + |G_\xi * I_1|^\nu} \left(\frac{1}{1 + \left(\frac{|\nabla G_\xi * I_1|}{K}\right)^2} - \frac{1}{1 + \left(\frac{|\nabla G_\xi * I_2|}{K}\right)^2} \right) \\ &\quad + \frac{1}{1 + \left(\frac{|\nabla G_\xi * I_2|}{K}\right)^2} \left(\frac{|G_\xi * I_1|^\nu}{(M_\xi^{I_1})^\nu + |G_\xi * I_1|^\nu} - \frac{|G_\xi * I_2|^\nu}{(M_\xi^{I_2})^\nu + |G_\xi * I_2|^\nu} \right). \end{aligned}$$

By using the convolution property, we have

$$\begin{aligned} \|g_{I_1} - g_{I_2}\|_{L^\infty} &\leq C(\xi, \nu, K, J) \|I(t)\|_{L^2} + \left\| \frac{|G_\xi * I_1|^\nu (M_\xi^{I_2})^\nu - |G_\xi * I_2|^\nu (M_\xi^{I_1})^\nu}{(M_\xi^{I_1})^\nu (M_\xi^{I_2})^\nu} \right\|_{L^\infty} \\ &\equiv C(\xi, \nu, K, J) \|I(t)\|_{L^2} + \mathcal{A}. \end{aligned} \quad (4.36)$$

Since $(\alpha \|G_\xi\|_{L^1})^\nu \leq (M_\xi^{I_i})^\nu$ for $i = 1, 2$, we see that,

$$\begin{aligned} \mathcal{A} &\leq \frac{1}{(\alpha \|G_\xi\|_{L^1})^{2\nu}} \left\| |G_\xi * I_1|^\nu (M_\xi^{I_2})^\nu - |G_\xi * I_2|^\nu (M_\xi^{I_1})^\nu \right\|_{L^\infty} \\ &\leq C(\alpha, \xi, \nu) \left\{ \left\| |G_\xi * I_1|^\nu \left\{ (M_\xi^{I_2})^\nu - (M_\xi^{I_1})^\nu \right\} \right\|_{L^\infty} \right. \\ &\quad \left. + \left\| (M_\xi^{I_1})^\nu \left\{ |G_\xi * I_1|^\nu - |G_\xi * I_2|^\nu \right\} \right\|_{L^\infty} \right\} \\ &\leq C(\alpha, \xi, \nu) \left\{ \left\| |G_\xi * I_2(x, t)|^\nu - |G_\xi * I_1(x, t)|^\nu \right\|_{L^\infty} + C \|I\|_{L^2} \right\} \\ &\leq C(\alpha, \xi, \nu, J) \|I(t)\|_{L^2}. \end{aligned}$$

Combining the above relation with (4.36), we have (4.35). Thus, using the above estimates in (4.34), we have

$$\frac{1}{2} \|I(s)\|_{L^2}^2 + \int_0^s \|I(t)\|_{L^2}^2 dt + C \|\nabla v(0)\|_{L^2}^2 \leq C \int_0^s (\|\nabla v(t)\|_{L^2}^2 + \|I(t)\|_{L^2}^2) dt.$$

Since $\|v(0)\|_{L^2}^2 \leq T \int_0^s \|I(t)\|_{L^2}^2 dt$, we have

$$\frac{1}{2} \|I(s)\|_{L^2}^2 + \int_0^s \|I(t)\|_{L^2}^2 dt + C\|v(0)\|_{H^1}^2 \leq C \int_0^s (\|v(t)\|_{H^1}^2 + \|I(t)\|_{L^2}^2) dt. \quad (4.37)$$

Set

$$w_i(\cdot, t) = \int_0^t I_i(\cdot, \tau) d\tau; \quad w(\cdot, t) = (w_1 - w_2)(\cdot, t), \quad 0 < t \leq T.$$

Observe that

$$v(x, 0) = w(x, s) \quad \text{and} \quad v(x, t) = w(x, s) - w(x, t) \quad \text{for } 0 < t \leq s.$$

Hence (4.37) reduces to

$$\begin{aligned} & \frac{1}{2} \|I(s)\|_{L^2}^2 + \int_0^s \|I(t)\|_{L^2}^2 dt + C\|w(s)\|_{H^1}^2 \\ & \leq \tilde{C}s \|w(s)\|_{H^1}^2 + C \int_0^s (\|w(t)\|_{H^1}^2 + \|I(t)\|_{L^2}^2) dt. \end{aligned} \quad (4.38)$$

Choose T_1 sufficiently small such that $C - \tilde{C}T_1 > 0$. Then, for $0 < s \leq T_1$, we have, from (4.38),

$$\|I(s)\|_{L^2}^2 + \|w(s)\|_{H^1}^2 \leq C \int_0^s (\|w(t)\|_{H^1}^2 + \|I(t)\|_{L^2}^2) dt. \quad (4.39)$$

Consequently, an application of Gronwall's lemma then implies $I \equiv 0$ on $[0, T_1]$. Finally, we utilize a similar logic on the intervals $(T_1, 2T_1]$, $(2T_1, 3T_1]$, ... step by step, and eventually deduce that $I_1 = I_2$ on $(0, T)$. This finishes the proof of Theorem 4.1.

Lemma 4.3. *Let I be a weak solution of the model (4.15)–(4.17), and $\beta_1 := \sup_{x \in \Omega} J(x) < \infty$. Then*

$$0 < \alpha \leq I(x, t) \leq \beta_1 \quad \text{for a.e. } (x, t) \in \Omega_T. \quad (4.40)$$

Proof. Integrating the equation (4.15) w.r.t. time variable and using (4.17), we get that

$$\partial_t I + (I - J) - \int_0^t \operatorname{div}(g_I(x, s) \nabla I) ds = 0 \quad \forall (x, t) \in \Omega_T. \quad (4.41)$$

Note that, $(I - \beta)_+ \in H^1$, where $(\cdot)_+$ is the truncated function defined as $(\theta)_+ = \max\{0, \theta\}$. Multiplying the PDE (4.41) by $(I - \beta_1)_+$ and then integrating over Ω to have

$$\frac{1}{2} \frac{d}{dt} \int_{\Omega} |(I - \beta_1)_+|^2 dx + \int_{\Omega} (I - J)(I - \beta_1)_+ dx + \int_0^t \int_{\{I \geq \beta_1\}} g_I(x, s) |\nabla I|^2 dx ds = 0.$$

Observe that, $g_I \geq 0$ and $(I - J)(I - \beta_1)_+ \geq 0$. Thus, we have $\frac{d}{dt} \int_{\Omega} |(I - \beta_1)_+|^2 dx \leq 0$. Again, since $J \leq \beta_1$, we obtain $\int_{\Omega} |(I - \beta_1)_+|^2 dx \leq 0$ for a.e. $t \in [0, T]$. Therefore, $I(x, t) \leq \beta_1$ for a.e. $(x, t) \in \Omega_T$.

Similarly, multiplying the equation (4.41) with $(I - \alpha)_- \in H^1$ and then integrating over Ω to conclude that $0 < \alpha \leq I(x, t)$ for a.e. $(x, t) \in \Omega_T$, where $(\cdot)_-$ is the truncated function defined as $(\theta)_- = \min\{0, \theta\}$. Hence (4.40) holds true. This completes the proof. \square

4.4 Numerical Implementation

To solve the present model numerically, we construct an explicit finite difference scheme. Using the finite difference formulas discussed in [section 1.3](#), the discretized form of the model (4.15) could be written as

$$(1 + \gamma\tau)I_{i,j}^{n+1} = (2 + \gamma\tau)I_{i,j}^n - I_{i,j}^{n-1} + \tau^2 \left\{ \nabla_x (g_{i,j}^n \nabla_x I_{i,j}^n) + \nabla_y (g_{i,j}^n \nabla_y I_{i,j}^n) \right\},$$

where

$$g_{i,j}^n = b(s_{i,j}^n) \cdot \frac{1}{1 + \left(\frac{|\nabla G_{\xi} * I_{i,j}^n|}{K} \right)^2},$$

with the initial conditions $I_{i,j}^0 = J_{i,j} = J(x_i, y_j)$, $I_{i,j}^1 = I_{i,j}^0$, $0 \leq i \leq M - 1$, $0 \leq j \leq N - 1$, and the boundary conditions as discussed in [section 1.3](#).

4.5 Computational Experiments

This section displayed the performance of the present model in terms of visual quality and quantitative results. We compare the despeckling result of the proposed model using three standard test images corrupted by different levels of speckle noise. We have artificially generated speckle noise with “looks” $L = \{1, 3, 5, 10, 33\}$ using MATLAB built-in gamma random noise generator function “gamrnd” as $\eta = \text{gamrnd}(L, 1/L, M, N)$ and then multiply with the ground truth images in

[Figure 4.1](#), where $M \times N$ is the image dimensions. All the numerical tests are performed under Windows 7 and MATLAB version *R2018b* running on a desktop computer with an Intel Core i5 dual-core CPU at 2.53 GHz with 4 GB of RAM. Image denoising results using the present model have been compared with the results of DDD model [\(4.2\)–\(4.4\)](#), ZZDB model [\(4.5\)–\(4.7\)](#), and Shan model [\(4.8\)–\(4.10\)](#). Apart from the artificially noisy images, we test our model on some real SAR images corrupted with different levels of speckle noise. In this process, the considered existing models are discretized using the same explicit numerical scheme used to discretize the proposed model. However, the numerical stability requirement for the explicit scheme is $\tau \leq h/\sqrt{\max g(x,t)}$ according to CFL stability criterion ([Li, 2009](#); [Zauderer, 2011](#); [Zhang et al., 2014](#)), where h denotes the length of the spatial intervals. We choose uniform time step sizes $\tau = 0.2$ and $\xi = 1$ for numerical experiments. In [Figure 4.2](#), we presented the restored results of a circle image using different choices of τ . From the results, it can be concluded that for smaller values of τ , numerical simulation takes more CPU time to achieve the optimal results, and for larger values of τ , the quality of the restored images diminishes gradually. On the other hand, for $\tau = 0.2$, qualitative and quantitative measures are exhibiting optimum results. The existing literature ([Cao et al., 2010](#); [Zeng et al., 2011](#); [Sun et al., 2016](#)) also has used $\tau \geq 0.2$ in their computations. Therefore, $\tau = 0.2$ seems to be a good choice for the numerical simulations.

4.5.1 Image Quality Measurement

Since the proposed model is claimed to be an improvement over the existing diffusion models, our main aim is to compare the edge detection and denoising results, in terms of both qualitative and quantitative measures. For each experiment, we compute the values of the parameters PSNR and MSSIM for the quantitative comparison with the other existing models. Also, to test the noise removal capability on real SAR images, we compute the SI for the restored image. Other typical qualitative measures have also been computed in terms of the ratio image, 2D contour plot, and 3D surface plot for the better visualization of the computational result for the proposed model as well as for the other discussed models.

4.5.2 Computational Results & Discussion

In Figures [4.3](#)–[4.5](#), we present the restored results of a boat image (Natural Image), which is contaminated by multiplicative speckle noise with $L = \{1, 3, 5\}$. From the quality of the reconstructed images, it is easy to perceive that the results computed

by the present model are more apparent than the results of the other discussed models.

In Figures 4.6–4.8, we describe the reconstructed results of a brick image (Texture Image), which is corrupted by speckle noise with $L = \{1, 3, 5\}$. From the figures, it is easy to see that the results computed by the present model are more apparent as well as less blurry than the results of other models, especially for the high noise level.

To check further the reconstruction capability of the present model, we illustrate the qualitative results of a circle image (Synthetic Image) which is corrupted by speckle noise with $L = \{1, 3, 5, 10\}$; see Figures 4.9–4.14. In the Figures 4.9–4.11, we demonstrate the despeckling images by the present model and the other discussed models when the image is corrupted by the noise level $L = \{1, 3, 5\}$. From these figures, we easily visualize the performance of the present model.

In Figure 4.12, we present the restored image along with their ratio image for a better comparison of the qualitative result. From the Figures 4.12b–4.12e, it can be easily concluded that the present model gives better results in terms of image despeckling than the other discussed models. Figure 4.12f represents the ratio image for the clear circle image Figure 4.1c and indicate that it has no background information. Now from the Figures 4.12g–4.12j, we can see that ratio image corresponding to the present model has very less background information which confirms that the present model works better in terms of edge preservation than the other models.

To visualize more on the noise removal ability, in Figures 4.13–4.14, we illustrate the contour maps and 3D surface plots corresponding to the clear circle image Figure 4.1c and for the images in Figures 4.12a–4.12e. One can easily observe that from the contour maps, and 3D surface plots, discussed existing models left some speckles in the homogeneous regions, but the present model produces fewer artifacts with better edge preservation.

Along with the qualitative comparison, the quantitative results in terms of PSNR and MSSIM values and CPU time (in seconds) are displayed in the Table 4.1 and corresponding parameter values for the numerical experiments are given in the Table 4.2. The highest values of PSNR and MSSIM for each noise level clearly shows that the suggested model is better than the other discussed models. Although the present method takes relatively more time in some cases to achieve the best despeckling results, the overall performance is more effective than the other three techniques.

Apart from the results for artificially noisy images, in Figure 4.15, we dis-

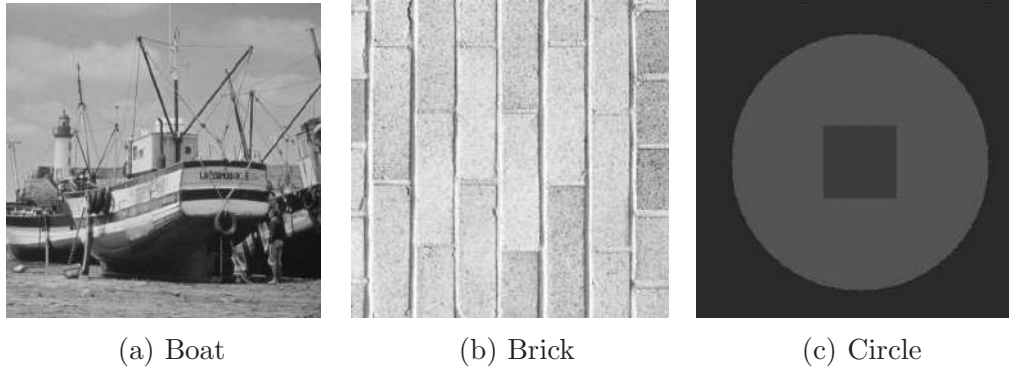


Figure 4.1: Clear test images.

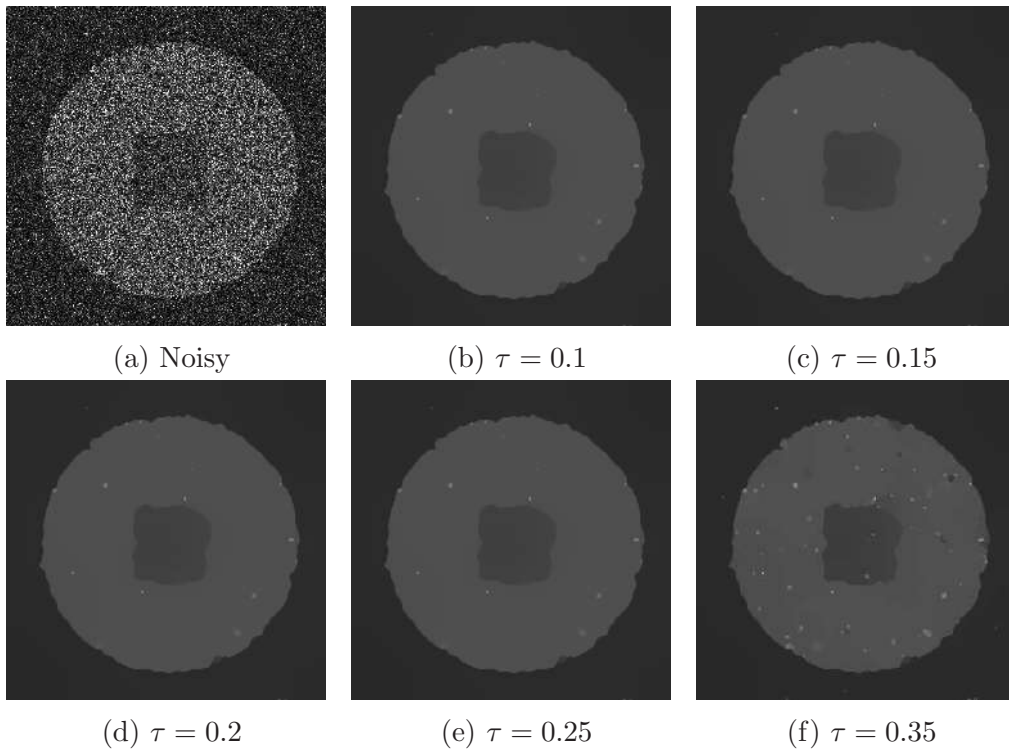


Figure 4.2: Restored image for different values of τ : $K = 0.5$, $\nu = 1$, and $\gamma = 0.5$. (a) Noisy image with $L = 1$. (b) MSSIM=0.96441, PSNR=34.6963, CPU time=69.8468s. (c) MSSIM=0.96441, PSNR=34.6963, CPU time=46.832s. (d) MSSIM=0.96441, PSNR=34.6960, CPU time =32.4649s. (e) MSSIM=0.96439, PSNR=34.6959, CPU time=27.48s. (f) MSSIM=0.94058, PSNR=33.8212, CPU time=15.3603s.

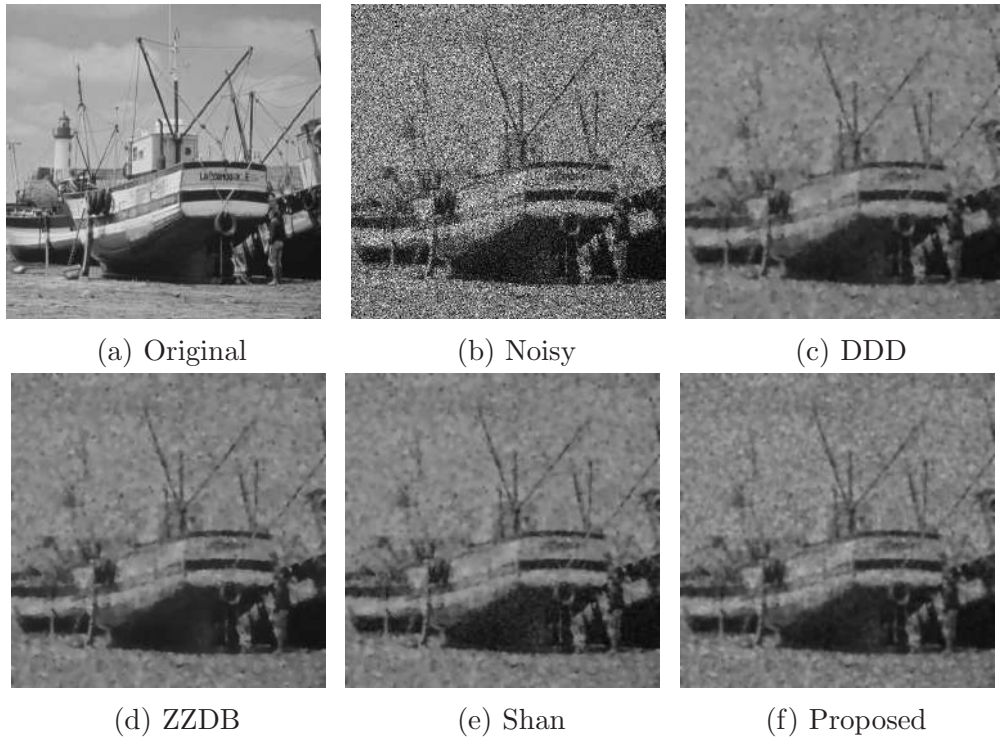


Figure 4.3: Image corrupted by speckle noise with $L = 1$ and restored by different models.

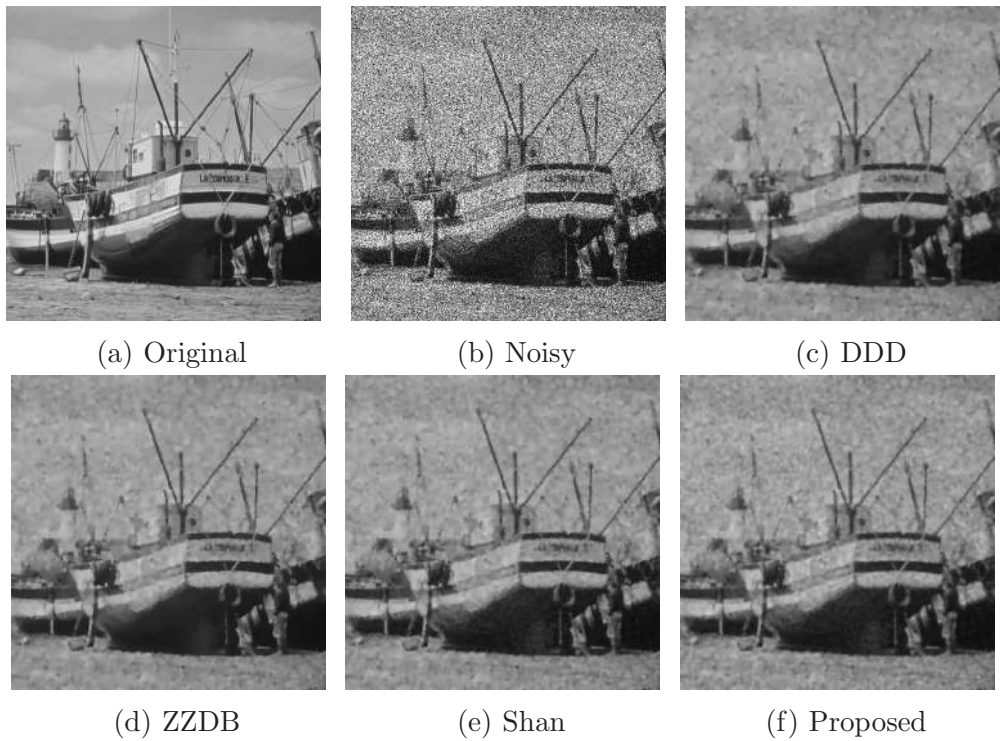


Figure 4.4: Image corrupted by speckle noise with $L = 3$ and restored by different models.

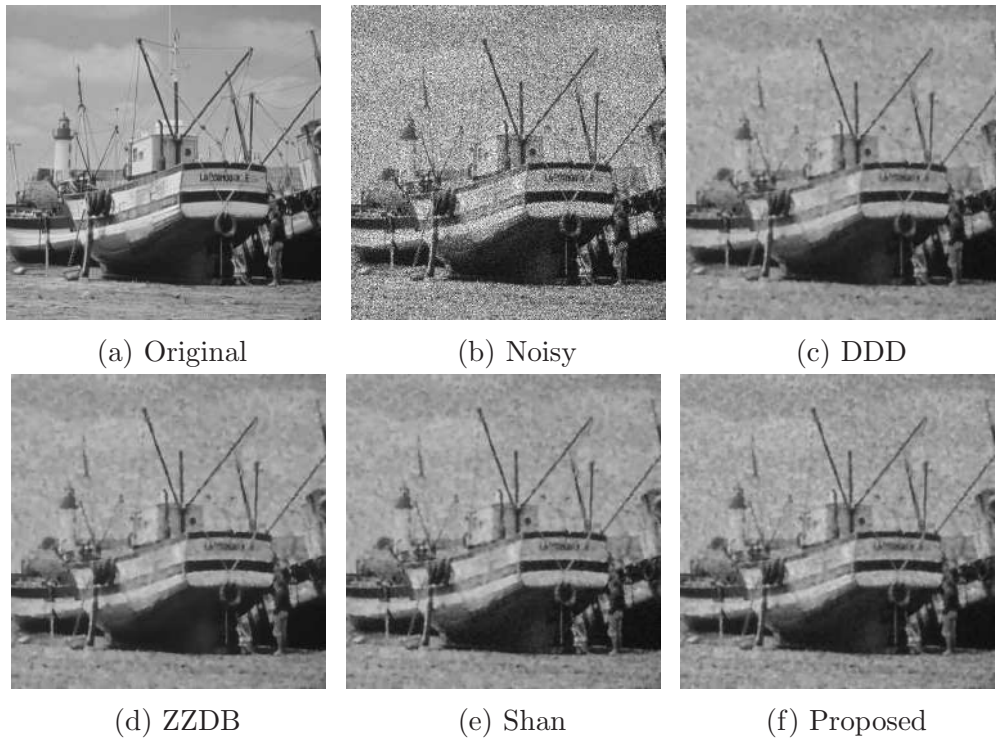


Figure 4.5: Image corrupted by speckle noise with $L = 5$ and restored by different models.

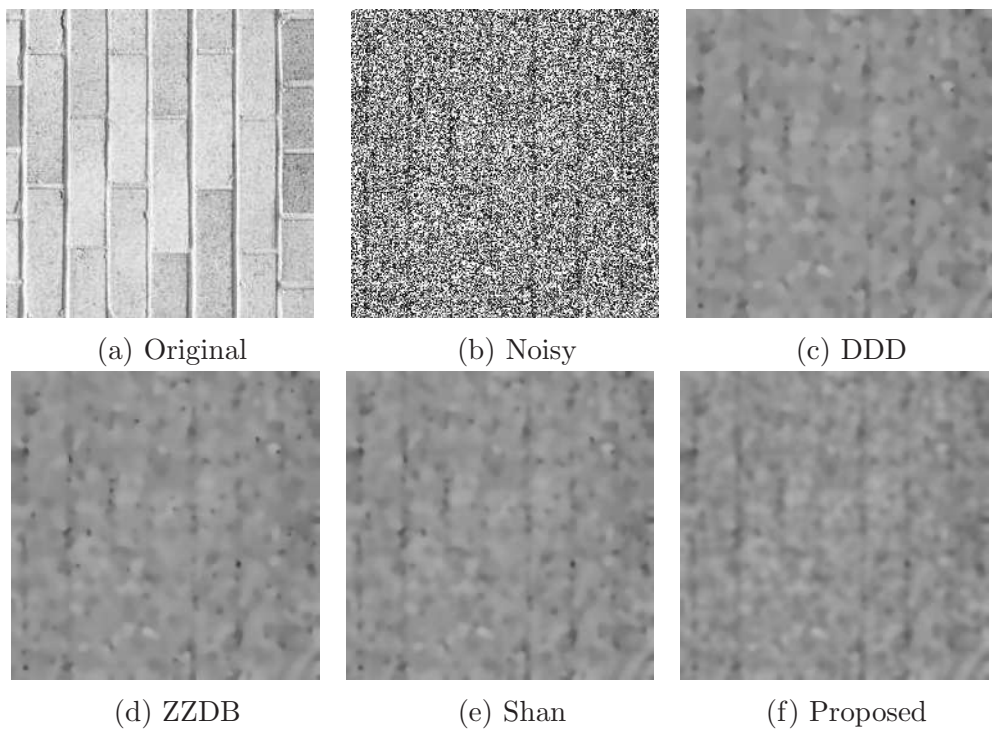


Figure 4.6: Image corrupted by speckle noise with $L = 1$ and restored by different models.

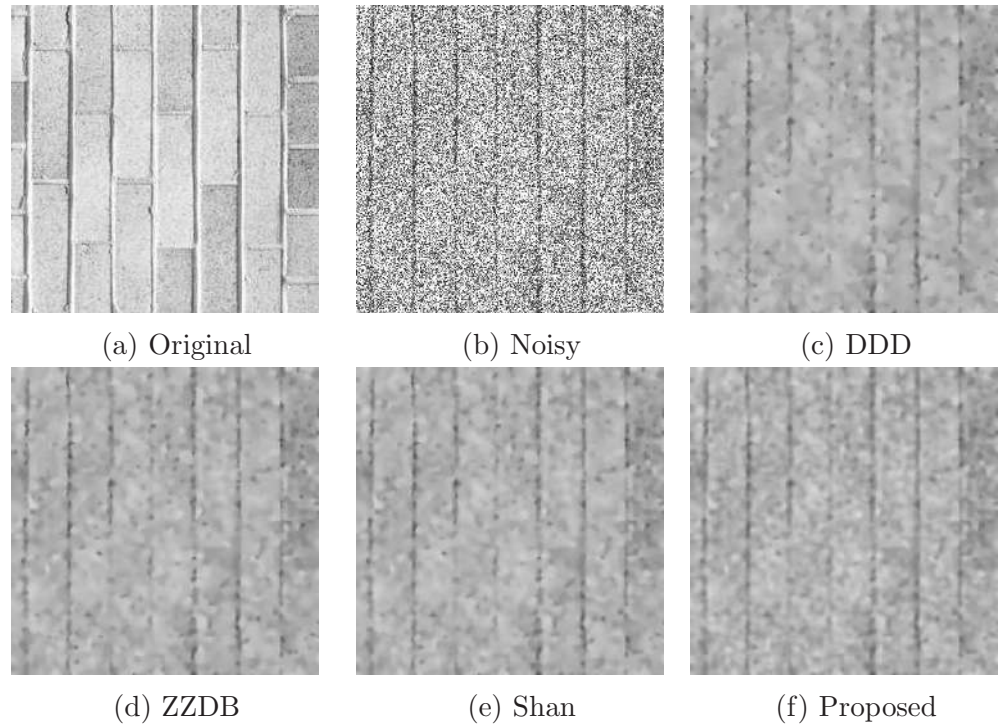


Figure 4.7: Image corrupted by speckle noise with $L = 3$ and restored by different models.

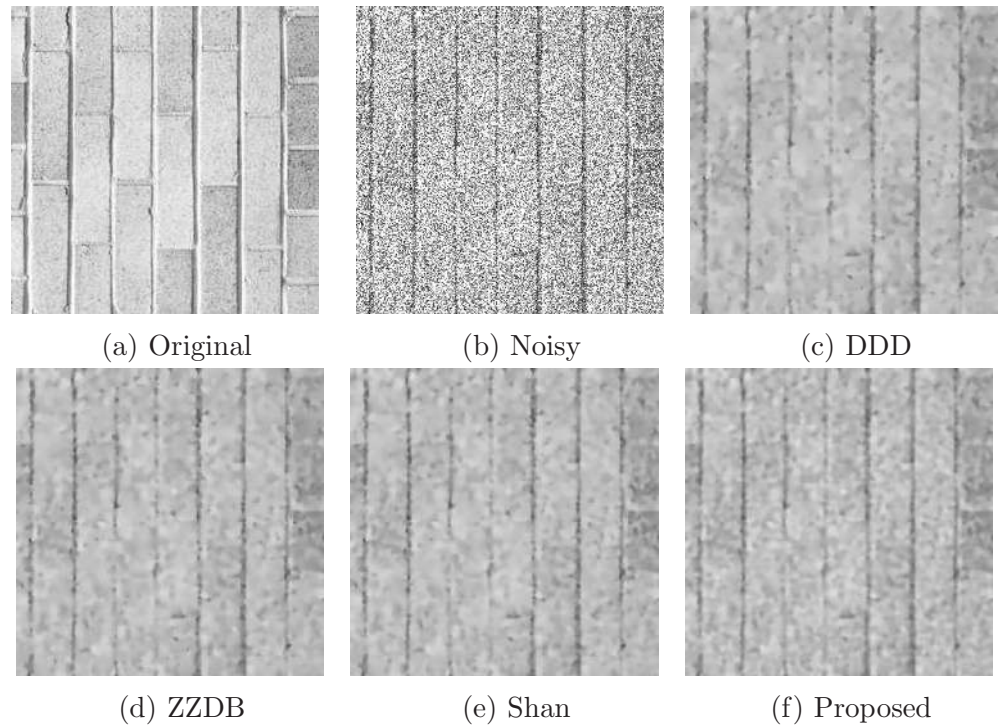


Figure 4.8: Image corrupted by speckle noise with $L = 5$ and restored by different models.

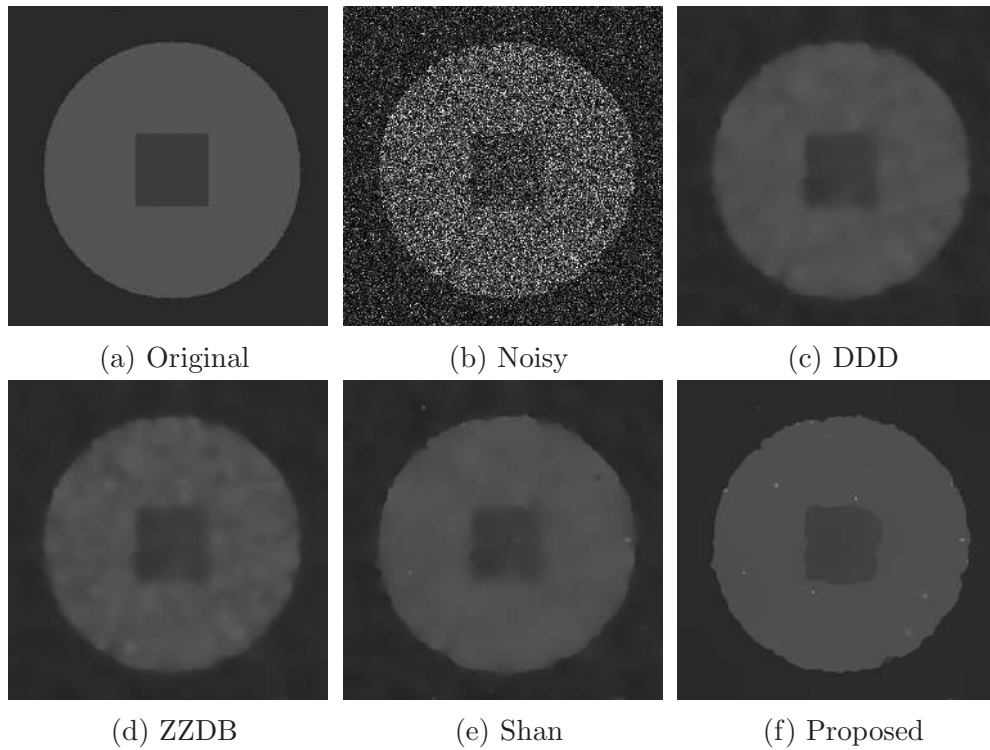


Figure 4.9: Image corrupted by speckle noise with $L = 1$ and restored by different models.

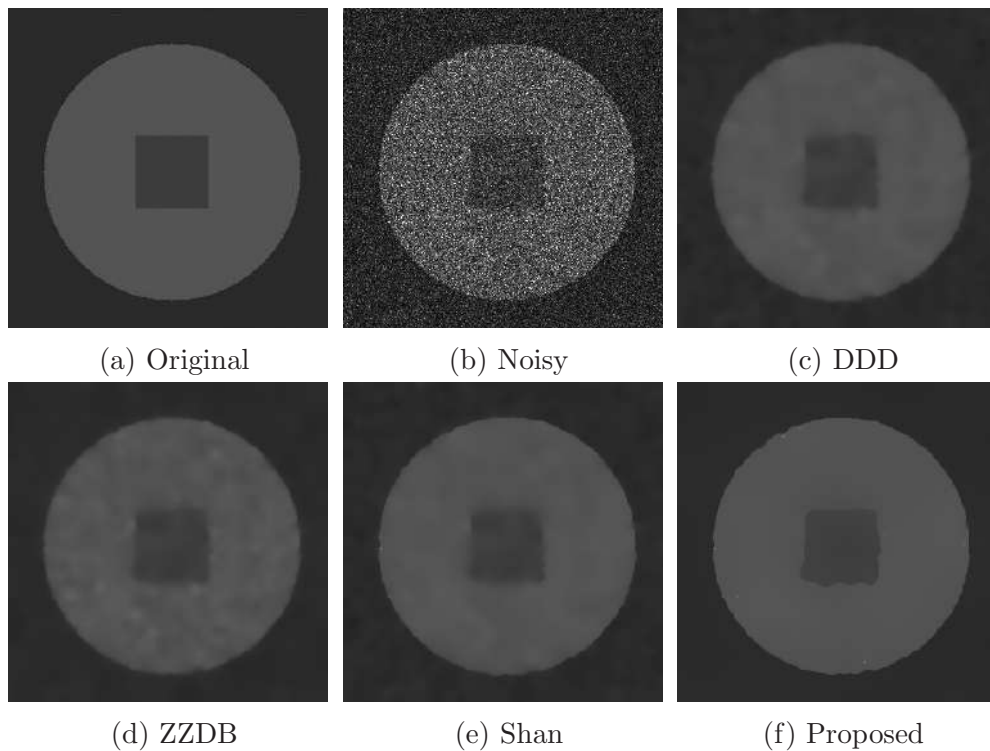


Figure 4.10: Image corrupted by speckle noise with $L = 3$ and restored by different models.

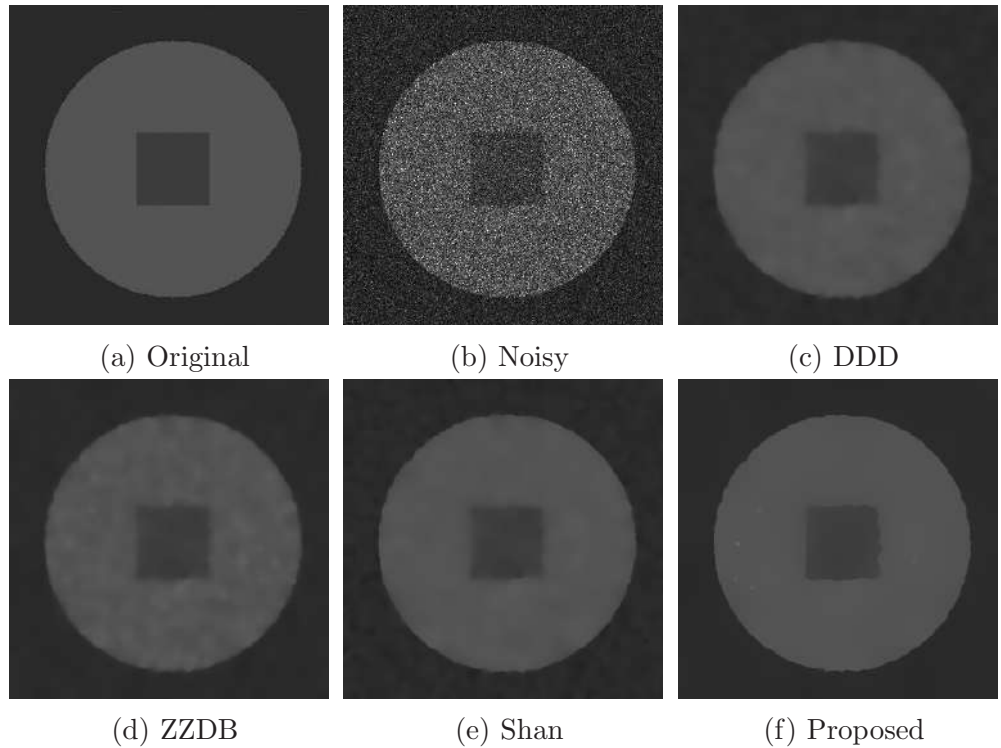


Figure 4.11: Image corrupted by speckle noise with $L = 5$ and restored by different models.

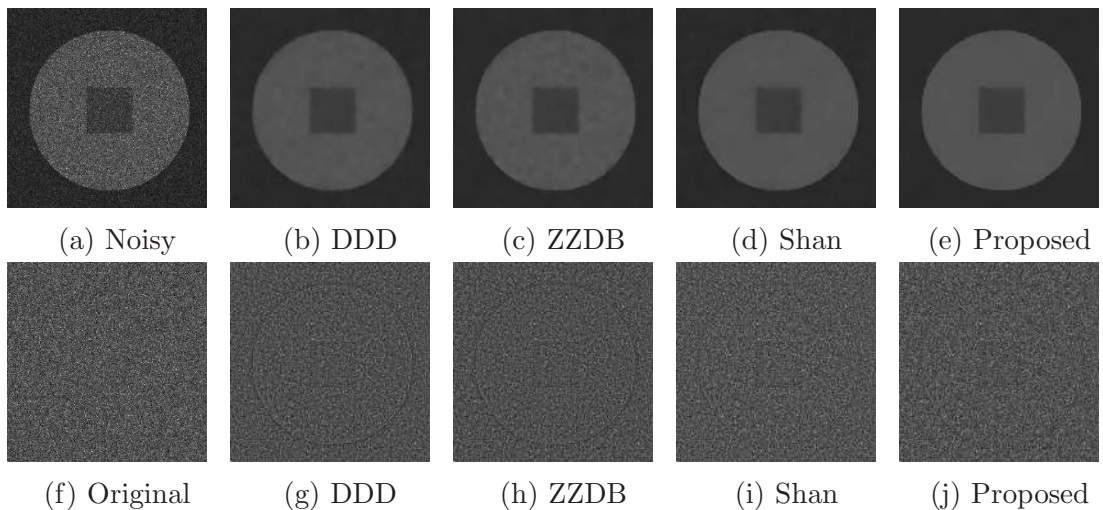


Figure 4.12: First row: (a) Image corrupted by speckle noise with $L = 10$. (b)–(e) Restored images by different models. Second row: (f) Ratio image for the clear image Figure 4.1c, (g)–(j) Ratio images for the restored images Figures 4.12b–4.12e.

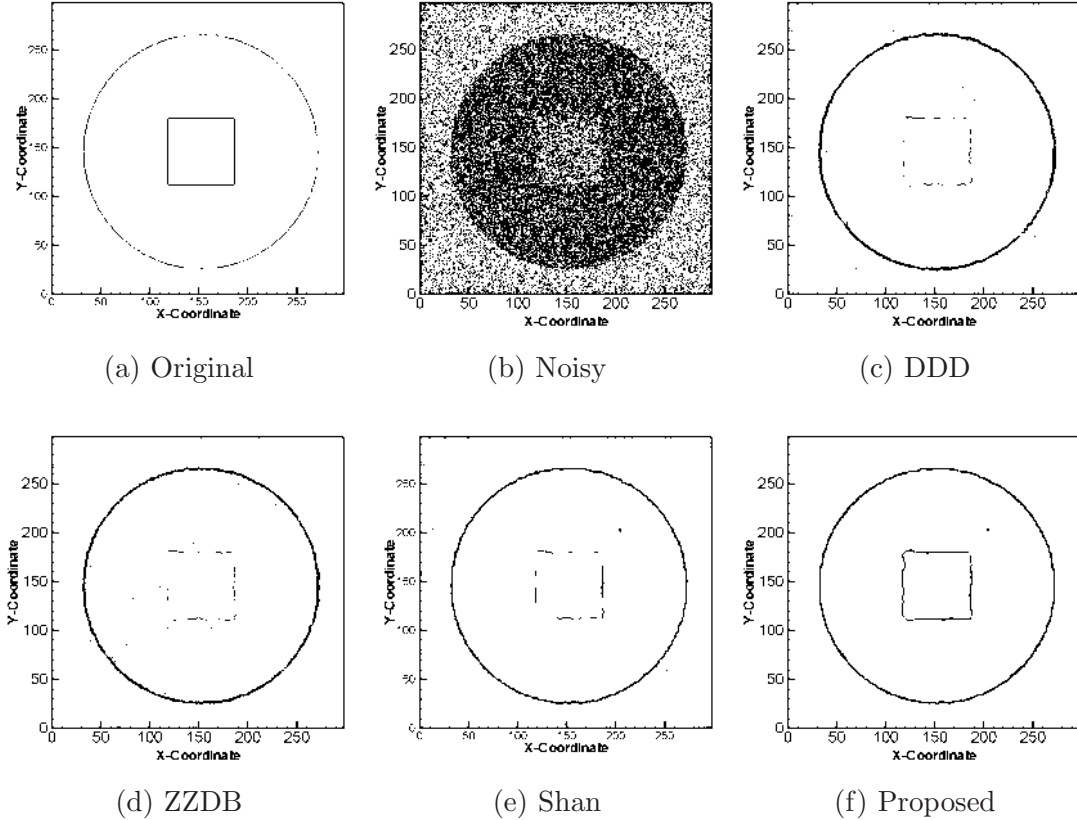


Figure 4.13: Contour maps of the clear circle image Figure 4.1c and the images Figure 4.12a–4.12e.

Table 4.1: MSSIM and PSNR values of despeckled images.

Image	L	DDD			ZZDB			Shan			Proposed		
		MSSIM	PSNR	Time(s)	MSSIM	PSNR	Time(s)	MSSIM	PSNR	Time(s)	MSSIM	PSNR	Time(s)
Boat	1	0.5508	16.93	51.38	0.5710	16.99	23.12	0.5975	17.10	26.23	0.6096	17.12	46.73
	3	0.6805	22.21	40.22	0.6815	22.31	18.45	0.7087	22.71	16.17	0.7347	22.85	15.22
	5	0.7204	24.05	32.88	0.7208	24.15	15.20	0.7508	24.43	15.51	0.7905	24.93	13.26
	10	0.7729	26.10	21.83	0.7743	26.22	11.62	0.8325	26.98	14.12	0.8422	27.12	8.76
	33	0.8468	28.65	11.05	0.8496	28.70	6.63	0.8941	29.57	7.45	0.9057	29.72	5.15
Brick	1	0.2872	12.13	9.10	0.2885	12.15	6.56	0.2930	12.17	5.98	0.2954	12.19	10.02
	3	0.3645	16.87	7.88	0.3651	16.88	3.37	0.3837	17.08	3.31	0.3861	17.11	8.26
	5	0.4174	18.60	6.17	0.4177	18.64	2.77	0.4291	19.34	2.74	0.4355	19.40	6.61
	10	0.4873	21.08	3.97	0.4876	21.14	2.07	0.4947	22.06	2.15	0.4960	22.18	3.32
	33	0.5920	24.74	1.89	0.5930	24.78	1.98	0.5943	25.40	1.12	0.5961	25.53	1.02
Circle	1	0.9457	33.68	19.21	0.9500	33.80	22.38	0.9582	34.30	59.06	0.9644	34.70	32.46
	3	0.9571	36.71	17.42	0.9602	36.86	12.73	0.9735	38.10	29.51	0.9770	39.43	11.76
	5	0.9616	37.63	13.86	0.9635	37.75	10.49	0.9765	39.36	28.58	0.9804	40.71	9.73
	10	0.9728	39.43	8.77	0.9733	39.54	6.22	0.9817	41.26	16.40	0.9865	42.85	5.72
	33	0.9795	41.72	3.74	0.9801	41.86	2.83	0.9870	43.64	6.38	0.9889	44.62	2.39

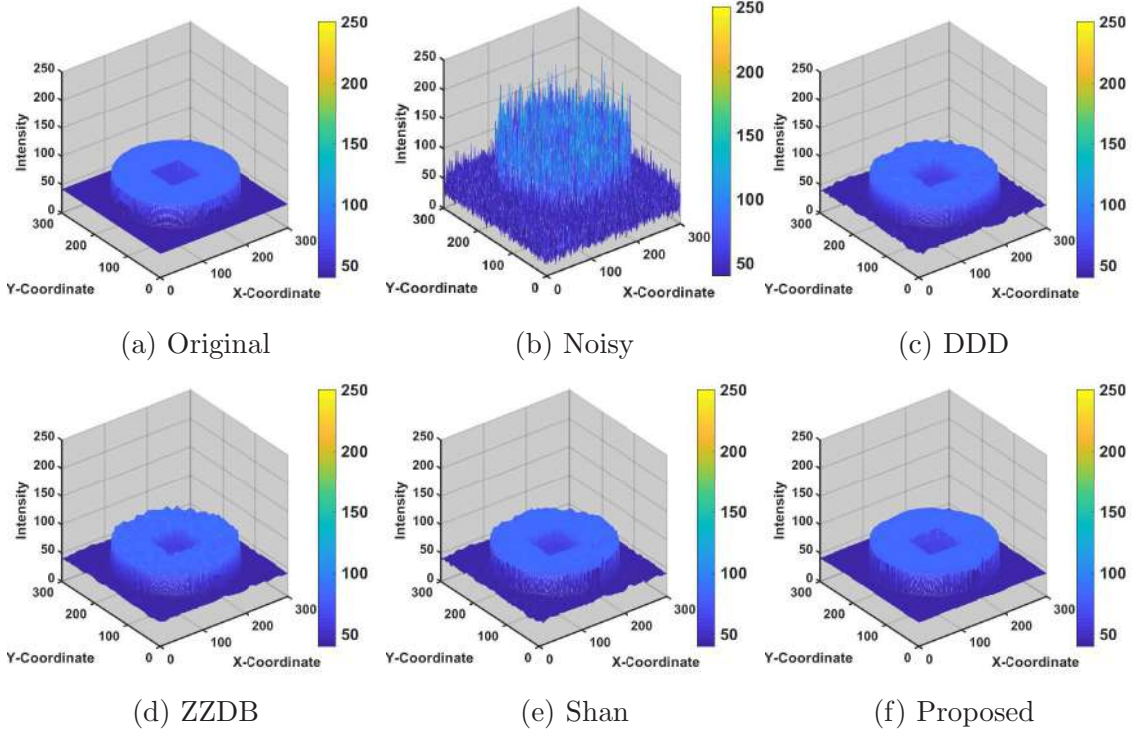


Figure 4.14: 3D surface plots of the clear circle image Figure 4.1c and the images Figure 4.12a–4.12e.

Table 4.2: Parameter values for the numerical experiments.

Image	L	DDD		ZZDB		Shan		Proposed		
		α	β	α	α	β	γ	ν	K	
Boat	1	1	0.01	1	1	1	5	1	2	
	3	1.1	0.02	1.2	1.2	1	4	1.5	2	
	5	1.2	0.03	1.3	1.3	1	2	1.5	1	
	10	1.5	0.08	1.4	1.4	1.2	2	2	1	
	33	2	0.1	1.5	1.5	1.5	2	3	1	
Brick	1	1	0.01	1	1	1	5	1	4	
	3	1.2	0.01	1.2	1.2	1	4	1.3	3	
	5	1.4	0.02	1.3	1.4	1	2	1.5	2	
	10	1.5	0.06	1.4	1.6	1	2	2	1	
	33	2	0.1	1.5	1.7	1	2	3	1	
Circle	1	1	0.01	2	1.5	2	0.5	1	0.5	
	3	1.5	0.01	2	1.5	2	1	1	0.8	
	5	1.5	0.01	2	2	2.25	1.8	1	1	
	10	1.5	0.01	2	2	2.25	2	1	1	
	33	2	0.01	2	2	2.5	2	1	1	

Table 4.3: SI values for the real SAR images using the proposed model.

Image	Noise-Level	Parameter			SI (Initial)	SI (Restored)
		γ	ν	K		
Figures 4.15a–4.15b	Multilook	5	2	4	0.4157	0.3046
Figures 4.15c–4.15d	Multilook	5	2	2	1.02	0.4022
Figures 4.15e–4.15f	Multilook	5	2	2	0.92	0.4857
Figures 4.15g–4.15h	Single-look	3	3	4	0.6394	0.4132

play the restored results for the four different real SAR images: (i) Space Radar Image of Kilauea, Hawaii ([JPL, 1994](#)), in Figures 4.15a–4.15b, (ii) SAR image of KOMPSAT/Arirang-5 of a portion of the Himalayan Arc ([eoPortal: Sharing Earth Observation Resources, 2005](#)), in Figures 4.15c–4.15d, (iii) High-resolution SAR image of Prague, Czech Republic ([eoPortal: Sharing Earth Observation Resources, 2005](#)), in Figures 4.15e–4.15f, (iv) One look radar image ([Agency, n.d.](#)), in Figures 4.15g–4.15h. Observing the restored images, one can conclude that the results seem to be well recovered with efficient shape and edge preservation. Along with the qualitative results the quantitative results in terms of speckle index values are displayed in the [Table 4.3](#).

4.6 Conclusion

This work proposes a telegraph diffusion model for image despeckling. Such a new method intends to preserve the image edges during the noise removal process. To overcome the limitations of gradient-based despeckling models as well as parabolic PDE based models, we consider a hybrid approach which combines a gray level indicator function with gradient-based diffusion in a telegraph diffusion framework for image despeckling. To the best of our knowledge, the gray level indicator-based telegraph diffusion model has not been used before for speckle noise suppression. Also, we prove the existence and uniqueness of weak solutions of the suggested model. Moreover, we prove the boundedness of the weak solution. Numerical experiments are performed to highlight the efficiency of the proposed model for image despeckling using different types of test images. Computational results of the present model, compared with the results of three recently developed models, indicate that the images are suitably recovered without introducing undesired artifacts. A potential direction that the telegraph diffusion model can be extended to handle texture preservation issues in various real-life images, which are degraded by mixed noises. We show the speckle noise removal capability of the present model on four different SAR images.

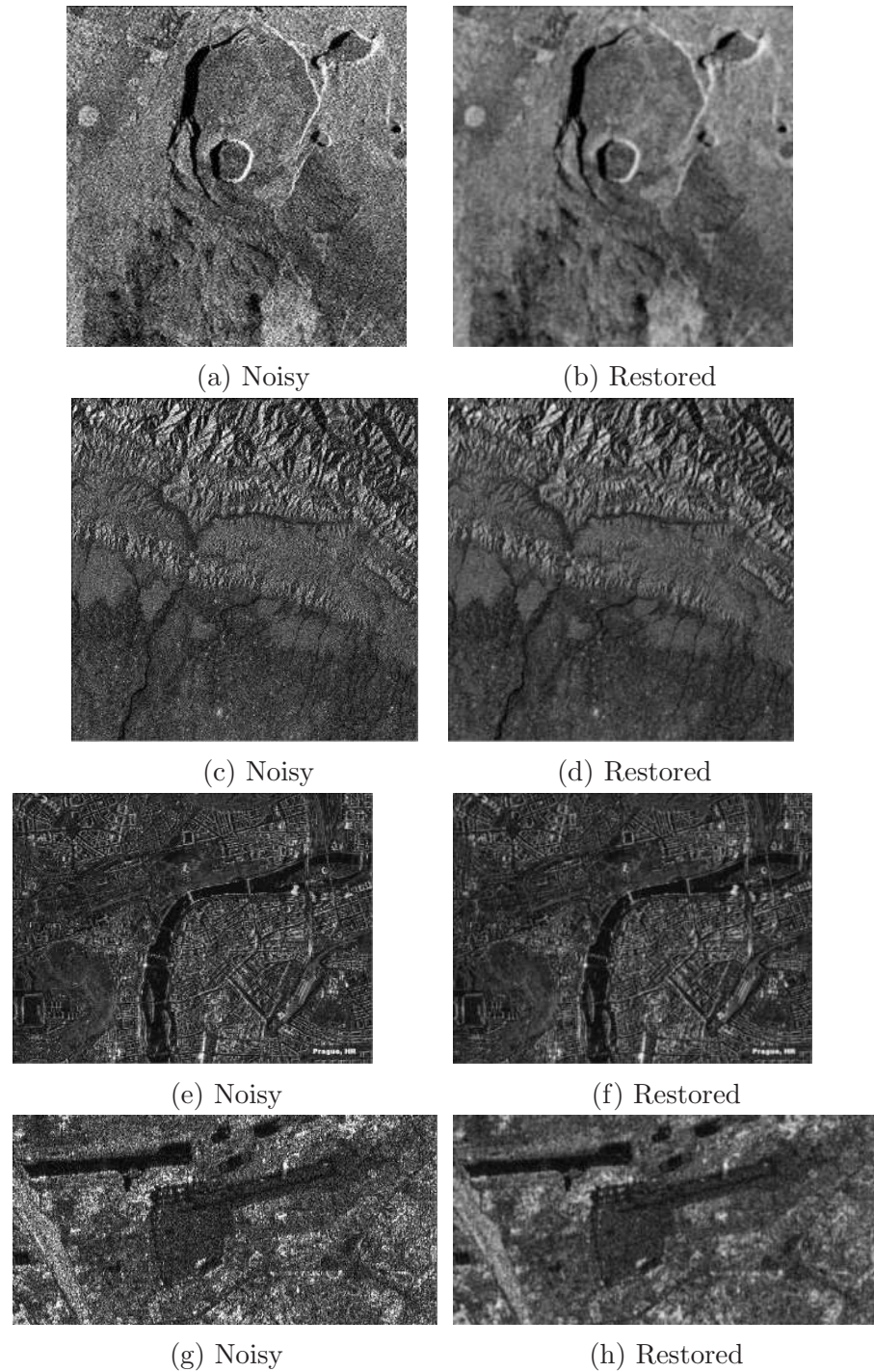


Figure 4.15: Real SAR images and restored images using the proposed model.

Chapter 5

An Efficient Nonlinear Hyperbolic-Parabolic Coupled PDE model for Image Despeckling

In this chapter, we extend the work explained in the previous chapter. In the last chapter, we have used a single hyperbolic-parabolic PDE model for image despeckling. Here, a separate equation is used to calculate the edge variable, which injects the past information of the edge variable into the diffusion process. Moreover, we prove the existence and uniqueness of a weak solution of the present model. Computed results are reported to show the effectiveness of the present approach over recently developed PDE based techniques.

5.1 General Introduction

Over the last two decades, nonlinear PDEs are extensively used to develop speckle-noise reduction models. Most popular PDE based approaches are nonlinear diffusion based methods ([Jin et al., 2000](#); [Yu and Acton, 2002](#); [Zhou et al., 2015, 2018](#); [Shan et al., 2019](#); [Jain and Ray, 2019](#)), and variational based methods ([Rudin et al., 2003](#); [Aubert and Aujol, 2008](#); [Shi and Osher, 2008](#); [Huang et al., 2010](#); [Jin and Yang, 2010, 2011](#); [Dong et al., 2013](#); [Jidesh and Bini, 2013](#); [Liu et al., 2013](#)). Most of the above models take the generalized form

$$\partial_t I = \operatorname{div}(g(x, t) \nabla I) + \lambda f(J, I) \quad \text{in } \Omega_T, \quad (5.1)$$

with the appropriate initial and boundary conditions. In (5.1), λ is a weighted parameter, the source term $f(J, I)$ is derived from the variational based approach

(Rudin *et al.*, 2003; Aubert and Aujol, 2008; Jin and Yang, 2011; Dong *et al.*, 2013), and $g(x, t)$ signifies the degree of denoising which preserves the image characteristics, e.g., textures and edges in the noise removal process. One can note that the above discussed PDE based models are parabolic type. Recently, Majee, Ray and Majee (2020) suggest the hyperbolic-parabolic PDE based model (the TDM model) (4.15)–(4.17) for image despeckling. When images are affected by very high-level speckle noise, the proper elimination of noise and preservation of the texture information in the images can be considered as a very challenging task. The parabolic PDE based restoration models depend entirely on the diffusion function $g(\cdot)$, to preserve the small variations in the images. In the single PDE based approaches, spatial regularization is enjoyed, for the diffusion coefficient, which cannot introduce the past knowledge into the diffusion process. To overcome these issues, in the present work, we propose a nonlinear coupled hyperbolic-parabolic model to deal with the speckle noise removal problem. Moreover, due to the interest in theoretical study, we establish the well-posedness of the proposed model in an appropriate function space. For simulation purpose, we opt an implicit numerical method to solve the present model and then apply it on different types of gray level images. To ensure the ability of the present model, a comparative study of the quality of the recovered image is carried out with recently developed models (Jain *et al.*, 2018; Shan *et al.*, 2019; Majee, Ray and Majee, 2020). Present model shows an exciting performance on image despeckling.

The rest of this chapter is organized as follows. In section 5.2 we demonstrate the proposed nonlinear coupled hyperbolic-parabolic model. In section 5.3, we study the well-posedness of the model. Section 5.4 describes the numerical implementation and despeckling ability of the present system. We conclude the work in Section 5.5.

5.2 The Proposed Method

To the best of our knowledge, most of the PDE based models for speckle noise removal are single and parabolic types. Inspired by the ideas of (Jain *et al.*, 2018) and (Majee, Ray and Majee, 2020), we propose the following improved nonlinear

hyperbolic-parabolic coupled PDE (HPCPDE) model

$$\partial_{tt}I + \gamma\partial_t I - \operatorname{div}\left(\frac{s^\alpha}{1+s^\alpha}\frac{1}{1+\iota|u_\xi|^\beta}\nabla I\right) = 0 \quad \text{in } \Omega_T, \quad (5.2)$$

$$\partial_t u = h(|\nabla I_\xi|) - u + \frac{\nu^2}{2}\Delta u \quad \text{in } \Omega_T, \quad (5.3)$$

$$\begin{cases} I(x, 0) = J(x), \partial_t I(x, 0) = 0, u(x, 0) = G_\xi * |\nabla J|^2 & \text{in } \Omega, \\ \partial_n I = 0 = \partial_n u & \text{on } \partial\Omega_T, \end{cases} \quad (5.4)$$

with $s := \frac{|I_\xi|}{M_\xi^T} \in [0, 1]$. In the above, J is the observed noisy image, $\alpha \geq 1$, $\beta \geq 1$, $\gamma > 0$, $\nu > 0$, and $\iota > 0$ are constants. $h : \mathbb{R}^+ \rightarrow \mathbb{R}^+$ is a bounded, Lipschitz continuous function. Moreover, u represents the edge strength at each scale. Here we utilize an extra equation to calculate the edge variable, which injects the past information into the diffusion process. To the best of our knowledge, the proposed despeckling model is the first work which utilizes the advantage of the nonlinear coupled hyperbolic-parabolic model for image despeckling.

5.3 Existence and Uniqueness of Weak Solution

This section is devoted to the wellposedness result of the proposed model (5.2)–(5.4). Due to the nonlinearity in the system, we first consider the associated linearized model and then use Schauder fixed point theorem (Evans, 1998) to complete the proof.

5.3.1 Technical framework & statement of the main result

Without loss of generality, we assume that $\gamma = 1$, $\iota = 1$, and $\nu = 1$ in the equations (5.2) and (5.3). Throughout this section, C denotes a generic positive constant and we write L^p , H^1 , $(H^1)'$ instead of $L^p(\Omega)$, $H^1(\Omega)$, $(H^1(\Omega))'$, respectively. We consider the solution space $W(0, T)$ for the proposed model (5.2)–(5.4) as $W(0, T) = W_1(0, T) \times W_2(0, T)$, where

$$\begin{aligned} W_1(0, T) &= \left\{ w \in L^\infty(0, T; H^1), \partial_t w \in L^\infty(0, T; L^2); \partial_{tt} w \in L^2(0, T; (H^1)') \right\}, \\ W_2(0, T) &= \left\{ w : w \in L^\infty(0, T; H^1); \partial_t w \in L^\infty(0, T; L^2) \right\}. \end{aligned}$$

Definition 5.1 (Weak solution). *A pair (I, u) is said to be a weak solution of (5.2)–(5.4), if*

- a) $I \in W_1(0, T)$, $u \in W_2(0, T)$ and (5.4) holds.

b) For all $\phi \in H^1$ and a.e. $t \in (0, T)$, there hold

$$\begin{aligned} \langle \partial_{tt} I, \phi \rangle + \int_{\Omega} \partial_t I \phi \, dx + \int_{\Omega} \frac{s^\alpha}{1+s^\alpha} \frac{1}{1+|u_\xi|^\beta} \nabla I \cdot \nabla \phi \, dx &= 0, \\ \int_{\Omega} \partial_t \phi \, dx + \frac{1}{2} \int_{\Omega} \nabla u \cdot \nabla \phi \, dx + \int_{\Omega} u \phi \, dx &= \int_{\Omega} h(|\nabla I_\xi|) \phi \, dx. \end{aligned}$$

Theorem 5.1. *The system (5.2)–(5.4) admits a unique weak solution $(I, u) \in W$ in the sense of Definition 5.1, provided the following two conditions hold:*

A.1 $J \in H^2$ satisfying $0 < \rho := \inf_{x \in \Omega} J(x)$.

A.2 $h : \mathbb{R}^+ \rightarrow \mathbb{R}^+$ is a bounded, Lipschitz continuous function with Lipschitz constant c_h such that

$$0 \leq h(\tilde{u}) \leq 1 \quad \forall \tilde{u} \in \mathbb{R}^+.$$

5.3.2 Linearized model & its wellposedness

For any positive constants $M_1, M_2 > 0$, define the convex set

$$\mathcal{B}_{M_1, M_2} = \begin{cases} \bar{I} \in W_1(0, T) : & \|\bar{I}\|_{L^\infty(0, T; H^1)} + \|\partial_t \bar{I}\|_{L^\infty(0, T; L^2)} \leq M_1 \|J\|_{H^1}, \\ 0 < \rho \leq \bar{I}(x, t) & \text{for a.e. } (x, t) \in \Omega_T, \\ \bar{u} \in W_2(0, T) : & \|\bar{u}\|_{L^\infty(0, T; L^2)} + \|\partial_t \bar{u}\|_{L^\infty(0, T; L^2)} \leq M_2 \|J\|_{L^2}. \end{cases}$$

For any fixed $(\bar{I}, \bar{u}) \in \mathcal{B}_{M_1, M_2}$, consider the linearized model:

$$\partial_{tt} I + \partial_t I - \operatorname{div}(\bar{g}(x, t) \nabla I) = 0 \quad \text{in } \Omega_T, \quad (5.5)$$

$$\partial_t u = h(|\nabla \bar{I}_\xi|) - u + \frac{1}{2} \Delta u \quad \text{in } \Omega_T, \quad (5.6)$$

with the condition (5.4), where the function \bar{g} is given by

$$\bar{g}(x, t) \equiv g_{\bar{I}, \bar{u}}(x, t) := \frac{|\bar{I}_\xi|^\alpha}{(M_\xi^{\bar{I}})^\alpha + |\bar{I}_\xi|^\alpha} \cdot \frac{1}{1+|\bar{u}_\xi|^\beta}.$$

Since $(\bar{I}, \bar{u}) \in \mathcal{B}_{M_1, M_2}$, a similar argument as in the proof of [Chapter 4, Claim 4.3.1] revels that

- i) $0 < \kappa \leq \bar{g} \leq 1$,
 - ii) $|\partial_t \bar{g}| \leq C$,
- (5.7)

where $\kappa, C > 0$ are constants depending only on $G_\xi, J, M_1, M_2, \beta, \alpha$, and ρ . Hence, thanks to the classical Galerkin method (Evans, 1998), one can show that there exists a unique weak solution $(I, u) \in W(0, T)$ of the linearized model (5.5)–(5.6) with the initial and boundary conditions (5.4).

Lemma 5.2. *The unique solution $(I, u) \in W(0, T)$ of the linearized model (5.5)–(5.6) with the conditions (5.4) satisfies the following:*

$$(a) \|I\|_{L^\infty(0,T;H^1)} + \|\partial_t I\|_{L^\infty(0,T;L^2)} \leq C\|J\|_{H^1},$$

$$(b) \int_0^T \|\partial_{tt} I\|_{(H^1)'}^2 dt \leq CT\|J\|_{H^1}^2,$$

$$(c) \|u\|_{L^\infty(0,T;H^1)} + \|\partial_t u\|_{L^\infty(0,T;L^2)} \leq C\|J\|_{H^1},$$

where $C > 0$ is a constant, depends only on $G_\xi, J, h, M_1, M_2, \alpha, \beta$, and ρ .

Proof. Since $\|\partial_t \bar{u}\|_{L^\infty(0,T;L^2)} \leq C\|J\|_{H^1}$, by following computations as in [Chapter 4, Lemma 4.2], one can show the validation of the estimates (a) and (b) of Lemma 5.2. To prove (c), we proceed as follows: multiply (5.6) by $\partial_t u$, integrate by parts over Ω , use Cauchy-Schwarz and Young's inequalities, and then integrate w.r.t. time between 0 to t . We have, for a.e. $t \in (0, T)$

$$\|u\|_{H^1}^2 + \int_0^t \|\partial_t u\|_{L^2}^2 ds \leq C(1 + t |\Omega|).$$

Moreover, since $u_0 \in H^2$ and $\bar{h}_t \in L^\infty(0, \mathcal{T}; L^2)$, by regularity theory (Evans, 1998), $\partial_t u \in L^\infty(0, \mathcal{T}; L^2)$ with

$$\|u\|_{H^1}^2 + \|\partial_t u\|_{L^2}^2 \leq C e^t (1 + t |\Omega|). \quad (5.8)$$

Hence (c) of Lemma 5.2 follows from (5.8). \square

5.3.3 Proof of Theorem 5.1

As mentioned earlier, we show the well-posedness of the system (5.2)–(5.4) via Schauder fixed point theorem. To do so, we introduce a non-empty, convex and

weakly compact subset W_0 of $W(0, T)$ defined by

$$\begin{aligned} W_0 = \left\{ (w, v) \in W(0, T) : & \|w\|_{L^\infty(0, T; H^1)} + \|\partial_t w\|_{L^\infty(0, T; L^2)} \\ & + \|\partial_{tt} w\|_{L^2(0, T; (H^1)')} \leq C \|J\|_{H^1}, \\ & \|v\|_{L^\infty(0, T; H^1)} + \|\partial_t v\|_{L^\infty(0, T; L^2)} \leq C \|J\|_{H^1}; \\ & 0 < \rho \leq w(x, t) \text{ for a.e. } (x, t) \in \Omega_T, \text{ and } (w, v) \text{ satisfies (5.4)} \right\}. \end{aligned}$$

Consider a mapping

$$\begin{aligned} \mathcal{P} : W_0 &\rightarrow W_0 \\ (w, v) &\mapsto (I_w, u_v). \end{aligned}$$

If we show that the mapping $\mathcal{P} : (w, v) \rightarrow (I_w, u_v)$ is weakly continuous from W_0 into W_0 , then by Schauder fixed point theorem, there exists $(w, v) \in W_0$ such that $(w, v) = \mathcal{P}(w, v)$. In other words, the coupled system (5.2)–(5.3) has a weak solution. In order to prove weak continuity of \mathcal{P} , let (w_k, v_k) be a sequence that converges weakly to some (w, v) in W_0 and let $(I_k, u_k) = (I_{w_k}, u_{v_k})$. We have to show that $\mathcal{P}(w_k, v_k) := (I_k, u_k)$ converges weakly to $\mathcal{P}(w, v) := (I_w, u_v)$.

Thanks to Lemma 5.2, one can use classical results of compact inclusion in Sobolev spaces (Adams, 1975) to extract subsequences $\{w_{k_n}\}$ of $\{w_k\}$, $\{v_{k_n}\}$ of $\{v_k\}$, $\{I_{k_n}\}$ of $\{I_k\}$ and $\{u_{k_n}\}$ of $\{u_k\}$, still denoted by same sequences $\{w_k\}$, $\{v_k\}$, $\{I_k\}$ and $\{u_k\}$, such that for some $(I, u) \in W_0$, the followings hold as $k \rightarrow \infty$:

$$\begin{aligned} w_k &\rightarrow w, \quad v_k \rightarrow v \quad \text{in } L^2(0, T; L^2) \text{ and a.e. on } \Omega_T, \\ G_\xi * w_k &\rightarrow G_\xi * w \quad \text{in } L^2(0, T; L^2) \text{ and a.e. on } \Omega_T, \\ |G_\xi * w_k|^\alpha &\rightarrow |G_\xi * w|^\alpha \quad \text{in } L^2(0, T; L^2) \text{ and a.e. on } \Omega_T, \\ \frac{|G_\xi * w_k|^\alpha}{(M_\xi^{w_k})^\alpha + |G_\xi * w_k|^\alpha} &\rightarrow \frac{|G_\xi * w|^\alpha}{(M_\xi^w)^\alpha + |G_\xi * w|^\alpha} \quad \text{in } L^2(0, T; L^2) \text{ and a.e. on } \Omega_T, \\ \partial_{x_i} G_\xi * w_k &\rightarrow \partial_{x_i} G_\xi * w \quad (i = 1, 2) \quad \text{in } L^2(0, T; L^2) \text{ and a.e. on } \Omega_T, \\ h(|\nabla G_\xi * w_k|) &\rightarrow h(|\nabla G_\xi * w|) \quad \text{in } L^2(0, T; L^2) \text{ and a.e. on } \Omega_T, \\ |G_\xi * v_k| &\rightarrow |G_\xi * v| \quad \text{in } L^2(0, T; L^2) \text{ and a.e. on } \Omega_T, \\ \frac{1}{1 + |G_\xi * v_k|^\beta} &\rightarrow \frac{1}{1 + |G_\xi * v|^\beta} \quad \text{in } L^2(0, T; L^2) \text{ and a.e. on } \Omega_T, \end{aligned}$$

$$\begin{aligned}
I_k &\rightarrow I, \quad u_k \rightarrow u \text{ weakly-* in } L^\infty(0, T; H^1), \\
I_k &\rightarrow I, \quad u_k \rightarrow u \text{ in } L^2(0, T; L^2), \\
\partial_t I_k &\rightarrow \partial_t I, \quad \partial_t u_k \rightarrow \partial_t u \text{ weakly-* in } L^\infty(0, T; L^2), \\
\partial_{tt} I_k &\rightarrow \partial_{tt} I \text{ weakly-* in } L^2(0, T; (H^1)').
\end{aligned}$$

In view of the above convergences, one can pass to the limit in (5.5)–(5.6) and obtain $(I, u) = \mathcal{P}(w, v)$. Moreover, since the solution of (5.5)–(5.6) is unique, the whole sequence $(I_k, u_k) = \mathcal{P}(w_k, v_k)$ converges weakly in W_0 to $(I, u) = \mathcal{P}(w, v)$. Hence \mathcal{P} is weakly continuous. Therefore, the system (5.2)–(5.4) admits a weak solution.

5.3.4 Uniqueness of weak solution

To prove the uniqueness of weak solutions of the proposed model (5.2)–(5.4), we use here a standard methodology (Evans, 1998). Let (I_1, u_1) and (I_2, u_2) be two weak solutions of (5.2)–(5.4). Then, we have

$$\partial_{tt} I + \partial_t I - \operatorname{div}(g_{I_1, u_1} \nabla I) = \operatorname{div}((g_{I_1, u_1} - g_{I_2, u_2}) \nabla I_2) \quad \text{in } \Omega_T, \quad (5.9)$$

$$\partial_t u - \Delta u + u = h(|\nabla G_\xi * I_1|) - h(|\nabla G_\xi * I_2|) \quad \text{in } \Omega_T, \quad (5.10)$$

$$\begin{cases} I(x, 0) = 0, \quad \partial_t I(x, 0) = 0, \quad u(x, 0) = 0 & \text{in } \Omega, \\ \partial_n I = 0 = \partial_n u & \text{on } \partial\Omega_T, \end{cases} \quad (5.11)$$

where $I = I_1 - I_2$ and $u = u_1 - u_2$. It suffices to show that $(I, u) \equiv (0, 0)$. To verify this, fix $0 < s < T$, and set for $i = 1, 2$,

$$v_i(t, \cdot) = \begin{cases} \int_t^s I_i(\cdot, \tau) d\tau, & 0 < t \leq s, \\ 0, & s \leq t < T. \end{cases} \quad (5.12)$$

Note that, for $t \in (0, T)$,

$$\begin{cases} \partial_t v_i(x, t) = -I_i(x, t), & i = 1, 2, \\ v_i(\cdot, t) \in H^1, \quad \partial_n v_i = 0 \quad \text{on } \partial\Omega \text{ in the sense of distribution.} \end{cases} \quad (5.13)$$

Set $v = v_1 - v_2$. Then $v(\cdot, s) = 0$. Now one can follow the same argumentation as in [Chapter 4, subsection 4.3.4] to arrive at

$$\begin{aligned} & \frac{1}{2}\|I(s)\|_{L^2}^2 + \int_0^s \|I(t)\|_{L^2}^2 dt + \frac{1}{2} \int_{\Omega} g_{I_1, u_1}(x, 0) |\nabla v(x, 0)|^2 dx \\ & \leq \frac{1}{2} \left| \int_0^s \int_{\Omega} |\nabla v|^2 \partial_t g_{I_1, u_1} dx dt \right| + \int_0^s \|(g_{I_1, u_1} - g_{I_2, u_2})(t)\|_{L^\infty} \|\nabla I_2(t)\|_{L^2} \|\nabla v(t)\|_{L^2} dt. \end{aligned} \quad (5.14)$$

Like in (5.7), there exist positive constants $\kappa_1, C_1 > 0$ such that

$$\kappa_1 \leq g_{I_1, u_1} \leq 1, \quad |\partial_t g_{I_1, u_1}| \leq C.$$

Moreover, by using property of convolution and the positive lower bound ρ of the solutions I_i , we get

$$\|(g_{I_1, u_1} - g_{I_2, u_2})(t)\|_{L^\infty} \leq C(\xi, \alpha, J, \rho) (\|I(t)\|_{L^2}^\alpha + \|u\|_{L^2}).$$

Thus we have, from (5.14)

$$\begin{aligned} & \frac{1}{2}\|I(s)\|_{L^2}^2 + \int_0^s \|I(t)\|_{L^2}^2 dt + C\|\nabla v(0)\|_{L^2}^2 \\ & \leq C \left(\int_0^s (\|\nabla v(t)\|_{L^2}^2 + \|I(t)\|_{L^2}^{2\alpha} + \|u(t)\|_{L^2}^2) dt \right) \\ & \leq C \left(\int_0^s (\|v(t)\|_{H^1}^2 + \|I(t)\|_{L^2}^2 + \|u(t)\|_{L^2}^2) dt \right), \end{aligned}$$

where in the last inequality, we have used the fact that $\alpha \geq 1$. Set

$$w_i(\cdot, t) = \int_0^t I_i(\cdot, \tau) d\tau; \quad w(\cdot, t) = (w_1 - w_2)(\cdot, t), \quad 0 < t \leq T.$$

Then, by using a similar argument as in [Chapter 4, subsection 4.3.4], we obtain

$$\begin{aligned} & \frac{1}{2}\|I(s)\|_{L^2}^2 + \int_0^s \|I(t)\|_{L^2}^2 dt + C\|w(s)\|_{H^1}^2 \\ & \leq \tilde{C}s\|w(s)\|_{H^1}^2 + C \int_0^s (\|w(t)\|_{H^1}^2 + \|I(t)\|_{L^2}^2 + \|u(t)\|_{L^2}^2) dt. \end{aligned}$$

Choose T_1 sufficiently small such that $C - \tilde{C}T_1 > 0$. Then, for $0 < s \leq T_1$, we have

$$\|I(s)\|_{L^2}^2 + \|w(s)\|_{H^1}^2 \leq C \int_0^s (\|w(t)\|_{H^1}^2 + \|I(t)\|_{L^2}^2 + \|u(t)\|_{L^2}^2) dt. \quad (5.15)$$

Now, by multiplying (5.10) by u and integrating over Ω , we have

$$\frac{d}{dt} \|u\|_{L^2}^2 + 2\|\nabla u\|_{L^2}^2 \leq C \left(\|h(|\nabla G_\xi * I_1|) - h(|\nabla G_\xi * I_2|)\|_{L^2}^2 + \|u\|_{L^2}^2 \right).$$

Since h is Lipschitz continuous, by using Young's inequality for convolution, we see that

$$\|h(|\nabla G_\xi * I_1|) - h(|\nabla G_\xi * I_2|)\|_{L^2}^2 \leq C(c_h, \xi) \|I\|_{L^2}^2.$$

Thus, we have, for $0 < s \leq T_1$,

$$u(s) \leq C \int_0^s \|I(t)\|_{L^2}^2 dt. \quad (5.16)$$

Adding (5.15) and (5.16), we finally get , for $0 < s \leq T_1$,

$$\|I(s)\|_{L^2}^2 + \|u(s)\|_{L^2}^2 + \|w(s)\|_{H^1}^2 \leq C \int_0^s \left(\|w(t)\|_{H^1}^2 + \|I(t)\|_{L^2}^2 + \|u(t)\|_{L^2}^2 \right) dt.$$

Hence by Gronwall's lemma, we see that $(I, u) \equiv (0, 0)$ on $[0, T_1]$. We repeatedly use the above argument on the intervals $(T_1, 2T_1]$, $(2T_1, 3T_1]$, ... step by step, and arrive at the conclusion that $I_1 = I_2$ and $u_1 = u_2$ on $(0, T)$. This completes the proof of Theorem 5.1.

For any weak solution (I, u) of (5.2)–(5.4), we next show the boundedness of I under the assumption that initial image J has a finite upper bound, whose proof follows from the proof of [Chapter 4, Lemma 4.3].

Lemma 5.3. *Let (I, u) be a weak solution of the system (5.2)–(5.4), and $\varrho := \sup_{x \in \Omega} J(x) < \infty$. Then*

$$0 < \rho \leq I(x, t) \leq \varrho \quad \text{for a.e. } (x, t) \in \Omega_T. \quad (5.17)$$

5.4 Computational Results & Discussion

This section presents the image despeckling performance of the present technique over three existing approaches: MCPDE model (1.27)–(1.31), Shan model (4.8)–(4.10), and TDM model (4.15)–(4.17).

5.4.1 Numerical Implementation

To solve the model (5.2)-(5.4) numerically, we opt a weighted θ -scheme (Jovanović and Süli, 2013). We replace the derivative terms in the model (5.2)–(5.4) using the finite difference formulas as discussed in section 1.3. Then using the weighted scheme (Jovanović and Süli, 2013), the discretized form of the equation (5.2) could be written as

$$(1 + 0.5\gamma\tau)I_{i,j}^{n+1} - \tau^2\theta_1 [\operatorname{div}(g\nabla I)]_{i,j}^{n+1} = 2I_{i,j}^n + \tau^2(1 - \theta_1 - \theta_2) [\operatorname{div}(g\nabla I)]_{i,j}^n \\ + \tau^2\theta_2 [\operatorname{div}(g\nabla I)]_{i,j}^{n-1} + (0.5\gamma\tau - 1)I_{i,j}^{n-1}, \quad (5.18)$$

where θ_1 and θ_2 are non negative weights. The superscript n denotes the value at the n^{th} time level t_n and $[\operatorname{div}(g\nabla I)]_{i,j}$

$$= 0.5 [(g_{i,j} + g_{i+1,j})I_{i+1,j} + (g_{i,j} + g_{i-1,j})I_{i-1,j} - (g_{i+1,j} + 2g_{i,j} + g_{i-1,j})I_{i,j}] \\ + 0.5 [(g_{i,j} + g_{i,j+1})I_{i,j+1} + (g_{i,j} + g_{i,j-1})I_{i,j-1} - (g_{i,j+1} + 2g_{i,j} + g_{i,j-1})I_{i,j}],$$

where

$$g_{i,j} = b(s_{i,j}) \frac{1}{1 + \iota|G_\xi * u_{i,j}|^\beta} \quad \text{with } b(s) = \frac{s^\alpha}{1 + s^\alpha}.$$

Moreover, $u(x_i, y_j, t_n) = u_{i,j}^n$ is calculated from the discretized equation of (5.3) as follows

$$(1 + \tau\theta)u_{i,j}^{n+1} - 0.5\tau\nu^2\theta\Delta u_{i,j}^{n+1} = \{1 - \tau(1 - \theta)\}u_{i,j}^n \\ + 0.5\tau\nu^2(1 - \theta)\Delta u_{i,j}^n + \tau\{h(|\nabla(G_\xi * I_{i,j}^n)|)\}, \quad (5.19)$$

where θ is a non negative weight parameter. We choose the weight parameter values $\theta_1 = 0.4$, $\theta_2 = 0.4$, and $\theta = 0.5$ for the numerical experiments. Also, choose the function h as $h(\varphi) = \epsilon + \min\{\varphi^2, K\}$, where K is square of the maximum gray level value of the image I and $\epsilon > 0$ is a very small number. The initial conditions are given as

$$I_{i,j}^0 = J(x_i, y_j), \quad I_{i,j}^1 = I_{i,j}^0, \quad u_{i,j}^0 = G_\xi * |\nabla I_{i,j}^0|^2, \quad 0 \leq i \leq M-1, \quad 0 \leq j \leq N-1,$$

with the boundary conditions as discussed in section 1.3. We solve both the systems (5.18) and (5.19) using Gauss Seidel iterative method (Wesseling, 1995; Langtangen, 2013; Hoffman and Frankel, 2018). We perform all the experiments

on three standard test images and two real images. The first three images are degraded by multiplying artificial speckle noise with “looks” $L = \{1, 3, 5, 10\}$ by using MATLAB program [Chapter 4, [section 4.5](#)]. All the numerical experiments are performed under Windows 7 and MATLAB version *R2019a* running on a desktop computer with an Intel i5 dual-core CPU at 2.53 GHz with 4 GB of RAM. We choose uniform time step sizes $\tau = 0.25$ and $\xi = 1$ for the numerical computations.

5.4.2 Results for the Artificially Noised Images

To compare the quantitative results, we compute the values of the parameters PSNR and MSSIM. Apart from the despeckled images, for qualitative comparison, we compute 2D contour plot, 3D surface plot etc., of the restored image.

In Figures [5.1–5.3](#), we present the restored results of a texture image which is contaminated by multiplicative speckle noise with $L = \{1, 3, 5\}$. From Figures [5.1–5.2](#), we can see that the MCPDE and Shan models failed to preserve the fine edges for very high noise level. TDM model works better, but the present model preserves the fine edges better than the other three models.

In Figures [5.4–5.6](#), we present the reconstructed results of a peppers image (Natural Image) which is corrupted by speckle noise with $L = \{1, 3, 5\}$. From [Figure 5.4](#), we see that the present model leave less speckle than the other three models.

To check further the reconstruction ability of the present model, Figures [5.7–5.11](#) illustrate the qualitative results of a circle image (Synthetic Image) which is corrupted by speckle noise with $L = \{1, 3, 5\}$.

In Figures [5.7–5.9](#) we demonstrate the despeckled images, and in the Figures [5.10–5.11](#) we illustrate the contour maps and 3D surface plots when the image is corrupted by $L = 5$. One can observe from the contour maps and 3D surface plots that MCPDE, Shan, and TDM models left some speckles in the homogeneous regions, but the present model produces fewer artifacts with better edge preservation.

Along with the quality of the full image in Figures [5.12–5.13](#), we demonstrate the restored results of a slice of the peppers image and texture image which are initially corrupted by speckle noise with $L = 10$. In Figures [5.12a](#) and [5.13a](#), we indicate the slice of the peppers and texture images, respectively. From the restored results in Figures [5.12c–5.12f](#) and in Figures [5.13c–5.13f](#), one can easily conclude that the restored signals computed by the proposed model are more closure to the clean signals in comparison to other discussed models.

Computational values of PSNR and MSSIM are presented in the [Table 5.1](#).

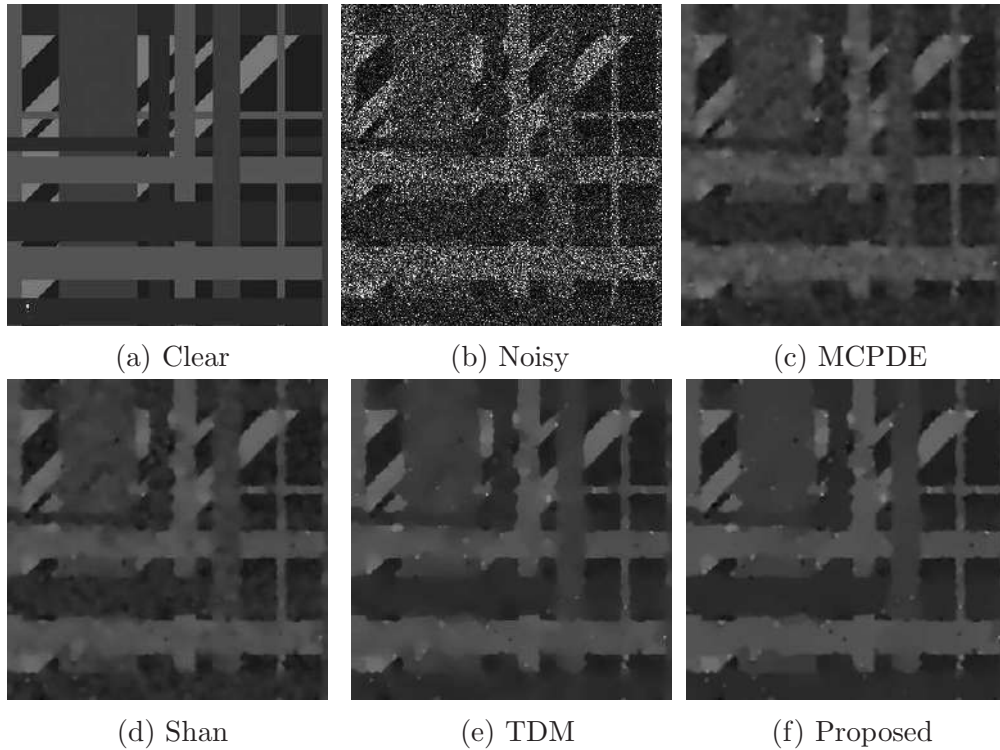


Figure 5.1: Image corrupted with speckle look $L = 1$ and restored by different models.

The highest values of PSNR and MSSIM for each noise level clearly shows that the present algorithm is better than the other three models considered here. Hence, the overall performance is better than the other discussed models.

5.4.3 Results for the Real Images

In this section, we show the image despeckling ability of the proposed model in real SAR and Ultrasound images. For the real-life images we have no prior information about the original noise-free image. Therefore, for the quantitative comparison with the other discussed models we calculate the values of three standard no-reference quantitative measures; i.e., SI, BRISQUE, and NSD.

In Figures 5.14–5.15, we present the despeckled results for a real SAR image. Figure 5.14 displays the visual comparison of the restored results of the original image, Figure 5.14a, with the despeckled images computed through the proposed and other discussed models. At a glance, one can observe from the restored images, Figure 5.14b–5.14e, that the present model preserves the texture and edges better than the other models. In Figure 5.15a, we plot the SI values versus the number of iterations to achieve the optimum SI value for the present and other models. In this graph, X-axis represents the number of iterations, and Y-axis represents the SI values. From the Figure 5.15a, one can observe that the present method takes

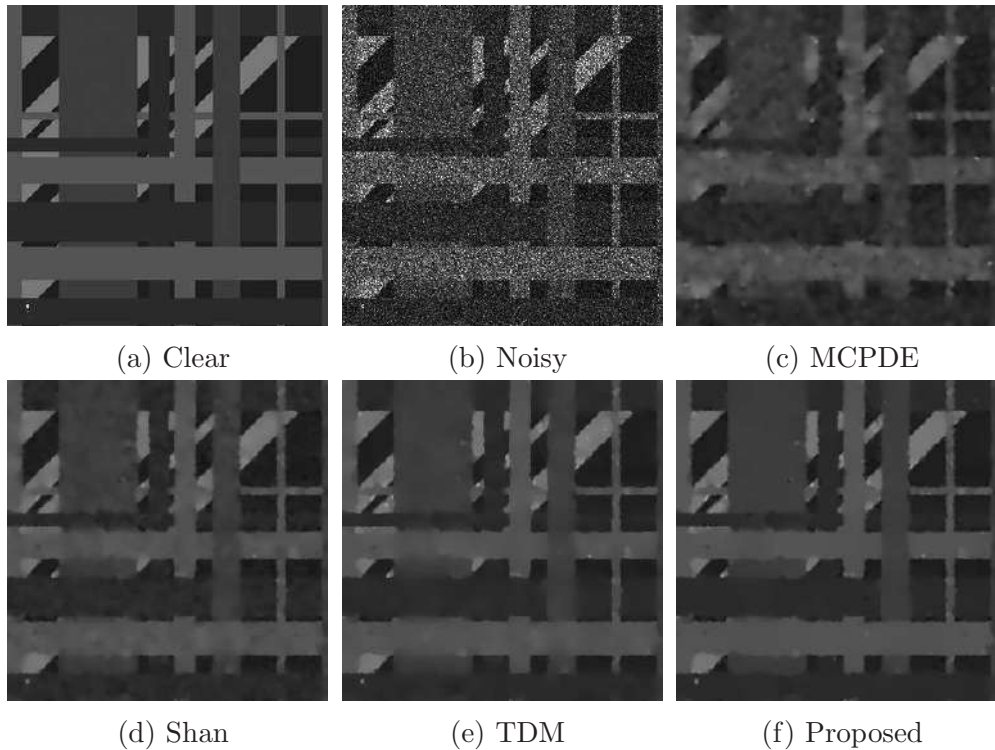


Figure 5.2: Image corrupted with speckle look $L = 3$ and restored by different models.

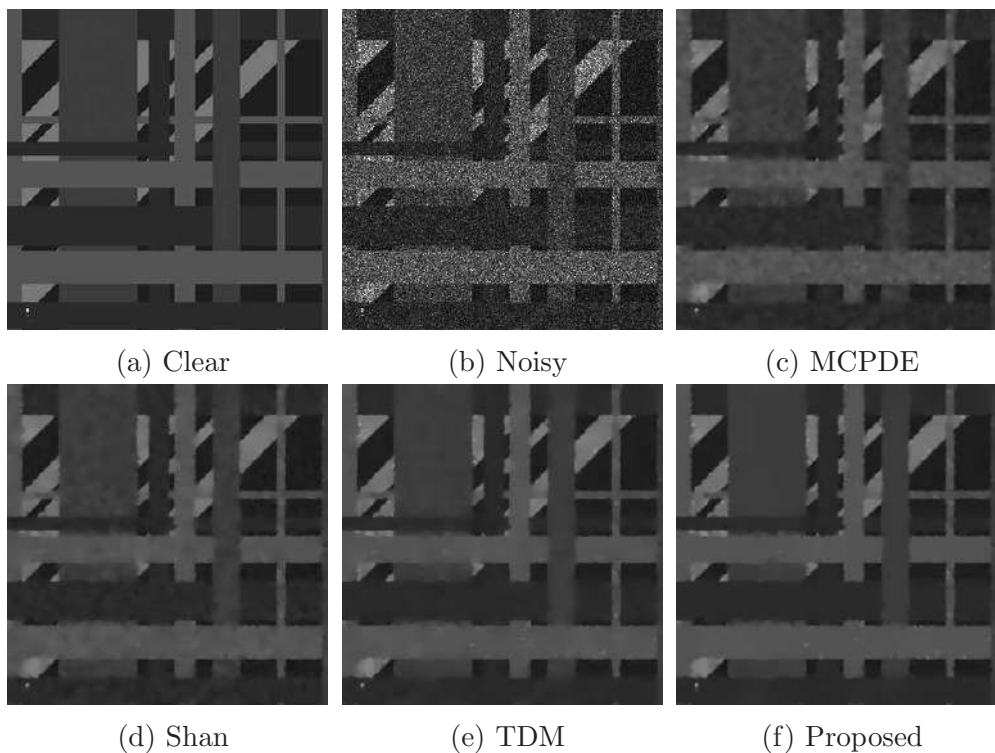


Figure 5.3: Image corrupted with speckle look $L = 5$ and restored by different models.

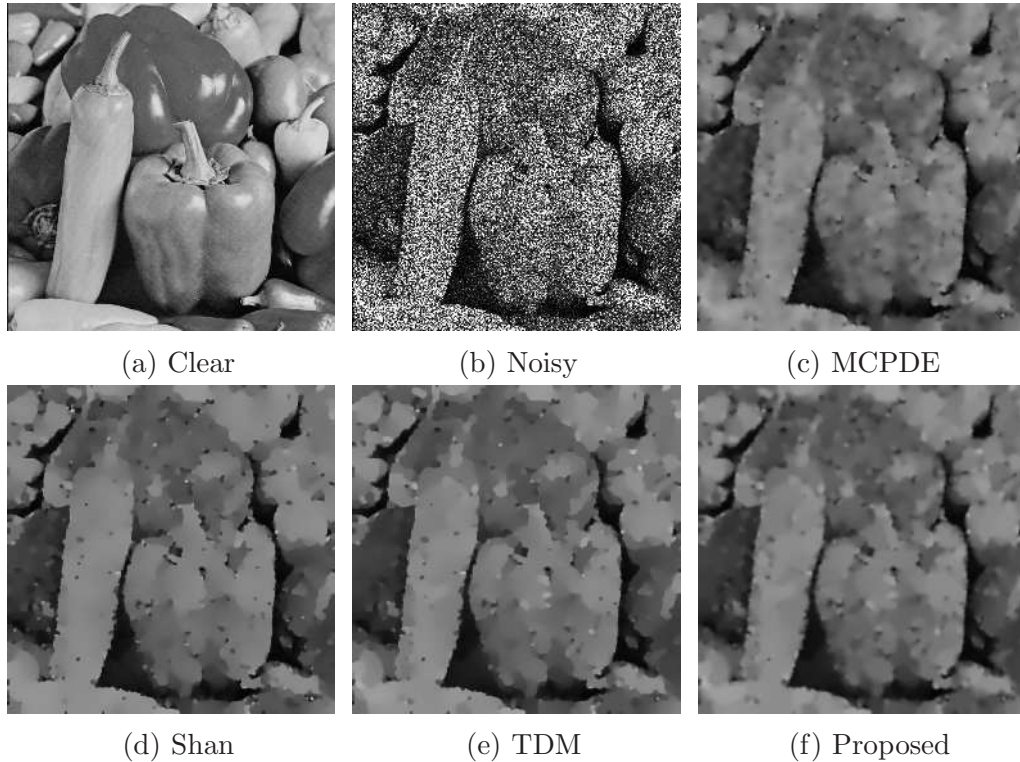


Figure 5.4: Image corrupted with speckle look $L = 1$ and restored by different models.

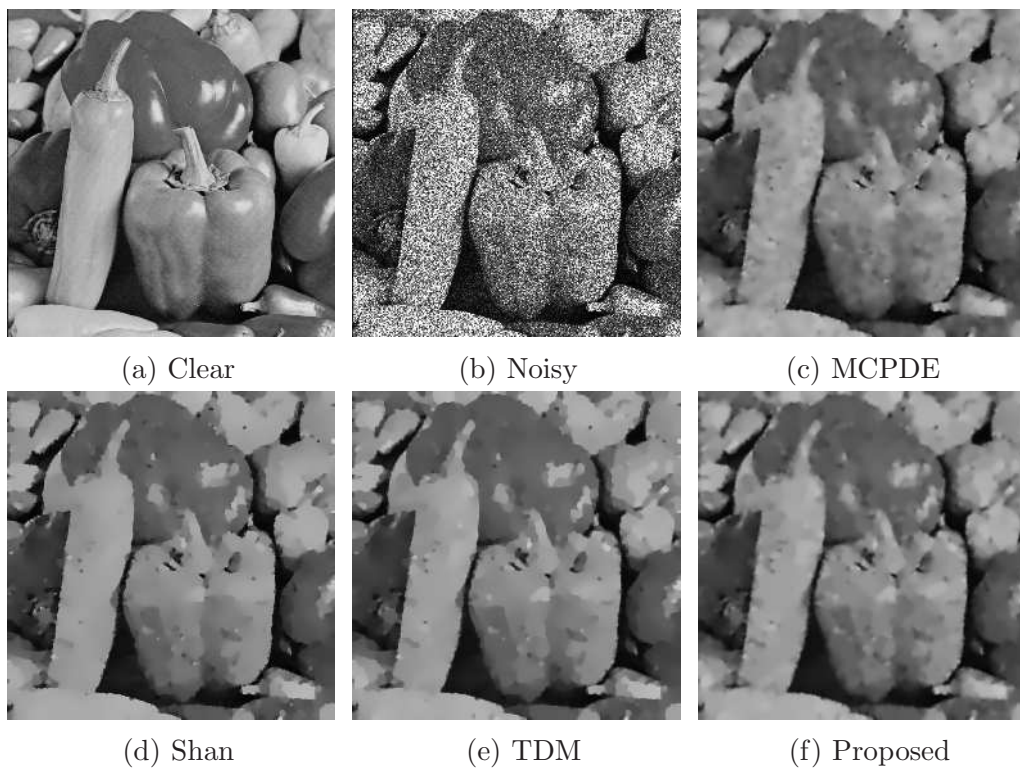


Figure 5.5: Image corrupted with speckle look $L = 3$ and restored by different models.

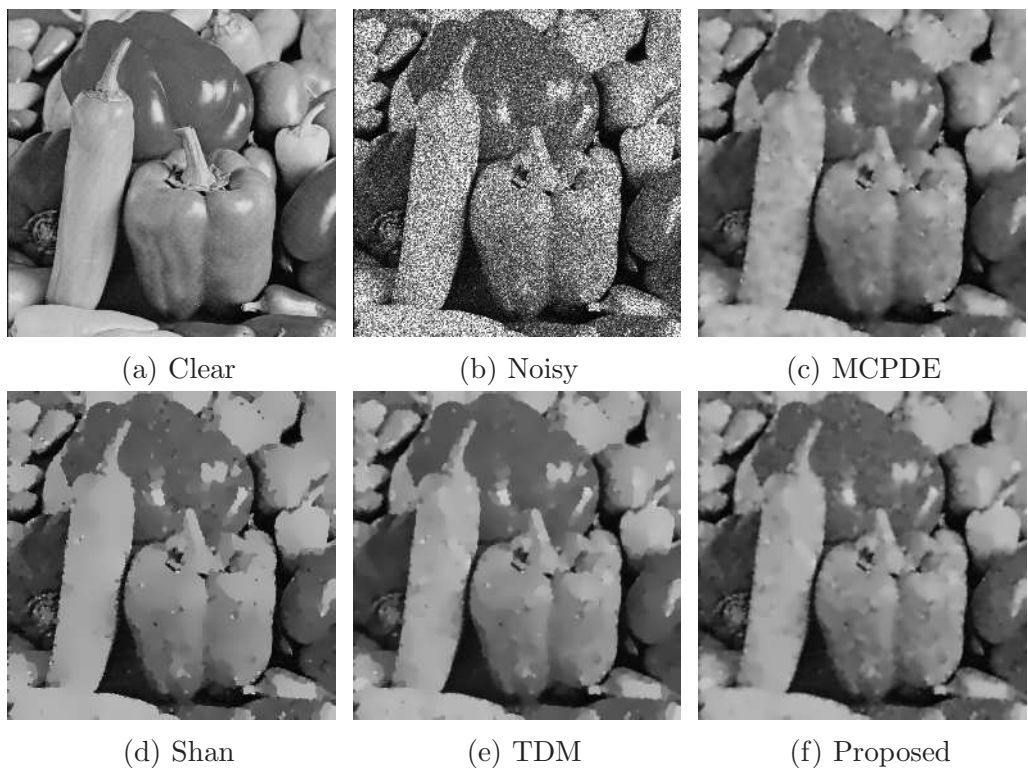


Figure 5.6: Image corrupted with speckle look $L = 5$ and restored by different models.

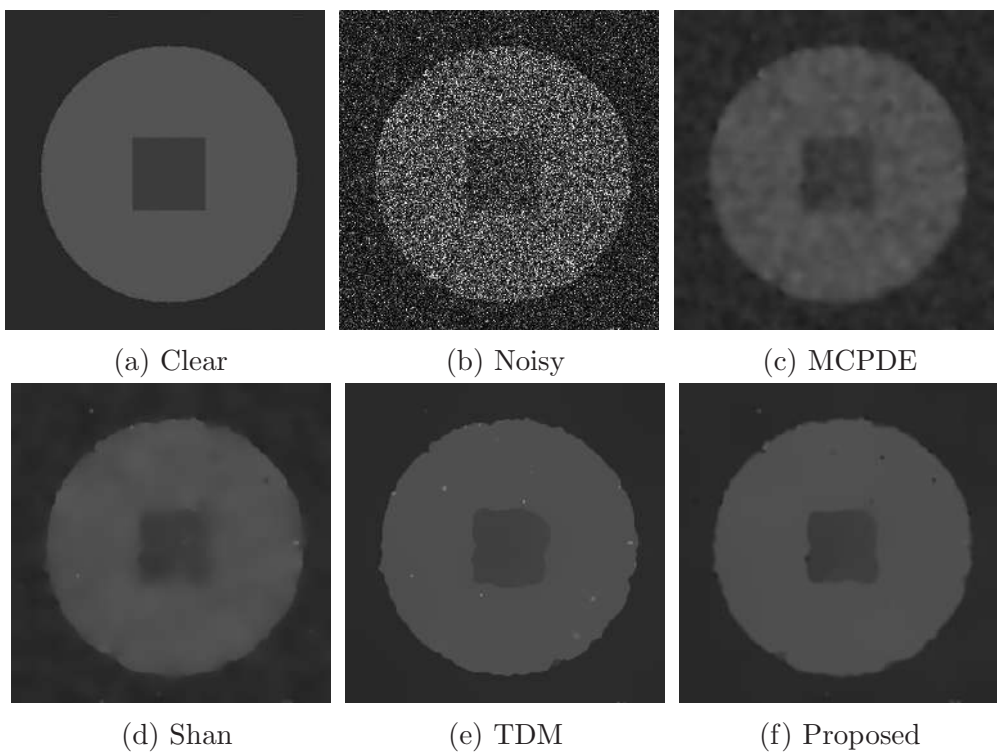


Figure 5.7: Image corrupted with speckle look $L = 1$ and restored by different models.

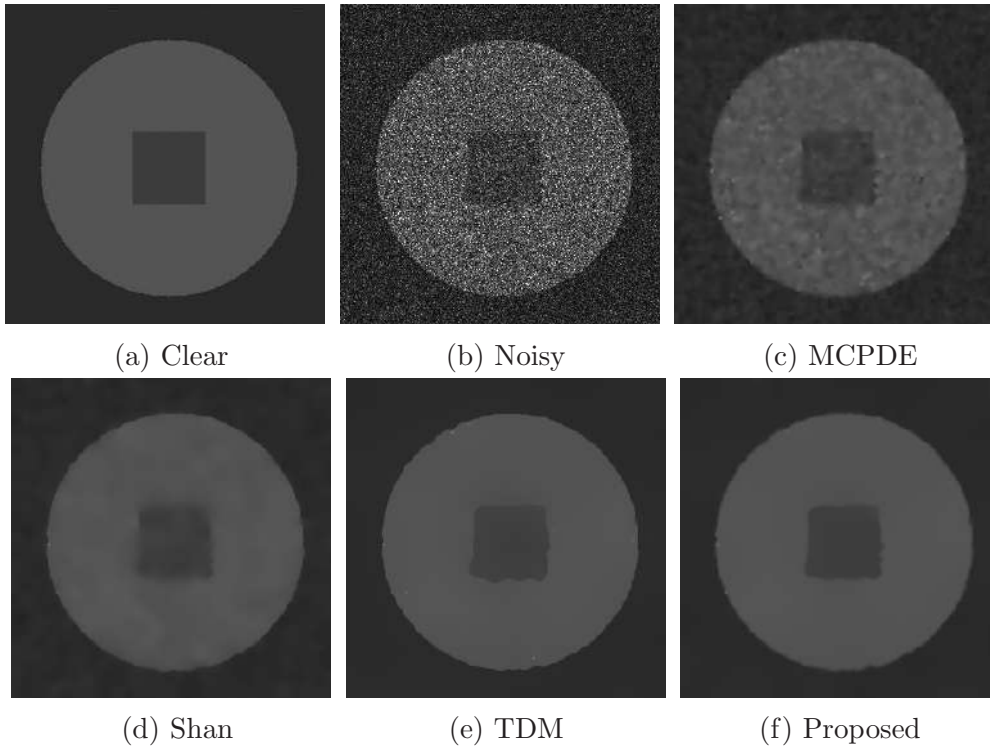


Figure 5.8: Image corrupted with speckle look $L = 3$ and restored by different models.

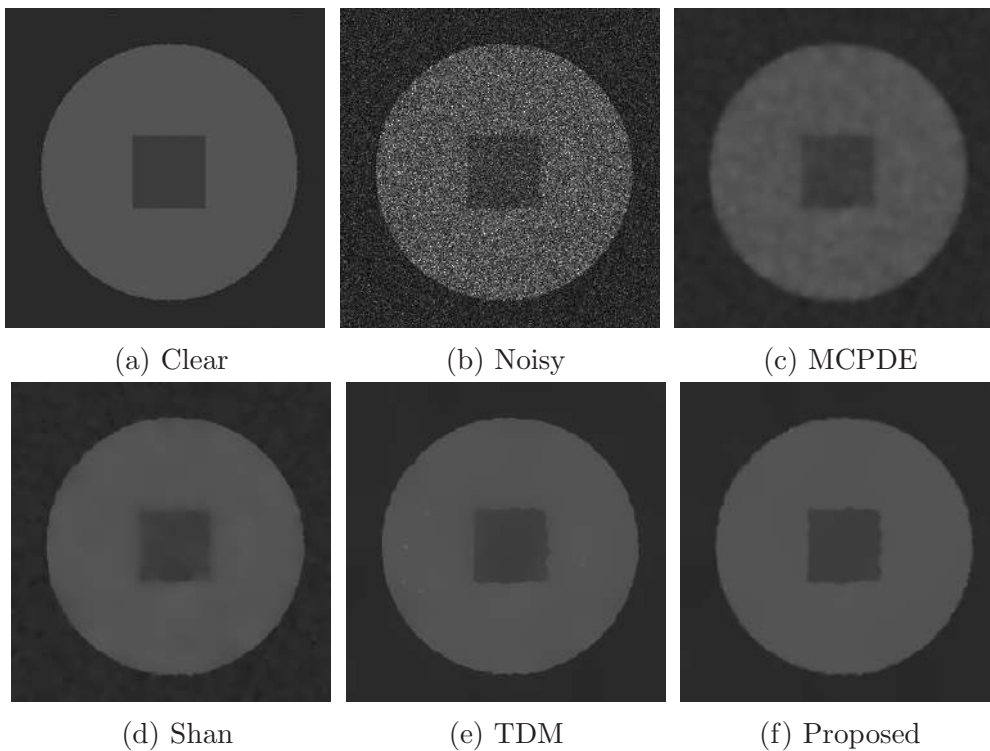


Figure 5.9: Image corrupted with speckle look $L = 5$ and restored by different models.

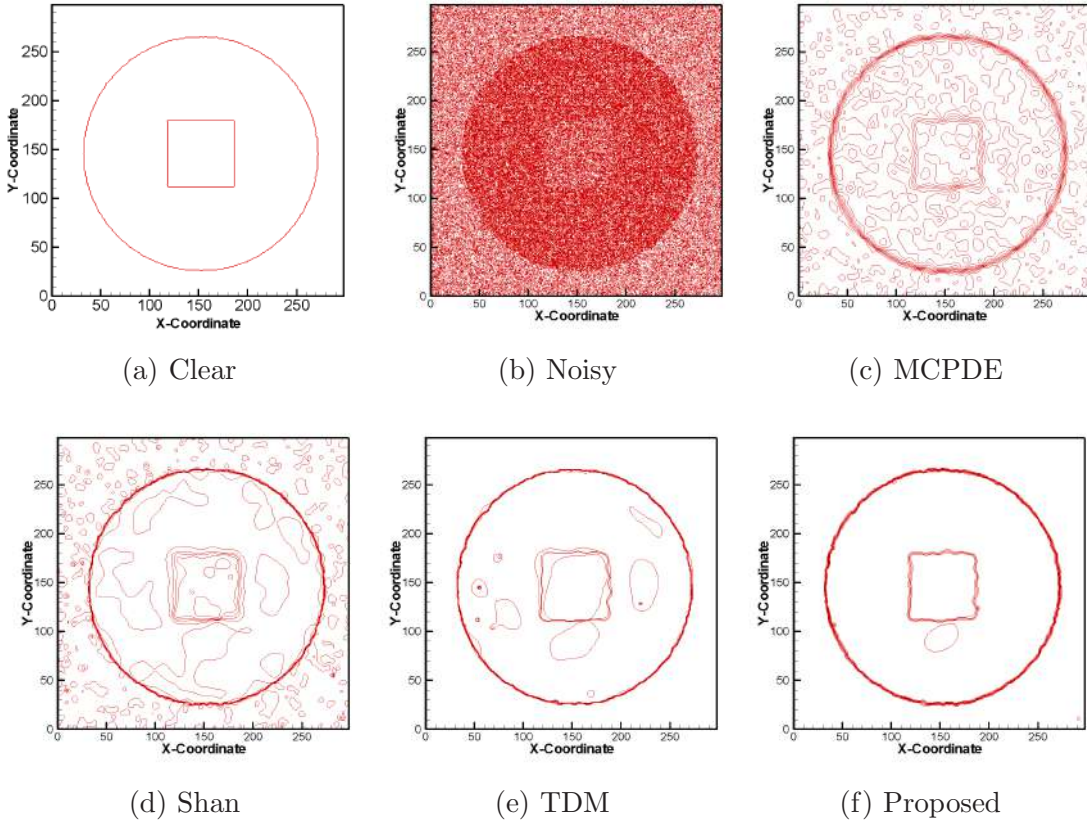


Figure 5.10: Contour plots of the images in Figure 5.9.

Table 5.1: MSSIM and PSNR values of despeckled images.

Image	L	MCPDE		Shan		TDM		Proposed Model	
		MSSIM	PSNR	MSSIM	PSNR	MSSIM	PSNR	MSSIM	PSNR
Circle	1	0.9245	32.71	0.9581	34.29	0.9643	34.69	0.9651	35.43
	3	0.9417	33.87	0.9734	38.09	0.9771	39.52	0.9782	40.00
	5	0.9512	36.39	0.9764	39.35	0.9805	40.72	0.9810	41.23
	10	0.9584	37.96	0.9815	41.24	0.9859	42.79	0.9887	43.23
Texture	1	0.7831	27.16	0.8125	27.61	0.8355	27.71	0.8360	27.83
	3	0.8424	29.98	0.8782	30.83	0.8925	31.05	0.8967	31.31
	5	0.8627	30.95	0.8979	31.87	0.9109	32.15	0.9164	32.47
	10	0.8911	32.63	0.9278	33.36	0.9322	33.79	0.9331	34.18
Peppers	1	0.5826	17.61	0.5827	17.56	0.5895	17.64	0.5905	17.83
	3	0.6938	22.51	0.7018	22.46	0.7019	22.55	0.7061	22.85
	5	0.7286	24.19	0.7155	23.73	0.7334	24.22	0.7395	24.67
	10	0.7761	26.10	0.7580	25.42	0.7782	26.16	0.7796	26.65

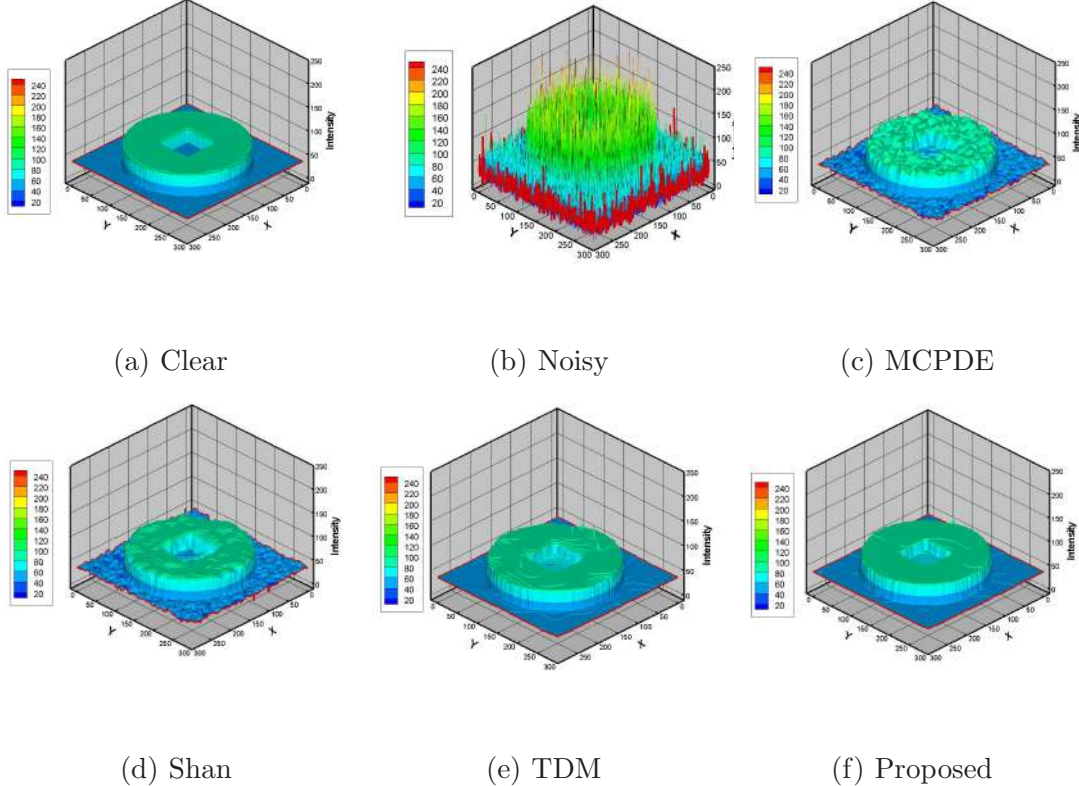


Figure 5.11: 3D surface plots of the images in Figure 5.9.

Table 5.2: Parameter values for the numerical experiments.

Image	L	MCPDE		Shan		TDM			Proposed				
		α	k	α	β	γ	ν	K	γ	α	β	ι	ν
Circle	1	1.5	10	1.5	2	10	1	1	1	1.5	1.8	2.5	0.1
	3	1.5	10	1.5	2	10	1	1	2	1.7	2	2.5	0.1
	5	1.5	10	2	2.25	5	1	1	2	1.7	2.2	2	0.1
	10	1.5	10	2	2.25	2	1	1	2	1.7	2.2	2	0.1
Texture	1	1	10	1.5	1.8	2	1.5	2	1	2	1	3	0.1
	3	1.2	10	1.8	2	2	1.5	2	2	2	1	3	0.1
	5	1.3	10	1.8	2	2	1.5	2	5	2.5	1	3	0.1
	10	1.5	10	2	2.5	2	1.5	2	5	2.5	1	3	0.1
Peppers	1	1.5	10	1.5	2	1	1.5	2	1	2	1	3	0.1
	3	1.5	10	1.5	2	1	1.5	2	2	2	1	3	0.1
	5	1.5	10	2	2.4	2	1.5	2	2	2.5	1	3	0.1
	10	1.5	10	2	2.4	2	1.5	2	2	2.5	1	3	0.1

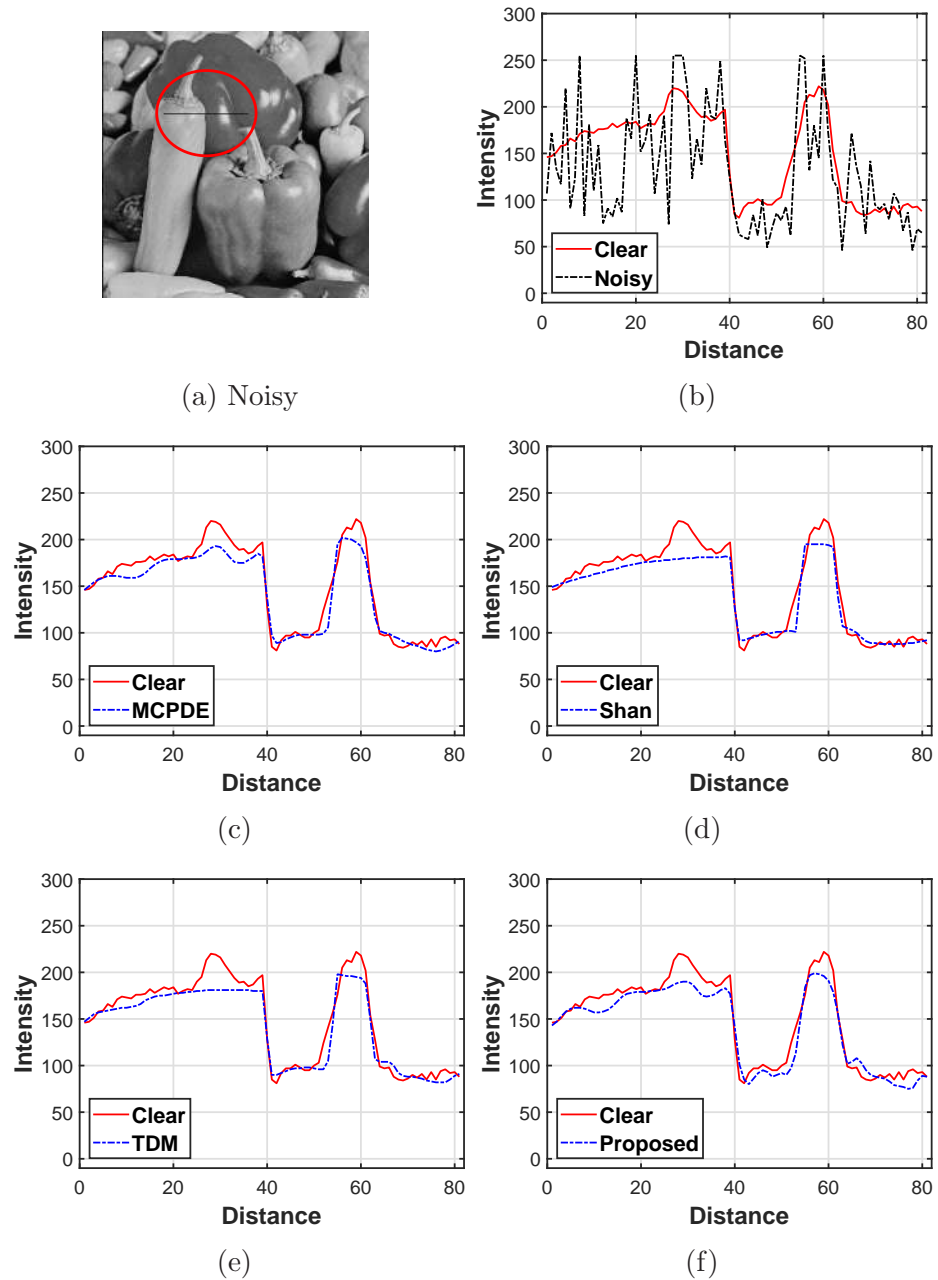


Figure 5.12: Part of the 88th slice of the peppers image corrupted with speckle look $L = 10$ and restored by different models.

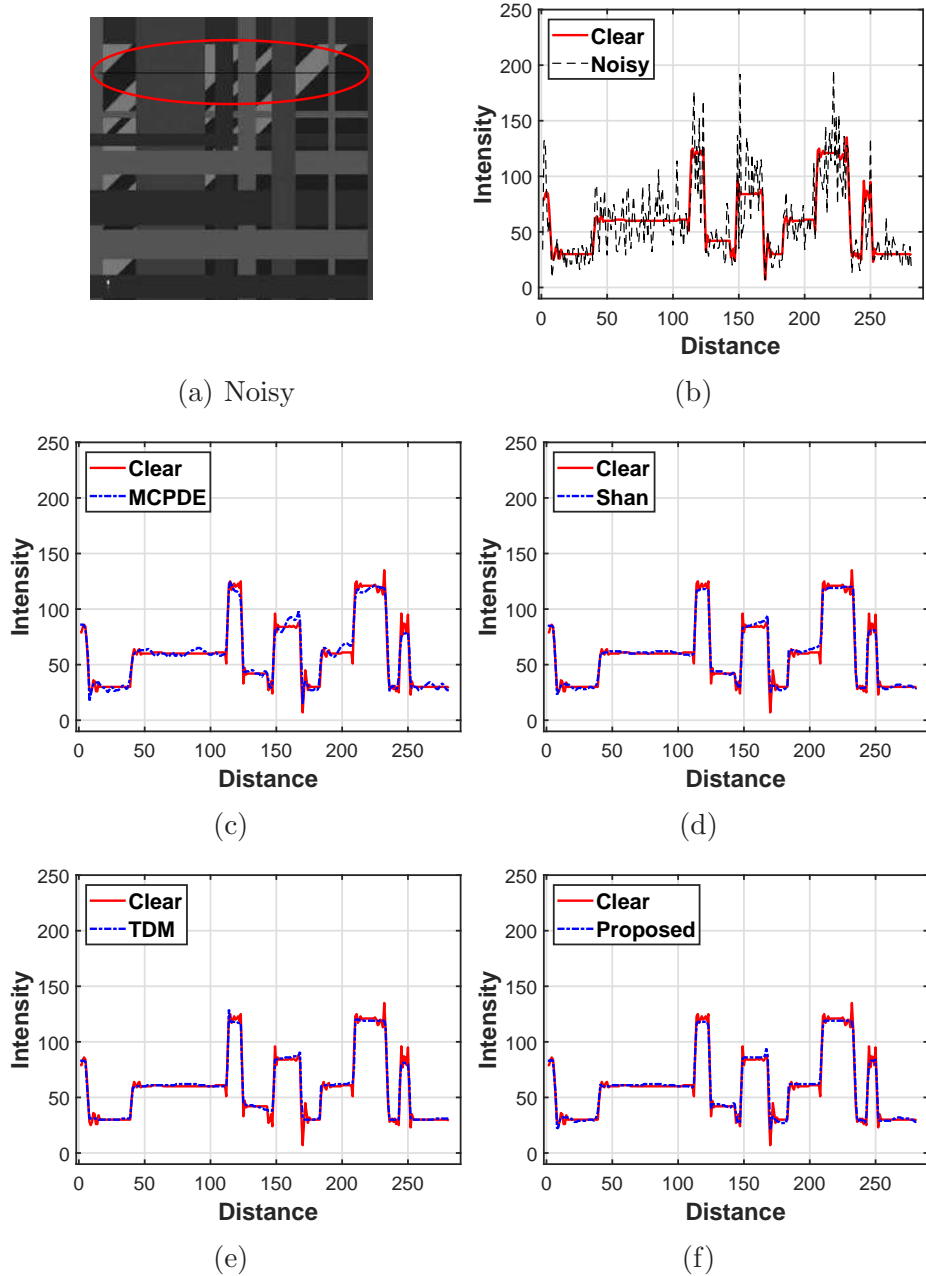


Figure 5.13: Part of the 60th slice of the texture image corrupted with speckle look $L = 10$ and restored by different models.

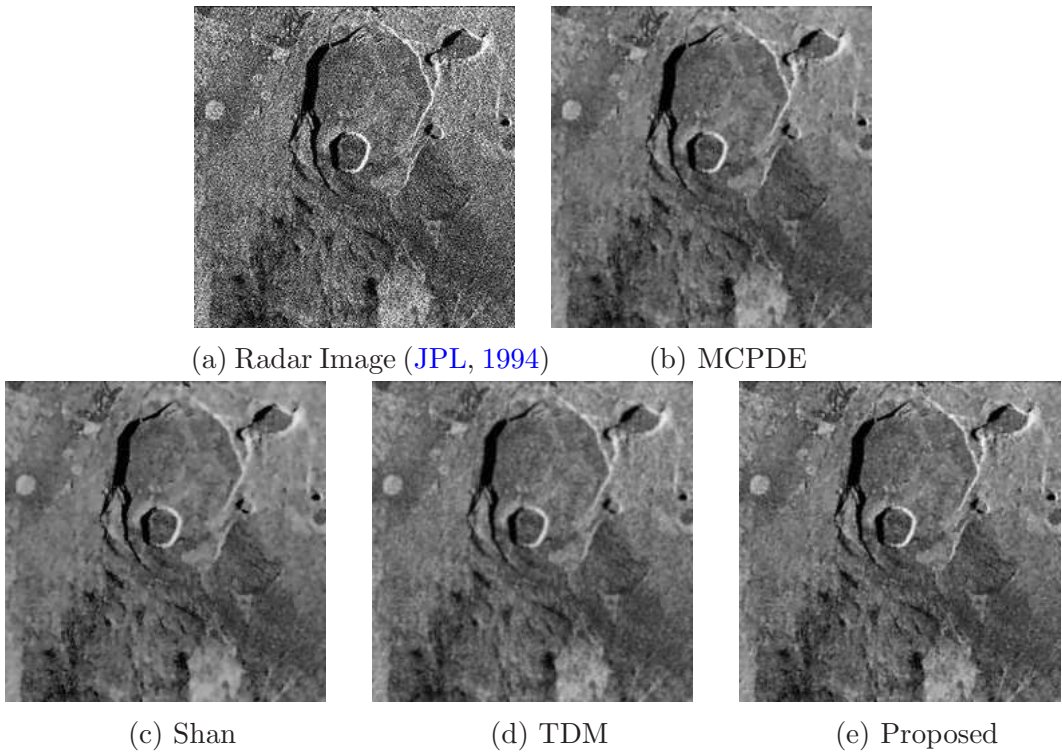


Figure 5.14: Space Radar Image and restored by different models.

the less number of iterations to achieve the optimum SI value, which is also the minimum among all the optimum values computed through the considered models. In Figure 5.15b, we plot the graph of improved BRISQUE values versus the number of iterations, computed by the same models as in Figure 5.15a. This figure also confirms that our proposed model produces best BRISQUE value with minimum number of iterations among all the considered models.

In Figure 5.16, we present the despeckled results of the Ultrasound image of fetal foot. From the despeckled images, it is clear that the result using present model is less blurry and more apparent than the despeckled results using other existing models. In Figures 5.17a and 5.17b, we plot the improved SI and NSD values respectively after 100 iterations for the same ultrasound image and for the same considered models. The lowest values of SI and NSD show that our proposed model performs better than the other three considered models.

5.5 Conclusion

In this work, we present a nonlinear hyperbolic-parabolic coupled system applied to image despeckling. Such an improve method preserves the image characteristics in the noise removal process, even at high noise level. To the best of our knowledge,

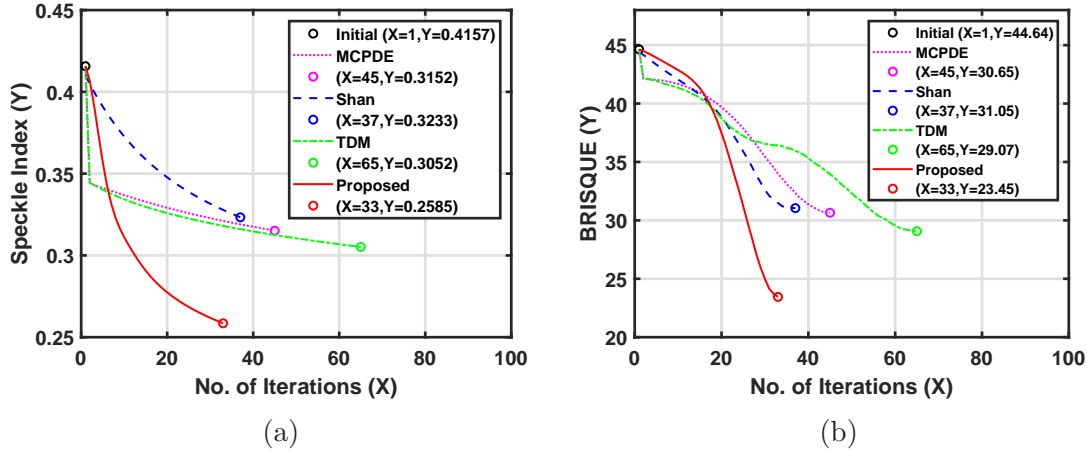


Figure 5.15: (a) Improved Speckle Index value vs. the corresponding iteration number for various models, (b) Improved BRISQUE values vs. the corresponding iteration number for various models. Parameter values for the numerical experiments: (i) MCPDE: $\alpha = 1.5, k = 10$, (ii) Shan: $\alpha = 1.5, \beta = 0.5$, (iii) TDM: $\gamma = 5, \nu = 2, K = 4$, (iv) Proposed: $\gamma = 5, \alpha = 2, \beta = 1, \iota = 0.1, \nu = 1$.

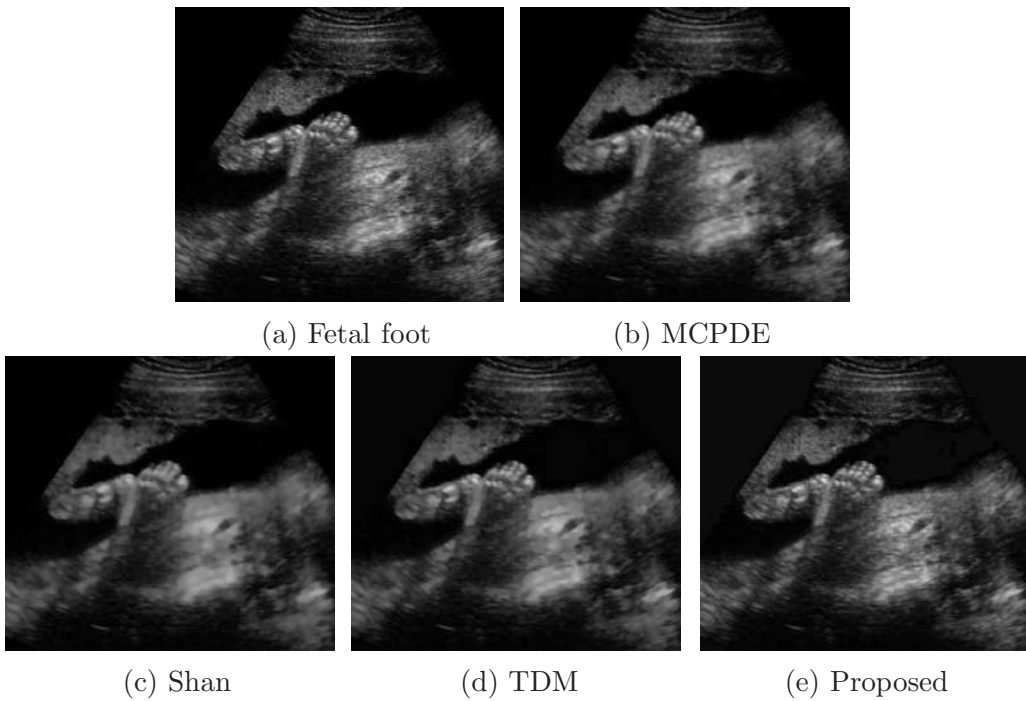


Figure 5.16: Ultrasound Image and restored by different models.

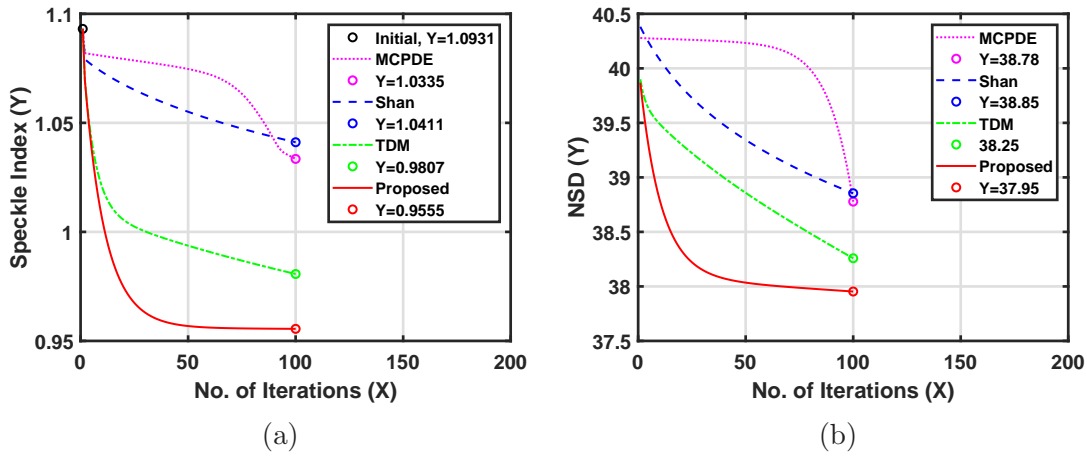


Figure 5.17: (a) Comparison of Speckle Index values after 100 iterations for various models, (b) Comparison of NSD values after 100 iterations for various models. Parameter values for the numerical experiments: (i) MCPDE: $\alpha = 1.5, k = 10$, (ii) Shan: $\alpha = 1.5, \beta = 0.8$, (iii) TDM: $\gamma = 2, \nu = 2, K = 4$, (iv) Proposed: $\gamma = 1, \alpha = 1, \beta = 2, \iota = 0.1, \nu = 0.1$.

coupled hyperbolic-parabolic PDE based model has not been used before for image speckle reduction. Moreover, we present the existence and uniqueness of the weak solution of the proposed model. We have performed numerical experiments on three different types of gray level test images (i.e., Natural Image, Texture image and Synthetic Image) and two real images (i.e., SAR and Ultrasound images). We compare the computed results with three recently developed models and overall study confirms that the proposed model is a better alternative for spackle noise removal. Also, unlike other existing models, proposed model can recover the best despeckled image from a corrupted image more efficiently without introducing any undesired artifacts. Therefore, the proposed model is an important addition to the field for image despakpling.

Chapter 6

A Fuzzy Edge Detector Driven Telegraph Total Variation Model For Image Despeckling

In this chapter, a fuzzy edge indicator based telegraph total variation model is discussed for image despeckling. The proposed model is derived from the total variation framework. We study the existence and uniqueness of weak solutions of a regularized version of the present model. The proposed model is then applied to different types of images, which are degraded by speckle noise. The despeckling results computed by the present model are reported, which found better in terms of noise removal and edge preservation, with respect to some of the existing well-known approaches.

6.1 General Introduction

In the last few decades, a rising figure of studies describes the statistical and the fundamental properties of the multiplicative speckle noise, usually for SAR and medical ultrasound images ([Jain and Ray, 2019](#)). Among the popular state-of-the-art despeckling approaches, PDE based methods are widely used to formulate the speckle noise removal strategies. In general, the PDE based image processing have their origin in the variational calculus ([Aubert and Kornprobst, 2006](#)). Typically, these variational methods can be defined as a combination of regularization and fidelity term. The first variational approach for multiplicative noise reduction is the RLO model ([1.32](#)) (explained earlier, in [section 1.2](#)). If the values of λ and μ in ([1.32](#)) are calculated dynamically (using gradient projection method), the RLO model ([1.32](#)) is not always convex ([Dong et al., 2013](#)). After that, Aubert and Aujol introduced the non-convex variational model ([1.34](#)) for multiplicative

speckle noise removal process, which is strictly convex for $I \in (0, 2J)$. A major shortcoming of the non-convex model is, which may not provide a globally optimum solution. Several authors have suggested convex functionals ([Shi and Osher, 2008](#); [Jin and Yang, 2010, 2011](#); [Dong et al., 2013](#)) with different fidelity terms to overcome this issue in the non-convex model. All the strategies mentioned above are efficient in image denoising. But under high noise levels, uncertainty emerges in the classification of the clean and affected pixels, which give an edge map with multiple false-positive edge pixels. However, due to the wave nature of the telegraph equation (1.17), it could upgrade the visual appearance of the located edges and preserves the high oscillatory patterns better than parabolic PDE. To overcome the similar issue of uncertainty and to obtain a meaningful decision, another emerging technique, namely fuzzy set theory, is used for speckle noise removal ([Hua and Jinwen, 2009](#); [Binaee and Hasanzadeh, 2014](#); [Babu and Sudha, 2016](#); [Nadeem et al., 2019](#)). The fuzzy logic-based approach is a two-stage architecture. At first, classify each pixel in an image into three different classes such as ‘edge’, ‘noise’, and ‘homogenous’ and then perform fuzzy filtering by using these detected edges and their impact on the neighboring pixels. Both steps are based on the fuzzy set theory which makes use of membership functions ([Klir and Yuan, 1995](#)). In the literature ([Aja et al., 2001](#); [Song and Tizhoosh, 2003](#); [Prasath and Delhibabu, 2014](#)), some hybrid fuzzy anisotropic diffusion methods are available for image denoising. In these techniques, fuzzy logic based diffusion coefficients are used to control the whole diffusion process instead of taking the image gradient dependent diffusion coefficient. The main issue with anisotropic diffusion based image denoising is the lack of description of the statistical properties in the present degradation. The total variational technique is more suitable for this. Moreover, we have mentioned earlier that the telegraph equation can upgrade the quality of the detected edges and can preserve the high oscillatory patterns in the images better than parabolic PDE. Hence, to prove the efficacy of the telegraph equation for speckle noise reduction, the present work suggests a new approach for image selective smoothing and restoration. The proposed telegraph equation is derived from the total variational approach. Moreover, to overcome the limitations of gradient-based edge detection, we introduce a robust fuzzy edge indicator function ([Chaira and Ray, 2008](#)) into the proposed framework, which is very efficient for edge detection. Furthermore, we study the existence and uniqueness of weak solutions of a regularized version of the proposed model. Finally, the present model is applied to some standard synthetic and natural test images, along with two different real SAR images corrupted by speckle noise. We use an explicit finite difference scheme to solve the

model numerically. The quality of despeckled images using the proposed model is compared with the results of some existing PDE based models. The computational results indicate that the proposed model works better than the other techniques considered here.

The rest of the chapter is organized as follows. Section 6.2 introduces the concept of fuzzy edge detection. Section 6.3 describes the proposed fuzzy edge detector induced telegraph total variation approach for image despeckling. In section 6.4, we study the existence and uniqueness of weak solutions of a regularized version of the present system. Section 6.5 describes the numerical implementation of the suggested model. In section 6.6, the simulated despeckling results obtained by the new algorithm are compared with the results of other existing PDE based methods. We conclude the paper in section 6.7.

6.2 Intuitionistic Fuzzy Sets

The existing speckle noise filtering methods fail to preserve significant information: namely to capture the edge information from noise, thereby suppressing the edges or enhancing the noise particle assuming by edges. Therefore, to preserve the image details along with smoothing, the theory of fuzzy set has gained much popularity in recent times (Ho and Ohnishi, 1995; Chaira and Ray, 2003; Becerikli and Karan, 2005). Atanassov (2003) proposed the concept of intuitionistic fuzzy set in which the author combined the degree of non-membership with some hesitation degree. Szmidt and Kacprzyk (2000) introduced some new distance measures between intuitionistic fuzzy sets with the generalization of the Hamming and the Euclidean distance. Next, using intuitionistic fuzzy sets, Chaira and Ray (2008) proposed a new measure, called intuitionistic fuzzy divergence (IFD) and its application to image edge detection. A fuzzy set P in a finite universal set $Y = \{y_1, y_2, \dots, y_n\}$ can be defined as

$$P = \{(y, \mu_P(y)) | y \in Y\},$$

where the membership function $\mu_P(y) : Y \rightarrow [0, 1]$ defines the measure of belongingness of an element y in the finite set Y . An intuitionistic fuzzy set, proposed by Attanassov, can be mathematically represented as

$$P = \{(y, \mu_P(y), \nu_P(y)) | y \in Y\},$$

where the functions $\mu_P(y), \nu_P(y) : Y \rightarrow [0, 1]$ are, respectively, the membership degree and the non-membership degree of an element y in a finite set Y with the

necessary condition

$$0 \leq \mu_P(y) + \nu_P(y) \leq 1.$$

Further, a third function, $\pi(y)$ is considered, which is known as the hesitation degree. So, with the introduction of hesitation degree, an intuitionistic fuzzy set P in Y may be described as

$$P = \{(y, \mu_P(y), \nu_P(y), \pi_P(y)) | y \in Y\},$$

with the condition

$$\mu_P(y) + \nu_P(y) + \pi_P(y) = 1.$$

In 2008, [Chaira and Ray \(2008\)](#) defined a new IFD considering the membership degree, the non-membership degree, and the hesitation degree as

$$F(I_{j,k}) = \max_N [\min_r (\text{IFD}(P, Q))],$$

where (j, k) is the pixel position in the image I , P and Q represents two intuitionistic fuzzy sets, N is the number of templates, and r is the number of elements in the template. The overall intuitionistic fuzzy divergence (IFD) between the image set P and template set Q , is calculated as

$$\begin{aligned} \text{IFD}(P, Q) = & \sum_j \sum_k \left\{ 2 - [1 - \mu_P(p_{jk}) + \mu_Q(q_{jk})] e^{\mu_P(p_{jk}) - \mu_Q(q_{jk})} \right. \\ & - [1 - \mu_Q(q_{jk}) + \mu_P(p_{jk})] e^{\mu_Q(q_{jk}) - \mu_P(p_{jk})} \\ & + (2 - [1 - (\mu_P(p_{jk}) - \mu_Q(q_{jk})) \\ & + (\pi_Q(q_{jk}) - \pi_P(p_{jk}))] e^{\mu_P(p_{jk}) - \mu_Q(q_{jk}) - (\pi_Q(q_{jk}) - \pi_P(p_{jk}))} \\ & - [1 - (\pi_Q(q_{jk}) - \pi_P(p_{jk})) + (\mu_P(p_{jk}) \\ & - \mu_Q(q_{jk}))] e^{\pi_Q(q_{jk}) - \pi_P(p_{jk}) - (\mu_P(p_{jk}) - \mu_Q(q_{jk}))} \Big) \right\}, \end{aligned}$$

where p_{jk} and q_{jk} represent the two pixels in the image set P and template set Q , respectively.

6.3 Proposed Telegraph Total Variation Model

6.3.1 The Proposed Model

Following the ideas of (Dong *et al.*, 2013), we consider the energy minimization problem

$$I^* := \operatorname{argmin}_{I \in S(\Omega)} \left\{ TV(I) + \lambda \int_{\Omega} \left(I + J \log \frac{1}{I} \right) dx \right\}. \quad (6.1)$$

The fidelity term taken in (6.1) is strictly convex for all I . Associated Euler-Lagrange equation for (6.1) can be written as

$$G(\nabla I, \nabla^2 I) - \lambda \left(1 - \frac{J}{I} \right) = 0 \text{ in } \Omega, \quad (6.2)$$

where ∇I and $\nabla^2 I$ represent the gradient and Hessian matrix of I concerning the space variable x . Note that the edge information obtained by (6.2) depends only on the image gradient, which produces broken and discontinued edges. As image edges and boundaries have fuzziness, which is caused by multiplicative speckle noise, we suggest the following fuzzy edge detector driven total variation for I

$$TV_{\theta}(I) = \int_{\Omega} \theta(I) |DI|. \quad (6.3)$$

In (6.3), the fuzzy edge indicator function $\theta(I) = 1 - F(I)$ works as a weight function in the well-known total variational framework and controls the amount of smoothing at different regions by providing pixel-wise edge characterization using the IFD function F . Hence, with the choice of the positive valued function θ , the fuzzy edge indicator function is much smaller at the region of edges or boundaries than the homogeneous region. Therefore, at the non-homogeneous region ($\theta(I) \rightarrow 0$) the smoothing process is slow while at the homogeneous region ($\theta(I) \rightarrow 1$) the speed of smoothing is very high. Another advantage of the use of θ is that it has the capability of identifying the noisy pixels from edges or boundaries based on the hesitation degree π . The above analysis leads us to propose a fuzzy edge detector driven convex total variation model for multiplicative speckle noise removal. Hence, using (6.3) we replace $TV(I)$ by $TV_{\theta}(I)$ in (6.1) and introduced the following model

$$I^* := \operatorname{argmin}_{I \in S(\Omega)} \left\{ \int_{\Omega} \theta(I) |DI| + \lambda \int_{\Omega} \left(I + J \log \frac{1}{I} \right) dx \right\}. \quad (6.4)$$

The associated Euler-Lagrange equation of (6.4) (ignoring the term $\theta'(I)|\nabla I|$) can be written as

$$\operatorname{div} \left(\theta(I) \frac{\nabla I}{|\nabla I|} \right) - \lambda \left(1 - \frac{J}{I} \right) = 0 \text{ in } \Omega, \quad (6.5)$$

where λ is the regularization parameter calculated as explained in (Dong *et al.*, 2013). This system provides the steady-state solution and thus fails to produce the best effect. Hence, it is more meaningful to use the following evolutionary version of (6.5)

$$\partial_t I = \operatorname{div} \left(\theta(I) \frac{\nabla I}{|\nabla I|} \right) - \lambda \left(1 - \frac{J}{I} \right) \text{ in } \Omega_T.$$

Moreover, our interest is to investigate the efficiency of the telegraph equation for image despeckling; therefore, our final proposed model (telegraph total variation model) takes the form

$$\left. \begin{aligned} \partial_{tt} I + \gamma \partial_t I &= \operatorname{div} \left(\theta(I) \frac{\nabla I}{|\nabla I|} \right) - \lambda \left(1 - \frac{J}{I} \right) && \text{in } \Omega_T, \\ \partial_n I &= 0 && \text{on } \partial\Omega_T, \\ I(x, 0) &= J(x), \quad \partial_t I(x, 0) = 0 && \text{in } \Omega. \end{aligned} \right\} \quad (6.6)$$

6.3.2 The advantages & novelty of the proposed model

The proposed approach possesses the following analogous advantages and novelty:

- The energy functional (6.4) is globally convex; therefore, it provides a unique minimizer.
- Since the proposed model consists of the telegraph equation, it would enhance the detect edges better than the diffusion based approaches in the noise removal process. In the existing literature, telegraph total variation model has been used only to remove the additive Gaussian noise. In the present study, for the first time, we have investigated the efficiency of the telegraph total variation model for the multiplicative speckle noise removal process.
- The fuzzy nature of speckle noise and edges is studied through the IFD function. In this fuzzy edge detection process, each noisy pixel in an image is mapped into different classes such as homogeneous, details, and edges; therefore, it controls the smoothing process better than other existing diffusion based methods.

- Based on all these inferences, the present work marks the first step towards the use of the telegraph equation, derived from the total variation framework with a fuzzy edge indicator function, to multiplicative speckle noise removal process.

6.4 Existence and Uniqueness of Weak Solution

In this section, we discuss the existence and uniqueness of weak solutions of a regularized version of the model (6.6). Consider the regularized model as

$$\partial_{tt}I + \gamma\partial_t I = \operatorname{div}\left(\frac{\theta(I_\xi)}{1+|\nabla I_\xi|}\nabla I\right) - \lambda\left(1 - \frac{J}{I}\right) \quad \text{in } \Omega_T, \quad (6.7)$$

$$\partial_n I = 0 \quad \text{on } \partial\Omega_T, \quad (6.8)$$

$$I(x, 0) = J(x), \quad \partial_t I(x, 0) = 0 \quad \text{in } \Omega, \quad (6.9)$$

Since the system (6.7)–(6.9) is nonlinear, we first consider the linearized model and then use Schauder fixed point theorem (Evans, 1998) to show the existence of a weak solution. For simplicity, we choose all the constants involved in the equations (6.7)–(6.9) equals to 1.

6.4.1 Technical framework & statement of the main result

Throughout this section, C denotes a generic positive constant and we write L^p , H^1 , $(H^1)'$ instead of $L^p(\Omega)$, $H^1(\Omega)$, $(H^1(\Omega))'$, respectively. Let us introduce the solution space W for the system (6.7)–(6.9):

$$W = \left\{ w \in L^\infty(0, T; H^1), \partial_t w \in L^\infty(0, T; L^2), \partial_{tt} w \in L^2(0, T; (H^1)') \right\}.$$

Note that, W is a Hilbert space equipped with the norm

$$\|w\|_W = \|w\|_{L^\infty(0, T; H^1)} + \|\partial_t w\|_{L^\infty(0, T; L^2)} + \|\partial_{tt} w\|_{L^2(0, T; (H^1)')}.$$

Definition 6.1. A function I is called a weak solution of the model (6.7)–(6.9), if $I \in W$ and satisfies (6.7) in the sense of distributions, i.e., for a.e. $t \in (0, T)$, there holds

$$\langle \partial_{tt} I, \phi \rangle + \int_{\Omega} \left(\partial_t I \phi + \frac{\theta(I_\xi)}{1+|\nabla I_\xi|} \nabla I \cdot \nabla \phi \right) dx = - \int_{\Omega} \left(1 - \frac{J}{I} \right) \phi dx, \quad \forall \phi \in H^1,$$

along with the initial and boundary conditions (6.8)–(6.9).

As we mentioned, our aim is to establish the existence and uniqueness of weak solutions of the model (6.7)–(6.9), and we will do so under the following assumptions:

A.1 The initial data J is an H^2 -valued function such that $0 < \alpha := \inf_{x \in \Omega} J(x)$.

A.2 The function $\theta : \mathbb{R} \rightarrow \mathbb{R}$ is a positive, bounded, and Lipschitz function. More precisely, there exist $\delta, C_\theta > 0$ such that

$$\begin{cases} \delta \leq \theta(\cdot) \leq 1, \\ |\theta(x) - \theta(y)| \leq C_\theta |x - y|, \quad \forall x, y \in \mathbb{R}. \end{cases}$$

Theorem 6.1. *Let the assumptions **A.1**–**A.2** be true. Then the model (6.7)–(6.9) has a weak solution. Moreover, in addition, if $\beta := \sup_{x \in \Omega} J(x) < \infty$, the solution is unique.*

6.4.2 Linearized model & existence of weak solution

For any positive constant $M_1 > 0$, define

$$W_{M_1} = \left\{ \bar{I} \in W : \|\bar{I}\|_{L^\infty(0,T;H^1)} + \|\partial_t \bar{I}\|_{L^\infty(0,T;L^2)} \leq M_1 \|J\|_{H^1}; \right. \\ \left. 0 < \alpha \leq \bar{I}(x, t) \text{ for a.e. } (x, t) \in \Omega_T \right\}.$$

For any $\bar{I} \in W_{M_1}$, consider the following linearized equation

$$\partial_{tt} I + \partial_t I - \operatorname{div}(\bar{g}(x, t) \nabla I) = -\left(1 - \frac{J}{\bar{I}}\right) \quad \text{in } \Omega_T, \quad (6.10)$$

with the conditions (6.8)–(6.9), where the function \bar{g} is given by

$$\bar{g}(x, t) \equiv g_{\bar{I}}(x, t) := \frac{\theta(\bar{I}_\xi)}{1 + |\nabla \bar{I}_\xi|}.$$

In view of the property of convolution and assumption **A.1** the following inequalities hold:

$$\kappa := \frac{\delta}{1 + M_1 C_\xi \|J\|_{H^1}} \leq \bar{g} \leq 1; \quad |\partial_t \bar{g}| \leq C, \quad (6.11)$$

for some constant $C > 0$, depending only on θ , Ω , M_1 , G_ξ , and J . Indeed, since

$$1 + |\nabla G_\xi * \bar{I}| \leq 1 + \|\nabla G_\xi\|_{L^2} \|\bar{I}\|_{L^\infty(0,T;L^2)} \leq 1 + C_\xi M_1 \|J\|_{H^1} \equiv 1 + M_1 C_\xi \|J\|_{H^1},$$

we see that

$$\frac{1}{1 + M_1 C_\xi \|J\|_{H^1}} \leq \frac{1}{1 + |\nabla G_\xi * \bar{I}|} \leq 1.$$

Therefore, thanks to the assumption [A.2](#), we obtain

$$\kappa := \frac{\delta}{1 + M_1 C_\xi \|J\|_{H^1}} \leq \frac{\theta(\bar{I}_\xi)}{1 + |\nabla \bar{I}_\xi|} := \bar{g}(x, t) \leq 1.$$

To see the second inequality of [\(6.11\)](#), notice that

$$\begin{aligned} |\partial_t \bar{g}| &\leq C_\theta |G_\xi * \partial_t \bar{I}| + |\nabla G_\xi * \partial_t \bar{I}| \\ &\leq C_\theta \|G_\xi\|_{L^2} \|\partial_t \bar{I}\|_{L^\infty(0, T; L^2)} + \|\nabla G_\xi\|_{L^2(\Omega)} \|\partial_t \bar{I}\|_{L^\infty(0, T; L^2)} \\ &\leq C(\theta, \Omega, G_\xi, J, M_1). \end{aligned}$$

Since \bar{g} satisfies [\(6.11\)](#), one can apply Galerkin method ([Evans, 1998](#)) to show that there exists a unique weak solution $I \in W$ of the linearized equation [\(6.10\)](#) with the conditions [\(6.8\)](#)–[\(6.9\)](#).

Energy Estimates

Note that $\partial_t I \in L^\infty(0, T; H^1)$. Multiplying equation [\(6.10\)](#) by $\partial_t I$ and integrating by parts we have

$$\begin{aligned} \frac{1}{2} \frac{d}{dt} \|\partial_t I\|_{L^2}^2 + \|\partial_t I\|_{L^2}^2 + \int_\Omega \bar{g} \nabla I \cdot \nabla (\partial_t I) dx &= \int_\Omega \left(\frac{J}{\bar{I}} - 1 \right) \partial_t I dx \\ &\leq \frac{1}{2} \left\| \frac{J}{\bar{I}} - 1 \right\|_{L^2}^2 + \frac{1}{2} \|\partial_t I\|_{L^2}^2. \end{aligned} \quad (6.12)$$

Note that, using integration by parts formula and [\(6.11\)](#), we have

$$\int_\Omega \bar{g} \nabla I \cdot \nabla (\partial_t I) dx \geq \frac{1}{2} \frac{d}{dt} \int_\Omega \bar{g} |\nabla I|^2 dx - \frac{C}{2} \|\nabla I\|_{L^2}^2. \quad (6.13)$$

Again, using [A.1](#), we get that

$$\begin{aligned} \left\| \frac{J}{\bar{I}} - 1 \right\|_{L^2}^2 &\leq \frac{1}{\alpha^2} \|J - \bar{I}\|_{L^2}^2 \leq \frac{2}{\alpha^2} \left(\|J\|_{H^1}^2 + \|\bar{I}\|_{H^1}^2 \right) \\ &\leq \frac{2}{\alpha^2} (1 + C^2) \|J\|_{H^1}^2. \end{aligned} \quad (6.14)$$

Combining the above two estimates, we get

$$\begin{aligned} \frac{d}{dt} \left[\|\partial_t I\|_{L^2}^2 + \int_{\Omega} \bar{g} |\nabla I|^2 dx \right] &\leq \frac{1+C^2}{\alpha^2} \|J\|_{H^1}^2 + C_1 \|\nabla I\|_{L^2}^2 + \|\partial_t I\|_{L^2}^2 \\ &\equiv C_2 + C_1 \|\nabla I\|_{L^2}^2 + \|\partial_t I\|_{L^2}^2. \end{aligned} \quad (6.15)$$

Thanks to the lower bound of \bar{g} as in (6.11), we observe that

$$\|\nabla I\|_{L^2}^2 \leq \frac{1}{\kappa} \int_{\Omega} \bar{g} |\nabla I|^2 dx. \quad (6.16)$$

and hence, we obtain from (6.15)

$$\frac{d}{dt} \left[\|\partial_t I\|_{L^2}^2 + \int_{\Omega} \bar{g} |\nabla I|^2 dx \right] \leq C_1 + C \left(\|\partial_t I\|_{L^2}^2 + \int_{\Omega} \bar{g} |\nabla I|^2 dx \right).$$

An application of Gronwall's lemma gives: for a.e. $t \in (0, T]$

$$\|\partial_t I(t)\|_{L^2}^2 + \|\nabla I(t)\|_{L^2}^2 \leq e^{Ct} (C_2 + tC_1), \quad (6.17)$$

where $C_2 = \|\partial_t I(0)\|_{L^2}^2 + \int_{\Omega} \bar{g}(x, 0) |\nabla I(x, 0)|^2 dx$. Since $I(x, t) = I(x, 0) + \int_0^t \partial_s I ds$, we have, applying Young's inequality and (6.17), also we have

$$\|I(t)\|_{L^2}^2 \leq 2\|J\|_{H^1}^2 + 2T^2 e^{CT} (C_2 + tC_1). \quad (6.18)$$

We combine (6.17) and (6.18) to conclude

$$\|I\|_{L^\infty(0,T;H^1)} + \|\partial_t I\|_{L^\infty(0,T;L^2)} \leq C\|J\|_{H^1}. \quad (6.19)$$

Multiplying the equation (6.10) by $\phi \in H^1$ with $\|\phi\|_{H^1} \leq 1$, and integrating over Ω , and then using Cauchy-Schwarz inequality along with (6.19) to obtain

$$\|\langle \partial_{tt} I, \phi \rangle\| \leq \{2C_4 + \sqrt{2(1+C^2)/\alpha^2}\} \|J\|_{H^1} \|\phi\|_{H^1}.$$

Hence, by the definition of norm in $(H^1)'$, we infer that $\|\partial_{tt} I\|_{(H^1)'} \leq C\|J\|_{H^1}$. Squaring and integrating over $(0, T)$, we obtain

$$\int_0^T \|\partial_{tt} I\|_{(H^1)'}^2 dt \leq CT\|J\|_{H^1}^2. \quad (6.20)$$

Passing to the limit

From (6.19) and (6.20), we introduce the subspace W_0 of W defined by

$$W_0 = \left\{ w \in W : \|w\|_W \leq C\|J\|_{H^1}, 0 < \alpha \leq w(x, t) \text{ for a.e. } (x, t) \in \Omega_T, \right. \\ \left. \text{and } w \text{ satisfies (6.9)} \right\}.$$

Moreover, one can prove that W_0 is a non-empty, convex and weakly compact subset of W . Consider a mapping

$$\begin{aligned} \mathcal{P} : W_0 &\rightarrow W_0 \\ w &\mapsto I_w. \end{aligned}$$

In order to use Schauder fixed point theorem on \mathcal{P} , only we need to prove that the mapping $\mathcal{P} : w \rightarrow I_w$ is weakly continuous from W_0 into W_0 . Let w_k be a sequence that converges weakly to some w in W_0 and let $I_k = I_{w_k}$. We have to show that $\mathcal{P}(w_k) := I_k$ converges weakly to $\mathcal{P}(w) := I_w$. From the classical results of compact inclusion in Sobolev spaces (Adams, 1975), we can extract subsequences of $\{w_k\}$ and $\{I_k\}$ still denoted by $\{w_k\}$ and $\{I_k\}$ respectively such that for some $I \in W_0$, we have, as $k \rightarrow \infty$

$$\left\{ \begin{array}{l} w_k \rightarrow w \text{ in } L^2(0, T; L^2) \text{ and a.e. on } \Omega_T, \\ \frac{1}{w_k} \rightarrow \frac{1}{w} \text{ in } L^2(0, T; L^2) \text{ and a.e. on } \Omega_T, \\ G_\xi * w_k \rightarrow G_\xi * w \text{ in } L^2(0, T; L^2) \text{ and a.e. on } \Omega_T, \\ \theta(G_\xi * w_k) \rightarrow \theta(G_\xi * w) \text{ in } L^2(0, T; L^2) \text{ and a.e. on } \Omega_T, \\ \partial_{x_i} G_\xi * w_k \rightarrow \partial_{x_i} G_\xi * w \ (i = 1, 2) \text{ in } L^2(0, T; L^2) \\ \text{and a.e. on } \Omega_T, \\ \frac{1}{1 + |\nabla G_\xi * w_k|} \rightarrow \frac{1}{1 + |\nabla G_\xi * w|} \text{ in } L^2(0, T; L^2) \\ \text{and a.e. on } \Omega_T, \\ \frac{\theta(G_\xi * w_k)}{1 + |\nabla G_\xi * w_k|} \rightarrow \frac{\theta(G_\xi * w)}{1 + |\nabla G_\xi * w|} \text{ in } L^2(0, T; L^2) \\ \text{and a.e. on } \Omega \times (0, T), \\ I_k \rightarrow I \text{ weakly-* in } L^\infty(0, T; H^1), \\ \partial_t I_k \rightarrow \partial_t I \text{ weakly-* in } L^\infty(0, T; L^2), \end{array} \right.$$

$$\begin{cases} \partial_{tt} I_k \longrightarrow \partial_{tt} I \text{ weakly-* in } L^2(0, T; (H^1)'), \\ I_k \longrightarrow I \text{ in } L^2(0, T; L^2), \\ \partial_{x_i} I_k \rightarrow \partial_{x_i} I \ (i = 1, 2) \text{ weakly-* in } L^\infty(0, T; L^2). \end{cases}$$

The above convergence allow us to pass to the limit in the equation (6.10) and obtain $I = \mathcal{P}(w)$. Moreover, since the solution of (6.10) is unique, the whole sequence $I_k = \mathcal{P}(w_k)$ converges weakly in W_0 to $I = \mathcal{P}(w)$. Hence \mathcal{P} is weakly continuous. Consequently, thanks to the Schauder fixed point theorem, there exists $w \in W_0$ such that $w = \mathcal{P}(w) = I_w$. Thus, the function I_w solves the system (6.7)–(6.9).

Lemma 6.2. *Let I be a weak solution of the system (6.7)–(6.9) with the property $\beta := \sup_{x \in \Omega} J(x) < \infty$, then*

$$0 < \alpha \leq I(x, t) \leq \beta \quad \text{for a.e. } (x, t) \in \Omega_T. \quad (6.21)$$

Proof. Since I is a weak solution of (6.7)–(6.9), we see that $(I - \beta)_+ \in H^1(\Omega)$, where $(\cdot)_+$ is the truncated function defined by as $(\Phi)_+ = \max\{0, \Phi\}$. Integrating the equation (6.7) w.r.t. to t , we have

$$\partial_t I + (I - J) - \int_0^t \operatorname{div}(g \nabla I) dt = \int_0^t \left(\frac{J}{I} - 1 \right) dt. \quad (6.22)$$

Multiply (6.22) by $(I - \beta)_+$ and integrating over Ω , we get

$$\begin{aligned} & \int_{\Omega} \partial_t I (I - \beta)_+ dx + \int_{\Omega} (I - J) (I - \beta)_+ dx + \\ & \int_0^t \int_{\{I \geq \beta\}} g |\nabla I|^2 dx dt = \int_0^t \int_{\{I \geq \beta\}} \left(\frac{J}{I} - 1 \right) (I - \beta)_+ dx dt \end{aligned} \quad (6.23)$$

One can note that, $g \geq 0$, $(I - J)(I - \beta)_+ \geq 0$, and $\int_{\{I \geq \beta\}} \left(\frac{J}{I} - 1 \right) (I - \beta)_+ dx \leq 0$. Therefore, we have $\frac{d}{dt} \int_{\Omega} |(I - \beta)_+|^2 dx \leq 0$. Again, since $J \leq \beta$, we obtain $\int_{\Omega} |(I - \beta)_+|^2 dx \leq 0$ for a.e. $t \in [0, T]$. Therefore, $I(x, t) \leq \beta$ for a.e. $(x, t) \in \Omega_T$. Similarly, multiplying (6.22) by $(I - \alpha)_- \in H^1$ and then integrating over Ω to conclude that $0 < \alpha \leq I(x, t)$ for a.e. $(x, t) \in \Omega_T$, where $(\cdot)_-$ is the truncated function defined as $(\Phi)_- = \min\{0, \Phi\}$. Hence (6.21) holds true. This completes the proof. \square

6.4.3 Uniqueness of weak solution

Following the idea as in (Evans, 1998), we prove the uniqueness of weak solutions of the model (6.7)–(6.9). Let I_1 and I_2 be two weak solutions of (6.7)–(6.9). Then for almost every $t \in (0, T)$, we have

$$\partial_{tt}I + \partial_t I - \operatorname{div}(g_{I_1}\nabla I) = \operatorname{div}((g_{I_1} - g_{I_2})\nabla I_2) - \frac{J}{I_1 I_2}I \text{ in } \Omega_T, \quad (6.24)$$

$$\partial_n I = 0 \quad \text{on } \partial\Omega_T, \quad (6.25)$$

$$I(x, 0) = 0, \quad \partial_t I(x, 0) = 0 \quad \text{in } \Omega. \quad (6.26)$$

where $I = I_1 - I_2$. It suffices to show that $I \equiv 0$. To verify this, fix $0 < s < T$, and set for $i = 1, 2$,

$$v_i(., t) = \begin{cases} \int_t^s I_i(., \tau) d\tau, & 0 < t \leq s, \\ 0, & s \leq t < T. \end{cases} \quad (6.27)$$

Note that, for $t \in (0, T)$,

$$\begin{cases} \partial_t v_i(x, t) = -I_i(x, t), & i = 1, 2, \\ v_i(\cdot, t) \in H^1, \quad \partial_n v_i = 0, & \text{on } \partial\Omega \\ \text{in the sense of distribution.} \end{cases} \quad (6.28)$$

Set $v = v_1 - v_2$. Then $v(\cdot, s) = 0$. Multiplying (6.24) by v , integrating over $\Omega \times (0, s)$ and using (6.25) and (6.26) along with the integration by parts formula, we obtain

$$\begin{aligned} & \int_0^s \int_\Omega (-\partial_t I \partial_t v - I \partial_t v + g_{I_1} \nabla I \cdot \nabla v) dx dt \\ &= - \int_0^s \int_\Omega (g_{I_1} - g_{I_2}) \nabla I_2 \cdot \nabla v dx dt - \int_0^s \int_\Omega \frac{J}{I_1 I_2} I v dx dt. \end{aligned}$$

We use (6.28) in the above equality, and then use Cauchy-Schwarz inequality along with the fact that $\frac{J}{I_1 I_2} \leq \frac{\beta}{\alpha^2}$ (using the result of Lemma 6.2), to get

$$\begin{aligned} & \frac{1}{2} \int_0^s \int_\Omega \partial_t(I^2) dx dt + \int_0^s \int_\Omega I^2 dx dt - \int_0^s \int_\Omega g_{I_1} \partial_t \nabla v \cdot \nabla v dx dt \\ & \leq \int_0^s \| (g_{I_1} - g_{I_2})(t) \|_{L^\infty} \| \nabla I_2(t) \|_{L^2} \| \nabla v(t) \|_{L^2} dt + \frac{\beta}{2\alpha^2} \int_0^s \| I(t) \|_{L^2}^2 dt \\ & \quad + \frac{\beta}{2\alpha^2} \int_0^s \| v(t) \|_{L^2}^2 dt. \end{aligned}$$

Now using the fact that

$$\begin{aligned} g_{I_1} \partial_t \nabla v \cdot \nabla v &= \frac{1}{2} \partial_t (g_{I_1} |\nabla v|^2) - \frac{1}{2} \partial_t g_{I_1} |\nabla v|^2, \\ \nabla v(x, s) &= 0, \end{aligned}$$

and (6.26), we have

$$\begin{aligned} &\frac{1}{2} \|I(s)\|_{L^2}^2 + \int_0^s \|I(t)\|_{L^2}^2 dt + \frac{1}{2} \int_{\Omega} g_{I_1}(x, 0) |\nabla v(x, 0)|^2 dx \\ &\leq \left| -\frac{1}{2} \int_0^s \int_{\Omega} |\nabla v|^2 \partial_t g_{I_1} dx dt \right| + \int_0^s \|(g_{I_1} - g_{I_2})(t)\|_{L^\infty} \|\nabla I_2(t)\|_{L^2} \|\nabla v(t)\|_{L^2} dt \\ &\quad + \frac{\beta}{2\alpha^2} \int_0^s \|I(t)\|_{L^2}^2 dt + \frac{\beta}{2\alpha^2} \int_0^s \|v(t)\|_{L^2}^2 dt. \end{aligned} \quad (6.29)$$

As seen in the proof of existence, there exist positive constants $\kappa_1, C_5 > 0$ such that

$$\kappa_1 \leq g_{I_1} \leq 1, \quad |\partial_t g_{I_1}| \leq C_5.$$

Moreover, one can use property of convolution along the stated assumption A.2 on θ to show that

$$\|(g_1 - g_2)(t)\|_{L^\infty} \leq C(\xi, \alpha, J) \|I(t)\|_{L^2}.$$

Thus, using the above estimates in (6.29), we have

$$\frac{1}{2} \|I(s)\|_{L^2}^2 + \int_0^s \|I(t)\|_{L^2}^2 dt + \frac{C_6}{2} \|\nabla v(0)\|_{L^2}^2 \leq C \left(\int_0^s \|I(t)\|_{L^2}^2 dt + \int_0^s \|v(t)\|_{H^1}^2 dt \right). \quad (6.30)$$

Observe from (6.27) that

$$\|v(0)\|_{L^2}^2 = \left\| \int_0^s I(t) dt \right\|_{L^2}^2 \leq T \int_0^s \|I(t)\|_{L^2}^2 dt. \quad (6.31)$$

Using (6.31) in (6.30), we have

$$\frac{1}{2} \|I(s)\|_{L^2}^2 + \int_0^s \|I(t)\|_{L^2}^2 dt + \frac{C_6}{2} \|v(0)\|_{H^1}^2 \leq C \left(\int_0^s \|I(t)\|_{L^2}^2 dt + \int_0^s \|v(t)\|_{H^1}^2 dt \right). \quad (6.32)$$

Set

$$w_i(., t) = \int_0^t I_i(., \tau) d\tau; \quad w(., t) = (w_1 - w_2)(., t), \quad 0 < t \leq T.$$

In view of the above definition and (6.28), we notice that

$$\begin{aligned} v(x, 0) &= v(x, s) + \int_0^s I(x, t) dt = \int_0^s I(x, t) dt = w(x, s) \\ v(x, t) &= w(x, s) - w(x, t), \quad 0 < t \leq s. \end{aligned}$$

Hence (6.32) reduces to

$$\begin{aligned} &\frac{1}{2} \|I(s)\|_{L^2}^2 + \int_0^s \|I(t)\|_{L^2}^2 dt + \frac{C_6}{2} \|w(s)\|_{H^1}^2 \\ &\leq C \int_0^s \|I(t)\|_{L^2}^2 dt + 2Cs \|w(s)\|_{H^1}^2 + 2C \int_0^s \|w(t)\|_{H^1}^2 dt. \end{aligned} \quad (6.33)$$

Choose T_1 sufficiently small such that

$$\frac{C_6}{2} - 2T_1C > 0.$$

Then, for $0 < s \leq T_1$, we have, from (6.33)

$$\|I(s)\|_{L^2}^2 + \|w(s)\|_{H^1}^2 \leq C \int_0^s (\|I(t)\|_{L^2}^2 + \|w(t)\|_{H^1}^2) dt,$$

for some constant $C > 0$. Consequently, an application of Gronwall's lemma then implies $I \equiv 0$ on $[0, T_1]$. Finally, we apply the same argument on the intervals $(T_1, 2T_1]$, $(2T_1, 3T_1]$, ... step by step, and eventually deduce that $I_1 = I_2$ on $(0, T)$. This completes the proof of Theorem 6.1.

6.5 Numerical Implementation

We use an explicit finite difference scheme to discretize the system (6.6). Using the finite difference formulas as discussed in section 1.3, the discretized form of the first equation of (6.6) could be written as

$$\begin{aligned} (1 + \gamma\tau)I_{i,j}^{n+1} &= (2 + \gamma\tau)I_{i,j}^n - I_{i,j}^{n-1} + \tau^2 \left\{ \nabla_x (g_{i,j}^n \nabla_x I_{i,j}^n) + \nabla_y (g_{i,j}^n \nabla_y I_{i,j}^n) \right\} \\ &\quad - \tau^2 \lambda^n \left(1 - \frac{J_{i,j}}{I_{i,j}^n} \right), \end{aligned} \quad (6.34)$$

where $g_{i,j}^n = \frac{\theta(I_{i,j}^n)}{|\nabla I_{i,j}^n| + \epsilon}$, λ^n is the value of λ at the n th iteration, the fuzzy edge indicator function can be calculated via, $\theta(I_{i,j}^n) = 1 - F(I_{i,j}^n)$, and $\epsilon > 0$ is a small number to avoid zero magnitude of the image gradient. The initial conditions are $I_{i,j}^0 = J_{i,j} = J(x_i, y_j)$, $I_{i,j}^1 = I_{i,j}^0$ and the boundary conditions are as discussed in [section 1.3](#).

6.6 Computational Results & Discussion

This section presents the qualitative and quantitative results of restored images, which are described in two subsections [6.6.3–6.6.4](#). First, we validate the despeckling efficiency of the proposed system [\(6.6\)](#) using synthetic and natural images. The numerical experiments using these images with ground truth information enable us to quantify the effectiveness of the proposed image despeckling model. Whereas, the ability of the system [\(6.6\)](#) is investigated using real SAR and ultrasound images, which illustrate the useful application of the present approach for image despeckling.

6.6.1 Setup and Parameters

To check the image despeckling ability of the system [\(6.6\)](#), we perform a large number of computational experiments using three different types of synthetic and natural images (see [Figure 6.1](#)), two real SAR images (see [Figure 6.8a](#) and [Figure 6.9a](#)), and two real ultrasound images (see [Figure 6.10a](#) and [Figure 6.11a](#)). For the study, synthetic and natural images are initially corrupted by multiplying speckle noise with “looks” $L = \{1, 3, 5, 10\}$ using MATLAB code [Chapter 4, [section 4.5](#)]. We compare the despeckled results computed by the proposed approach with the results of the AA model [\(1.34\)](#), Dong model [\(4.1\)](#), DDD model [\(4.2\)–\(4.4\)](#), and ZZDB model [\(4.5\)–\(4.7\)](#). To approximate the above explained PDE models we use the similar numerical method as discussed in [section 6.5](#). The time step size ($\tau = 0.2$) and the stopping criterion are kept same for all considered models. Also, for fair and effective comparison, different parameters of the considered models are optimized manually to obtain their best performance level. The numerical results are computed using MATLAB (*R2019b*) program running on a desktop computer under Windows 7 with an Intel Core i5 dual-core CPU at 2.53 GHz with 4 GB of RAM.

6.6.2 Image Quality Measurement

Since the suggested approach is claimed to be an improvement over the existing PDE based models, our aim is to compare the denoising results in terms of visual quality and quantitative measures. We compute the values of four standard parameters PSNR, MSSIM, SI, and BRISQUE for the quantitative comparison of the despeckled images computed by different approaches. Also, we compute the ratio image, the 2D contour plot, and 3D surface plot for better comparison of computed results obtained by the present model as well as by the other considered models.

6.6.3 Results on Synthetic Images

To judge the despeckling ability of the proposed approach, in [Figure 6.2](#), we show the visual comparison of the despeckled images for the boat image [6.1a](#), which is initially degraded by the speckle noise with $L = \{3, 10\}$. Quality of the recovered images describes that the filtered image obtained by the proposed filter is more intimate to the noise-free image than the results of the other discussed models. The present technique preserves the texture information more efficiently.

Further, the demonstration of results for a brick image, degraded by speckle noise with $L = \{3, 10\}$, is displayed in [Figure 6.3](#). This image contains a lot of fine texture information along with homogeneous regions. From the quality of the despeckled images, it can be observed that the restored image computed by the proposed method is more accurate and less blurry than the despeckled images calculated by the other existing approaches. Also, to analyze the image quality, we have shown the ratio images of the corresponding despeckled images. Figures [6.4a–6.4f](#) describe the ratio image for the original brick image [6.1b](#) and the restored images [6.3h–6.3l](#). From figures [6.4b–6.4f](#), one can notice that the ratio image computed by the proposed algorithm has very less background information which indicates that the proposed approach preserves the image edges better than the other methods in the noise removal process. Besides the full surface of the despeckled images, in figures [6.4g–6.4j](#) we have displayed the result for the three particular slices of the brick image. These figures demonstrate the one-dimensional (1D) profile of the slice of the clean, corrupted, and restored images. From these figures, it can be concluded that the 1D profiles calculated by the proposed method are more approaching to the profiles of the corresponding clean signals than the results of the other techniques.

Further, to confirm the image despeckling ability of the present model, [Figure 6.5](#) illustrates the restored results for a circle image corrupted by speckle noise

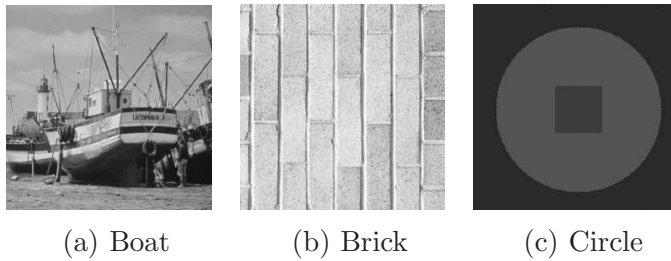
**Figure 6.1:** Clear images.**Table 6.1:** MSSIM, PSNR, and SI values of despeckled images.

Image	L	AA			Dong			DDD			ZZDB			Proposed		
		MSSIM	PSNR	SI	MSSIM	PSNR	SI									
Boat	1	0.5577	16.90	0.3695	0.5526	16.78	0.3368	0.5510	16.92	0.3417	0.5705	16.98	0.3289	0.5816	17.04	0.3162
	3	0.6780	22.40	0.3759	0.6680	22.41	0.3712	0.6806	22.20	0.3720	0.6810	22.30	0.3569	0.6976	22.54	0.3472
	5	0.7210	24.27	0.3783	0.7128	24.27	0.3755	0.7205	24.06	0.3662	0.7200	24.14	0.3637	0.7386	24.46	0.3558
	10	0.7757	26.16	0.3796	0.7658	26.17	0.3782	0.7729	26.11	0.3794	0.7745	26.20	0.3709	0.7885	26.39	0.3658
Brick	1	0.2875	12.10	0.0816	0.2874	12.18	0.0805	0.2873	12.14	0.0779	0.2880	12.16	0.0728	0.2961	12.23	0.0719
	3	0.3710	16.95	0.0933	0.3737	17.00	0.0901	0.3646	16.86	0.0879	0.3650	16.87	0.0865	0.3823	17.09	0.0854
	5	0.4167	19.17	0.0998	0.4174	19.21	0.0978	0.4176	18.61	0.0955	0.4175	18.65	0.0923	0.4234	19.32	0.0908
	10	0.4790	21.84	0.1063	0.4855	21.86	0.1051	0.4874	21.88	0.1043	0.4877	21.90	0.1005	0.4889	22.00	0.0996
Circle	1	0.9510	33.19	0.3106	0.9501	32.22	0.3165	0.9458	33.69	0.3219	0.9502	33.48	0.3098	0.9670	34.87	0.2982
	3	0.9633	36.88	0.3270	0.9654	36.89	0.3245	0.9572	36.72	0.3271	0.9603	36.90	0.3215	0.9765	38.90	0.3163
	5	0.9688	37.85	0.3285	0.9688	37.86	0.3271	0.9617	37.64	0.3289	0.9634	37.58	0.3249	0.9784	39.82	0.3198
	10	0.9726	39.65	0.3291	0.9756	39.67	0.3279	0.9761	39.86	0.3290	0.9732	39.49	0.3253	0.9821	41.40	0.3241

with $L = \{3, 10\}$. From the restored images, one can recognize that the suggested technique provides reliable image denoising effects than the other existing methods. In Figure 6.6, we presents the 2D contour plots and 3D surface plots of the images 6.5g–6.5l for better comparison of the qualitative result. From the contour maps 6.6a–6.6f, one can easily observe that the existing algorithms, left serious speckles in the homogeneous areas but the proposed technique provides fewer speckles with better edge preservation. Also, the 3D surface plots 6.6g–6.6l showing a better image smoothing ability of the present method than the other existing technique.

Besides the qualitative performances, the quantitative values are described in Table 6.1. For convenient comparison, the best results for all the parameters are highlighted in the table. The higher MSSIM and PSNR values and smaller SI values justify the superiority of the proposed approach. Considering the quantitative analysis, we note that the proposed method performs better as compared to other PDE based techniques.

Moreover, Figure 6.7 displays the convergence rate of PSNR value with respect to the number of iteration. This figure shows that the proposed algorithm achieves the higher PSNR value in relatively fewer iterations.

From the overall image despeckling study on synthetic and natural images, it can be concluded that the proposed method preserves the texture pattern and edge information more efficiently than the other existing PDE based approaches.

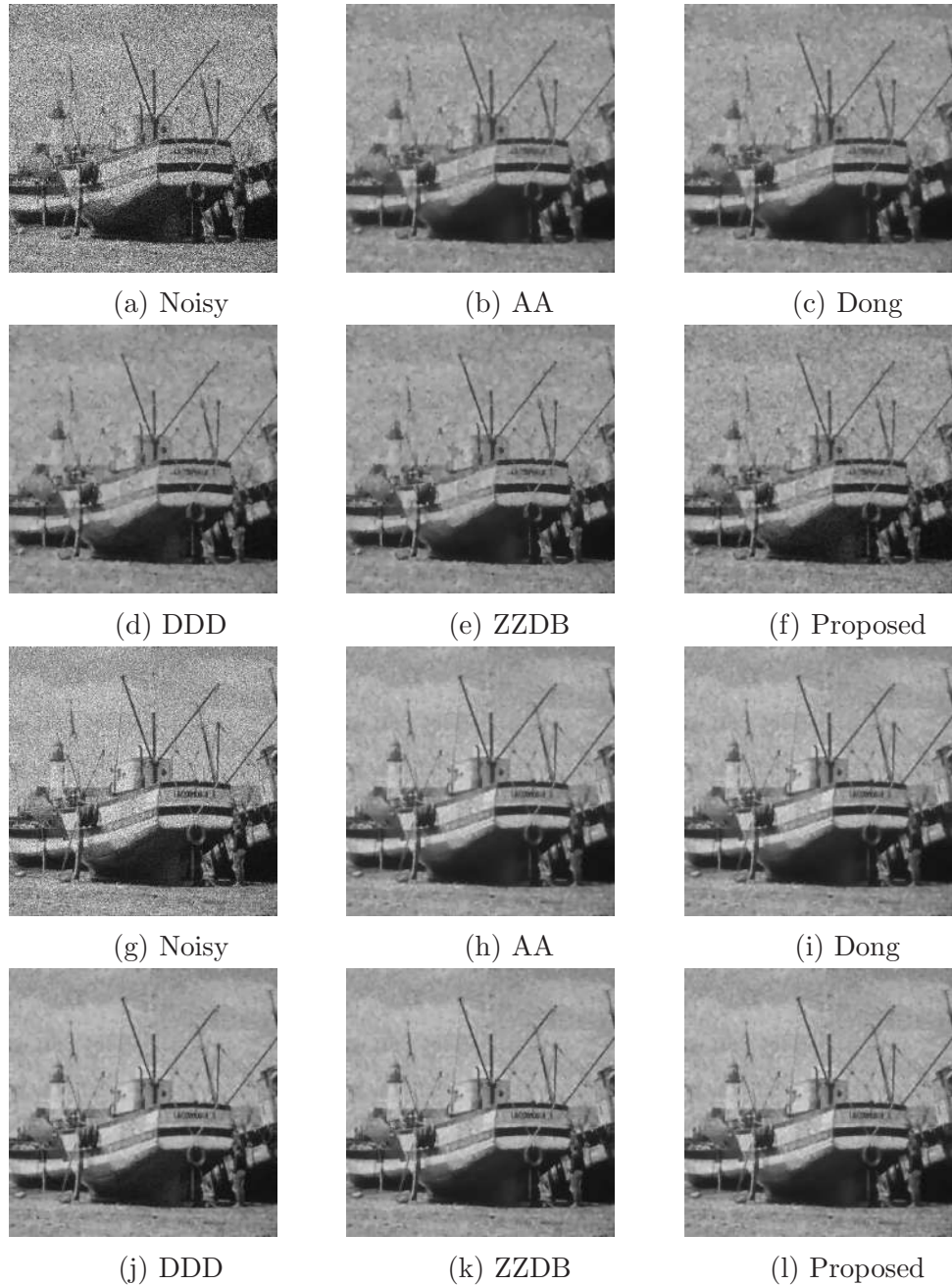


Figure 6.2: Boat image (512×512). (a) Speckled image: $L = 3$. (b)–(f) Despeckled by various approaches. (g) Speckled image: $L = 10$. (h)–(l) Despeckled by various approaches.

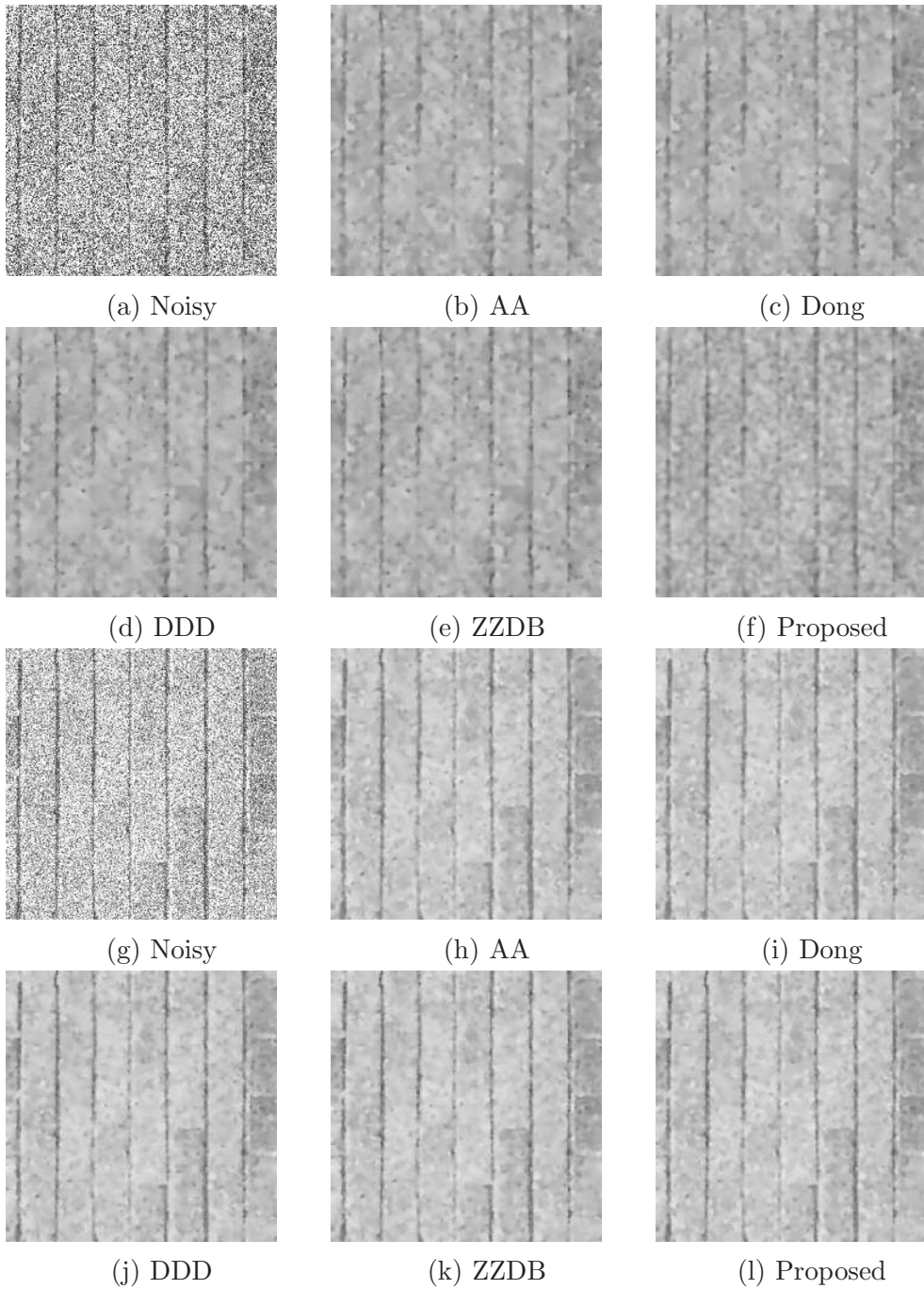


Figure 6.3: Brick image (256×256). (a) Speckled image: $L = 3$. (b)–(f) Despeckled by various approaches. (g) Speckled image: $L = 10$. (h)–(l) Despeckled by various approaches.

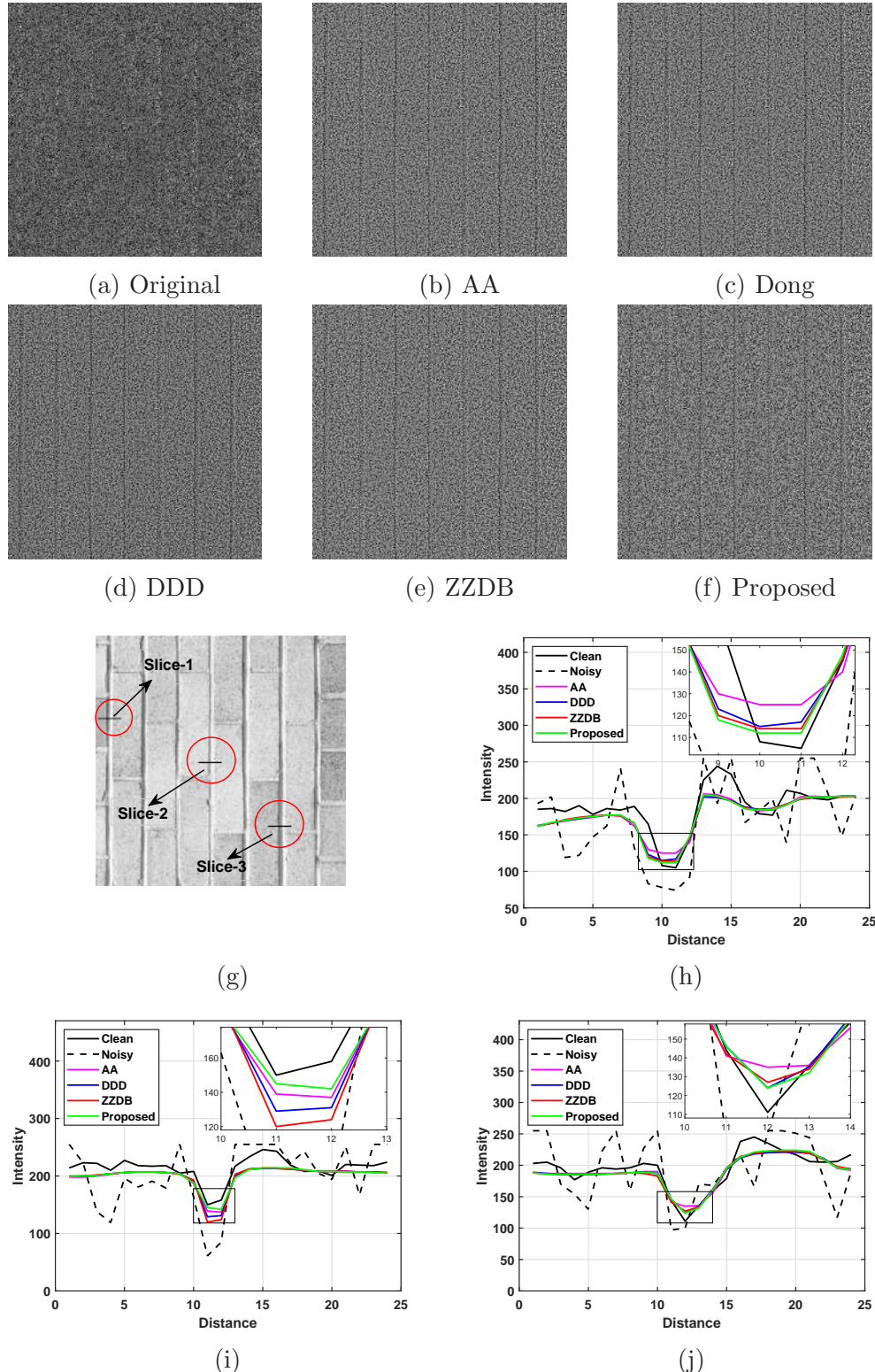


Figure 6.4: (a) Ratio image for the original image 6.1b, (b)–(f) Ratio images for the despeckled images 6.3h–6.3l. (g) Indicate the one-dimensional slices. (h) Results for the Slice-1. (i) Results for the Slice-2. (j) Results for the Slice-3.

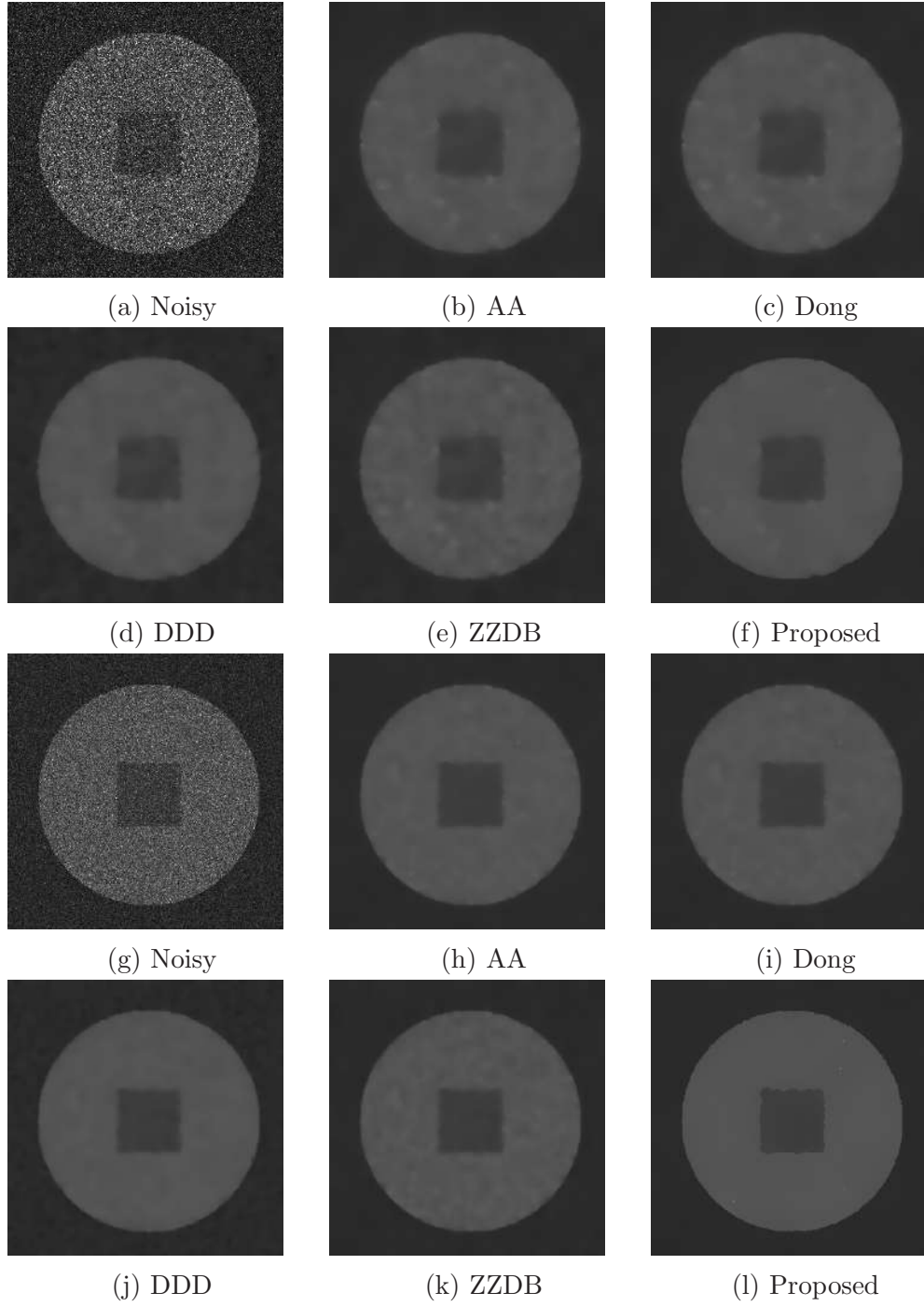


Figure 6.5: Circle image (299×299). (a) Speckled image: $L = 3$. (b)–(f) Despeckled by various approaches. (g) Speckled image: $L = 10$. (h)–(l) Despeckled by various approaches.

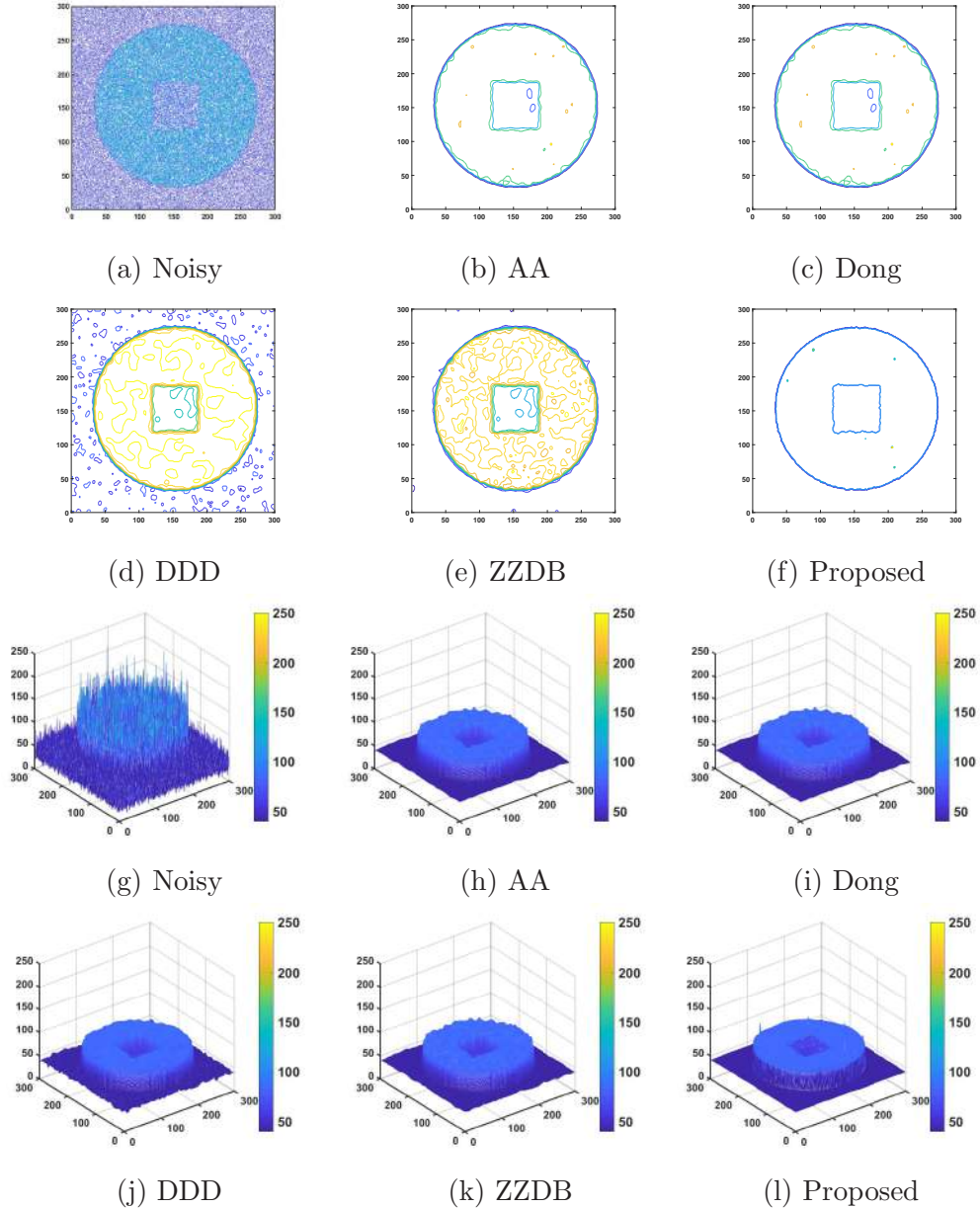


Figure 6.6: (a)–(f) 2D Contour map of the images 6.5g–6.5l. (g)–(l) 3D surface plot of the images 6.5g–6.5l.

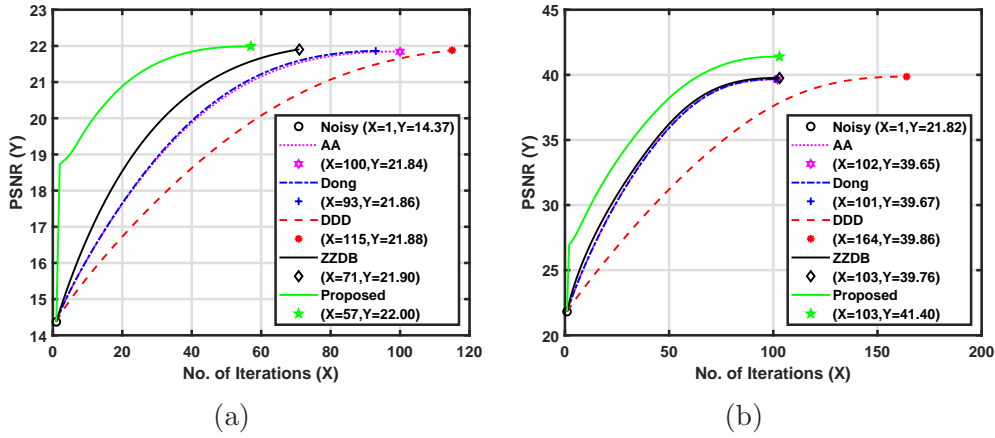


Figure 6.7: Improved PSNR value vs. the corresponding iteration number for various models. (a) Results for the brick image; 6.3g–6.3l. (b) Results for the circle image; 6.5g–6.5l.

6.6.4 Results on Real Images

This section demonstrates the application of the proposed model for despeckling of real SAR and ultrasound images. Although the SAR and ultrasound images are powerful tools, the presence of multiplicative speckle noise degrades the quality of images and makes their interpretation (e.g., in recognition of regions, target detection, classification, etc.) more challenging and unreliable. Hence the noise removal is essential for high-level image analysis. Here, we illustrate the despeckling results for two real SAR images ([Agency, n.d.](#); [eoPortal: Sharing Earth Observation Resources, 2005](#)) and two real ultrasound images. Both the images are restored using the existing PDE models and the proposed method. The same parameter values are used as described in [subsection 6.6.1](#).

[Figure 6.8](#) displays the filtered images of a real SAR image (SAR Image-1) obtained by the different methods. Observing the results, one can conclude that the result obtained by the present method seems to be better despeckled with efficient pattern and edge preservation than other approaches. Moreover, the proposed approach can efficiently preserve the spatial resolution as well as significantly reduce the speckle effect.

The next despeckling result is computed for a real SAR image (SAR Image-2) of the Himalayan Arc, as displayed in [Figure 6.9](#). In contrast to the previous SAR image, the presence of fine textures are much high in this image. The quality of the recovered image utilizing the present filter is promising in terms of variance reduction as well as the preservation of edges, structured regions, and bright scatters.

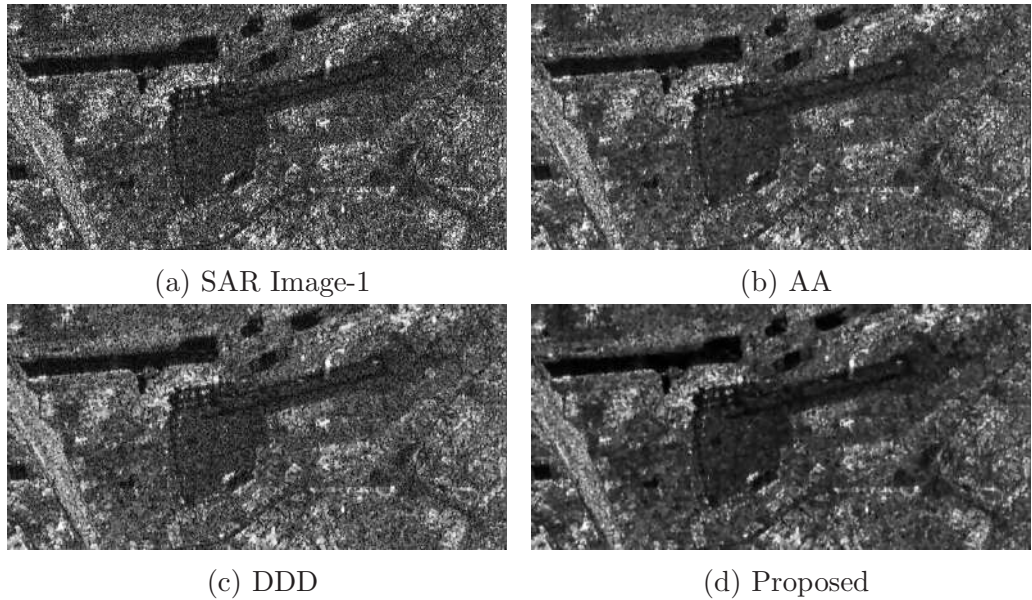


Figure 6.8: (a) SAR Image-1: One look radar image ([Agency, n.d.](#)). (b)–(d) Restored by different models.

Further, to check the image despeckling ability of the proposed method, in [Figure 6.10](#), we present the despeckled results of a real ultrasound image of the fetal foot. The pattern of the object edges, such as face and foot and their intensities, are well improved and preserved by the suggested approach compared with other considered methods.

The next despeckling result is made on a liver cyst image, as displayed in [Figure 6.11](#). Comparing the despeckled images, one can observe that the suggested method describes a better result than the other approaches.

Moreover, [Figure 6.12](#) displays the convergence rate of relative error with respect to the number of iteration. This figure depicts that the present method satisfies the stopping criterion in relatively fewer iterations.

Besides the visual description of the despeckled images, the quantitative results are also described in [Table 6.2](#). Lower values of both the quantitative measures indicate the ability of the proposed model. Therefore, comparing with the results of existing models, it is easy to conclude that the proposed method is effective and promising for the speckle reduction in real SAR and ultrasound images.

6.7 Conclusion

This work proposes a novel and efficient fuzzy edge detector based adaptive telegraph total variation model for image despeckling. The goal of such a new adaptive filtering scheme is to preserve edges efficiently when the model is applied to image

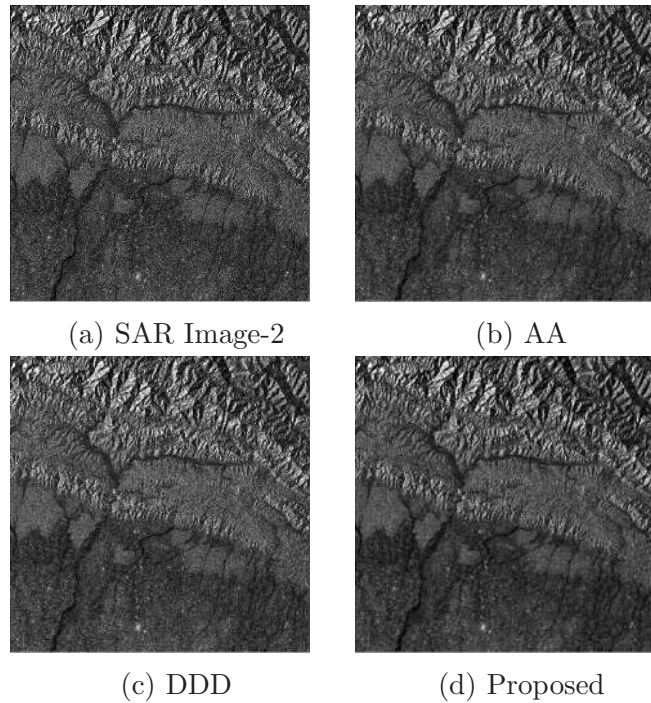


Figure 6.9: (a) SAR Image-2: Image of KOMPSAT/Arirang-5 of a part of the Himalayan Arc ([eoPortal: Sharing Earth Observation Resources, 2005](#)). (b)–(d) Restored by different models.

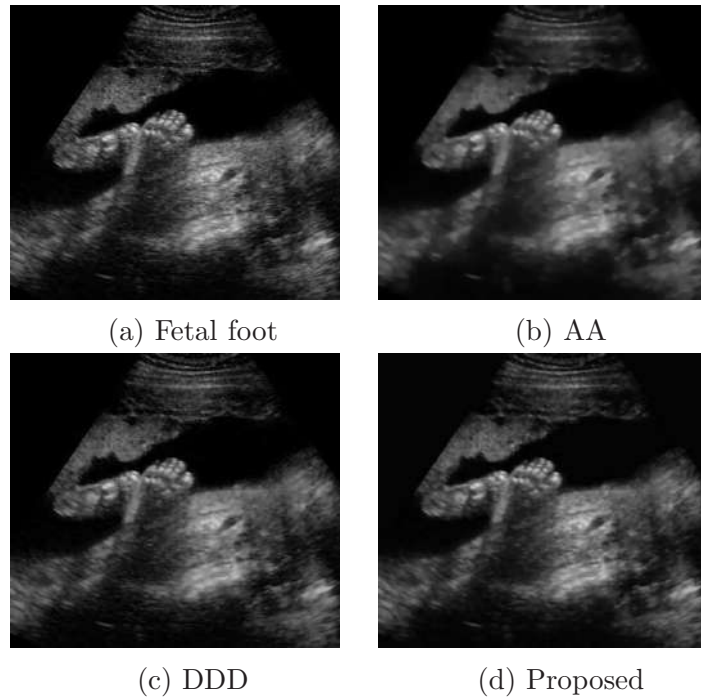


Figure 6.10: A Ultrasound image of fetal foot and restored by different models.

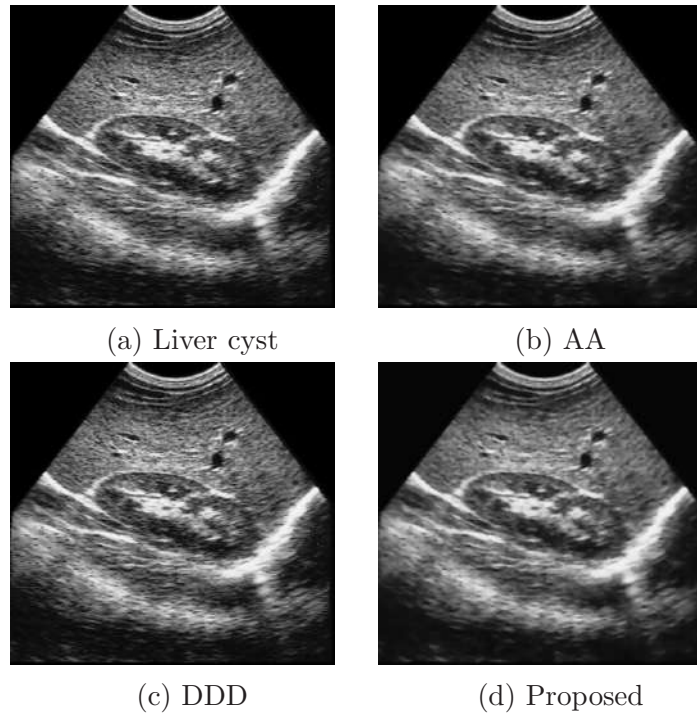


Figure 6.11: A Ultrasound image of liver cyst and restored by different models.

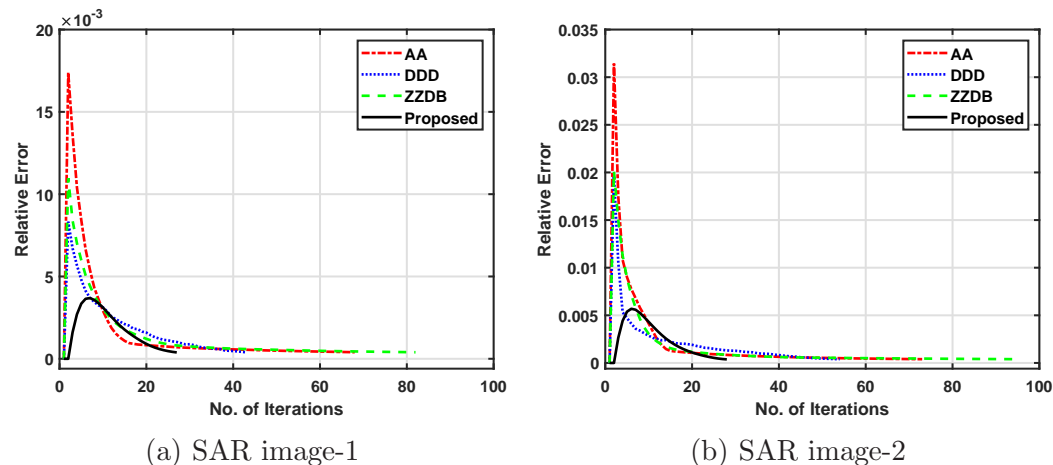


Figure 6.12: Relative error vs. the iteration number for various models.

Table 6.2: Comparison of SI and BRISQUE (BQ) values of despeckled images.

Image	AA		Dong		DDD		ZZDB		Proposed	
	SI	BQ	SI	BQ	SI	BQ	SI	BQ	SI	BQ
SAR Image-1	0.5076	43.21	0.5034	43.99	0.5283	42.83	0.4806	42.56	0.4398	42.45
SAR Image-2	0.6985	45.26	0.6874	45.58	0.6845	43.96	0.6563	40.75	0.6270	38.38
Fetal foot	1.052	45.40	1.055	42.80	1.0642	40.17	1.0507	40.94	1.024	39.09
Liver cyst	0.8480	39.28	0.8484	41.15	0.8580	40.39	0.8252	45.95	0.8101	38.18

despeckling. To overcome the limitations present in the existing gradient-based despeckling models, we considered a hybrid approach where we combine a robust fuzzy edge indicator function with a telegraph total variation model for image selective smoothing and restoration. To the best of our knowledge, the fuzzy edge detector driven telegraph total variation model has not been used before for speckle noise suppression. Also, we study the existence and uniqueness of weak solutions of a regularized version of the proposed model. Extensive numerical experiments have been conducted to highlight the efficiency and reliability of the proposed technique for image despeckling using different types of synthetic, natural, and real images. From the numerical experiments, it is confirmed that the proposed approach has better image despeckling ability than the other existing PDE based methods. Hence the suggested framework indicates a potential direction for the noise removal process when images are degraded by speckle noise.

Chapter 7

A Computational Study On Color Images

In this chapter, we represent the color image denoising results using the proposed methods discussed in [Chapter 2–5](#) and deblurring results using the Maximum entropy method proposed by [Jannetta \(2005\)](#). Most of the real-world images are color images which can be represented by a combination of three colors, i.e., red, green and blue (RGB image see [subsection 1.1.1](#)) and contain better visible effects than a grayscale image in terms of visual understanding. The edge information of color images are more copious than those of grayscale images. To find the computational (denoising or deblurring) results for a color image I , first we separate the three color channels (red channel, green channel, and blue channel) and then simulate each separated color channel using the considered technique for grayscale images. After each iteration combine them using the MATLAB built-in function “cat”. After that, terminate the simulation process using the stopping criterion as discussed in [section 1.3](#). Here our main objective is to extend our proposed models, as well as the maximum entropy method (MEM) for color image denoising. After verifying the performances of these models, we can extend/modify these models to obtain better color image denoising performance, which can be a future scope for research. All the numerical experiments are performed using MATLAB version *R2019a* running on a Windows 7 desktop computer with an Intel Core i5 dual-core CPU at 2.53 GHz with 4 GB of RAM.

7.1 Color Image Denoising

In this section, we represent the restored results of four color images, presented in [Figure 7.1](#), which are initially corrupted by different levels of noises. To obtain the computational results, we use our proposed models discussed in [Chapter 2–5](#). We use the ACPDE model (equations [\(2.2\)–\(2.5\)](#) in Chapter 2) and TCPDE model

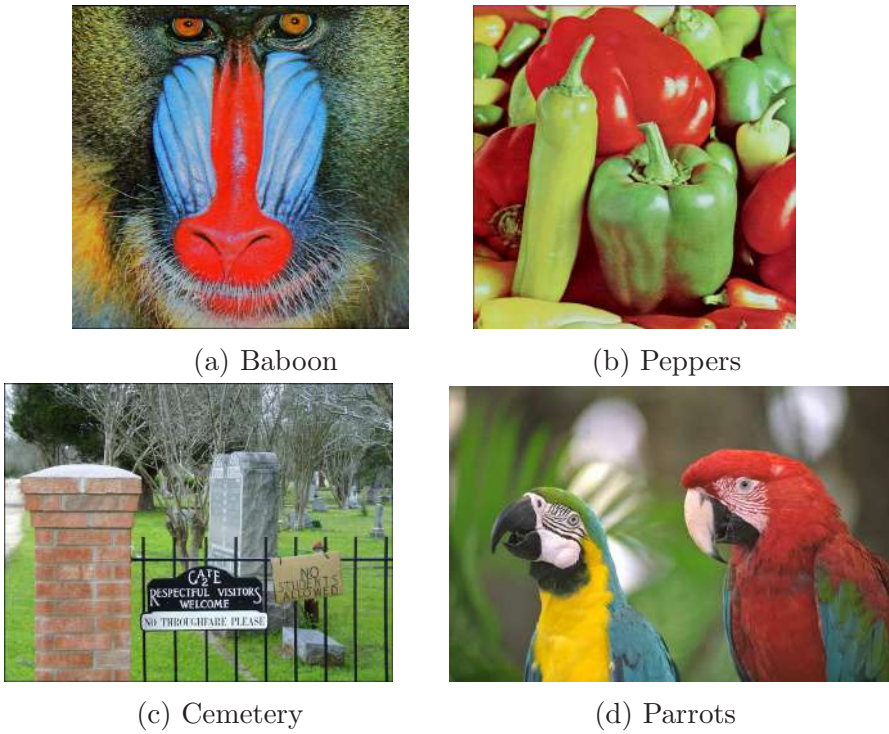


Figure 7.1: Clear images.

(equations (3.5)–(3.9) in Chapter 3) for the additive Gaussian noise removal process, and the TDM model (equations (4.15)–(4.17) in Chapter 4) and HPCPDE model (equations (5.2)–(5.4) in Chapter 5) for the multiplicative speckle noise removal process. For all the restored images we calculate the PSNR values to verify the image denoising performance of the models.

7.1.1 Results for Additive Gaussian Noise

In this section, we describe the restored results when images are degraded by additive Gaussian noise. We artificially add additive Gaussian noise of mean $\mu = 0$ and standard deviation $\sigma = 50$ with the images presented in Figure 7.1 using MATLAB program [Chapter 2, [section 2.4](#)]. Figures 7.2–7.5 represent the restored results. From the restored images one can observe that both the approaches remove the noise significantly as well as preserves the image structure efficiently. Also, the PSNR value of each denoised image increases significantly.

7.1.2 Results for Multiplicative Speckle Noise

In this section we describe the restored results when images are degraded by multiplicative speckle noise. Here, images in Figure 7.1 are corrupted by multiplying artificial speckle noise with “looks” $L = 10$ using MATLAB program [Chapter 4,

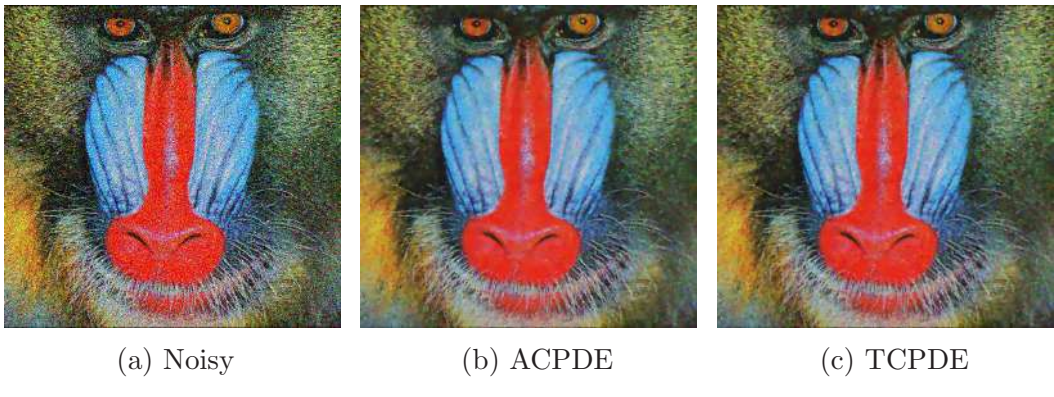


Figure 7.2: (a) PSNR=15.00, (b) 20.90, (c) PSNR=21.05.

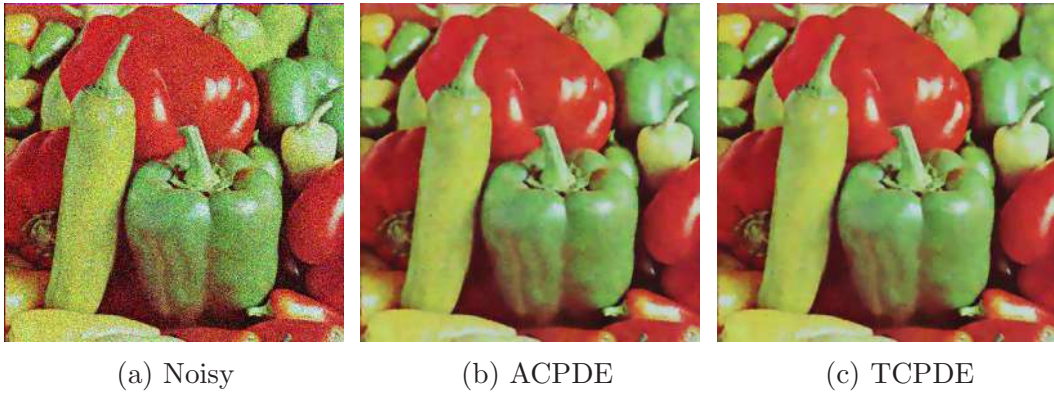


Figure 7.3: (a) PSNR=15.03, (b) 25.80, (c) PSNR=25.99.

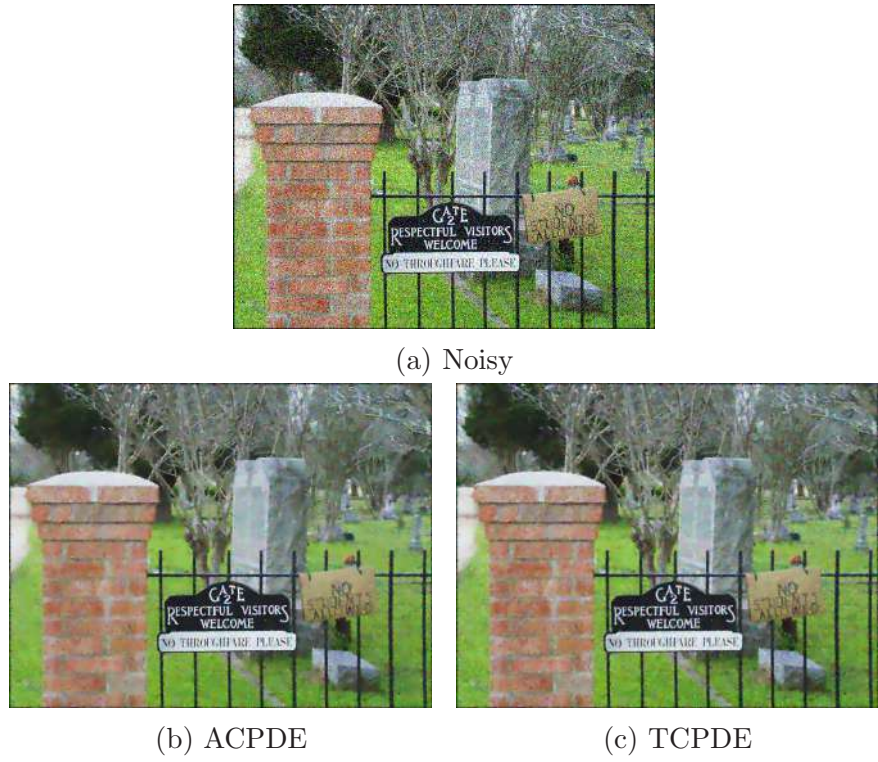


Figure 7.4: (a) PSNR=14.73, (b) 22.65, (c) PSNR=22.70.

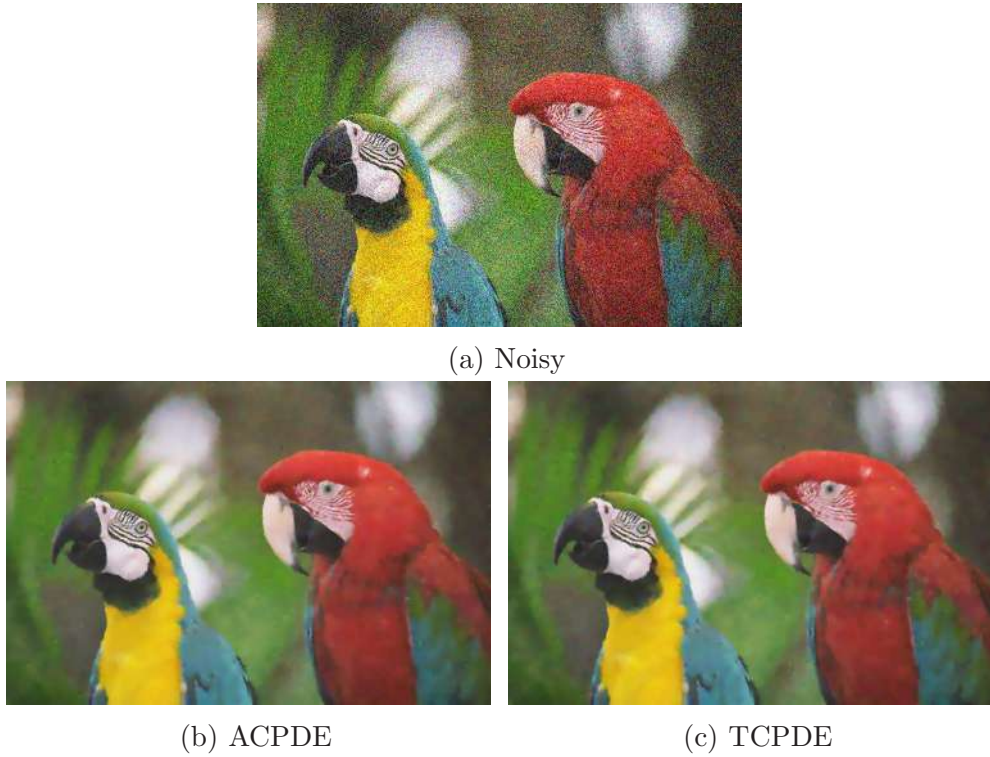


Figure 7.5: (a) PSNR=14.89, (b) 28.38, (c) PSNR=28.51.

section 4.5]. Figures 7.6–7.9 represents the restored images. From the restored images one can find that both the approaches remove the noise efficiently as well as preserve the image structure carefully. Also, the PSNR value of each denoised image increases significantly.

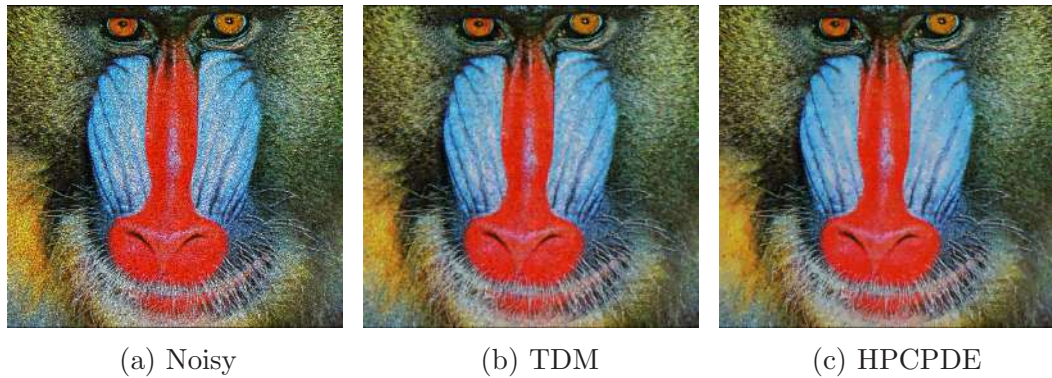


Figure 7.6: (a) PSNR=17.84, (b) 22.55, (c) PSNR=22.73.

7.2 Color Image Deblurring

Our future research interest is the application of a non-extensive entropy-based algorithm for image restoration when the images are degraded by the blurring

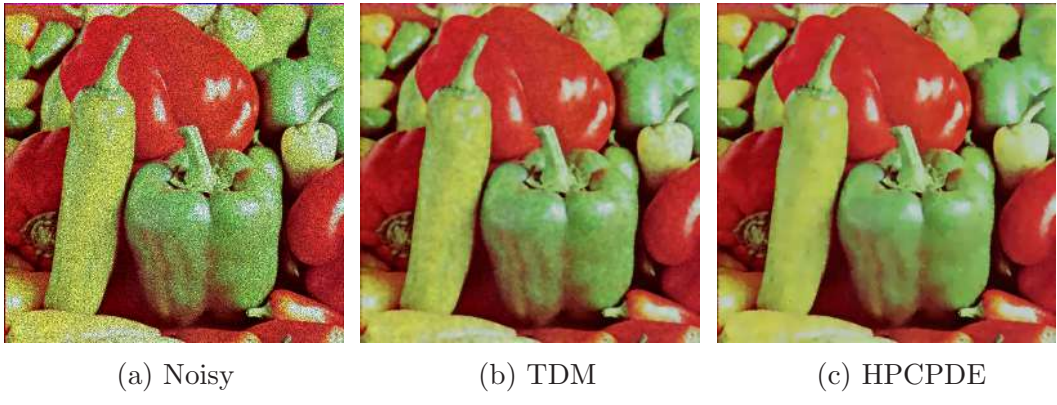


Figure 7.7: (a) PSNR=17.13, (b) 27.11, (c) PSNR=27.99.

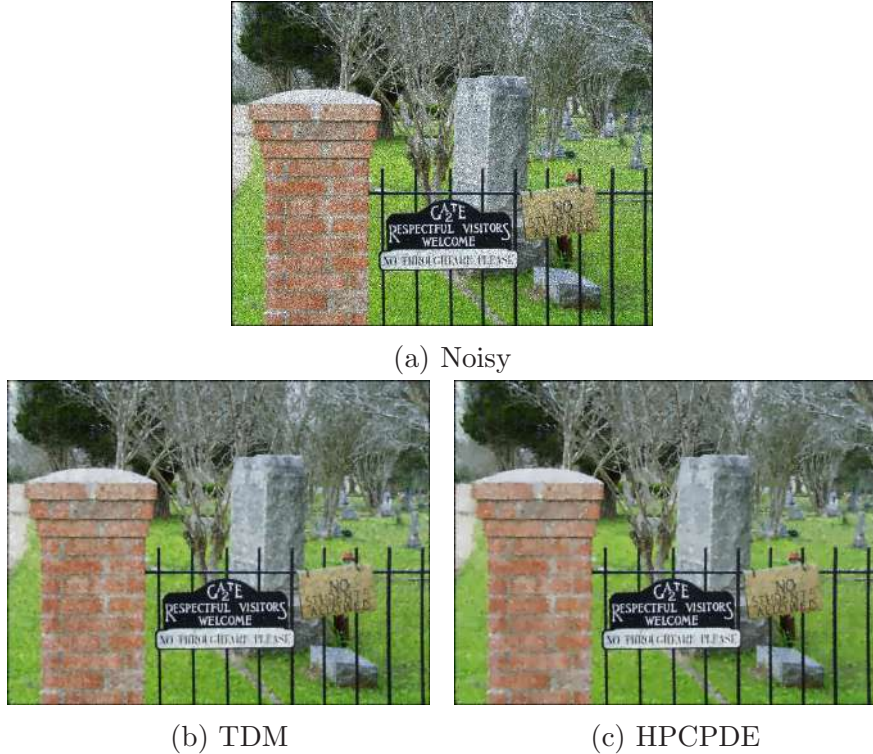


Figure 7.8: (a) PSNR=16.83, (b) 23.65, (c) PSNR=24.08.

effect as well as the additive/multiplicative noises. To date, various techniques are proposed to handle this issue, but each method has some advantages and limitations. In medical imaging, the images produced by the imaging system are mostly shadowgrams: the X-ray source and the geometry of the imaging system influence the size and intensity of the produced images. Due to the finite size of x-ray source images are blurred, and for the safety of the patient, x-ray exposure kept as low as possible, which limits the number of photons for image formation and introduces the noisy effect in the generated images. In such systems, the actual image degraded by convolving with a point spread function (PSF), even the

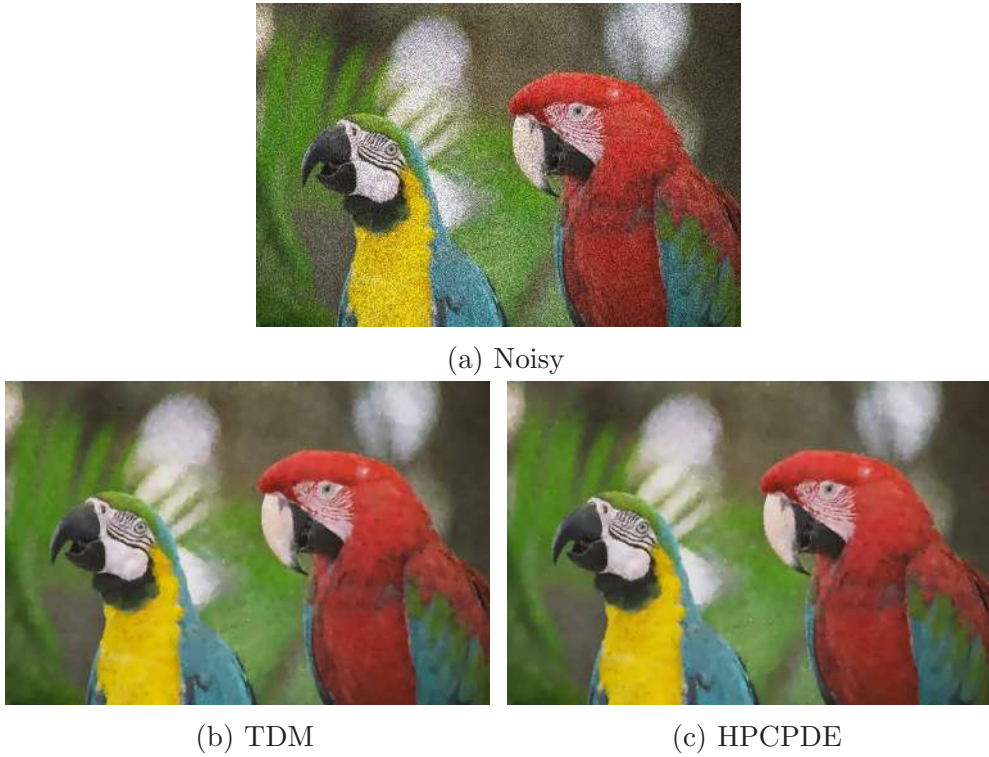


Figure 7.9: (a) PSNR=17.91, (b) 28.47, (c) PSNR=28.61.

addition of noise (see the relation (1.1)). In such cases, the image restoration using traditional inverse filtering has limited applications because the PSF matrix is ill-conditioned. However, the MEM is an alternative approach to restore an actual image from noisy data. The entropy is utilized as a regularization part in the functional to constrain the solution and provide the simplest possible compatibility with the data. In the middle of the 19th century, the notion of entropy was first introduced by Rudolf Clausius in thermodynamics. Several years later, in 1877, Boltzmann derived the entropy expression for statistical mechanics where entropy represents the measure of disorder in a thermodynamical system. In 1948, Shannon ([Shannon, 1948](#)) introduce the idea of entropy of an image that comes from the information theory and entropy is defined as

$$H(X) = - \sum_i p_i \ln(p_i), \quad (7.1)$$

where X is a discrete image variable with the pixels $x_1, x_2, x_3, \dots, x_N$ and p_i is the probability associated with each x_i . In the information-theoretic approach, the source with maximum entropy gives the more amount of knowledge. After that, the connection between statistical mechanics and information theory was founded by Jaynes ([Jaynes, 1957a,b, 1968](#)). He stated that Maximum Entropy

(MaxEnt) is a general postulate in setting up distributions from incomplete information. Frieden has first introduced the MEM based image restoration technique in his milestone work ([Frieden, 1972](#)). A few years later, using the same principle [Gull and Daniell \(1978\)](#) and [Cornwell and Evans \(1985\)](#) were published two famous works on the restoration of radio astronomy images. In 1989, John Skilling addressed a Bayesian interpretation of this strategy and emphasized the fact that it is the usually adequate method for allowing prior probabilities ([Skilling, 2013](#)). MEM handles the restoration technique as a statistical inference process based on Bayes's rule to obtain the most feasible image I knowing the information J :

$$P(I|J) \propto P(J|I) \times P(I), \quad (7.2)$$

where $P(|)$ denotes the conditional probability. The equation can be written in words as:

$$\text{Posterior} \propto \text{Likelihood} \times \text{Prior}, \quad (7.3)$$

The likelihood $P(J|I)$ is derived from our knowledge of the relation [\(1.1\)](#), and the likelihood term is quantified by the $\chi^2 \sim \frac{\sum_{\text{pixels}} (J - \mathcal{O}I)^2}{\sigma^2}$ distribution:

$$P(J|I) \propto \exp(-\chi^2/2), \quad (7.4)$$

where σ^2 is the variance in the noise. The prior $P(I)$ is the probability that would be assigned to a precise restoration I prior to the introduction of observational constraints. It is assumed that each luminance quantum has an equal a priori chance of falling into any pixel, in which case it is easy to show that

$$P(I) \propto \exp(S), \quad (7.5)$$

where S denotes the entropy ([Shannon, 1948](#)) of the hidden image I . The strict definition of posterior probability is therefore:

$$P(I|J) \propto \exp(S - \chi^2/2). \quad (7.6)$$

Here, the objective is to find the values of I , which maximize this probability $P(I|J)$. As it is not possible to determine analytically, a numerical technique must be applied. In practice, a reasonable adjustment of the equation [\(7.6\)](#) is utilized as:

$$P(I|J) \propto \exp(\alpha S - \chi^2) = \exp(Q), \quad (7.7)$$

where, $Q = \alpha S - \chi^2$ and α is a weight parameter. Given the data, the maximum likelihood principle applies by maximizing $P(I|J)$. Taking the logarithm, we thus need to maximize

$$\ln(P(I|J)) \propto (\alpha S - \chi^2), \quad (7.8)$$

which is a linear combination of two terms: the entropy of the image, and a portion corresponding to χ^2 which statistically estimates the disparity between the data and the predictions of the model. The solution is calculated by minimizing

$$E = \frac{\sum_{pixels} (J - \mathcal{O}I)^2}{2\sigma^2} - \alpha S, \quad (7.9)$$

where α can be treated as a Lagrangian multiplier or a parameter that determines the relative weight between the goodness-of-fit and the entropy S . Several expressions for entropy S have been suggested in the literature ([Burg, 1967](#); [Frieden, 1975](#); [Gull and Skilling, 1990](#)).

Images recovered by Historic MEM tend to be grainy in appearance at the very finest scales: there can often be very little correlation between neighboring pixels within the image. One of the axioms of MEM is that pixel correlations should not be included in the restored image, that is to say, restoration in one part of an image should not affect recovery in another part ([Skilling, 1988](#)). However, such pixel correlations more often than not exist in the real world and usually between neighboring pixels. In ([Jannetta, 2005](#)) suggest a hybrid formulation of Historic entropy that allows pixel correlation in the restored image. The authors in ([Jannetta, 2005](#)) chosen a different image formation model than Historic MEM. They choose the forward map for the imaging system as

$$J = \mathcal{O} * C * I + \eta = \mathcal{O} * V + \eta, \quad (7.10)$$

The Intrinsic Correlation Function (ICF), denoted by C , maps the hidden image to the visible image V and the visible image V map to the observed data J through the convolution with a PSF \mathcal{O} and further corrupted by noise η . The restoration process is the same as the Historic MEM, the only difference from ([Skilling, 1988](#)) in the form of the entropic prior ([Jannetta, 2005](#)). In this section, we reproduce image restoration results using the Maximum Entropy Method ([Jannetta, 2005](#)) for color images when an image variable I follows the additive noise model (1.1). To reproduce the image restoration results using MEM ([Jannetta, 2005](#)), we have artificially degraded the original images represented in [Figure 7.1](#), [Figure 7.14a](#), and [Figure 7.15a](#). We first convolve a clear image I with the blurring effect function

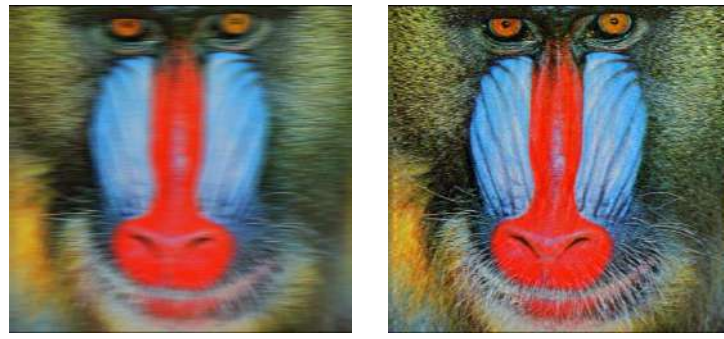


Figure 7.10: A degraded baboon image and restored by MEM.

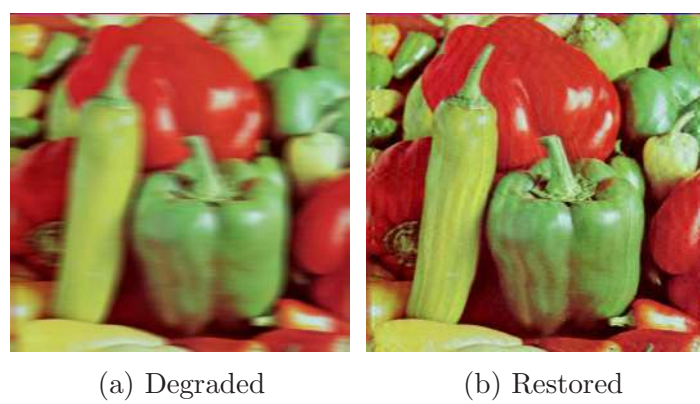


Figure 7.11: A degraded peppers image and restored by MEM.

\mathcal{O} (we use MATLAB built-in function “fspecial(‘motion’, len, theta)” as \mathcal{O} with len=20 and theta=0) and then add Gaussian noise η with the blurred image using MATLAB built-in function “imnoise” with mean $\mu = 0$ and variance $\sigma^2 = 0.00001$. From the restored images one can conclude that the MEM works well for image deblurring, but needs to be modified for better denoising effect. Our future interest is the study of image deblurring when the images are corrupted with multiplicative noise (see model (1.2)).

7.3 Conclusion & Future Scope

In this chapter, we present the color image denoising ability of the proposed models discussed in Chapters 2–5. Both ACPDE and TCPDE models remove noise efficiently and preserve the image characteristics significantly when the images are degraded by additive Gaussian noise. Also, the TDM and HCPDDE models can remove noise and preserve the edge/textture information efficiently when the images are degraded by multiplicative speckle noise. Moreover, we reproduce image restoration results using the Maximum Entropy Method ([Jannetta, 2005](#)) for



(a) Degraded



(b) Restored

Figure 7.12: A degraded cemetery image and restored by MEM.

(a) Degraded



(b) Restored

Figure 7.13: A degraded parrots image and restored by MEM.

(a) Original

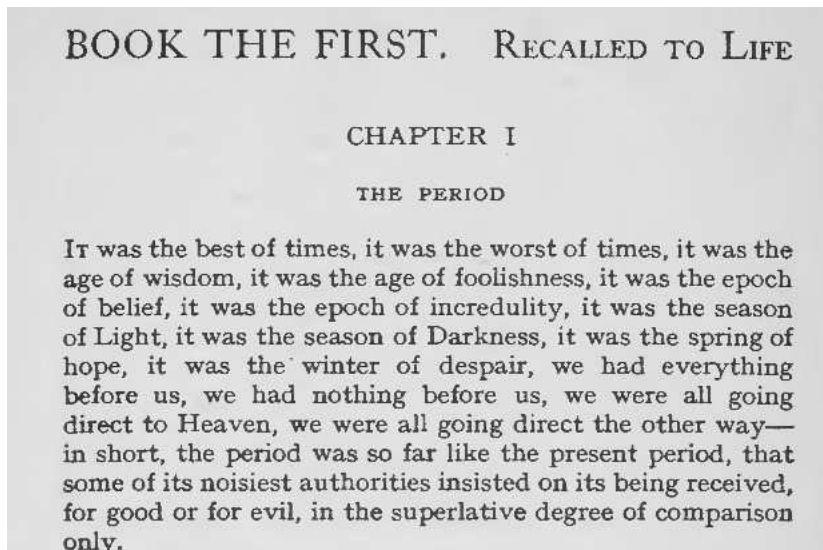


(b) Degraded

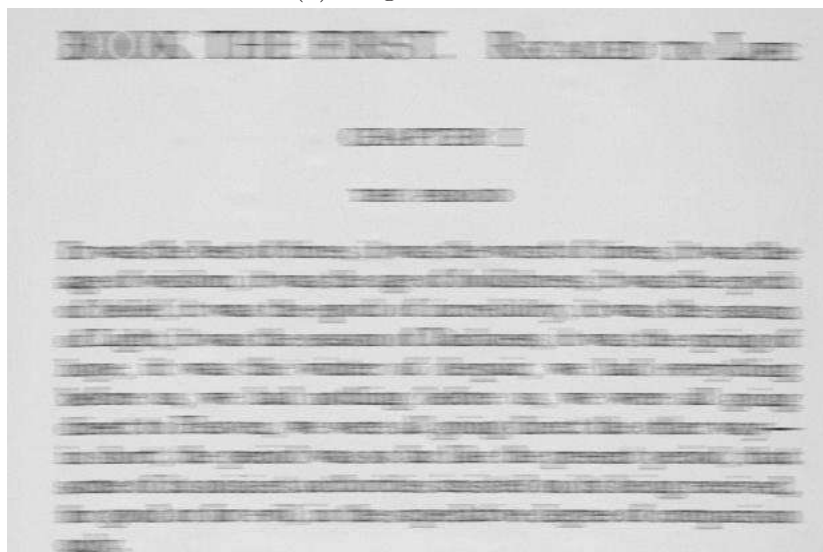


(c) Restored

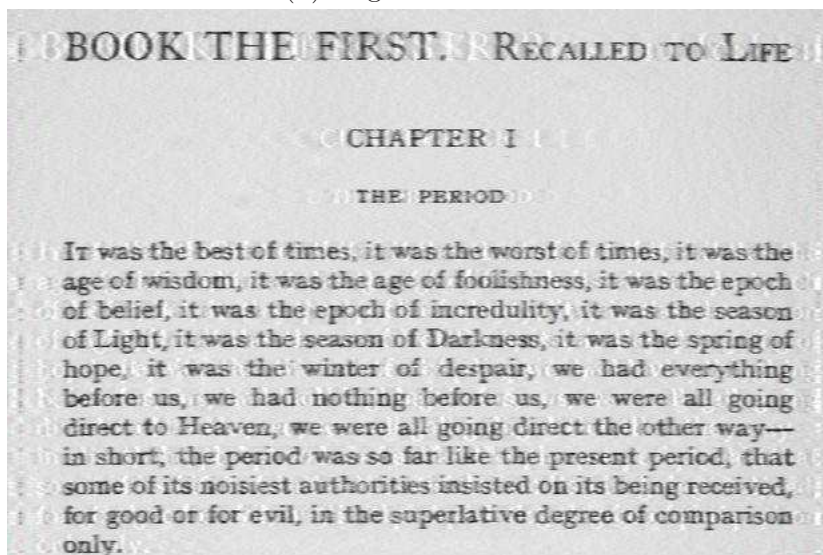
Figure 7.14: A degraded rapids image and restored by MEM.



(a) Original



(b) Degraded



(c) Restored

Figure 7.15: A degraded text image and restored by MEM.

color images when an image degraded by blurring effect as well as additive Gaussian noise. Overall, the results are convincing but some improvements will make them more productive. We shall consider this problem in the future. Many researchers have applied the entropy-based techniques for image restoration; most of them used the concept of Shannon entropy or relative Shannon entropy (Kullback-Leibler divergence) or a little modification of relative Shannon entropy to construct the optimization function. Best of our knowledge, no one has used the concept of more generalization of the Shannon entropy for image restoration. Hence the application of a non-extensive entropy-based algorithm for image restoration when the images are degraded by the blurring effect as well as the additive/multiplicative noises is an exciting future direction, which needs to be explored in future.

Chapter 8

Conclusion and Future Scope

8.1 General Conclusions

This thesis is concerned with the development of novel PDE-based image denoising models with studies of their well-posedness. We start with a coupled parabolic PDE based model and then switch our focus on hyperbolic-parabolic PDE based models. Our first two proposed models are associated with the additive Gaussian noise removal process, and the next three are associated with the multiplicative speckle noise removal process. For each model, numerical experiments are performed over various gray level test images to confirm the noise removal capability. Experimental results are compared with the results of several existing PDE based models, and we determine that the proposed models always perform better in terms of noise removal and feature preservation in the digital images as compared to other existing models.

8.2 Major Contributions

The significant contributions of this dissertation are described as follows:

- In [Chapter 2](#), we have introduced a new version of the coupled diffusion system previously proposed by Jain et al. ([Jain, 2018](#)) and established the well-posedness of the model. Also, compare the image denoising ability of the model with several existing techniques and confirm that our model performs better than the existing models consider for the comparisons.
- The development of a hybrid telegraph coupled PDE system for additive Gaussian noise removal process is discussed in [Chapter 3](#). This novel framework interpolates among two telegraph diffusion equations and a diffusion equation. The suggested approach can significantly preserve the high oscillatory and texture pattern in an image in the noise removal process, even in a

low signal-to-noise ratio. First, we verify that the system has a unique global weak solution using Banach's fixed point theorem. Then apply this model over a set of gray level images to illustrate the superiority of the proposed model over the recently developed telegraph diffusion-based models as well as the method discussed in [Chapter 2](#).

- In the next three consecutive chapters, we deal with the multiplicative noise removal process which is more complicated than the additive noise removal problem. In [Chapter 4](#), the concept of telegraph-diffusion equation is employed for the first time for multiplicative speckle removal process. A modified version of the gray level indicator function proposed by [Zhou et al. \(2015\)](#) introduces into a telegraph-diffusion equation. In the present system, the diffusion process utilizes the benefit of gray level indicator function as well as the gradient-based edge detector function in a telegraph-diffusion based framework. This technique preserves the high oscillatory and texture patterns in the images during the noise removal process better than diffusion-based filters. Moreover, we establish the well-posedness of the model using Schauder fixed point theorem. A computational study performed to highlight the effectiveness of the present model on different types of test images. Computational results using the present model indicate that the images are suitably recovered without introducing undesired artifacts as compared to recently developed PDE based models.
- Extending the work of [Chapter 4](#), we have suggested a nonlinear coupled hyperbolic-parabolic PDE system for image despeckling in [Chapter 5](#). A different equation is used to calculate the edge variable, which improves the present technique over the method discussed in chapter [Chapter 4](#). Due to the introduction of this extra equation injects the past information of the edge variable into the diffusion process and preserves the image edges better than the single equation-based models. Also, we have established the well-posedness of the proposed system. Computational studies are reported to demonstrate the noise removal, as well as the structure preservation ability of the present model. The proposed model is applied on a set of artificially noisy images and real images. Computational results are compared with the results of recently developed approaches. Overall, our study confirms that the present technique is more efficient than other existing PDE-based models for image despeckling.

- In **Chapter 6**, we have proposed a hyperbolic-parabolic type PDE model, with a fuzzy edge detector, for image despeckling. This model is derived from the total variation framework, combining in a telegraph equation and a fuzzy edge indicator function. This new approach enjoys the benefits of both the telegraph equation as well as the fuzzy edge detector function, which removes the image noise sufficiently as well as preserves the structural details of the image efficiently. Also, we have established the existence and uniqueness of a weak solution of a regularized version of the proposed model using Schauder fixed point theorem. We apply this approach to natural and real SAR images. The computational results of this model are reported, which found better in terms of noise reduction and detail preservation, compared to various existing approaches. To the best of our knowledge, this is the first work that utilizes a telegraph total variation model for speckle noise removal process.

In **Chapter 7**, we apply our proposed models discussed in **Chapter 2–5** for color (RGB) image restoration. First, we compare the results obtained by first two proposed models in **Chapter 2 & 3** for additive Gaussian noise removal. Then, we compare the results of color (RGB) image restoration for image despacckling using two other proposed models discussed in **Chapter 4 & 5**. Finally, we discuss Entropy-based color image denoising as well as deblurring (MEM) model.

8.3 Future Scopes

Some scopes of future research from this thesis are mentioned as follows:

- In **Chapter 2**, to solve the proposed system numerically, we have used a second-order accurate implicit finite difference method. One can use a higher-order accurate numerical scheme to solve this system, along with the stability analysis of the numerical scheme for the suggested model, which could be an excellent future research work.
- In **Chapter 3**, we have described a coupled telegraph-diffusion system for additive Gaussian noise removal process, One can extend this model for the multiplicative noise removal process. Moreover, we have solved the system using an explicit finite difference method. Still, one can solve the system using an implicit finite difference method to get a higher-order accurate numerical solution.

- In **Chapter 4**, we have proposed a telegraph-diffusion based model for multiplicative speckle noise removal process. One can extend this study for other types of multiplicative noise e.g., Poisson noise, Rayleigh noise etc. Also, one can use an implicit finite difference scheme to solve this system.
- All the PDE based models discussed in **Chapter 2–6** are of integer order. One can extend these models to fractional order. In the present scenario, research on fractional-order differential equations is an exciting research area for real-life applications as well as for the theoretical study. Additionally, all the developed models in **Chapter 2–6** are of deterministic types; each pixel of the image is treated as an unknown and deterministic variable. But due to the random characteristics of the noise component, it would be a more suitable choice if one assumes that each pixel of a degraded image is an unknown with stochastic nature. Accordingly, one can extend these deterministic PDE models to stochastic PDE models, which could be a more relevant study to image denoising problem.
- In **Chapter 7**, we have computed the image restoration results using the MEM ([Jannetta, 2005](#)), when an image follows the noise model (1.1). One can use the MEM for image restoration problem when an image follows the noise model (1.2), which could be an excellent future research work.

Bibliography

- Achim, A., Bezerianos, A. and Tsakalides, P. (2001). Novel bayesian multiscale method for speckle removal in medical ultrasound images, *IEEE transactions on medical imaging* **20**(8): 772–783.
- Adams, R. (1975). *Sobolev spaces, Pure and Applied Mathematics Series of Monographs and Textbooks*, Vol. 65, Academic Press, New York, London.
- Agency, E. S. (n.d.). Esa earth online.
URL: <https://earth.esa.int/handbooks/asar/CNTR1-4.html>
- Aiazzi, B., Alparone, L. and Baronti, S. (1998). Multiresolution local-statistics speckle filtering based on a ratio laplacian pyramid, *IEEE Transactions on Geoscience and Remote Sensing* **36**(5): 1466–1476.
- Aja-Fernández, S. and Alberola-López, C. (2006). On the estimation of the coefficient of variation for anisotropic diffusion speckle filtering, *IEEE Transactions on Image Processing* **15**(9): 2694–2701.
- Aja, S., Alberola, C. and Ruiz, A. (2001). Fuzzy anisotropic diffusion for speckle filtering, *2001 IEEE International Conference on Acoustics, Speech, and Signal Processing. Proceedings (Cat. No. 01CH37221)*, Vol. 2, IEEE, pp. 1261–1264.
- Alparone, L., Baronti, S. and Carla, R. (1995). Two-dimensional rank-conditioned median filter, *IEEE Transactions on Circuits and Systems II: Analog and Digital Signal Processing* **42**(2): 130–132.
- Alparone, L. and Garzelli, A. (1998). Decimated geometric filter for edge-preserving smoothing of non-white image noise, *Pattern recognition letters* **19**(1): 89–96.
- Alvarez, L., Guichard, F., Lions, P.-L. and Morel, J.-M. (1993). Axioms and fundamental equations of image processing, *Archive for rational mechanics and analysis* **123**(3): 199–257.
- Alvarez, L., Lions, P.-L. and Morel, J.-M. (1992). Image selective smoothing and edge detection by nonlinear diffusion. ii, *SIAM Journal on numerical analysis* **29**(3): 845–866.
- Amann, H. (2007). Time-delayed perona-malik type problems, *Acta Math. Univ. Comenianae* **76**(1): 15–38.

- Araújo, A., Barbeiro, S. and Serranho, P. (2012). Stability of finite difference schemes for complex diffusion processes, *SIAM Journal on Numerical Analysis* **50**(3): 1284–1296.
- Araújo, A., Barbeiro, S. and Serranho, P. (2015). Stability of finite difference schemes for nonlinear complex reaction–diffusion processes, *IMA Journal of Numerical Analysis* **35**(3): 1381–1401.
- Argenti, F., Lapini, A., Bianchi, T. and Alparone, L. (2013). A tutorial on speckle reduction in synthetic aperture radar images, *IEEE Geoscience and remote sensing magazine* **1**(3): 6–35.
- Armstrong, S., Kokaram, A. and Rayner, P. (1997). Nonlinear interpolation of missing data using min-max functions, *IEEE International Conference on Non-linear Signal and Image Processing*, Mackinac Island, USA.
- Atanassov, K. T. (2003). Intuitionistic fuzzy sets: past, present and future., *EUSFLAT Conf.*, pp. 12–19.
- Aubert, G. and Aujol, J.-F. (2008). A variational approach to removing multiplicative noise, *SIAM Journal on Applied Mathematics* **68**(4): 925–946.
- Aubert, G. and Kornprobst, P. (2006). *Mathematical problems in image processing: partial differential equations and the calculus of variations*, Vol. 147, Springer.
- Averbuch, A., Epstein, B., Rabin, N. and Turkel, E. (2006). Edge-enhancement postprocessing using artificial dissipation, *IEEE transactions on image processing* **15**(6): 1486–1498.
- Babu, J. J. J. and Sudha, G. F. (2016). Adaptive speckle reduction in ultrasound images using fuzzy logic on coefficient of variation, *Biomedical Signal Processing and Control* **23**: 93–103.
- Baravdish, G., Svensson, O., Gulliksson, M. and Zhang, Y. (2019). Damped second order flow applied to image denoising, *IMA Journal of Applied Mathematics* **84**(6): 1082–1111.
- Barbu, T., Barbu, V., Biga, V. and Coca, D. (2009). A pde variational approach to image denoising and restoration, *Nonlinear Analysis: Real World Applications* **10**(3): 1351–1361.
- Becerikli, Y. and Karan, T. M. (2005). A new fuzzy approach for edge detection, *International Work-Conference on Artificial Neural Networks*, Springer, pp. 943–951.
- Belahmidi, A. and Chambolle, A. (2005). Time-delay regularization of anisotropic diffusion and image processing, *ESAIM: Mathematical Modelling and Numerical Analysis* **39**(2): 231–251.
- Bertero, M. and Boccacci, P. (1998). *Introduction to inverse problems in imaging*, CRC press.

- Binaee, K. and Hasanzadeh, R. P. (2014). An ultrasound image enhancement method using local gradient based fuzzy similarity, *Biomedical Signal Processing and Control* **13**: 89–101.
- Boncelet, C. (2009). Image noise models, *The Essential Guide to Image Processing*, Elsevier, pp. 143–167.
- Boyat, A. K. and Joshi, B. K. (2015). A review paper: noise models in digital image processing, *arXiv preprint arXiv:1505.03489*.
- Buades, A., Coll, B. and Morel, J.-M. (2005a). A non-local algorithm for image denoising, *Computer Vision and Pattern Recognition, 2005. CVPR 2005. IEEE Computer Society Conference on*, Vol. 2, IEEE, pp. 60–65.
- Buades, A., Coll, B. and Morel, J.-M. (2005b). A review of image denoising algorithms, with a new one, *Multiscale Modeling & Simulation* **4**(2): 490–530.
- Burckhardt, C. B. (1978). Speckle in ultrasound b-mode scans, *IEEE Transactions on Sonics and ultrasonics* **25**(1): 1–6.
- Burg, J. (1967). Maximum entropy spectral analysis, reprinted in modern spectrum analysis (1978), DG Childers.
- Cao, Y., Yin, J., Liu, Q. and Li, M. (2010). A class of nonlinear parabolic-hyperbolic equations applied to image restoration, *Nonlinear Analysis: Real World Applications* **11**(1): 253–261.
- Caselles, V., Sapiro, G. and Chung, D. H. (2000). Vector median filters, inf-sup operations, and coupled pde's: Theoretical connections, *Journal of Mathematical Imaging and Vision* **12**(2): 109–119.
- Castleman, K. (1993). Digital image processing.
- Catté, F., Lions, P.-L., Morel, J.-M. and Coll, T. (1992). Image selective smoothing and edge detection by nonlinear diffusion, *SIAM Journal on Numerical analysis* **29**(1): 182–193.
- Chaira, T. and Ray, A. (2008). A new measure using intuitionistic fuzzy set theory and its application to edge detection, *Applied soft computing* **8**(2): 919–927.
- Chaira, T. and Ray, A. K. (2003). Segmentation using fuzzy divergence, *Pattern Recognition Letters* **24**(12): 1837–1844.
- Chambolle, A., De Vore, R. A., Lee, N.-Y. and Lucier, B. J. (1998). Nonlinear wavelet image processing: variational problems, compression, and noise removal through wavelet shrinkage, *IEEE Transactions on Image Processing* **7**(3): 319–335.
- Chambolle, A. and Lions, P.-L. (1997). Image recovery via total variation minimization and related problems, *Numerische Mathematik* **76**(2): 167–188.

- Chan, T. F. and Shen, L. (1987). Stability analysis of difference schemes for variable coefficient schrödinger type equations, *SIAM journal on numerical analysis* **24**(2): 336–349.
- Chen, Y., Barcelos, C. A. Z. and Mair, B. A. (2001). Smoothing and edge detection by time-varying coupled nonlinear diffusion equations, *Computer Vision and Image Understanding* **82**(2): 85–100.
- Chen, Y. and Bose, P. (2001). On the incorporation of time-delay regularization into curvature-based diffusion, *Journal of Mathematical Imaging and Vision* **14**(2): 149–164.
- Chen, Y. and Levine, S. (2002). Image recovery via diffusion tensor and time-delay regularization, *Journal of Visual Communication and Image Representation* **13**(1-2): 156–175.
- Chen, Y. and Wunderli, T. (2002). Adaptive total variation for image restoration in bv space, *Journal of Mathematical Analysis and Applications* **272**(1): 117–137.
- Cornwell, T. J. and Evans, K. (1985). A simple maximum entropy deconvolution algorithm, *Astronomy and Astrophysics* **143**: 77–83.
- Cottet, G.-H. and Ayyadi, M. E. (1998). A volterra type model for image processing, *IEEE transactions on image processing* **7**(3): 292–303.
- Cottet, G.-H. and Germain, L. (1993). Image processing through reaction combined with nonlinear diffusion, *Mathematics of Computation* pp. 659–673.
- Coupé, P., Hellier, P., Kervrann, C. and Barillot, C. (2008). Bayesian non local means-based speckle filtering, *Biomedical Imaging: From Nano to Macro, 2008. ISBI 2008. 5th IEEE International Symposium on*, IEEE, pp. 1291–1294.
- Crimmins, T. R. (1985). Geometric filter for speckle reduction, *Applied optics* **24**(10): 1438–1443.
- Deledalle, C.-A., Denis, L. and Tupin, F. (2009). Iterative weighted maximum likelihood denoising with probabilistic patch-based weights, *IEEE Transactions on Image Processing* **18**(12): 2661–2672.
- Deng, L., Zhu, H., Yang, Z. and Li, Y. (2019). Hessian matrix-based fourth-order anisotropic diffusion filter for image denoising, *Optics & Laser Technology* **110**: 184–190.
- DeVore, R. A., Jawerth, B. and Lucier, B. J. (1992). Image compression through wavelet transform coding, *IEEE Transactions on information theory* **38**(2): 719–746.
- Dewaele, P., Wambacq, P., Oosterlinck, A. and Marchand, J.-L. (1990). Comparison of some speckle reduction techniques for sar images, *Proceedings 10th annual international geoscience & remote sensing symposium, IGARSS'90*, Vol. 3, IEEE, pp. 2417–2422.

- Dong, G., Guo, Z. and Wu, B. (2013). A convex adaptive total variation model based on the gray level indicator for multiplicative noise removal, *Abstract and Applied Analysis*, Vol. 2013, Hindawi Publishing Corporation.
- Elliott, C. and Smitheman, S. (2009). Numerical analysis of the tv regularization and H^{-1} fidelity model for decomposing an image into cartoon plus texture, *IMA Journal of Numerical Analysis* **29**(3): 651–689.
- Elyasi, I. and Pourmina, M. A. (2016). Reduction of speckle noise ultrasound images based on tv regularization and modified bayes shrink techniques, *Optik* **127**(24): 11732–11744.
- eoPortal: Sharing Earth Observation Resources (2005). Kompsat-5.
URL: <https://directory.eoportal.org/web/eoportal/satellite-missions/k/kompsat-5>
- Evans, L. (1998). *Partial Differential Equations, Graduate Studies in Mathematics*, Vol. 19, American Mathematical Society, Providence, Rhode Island.
- Evans, L. C. (2010). *Partial differential equations*, Vol. 19, American Mathematical Soc.
- Evans, L. C. and Gariepy, R. F. (2015). *Measure theory and fine properties of functions*, CRC press.
- Fabbrini, L., Greco, M., Messina, M. and Pinelli, G. (2013). Improved edge enhancing diffusion filter for speckle-corrupted images, *IEEE Geoscience and Remote Sensing Letters* **11**(1): 99–103.
- Frieden, B. R. (1972). Restoring with maximum likelihood and maximum entropy, *JOSA* **62**(4): 511–518.
- Frieden, B. R. (1975). Image enhancement and restoration, *Picture processing and digital filtering*, Springer, pp. 177–248.
- Frost, V. S., Stiles, J. A., Shanmugan, K. S. and Holtzman, J. C. (1982). A model for radar images and its application to adaptive digital filtering of multiplicative noise, *IEEE Transactions on pattern analysis and machine intelligence* (2): 157–166.
- Gallay, T. and Raugel, G. (1998). Scaling variables and asymptotic expansions in damped wave equations, *Journal of differential equations* **150**(1): 42–97.
- Geman, S. and Geman, D. (1984). Stochastic relaxation, gibbs distributions, and the bayesian restoration of images, *IEEE Transactions on pattern analysis and machine intelligence* (6): 721–741.
- Ghislain, P. K., Loum, G. L. and Nouho, O. (2017). Adaptation of telegraph diffusion equation for noise reduction on images, *International Journal of Image and Graphics* **17**(02): 1750010.

- Gonzalez, R. C. and Woods, R. E. (2002). Digital image processing.
- Goodman, J. W. (1976). Some fundamental properties of speckle, *JOSA* **66**(11): 1145–1150.
- Guidotti, P. (2012). A backward–forward regularization of the perona–malik equation, *Journal of Differential Equations* **252**(4): 3226–3244.
- Guidotti, P. (2015). Anisotropic diffusions of image processing from perona-malik on, *Advanced Studies in Pure Mathematics* **99**: 20XX.
- Gull, S. F. and Daniell, G. J. (1978). Image reconstruction from incomplete and noisy data, *Nature* **272**(5655): 686–690.
- Gull, S. F. and Skilling, J. (1984). Maximum entropy method in image processing, *IEE Proceedings F (Communications, Radar and Signal Processing)*, Vol. 131, IET, pp. 646–659.
- Gull, S. and Skilling, J. (1990). The memsys5 user's manual, *Maximum Entropy Data Consultants Ltd, Royston*.
- Guo, Z., Yin, J. and Liu, Q. (2011). On a reaction–diffusion system applied to image decomposition and restoration, *Mathematical and Computer Modelling* **53**(5): 1336–1350.
- Hadamard, J. (2003). *Lectures on Cauchy's problem in linear partial differential equations*, Courier Corporation.
- Hao, X., Gao, S. and Gao, X. (1999). A novel multiscale nonlinear thresholding method for ultrasonic speckle suppressing, *IEEE Transactions on Medical Imaging* **18**(9): 787–794.
- Hao, Y., Xu, J., Li, S. and Zhang, X. (2015). A variational model based on split bregman method for multiplicative noise removal, *AEU-International Journal of Electronics and Communications* **69**(9): 1291–1296.
- Ho, K. H. and Ohnishi, N. (1995). Fedge fuzzy edge detection by fuzzy categorization and classification of edges, *International Workshop on Fuzzy Logic in Artificial Intelligence*, Springer, pp. 182–196.
- Hoffman, J. D. and Frankel, S. (2018). *Numerical methods for engineers and scientists*, CRC press.
- Hua, C. and Jinwen, T. (2009). Speckle reduction of synthetic aperture radar images based on fuzzy logic, *2009 First International Workshop on Education Technology and Computer Science*, Vol. 1, IEEE, pp. 933–937.
- Huang, L.-L., Xiao, L. and Wei, Z.-H. (2010). Multiplicative noise removal via a novel variational model, *EURASIP Journal on image and video processing* **2010**(1): 1.

- Huang, Y.-M., Ng, M. K. and Wen, Y.-W. (2009). A new total variation method for multiplicative noise removal, *SIAM Journal on Imaging Sciences* **2**(1): 20–40.
- Hummel, R. A. (1987). Representations based on zero-crossings in scale-space, *Readings in Computer Vision*, Elsevier, pp. 753–758.
- Jain, S. K. (2018). *A Class of Non-Linear Coupled Partial Differential Equation based Models for Image Restoration with Its Numerical Realization*, PhD thesis, Indian Institute of Technology Mandi.
- Jain, S. K., Majee, S., Ray, R. K. and Majee, A. K. (2019). Analysis and simulation of a coupled diffusion based image denoising model, *arXiv preprint arXiv:1907.04526*.
- Jain, S. K. and Ray, R. K. (2015). A non-linear diffusion based partial differential equation model for noise reduction in images, *Information Systems Design and Intelligent Applications*, Springer, pp. 429–438.
- Jain, S. K. and Ray, R. K. (2016). Edge detectors based telegraph total variational model for image filtering, *Information Systems Design and Intelligent Applications*, Springer, pp. 119–126.
- Jain, S. K. and Ray, R. K. (2019). Non-linear diffusion models for despeckling of images: achievements and future challenges, *IETE Technical Review* pp. 1–17.
- Jain, S. K., Ray, R. K. and Bhavsar, A. (2015a). A comparative study of iterative solvers for image de-noising, *Proceedings of the 3rd International Conference on Frontiers of Intelligent Computing: Theory and Applications (FICTA) 2014*, Springer, pp. 307–314.
- Jain, S. K., Ray, R. K. and Bhavsar, A. (2015b). Iterative solvers for image de-noising with diffusion models: A comparative study, *Computers & Mathematics with Applications* **70**(3): 191–211.
- Jain, S. K., Ray, R. K. and Bhavsar, A. (2018). A nonlinear coupled diffusion system for image despeckling and application to ultrasound images, *Circuits, Systems, and Signal Processing* pp. 1–30.
- Jannetta, A. (2005). *Advanced deconvolution techniques and medical radiography*, PhD thesis, Northumbria University.
- Jannetta, A., Jackson, J., Kotre, C., Birch, I., Robson, K. and Padgett, R. (2004). Mammographic image restoration using maximum entropy deconvolution, *Physics in Medicine & Biology* **49**(21): 4997–5010.
- Jaynes, E. T. (1957a). Information theory and statistical mechanics, *Physical review* **106**(4): 620.
- Jaynes, E. T. (1957b). Information theory and statistical mechanics. ii, *Physical review* **108**(2): 171.

- Jaynes, E. T. (1968). Prior probabilities, *IEEE Transactions on systems science and cybernetics* **4**(3): 227–241.
- Jidésh, P. and Bini, A. (2013). A complex diffusion driven approach for removing data-dependent multiplicative noise, *International Conference on Pattern Recognition and Machine Intelligence*, Springer, pp. 284–289.
- Jin, J. S., Wang, Y. and Hiller, J. (2000). An adaptive nonlinear diffusion algorithm for filtering medical images, *IEEE Transactions on Information Technology in Biomedicine* **4**(4): 298–305.
- Jin, Z. and Yang, X. (2010). Analysis of a new variational model for multiplicative noise removal, *Journal of Mathematical Analysis and Applications* **362**(2): 415–426.
- Jin, Z. and Yang, X. (2011). A variational model to remove the multiplicative noise in ultrasound images, *Journal of Mathematical Imaging and Vision* **39**(1): 62–74.
- Jovanović, B. S. and Süli, E. (2013). *Analysis of finite difference schemes: for linear partial differential equations with generalized solutions*, Vol. 46, Springer Science & Business Media.
- JPL (1994). Space radar image of kilauea.
URL: <https://photojournal.jpl.nasa.gov/catalog/PIA01763>
- Kichenassamy, S. (1997). The perona–malik paradox, *SIAM Journal on Applied Mathematics* **57**(5): 1328–1342.
- Kim, J., Kim, S., Lee, D. and Lim, H. (2001). Signal processing using fourier & wavelet transform for pulse oximetry, *Technical Digest. CLEO/Pacific Rim 2001. 4th Pacific Rim Conference on Lasers and Electro-Optics (Cat. No. 01TH8557)*, Vol. 2, IEEE, pp. II–II.
- Kirsch, A. (2011). *An introduction to the mathematical theory of inverse problems*, Vol. 120, Springer Science & Business Media.
- Klir, G. J. and Yuan, B. (1995). *Fuzzy sets and fuzzy logic: theory and applications*, Vol. 574, Prentice Hall PTR New Jersey.
- Koenderink, J. J. (1984). The structure of images, *Biological cybernetics* **50**(5): 363–370.
- Krissian, K. and Aja-Fernández, S. (2009). Noise-driven anisotropic diffusion filtering of mri, *IEEE transactions on image processing* **18**(10): 2265–2274.
- Krissian, K., Westin, C.-F., Kikinis, R. and Vosburgh, K. G. (2007). Oriented speckle reducing anisotropic diffusion, *IEEE Transactions on Image Processing* **16**(5): 1412–1424.
- Kuan, D. T., Sawchuk, A. A., Strand, T. C. and Chavel, P. (1985). Adaptive noise smoothing filter for images with signal-dependent noise, *IEEE Transactions on Pattern Analysis and Machine Intelligence* (2): 165–177.

- Langtangen, H. P. (2013). *Computational partial differential equations: numerical methods and diffpack programming*, Vol. 2, Springer Science & Business Media.
- Lee, J.-S. (1980). Digital image enhancement and noise filtering by use of local statistics, *IEEE transactions on pattern analysis and machine intelligence* **(2)**: 165–168.
- LeVeque, R. J. (2007). *Finite difference methods for ordinary and partial differential equations: steady-state and time-dependent problems*, Vol. 98, SIAM.
- Li, Z. (2009). *Numerical Solutions to Partial Differential Equations*, Beijing: Higher Education Press.
- Lions, J. L. (1968). *Contrôle Optimal de Systèmes Gouvernés par des Équations aux Dérivées Partielles*, Dunod, Paris.
- Lions, J. L. and Magenes, E. (1972). *Non-homogeneous boundary value problems and applications*, Vol. 2, Springer Science & Business Media.
- Liu, M. and Fan, Q. (2016). A modified convex variational model for multiplicative noise removal, *Journal of Visual Communication and Image Representation* **36**: 187–198.
- Liu, Q., Li, X. and Gao, T. (2013). A nondivergence p-laplace equation in a removing multiplicative noise model, *Nonlinear Analysis: Real World Applications* **14**(5): 2046–2058.
- Liu, X., Huang, L. and Guo, Z. (2011). Adaptive fourth-order partial differential equation filter for image denoising, *Applied Mathematics Letters* **24**(8): 1282–1288.
- Liu, X., Lai, C.-H. and Pericleous, K. A. (2015). A fourth-order partial differential equation denoising model with an adaptive relaxation method, *International Journal of Computer Mathematics* **92**(3): 608–622.
- Loizou, C. P., Pattichis, C. S., Christodoulou, C. I., Istepanian, R. S., Pantziaris, M. and Nicolaides, A. (2005). Comparative evaluation of despeckle filtering in ultrasound imaging of the carotid artery, *IEEE transactions on ultrasonics, ferroelectrics, and frequency control* **52**(10): 1653–1669.
- Luo, H., Zhu, L. and Ding, H. (2006). Coupled anisotropic diffusion for image selective smoothing, *Signal Processing* **86**(7): 1728–1736.
- Lysaker, M., Lundervold, A. and Tai, X.-C. (2003). Noise removal using fourth-order partial differential equation with applications to medical magnetic resonance images in space and time, *IEEE Transactions on image processing* **12**(12): 1579–1590.
- Majee, S., Jain, S. K., Ray, R. K. and Majee, A. K. (2019). A fuzzy edge detector driven telegraph total variation model for image despeckling, *arXiv preprint* .
URL: <https://128.84.21.199/abs/1908.01134>

- Majee, S., Jain, S. K., Ray, R. K. and Majee, A. K. (2020). On the development of a coupled nonlinear telegraph-diffusion model for image restoration, *Computers & Mathematics with Applications* **80**(7): 1745–1766.
- Majee, S., Ray, R. K. and Majee, A. K. (2020). A gray level indicator-based regularized telegraph diffusion equation applied to image despeckling, *SIAM Journal on Imaging Sciences* **13**(2): 844–870.
- Masnou, S. (2002). Disocclusion: a variational approach using level lines, *IEEE Transactions on Image Processing* **11**(2): 68–76.
- Meer, P., Park, R.-H. and Cho, K. (1994). Multiresolution adaptive image smoothing, *CVGIP: Graphical Models and Image Processing* **56**(2): 140–148.
- Metzger, G. (2012). *Transmission lines with pulse excitation*, Elsevier.
- Mikula, K. (2002). Image processing with partial differential equations, *Modern methods in scientific computing and applications*, Springer, pp. 283–321.
- Mittal, A., Moorthy, A. K. and Bovik, A. C. (2012). No-reference image quality assessment in the spatial domain, *IEEE Transactions on Image Processing* **21**(12): 4695–4708.
- Nadeem, M., Hussain, A. and Munir, A. (2019). Fuzzy logic based computational model for speckle noise removal in ultrasound images, *Multimedia Tools and Applications* pp. 1–18.
- Nakamura, J. (2016). *Image sensors and signal processing for digital still cameras*, CRC press.
- Nitzberg, M. and Shiota, T. (1992). Nonlinear image filtering with edge and corner enhancement, *IEEE transactions on pattern analysis and machine intelligence* **14**(8): 826–833.
- Nolen, J. (2009). Partial differential equations and diffusion processes, *Technical report*, Technical report, Stanford University. Department of Mathematics.
- Nordström, N. (1990). *Biased anisotropic diffusion—a unified regularization and diffusion approach to edge detection*, Springer.
- Perona, P. and Malik, J. (1990). Scale-space and edge detection using anisotropic diffusion, *IEEE Transactions on Pattern Analysis and Machine Intelligence* **12**(7): 629–639.
- Petrou, M. and Petrou, C. (2010). *Image processing: the fundamentals*, John Wiley & Sons.
- Prager, R., Gee, A., Treece, G. and Berman, L. (2001). Speckle detection in ultrasound images using first order statistics, *University of Cambridge, Department of Engineering*.

- Prasath, V. S. and Delhibabu, R. (2014). Image restoration with fuzzy coefficient driven anisotropic diffusion, *International Conference on Swarm, Evolutionary, and Memetic Computing*, Springer, pp. 145–155.
- Prasath, V. S. and Singh, A. (2010a). A hybrid convex variational model for image restoration, *Applied Mathematics and Computation* **215**(10): 3655–3664.
- Prasath, V. S. and Singh, A. (2012). An adaptive diffusion scheme for image restoration and selective smoothing, *International Journal of Image and Graphics* **12**(01): 1250003.
- Prasath, V. S. and Vorotnikov, D. (2014). On a system of adaptive coupled pdes for image restoration, *Journal of mathematical imaging and vision* **48**(1): 35–52.
- Prasath, V. and Singh, A. (2010b). Well-posed inhomogeneous nonlinear diffusion scheme for digital image denoising, *Journal of Applied Mathematics* **2010**.
- Ratner, V. and Zeevi, Y. Y. (2007). Image enhancement using elastic manifolds, *Image Analysis and Processing, 2007. ICIAP 2007. 14th International Conference on*, IEEE, pp. 769–774.
- Ratner, V. and Zeevi, Y. Y. (2011). Denoising-enhancing images on elastic manifolds, *IEEE transactions on image processing* **20**(8): 2099–2109.
- Ring, W. (2000). Structural properties of solutions to total variation regularization problems, *ESAIM: Mathematical Modelling and Numerical Analysis* **34**(4): 799–810.
- Rudin, L. I. (1987). Images, numerical analysis of singularities and shock filters.
- Rudin, L. I., Osher, S. and Fatemi, E. (1992). Nonlinear total variation based noise removal algorithms, *Physica D: Nonlinear Phenomena* **60**(1): 259–268.
- Rudin, L., Lions, P.-L. and Osher, S. (2003). Multiplicative denoising and deblurring: Theory and algorithms, *Geometric Level Set Methods in Imaging, Vision, and Graphics*, Springer, pp. 103–119.
- Scherzer, O. (2010). *Handbook of mathematical methods in imaging*, Springer Science & Business Media.
- Shan, X., Sun, J. and Guo, Z. (2019). Multiplicative noise removal based on the smooth diffusion equation, *Journal of Mathematical Imaging and Vision* pp. 1–17.
- Shannon, C. E. (1948). A mathematical theory of communication, *Bell system technical journal* **27**(3): 379–423.
- Shi, J. and Osher, S. (2008). A nonlinear inverse scale space method for a convex multiplicative noise model, *SIAM Journal on Imaging Sciences* **1**(3): 294–321.
- Shi, Y. and Chang, Q. (2006). New time dependent model for image restoration, *Applied mathematics and computation* **179**(1): 121–134.

- Siddig, A., Guo, Z., Zhou, Z. and Wu, B. (2018). An image denoising model based on a fourth-order nonlinear partial differential equation, *Computers & Mathematics with Applications* **76**(5): 1056–1074.
- Skilling, J. (1988). The axiom of maximum entropy maximum entropy and bayesian methods in science and engineering, *Dordrecht: Kluwer* **1**: 173–188.
- Skilling, J. (2013). *Maximum Entropy and Bayesian Methods: Cambridge, England, 1988*, Vol. 36, Springer Science & Business Media.
- Song, J. and Tizhoosh, H. (2003). Fuzzy anisotropic diffusion: a rule-based approach, *Proceeding of the 7th World Multiconference on Systemics, Cybernetics and Informatics*, pp. 241–246.
- Stephane, M. (1999). A wavelet tour of signal processing, *The Sparse Way*.
- Sudha, S., Suresh, G. and Sukanesh, R. (2009). Speckle noise reduction in ultrasound images by wavelet thresholding based on weighted variance, *International journal of computer theory and engineering* **1**(1): 7.
- Sun, J., Yang, J. and Sun, L. (2016). A class of hyperbolic-parabolic coupled systems applied to image restoration, *Boundary Value Problems* **2016**(1): 187.
- Szmidt, E. and Kacprzyk, J. (2000). Distances between intuitionistic fuzzy sets, *Fuzzy sets and systems* **114**(3): 505–518.
- Tai, X.-C., Lie, K.-A., Chan, T. F. and Osher, S. (2006). *Image Processing Based on Partial Differential Equations: Proceedings of the International Conference on PDE-Based Image Processing and Related Inverse Problems, CMA, Oslo, August 8-12, 2005*, Springer Science & Business Media.
- Tauber, C., Batatia, H. and Ayache, A. (2004). A robust speckle reducing anisotropic diffusion, *2004 International Conference on Image Processing, 2004. ICIP'04.*, Vol. 1, IEEE, pp. 247–250.
- Teboul, S., Blanc-Feraud, L., Aubert, G. and Barlaud, M. (1998). Variational approach for edge-preserving regularization using coupled pdes, *IEEE Transactions on Image Processing* **7**(3): 387–397.
- Teuber, T. and Lang, A. (2012). A new similarity measure for nonlocal filtering in the presence of multiplicative noise, *Computational Statistics & Data Analysis* **56**(12): 3821–3842.
- Thanh, D. N., Prasath, V. S. and Hieu, L. M. (2019). A review on ct and x-ray images denoising methods, *Informatica* **43**: 151–159.
- Theljani, A. (2015). *Partial differential equations methods and regularization techniques for image inpainting*, PhD thesis.
- Tikhonov, A. N. and Arsenin, V. I. (1977). *Solutions of ill-posed problems*, Vol. 14, Winston, Washington, DC.

- Tsai, Y.-H. R. and Osher, S. (2005). Total variation and level set methods in image science, *Acta Numerica* **14**: 509–573.
- Tur, M., Chin, K.-C. and Goodman, J. W. (1982). When is speckle noise multiplicative?, *Applied Optics* **21**(7): 1157–1159.
- Wang, Z., Bovik, A. C., Sheikh, H. R. and Simoncelli, E. P. (2004). Image quality assessment: from error visibility to structural similarity, *Image Processing, IEEE Transactions on* **13**(4): 600–612.
- Wei, G. and Jia, Y. (2002). Synchronization-based image edge detection, *EPL (Europhysics Letters)* **59**(6): 814.
- Weickert, J. (1997). A review of nonlinear diffusion filtering, *Scale-space theory in computer vision*, Springer, pp. 1–28.
- Weickert, J. (1998). *Anisotropic diffusion in image processing*, Vol. 1, Teubner Stuttgart.
- Weickert, J. (2001). Applications of nonlinear diffusion in image processing and computer vision, *Acta Math. Univ. Comenianae* **70**(1): 33–50.
- Weickert, J. and Benhamouda, B. (1997). A semidiscrete nonlinear scale-space theory and its relation to the perona—malik paradox, *Advances in computer vision*, Springer, pp. 1–10.
- Wesseling, P. (1995). Introduction to multigrid methods.
- White, R. G. (1994). A simulated annealing algorithm for sar and mti image cross-section estimation, *Proc. SPIE*, Vol. 2316, vol, pp. 137–145.
- Witkin, A. P. (1983). Scale-space filtering, *Proc. Eighth Int. Joint Conf. on Artificial Intelligence (IJCAI '83, Karlsruhe, Aug. 8–12, 1983)*, Vol. 2, pp. 1019–1022.
- Xu, J., Hao, Y., Li, M. and Zhang, X. (2019). A novel variational model for image decomposition, *Signal, Image and Video Processing* **13**(5): 967–974.
- Yang, Y.-Q. and Zhang, C.-Y. (2014). Kernel based telegraph-diffusion equation for image noise removal, *Mathematical Problems in Engineering* **2014**.
- Yaroslavsky, L. P. (2014). Fast transforms in image processing: compression, restoration, and resampling, *Advances in Electrical Engineering* **2014**.
- You, Y.-L. and Kaveh, M. (1998). Image enhancement using fourth order partial differential equations, *Conference Record of Thirty-Second Asilomar Conference on Signals, Systems and Computers (Cat. No. 98CH36284)*, Vol. 2, IEEE, pp. 1677–1681.
- You, Y.-L. and Kaveh, M. (2000). Fourth-order partial differential equations for noise removal, *IEEE Transactions on Image Processing* **9**(10): 1723–1730.

- Yu, Y. and Acton, S. T. (2002). Speckle reducing anisotropic diffusion, *IEEE Transactions on image processing* **11**(11): 1260–1270.
- Zanella, R., Porta, F., Ruggiero, V. and Zanetti, M. (2018). Serial and parallel approaches for image segmentation by numerical minimization of a second-order functional, *Applied Mathematics and Computation* **318**: 153–175.
- Zanetti, M., Ruggiero, V. and Miranda Jr, M. (2016). Numerical minimization of a second-order functional for image segmentation, *Communications in nonlinear science and numerical simulation* **36**: 528–548.
- Zauderer, E. (2011). *Partial differential equations of applied mathematics*, Vol. 71, John Wiley & Sons.
- Zeng, W., Lu, X. and Tan, X. (2011). A class of fourth-order telegraph-diffusion equations for image restoration, *Journal of Applied Mathematics* **2011**.
- Zhang, F., Yoo, Y. M., Koh, L. M. and Kim, Y. (2007). Nonlinear diffusion in laplacian pyramid domain for ultrasonic speckle reduction, *IEEE Transactions on Medical Imaging* **26**(2): 200–211.
- Zhang, W., Li, J. and Yang, Y. (2014). A class of nonlocal tensor telegraph-diffusion equations applied to coherence enhancement, *Computers & Mathematics with Applications* **67**(8): 1461–1473.
- Zhang, W., Li, J. and Yang, Y. (2015). Spatial fractional telegraph equation for image structure preserving denoising, *Signal Processing* **107**: 368–377.
- Zhang, X. and Ye, W. (2017). An adaptive fourth-order partial differential equation for image denoising, *Computers & Mathematics with Applications* **74**(10): 2529–2545.
- Zheng, S. (1995). *Nonlinear parabolic equations and hyperbolic-parabolic coupled systems*, CRC Press.
- Zhou, Z., Guo, Z., Dong, G., Sun, J., Zhang, D. and Wu, B. (2015). A doubly degenerate diffusion model based on the gray level indicator for multiplicative noise removal, *IEEE Transactions on Image Processing* **24**(1): 249–260.
- Zhou, Z., Guo, Z., Zhang, D. and Wu, B. (2018). A nonlinear diffusion equation-based model for ultrasound speckle noise removal, *Journal of Nonlinear Science* **28**(2): 443–470.